

Characterisation of coated lightweight brake rotors

by

Abdulwahab Ali Alnaqi

Submitted in accordance with the requirements

for the degree of Doctor of Philosophy

The University of Leeds

School of Mechanical Engineering

July 2014

The candidate confirms that the work submitted is his own and that appropriate credit has been given where reference has been made to the work of others.

This copy has been supplied on the understanding that it is copyright material and that no quotation from the thesis may be published without proper acknowledgement.

Intellectual Property and Publication Statements

The candidate confirms that the work submitted is his own, except where work which has formed part of jointly-authored publications has been included. The contribution of the candidate and the other authors to this work has been explicitly indicated below. The candidate confirms that appropriate credit has been given within the thesis where reference has been made to the work of others.

Paper	Chapter
G. Bozic, A. A. Alnaqi, P. C. Brooks, and D. C. Barton, "Thermal Characterisation of Lightweight Brake Rotors for Passenger Car Application Using A small Scale Brake Dynamometer and One Dimensional Model," <i>Eurobrake 2012</i> , Germany, 2012.	Ch. 1, 2, 4 and 5
A. A. Alnaqi, D. C. Barton, and P. C. Brooks, <i>Thermal Performance of Monolithic and Coated Disc Brakes Using Abaqus and Matlab Software</i> , Vienna, Austria, SIMULIA Community Conference, 2013.	Ch. 1, 2, 4 and 5
A. A. Alnaqi, S. Shrestha, P. C. Brooks, and D. C. Barton, "Thermal Performance of PEO Coated Lightweight Brake Rotors Compared with Grey Cast Iron," <i>Eurobrake 2014</i> , France, 2014.	Ch. 1, 2, 6 and 7
A. A. Alnaqi, S. Shrestha, P. C. Brooks, and D. C. Barton, "Optimisation of alumina coated lightweight brake rotor," <i>SAE 2014</i> , USA, 2014.	Ch. 1, 2, 7 and 9
A. A. Alnaqi, D. C. Barton, and P. C. Brooks, "Reduced scale thermal characterization of automotive disc brake," <i>Applied thermal engineering</i> , 2014.	Ch. 1, 2, 6 and 7
A. A. Alnaqi, S. Kosarieh, D. C. Barton, P. C. Brooks, and S. Shrestha, "Material characterisation of lightweight disc brake rotors," 2014.	Ch. 1, 2, 3 and 8

The candidate undertook major tasks of the work presented in these published papers, such as undertaking experimental works, design, analysing and presenting the results. The co-authors reviewed and guided the candidate and provided valuable discussion.

This copy has been supplied on the understanding that it is copyright material and that no quotation from the thesis may be published without proper acknowledgement.

The right of Abdulwahab A. A. Alnaqi to be identified as Author of this work has been asserted by him in accordance with the Copyright, Designs and Patents Act 1988.

To my wife, Hussah', who has been patient, supportive, and shared many sacrifices during the completion of this thesis. Also, to my little sons, Mohammad and Ali, who are a constant source of happiness. To my parents for their endless support.

Acknowledgement

First and foremost I would like to offer my sincerest gratitude to my supervisors, Professor David Barton and Dr. Peter Brooks, for their support and encouragement during my PhD research. Your advice on both my career as well as on my research has been priceless. One simply could not wish for better or friendlier supervisors.

I also owe my deepest thanks to Tony Wiese and David Readman for their help and support in the laboratory during the experimental work. Special thanks to Tony Wiese for his support in the research and for being a great friend.

Moreover, I would like to thank Professor Suman Shrestha from Keronite International Ltd for his support and valuable advice throughout this research. Also, special thanks to my colleagues Abdulaziz Alghatani, Ranvir kalare and Shahriar Kosarieh for sharing experiences, knowledge and advice.

I would also like to thank the Public Authority for Applied Education and Training and the Kuwait National Government for their financial support throughout my study.

Finally, I would like to express my love and appreciation to my family in Kuwait for their infinite love and support. Furthermore, I would like to express my special thanks for my beloved wife, Hussah, and my lovely sons, Mohammad and Ali, for sharing good and hard times during my PhD.

Abstract

Numerical and experimental studies were undertaken using lightweight brake rotors to reduce vehicle weight and thereby improve fuel efficiency and vehicle emissions. Abaqus finite element and Matlab software were used to construct one dimensional (1D), two dimensional (2D) and three dimensional (3D) thermal models to investigate the general thermal performance of disc brakes to develop a valid method of reduced scale testing. Five small scale solid brake rotors were investigated experimentally: grey cast iron, wrought aluminium alloy (6082), the same 6082 alloy with an alumina surface layer applied by plasma electrolytic oxidation (PEO), cast aluminium MMC (AMC640XA) and the same MMC with a PEO alumina surface layer. The disc and pad temperatures, brake pressure, coefficient of friction and brake torque were monitored during the tests for each material. Surface morphology, microstructure and micro hardness of the coatings and substrate were evaluated before and after the tests. Numerical simulations confirmed the equivalence between the full and small scale disc thermal performance using the proposed scaling methodology and also provide a good agreement with the experimental results.

The coated 6082 alloy rotor was shown to give good thermal and friction performance up to relatively high rubbing surface temperatures of around 500°C. This rotor failed at a surface temperature of about 550°C due to brittle fracture of the wrought aluminium substrate. The proposed scaling methodology was shown to be a valid method of investigating a rotor design concept in the laboratory at low cost and reduced operating time. The PEO coating on aluminium alloy was denser and more uniform compared to the PEO coating on aluminium MMC. In addition, the PEO coating improved the hardness and thermal resistance of both the aluminium alloy and aluminium MMC. A sensitivity analysis based on the Taguchi approach was carried out on the PEO coated aluminium alloy rotor to investigate the effect of various parameters on thermal performance. Optimisation of the structure was carried out using a genetic algorithm to design coated aluminium alloy discs that are potentially technically viable on small-medium passenger cars.

Keywords: lightweight rotor, finite element model, plasma electrolytic oxidation, optimisation, material characterisation, brake dynamometer and scaling methodology.

List of Contents

Acknowledgement	iv
Abstract.....	v
List of Contents	vi
Nomenclature.....	xvi
List of Abbreviations.....	xxi
List of Figures.....	xxii
List of Tables	xxxii
Chapter 1: Introduction	1
1.1 Research overview and background.....	1
1.2 Research aim and objectives	7
1.2.1 Aim.....	7
1.2.2 Objectives.....	7
1.3 Structure of remainder of thesis	7
Chapter 2: Literature Review	10
2.1 Overview	10
2.2 Disc brake system overview	11
2.3 Thermal analysis of rotors.....	14
2.3.1 Simple one-dimensional analysis	15
2.3.2 Finite element analysis	19
2.3.3 Experimental analysis	22

2.4	Scaling methodologies	23
2.5	Investigation of disc brake rotor material	25
2.6	Aluminium alloys.....	27
2.6.1	General background	27
2.6.2	Aluminium alloys classifications and properties	28
2.6.3	Aluminium alloys applications	30
2.6.4	Surface engineering on aluminium alloys and aluminium metal matrix composite	31
2.7	Aluminium metal matrix composite.....	31
2.7.1	General background	31
2.7.2	Aluminium metal matrix composite classifications and properties	32
2.7.3	Aluminium metal matrix composite applications	32
2.7.4	Surface engineering of aluminium metal matrix composite	33
2.8	Coating technologies.....	33
2.8.1	Keronite PEO coating technology.....	36
2.9	Design of experiment (DoE) and optimisation analysis	40
2.10	Summary of the findings and implications for the current research	42
Chapter 3: Material and characterisation method		45
3.1	Introduction.....	45
3.2	Materials.....	45
3.2.1	Grey cast iron	46

3.2.2	Aluminium alloy	46
3.2.3	Aluminium metal matrix composite.....	47
3.2.4	PEO coating	47
3.2.5	Brake pad material	48
3.3	Sample preparation and metallographic preparation of samples	49
3.4	Experimental techniques	52
3.4.1	Optical microscopy of materials	53
3.4.2	Scanning Electron Microscopy (SEM) and Energy-Dispersive X-ray analysis (EDX).....	53
3.4.2.1	SEM and EDX fundamentals	53
3.4.2.2	SEM and EDX sample preparation	55
3.4.3	Micro-Hardness tests.....	58
3.4.4	Roughness analysis	59
3.4.5	Geometry measurement	60
3.5	Summary	62
Chapter 4: One-dimensional thermal models		63
4.1	Introduction	63
4.2	Background and theories.....	64
4.2.1	Fourier's law for heat conduction	64
4.2.2	Newton's law of cooling	65
4.2.3	Radiation heat transfer	66

4.2.4	Thermal contact resistance	66
4.2.5	Braking energy and power of the vehicle	66
4.3	One-dimensional thermal model theory	68
4.3.1	Assumption	68
4.3.2	Formulation	69
4.3.3	Initial condition parameters and initialization.....	74
4.3.4	Solution procedure	77
4.3.5	Matlab model structure	79
4.3.6	Sensitivity analysis.....	81
4.3.7	Limitations	82
4.4	Abaqus One Dimensional Model.....	83
4.5	Validation of the One-dimensional Matlab model.....	86
4.5.1	Validation of the 1D model against literature	86
4.5.2	Validation of the 1D Matlab model with 1D Abaqus model	88
4.6	Coating layer study	88
4.6.1	Thermal resistance modelling	89
4.6.2	Mesh density analysis	92
4.6.3	Sub-modelling analysis	94
4.7	Controlling the Abaqus model through Matlab code.....	99
4.7.1	Problem definition.....	99
4.7.2	Solution procedure	99

4.7.3	Benefits	101
4.8	Parametric study.....	101
4.8.1	Effects of disc materials	101
4.8.2	Effects of convective heat loss	102
4.8.3	Effects of disc thickness.....	103
4.8.4	Effects of pad material	104
4.8.5	Effects of initial vehicle velocity	105
4.8.6	Effects of vehicle mass.....	106
4.8.7	Effect of rotating heat source	107
4.8.8	Effect of coating thickness	108
4.9	Summary	109
Chapter 5: Scaling methodologies and test rig design.....		111
5.1	Introduction	111
5.2	Scaling methodologies	112
5.2.1	Scaling method.....	112
5.2.2	Scaling principle.....	112
5.2.2.1	Rotational inertia.....	112
5.2.2.2	Disc mass	114
5.2.2.3	Brake torque	115
5.2.2.4	Functional parameter.....	116
5.2.3	Selection of vehicle for scaling	119

5.2.4	Scaling summary	120
5.3	Test rig design and development.....	122
5.3.1	Small scale brake dynamometer	122
5.3.1.1	General layout	123
5.3.1.2	Load calculations and design	124
5.3.1.3	Clutch and actuator selection	126
5.3.1.4	Main shaft design	128
5.3.1.5	Brake system selection and design.....	129
5.3.1.6	Data acquisition and sensors	133
5.3.1.7	Test rig specification and limitation.....	142
5.3.2	Full scale brake dynamometer	143
5.3.2.1	General layout	143
5.3.2.2	Small scale disc adapter	145
5.3.2.3	Data acquisition and sensors	145
5.3.2.4	Test rig specification and limitation.....	148
5.3.3	Comparison between full and small scale rigs.....	148
5.4	Calibration and commissioning of test rigs.....	150
5.4.1	Test rig setup and configuration.....	150
5.4.2	Sensor calibration.....	154
5.4.3	Test rig commissioning	161
5.5	Requisition of test samples.....	163

5.6	Summary	164
Chapter 6: Thermal analysis using finite element models		165
6.1	Introduction	165
6.2	Two dimensional axisymmetric transient thermal model for small scale discs..	167
6.2.1	Model setup and boundary conditions	167
6.2.2	Mesh sensitivity analysis	168
6.3	Three dimensional coupled temperature model for small scale discs.....	170
6.3.1	Model setup	170
6.3.2	Mesh sensitivity analysis	174
6.4	Comparison between the finite element models	176
6.5	Two dimensional axisymmetric model for full scale disc	178
6.6	Two dimensional axisymmetric model for a small scale disc with coating..	179
6.7	Summary	179
Chapter 7: Experimental and numerical results		181
7.1	Introduction	181
7.2	Test matrix development.....	183
7.3	Experimental and numerical results	185
7.3.1	Characteristics of thermal results for small scale discs.....	185
7.3.2	Full scale disc	197
7.3.3	Coefficient of friction.....	199

7.3.4	Observation of the coating layer during the test	202
7.4	Scaling methodology validation.....	204
7.5	Thermal performance of the failed coated wrought aluminium alloy disc brake rotor	210
7.6	Summary	212
Chapter 8: Material characterisation results		214
8.1	Introduction	214
8.2	Microstructure and morphology analysis.....	214
8.2.1	Before braking tests.....	214
8.2.1.1	Wrought aluminium alloy substrate	214
8.2.1.2	Aluminium metal matrix composite substrate	217
8.2.1.3	Plasma electrolytic oxidation coating	220
8.2.1.4	Brake pads	228
8.2.2	After braking tests	230
8.2.2.1	Disc brake rotor.....	230
8.2.2.2	Brake pads	237
8.3	Surface hardness measurements.....	238
8.4	Roughness analysis	239
8.5	Coating durability and transfer layer analysis.....	239
8.6	Characterisation of the failed coated wrought aluminium disc brake rotor ..	242
8.7	Summary	244

Chapter 9: Design of experiment and optimisation analysis	246
9.1 Introduction	246
9.2 Nominated finite element models	246
9.3 The Taguchi study	247
9.3.1 Fundamentals	247
9.3.2 Uncoated disc brake rotor	248
9.3.3 Coated disc brake rotor	254
9.4 Optimisation analysis	258
9.5 Validation of the optimum results	263
9.6 Summary	266
Chapter 10: Discussion of key findings	267
10.1 Introduction	267
10.2 The importance of numerical and experimental analysis in the area of lightweight disc brake rotor	267
10.3 Application of surface engineering techniques to understand the capabilities of aluminium alloy brake rotors	271
10.4 Importance of optimisation analysis for coated aluminium alloy rotors.....	272
10.5 Industrial and academic implications for the current work.....	273
10.6 Summary	273
Chapter 11: Conclusions and future work	275
11.1 Conclusion	275
11.2 Suggestions for future work	277

REFERENCES.....	279
APPENDIX A: ASSEMBLY AND DISASSEMBLY PROCEDURE	293
APPENDIX B: TEST RIG COMISSIONING OUTPUT	295
APPENDIX C: LIST OF PUBLICATIONS	296

Nomenclature

α	Thermal diffusivity	$[m^2 / s]$
γ	The ratio of heat flux into the pad to the total heat flux	[---]
τ	Brake torque	$[Nm]$
ξ	Heat flux correction factor	[---]
μ_a	The viscosity of the air	$[kg / ms]$
μ	The coefficient of friction	[---]
α_d	Average angular deceleration of the disc	$[rad / s^2]$
ρ	Material density	$[kg / m^3]$
ρ_a	The density of the air	$[kg / m^3]$
ε	Emissivity	[---]
σ	Stefan-Boltzmann constant	$[W / m^2 K^4]$
θ_p	Pad arc angle	[°]
$\omega_{i/f}$	Initial/final rotational speed	$[rad / s]$
ω_S	Small scale rotational speed	$[rad / s]$
ω_F	Full scale rotational speed	$[rad / s]$
A	Pad area	$[m^2]$
A_F	Full scale pad area	$[m^2]$
A_S	Small scale pad area	$[m^2]$

A_{piston}	Caliper piston cross-sectional area	$[m^2]$
A_{cyl}	Master cylinder cross-sectional area	$[m^2]$
a	Deceleration of the vehicle	$[m/s^2]$
c_d	Disc circumference at mean rubbing radius	$[m]$
c_p	Specific heat capacity	$[J/kg.K]$
d	Rate of deceleration	$[g]$
d_o	Brake disc outer diameter	$[m]$
d_p	Circumferential distance at mean rubbing radius	$[m]$
d_r	Ratio of disc outer diameter to inner rubbing diameter	$[m]$
d_i	Wheel rolling diameter	$[m]$
E_b	Braking energy	$[J]$
E_F	Total energy for full scale	$[kg.m^2/s^2]$
\dot{E}_g	Rate of thermal energy generation	$[W]$
\dot{E}_{in}	Rate of energy transfer into a control volume	$[W]$
\dot{E}_{out}	Rate of energy transfer out of a control volume	$[W]$
E_s	Total energy for small scale	$[kg.m^2/s^2]$
\dot{E}_{st}	Rate of stored energy within a control volume	$[W]$
F	Deceleration force	$[N]$

F_{cyl}	Master cylinder force	[N]
F_f	Brake force at each front wheel	[N]
F_n	Normal force at mean rubbing radius	[N]
F_t	Tangential force at mean rubbing radius	[N]
h	Convective heat transfer coefficient	[W / m ² .K]
h_{cond}	Thermal contact conductance	[W / m ² .K]
I	Mass moment of inertia of rotating object	[kg.m ²]
I_F	Full scale rotational inertia	[kg.m ²]
I_S	Small scale rotational inertia	[kg.m ²]
k	Thermal conductivity coefficient	[W / m.K]
k_a	Thermal conductivity coefficient of the air	[W / m.K]
L_R	Brake disc thickness	[m]
K	Correction factor of rotating masses	[---]
m	Vehicle Mass	[kg]
m_d	Disc mass	[kg]
M	Vehicle corner mass	[kg]
M_F	Full scale vehicle corner mass	[kg]
M_S	Small scale vehicle corner mass	[kg]
N_n	Number of nodal points`	[---]

P_F	Full scale contact pressure	[Pa]
P_S	Small scale contact pressure	[Pa]
P_b	Braking power on a single front tyre of the vehicle	[Nm / s]
\dot{q}	Heat flux per unit volume	[W / m ³]
Q	Heat energy quantity	[J]
q_x''	Heat flux per unit area	[W / m ²]
q_{conv}''	Convective heat flux per unit area	[W / m ²]
q_{rad}''	Radiation heat flux per unit area	[W / m ²]
q_x	Heat rate by conduction	[W]
r_d	Mean rubbing radius of disc brake	[m]
r_{dF}	Mean rubbing radius of full scale disc brake	[m]
r_{dS}	Mean rubbing radius of small scale disc brake	[m]
R	Tyre radius	[m]
R_{cond}	Thermal contact resistance	[m ² K / W]
R_e	Effective rolling radius	[m]
R_{eF}	Full scale effective rolling radius	[m]
R_{eS}	Small scale effective rolling radius	[m]
R_G	Radius of gyration	[m]

Re	Reynolds number	[---]
S	Scaling factor	[---]
tc	Brake disc thickness	[m]
ts	Coating thickness	[m]
t_s	Stop time	[s]
T	Temperature	[$^{\circ}C$]
T_{sur}	Absolute Temperature of the surface	[$^{\circ}C$]
T_s	Surface Temperature	[$^{\circ}C$]
T_{∞}	Surroundings temperature	[$^{\circ}C$]
$v_{i/f}$	Initial/final forward vehicle velocity	[km/h]
v_s	Sliding velocity	[m/s]
w_p	Radial pad thickness	[m]
x_f	The proportion of braking at the front axle	[---]
x_r	The proportion of braking at the rear axle	[---]

Note: subscripts C/R indicate coating/substrate (rotor) for all variables. Subscript P indicates Pad for all variables.

List of Abbreviations

+ve	Positive
-ve	Negative
1D	One Dimension
2D	Two Dimension
3D	Three Dimension
Al	Aluminium
Al-MMC	Aluminium metal matrix composite
Al-Alloy	Wrought aluminium alloy
CAD	Computer-Aided Design
DC	Direct Current
EDX	Energy-dispersive X-ray spectroscopy
FEA	Finite Element Analysis
GCI	Grey cast iron
PEO	Plasma electrolytic oxidation
PhD	Doctor of Philosophy
SAE	Society of Automotive Engineering
S/N ratio	Signal to Noise Ratio
SEM	Scanning electron microscope
TCR	Thermal contact resistance

List of Figures

Figure 2.1: Literature review overview.....	11
Figure 2.2: Basic components of an automotive brake system [51].	13
Figure 2.3: Schematic diagram of both disc and drum brakes [51].	13
Figure 2.4: Calculated temperature rise of the brake components during the Alpine test [13].	18
Figure 2.5: History of aluminium production in main countries and regions since 1950 [67].	27
Figure 2.6: Aluminium alloy designation system [68].....	28
Figure 2.7: World consumption of aluminium by application [69].	30
Figure 2.8: Global MMC outlook by application/segment, 2004-2013 KG 1,000S [77].	33
Figure 2.9: Keronite PEO process [90].	37
Figure 2.10: Cross-sectional BSEM image of Keronite coating on AA2219 alloy [30].	39
Figure 2.11: XRD analysis of Keronite coating on AA2219 alloy [30].	39
Figure 3.1: EDX image of the brake pad before the brake testing.....	49
Figure 3.2: Automatic mounting press machine.	50
Figure 3.3: Preparing the coating and cross-sectional view samples.....	50
Figure 3.4: Preparing the small scale brake rotor rubbing surface samples for material characterisation analysis.....	51
Figure 3.5: Complete procedure used to prepare the sample.	52
Figure 3.6: Leica microscope (LEICA CTR6000 and LEICA DM600M).	53

Figure 3.7: The Scanning Electron Microscopy machine with the integrated Energy-Dispersive X-ray system (Carl Zeiss EVO MA15 SEM machine with integrated Oxford Instrument INCA 250 EDX system).	54
Figure 3.8: Types of sample used in the SEM analysis.	55
Figure 3.9: Main components used in preparing the sample for the SEM analysis.	56
Figure 3.10: EMSCOPE TB500 SEM Carbon Coater.	57
Figure 3.11: EMSCOPE SC500 Gold Sputter Coater.	57
Figure 3.12: Sample surface before and after coating.	58
Figure 3.13: Micro Vickers Hardness Testing Machine (Mitutoyo HM-122 Hardness testing machine).	59
Figure 3.14: NP Flex optical interferometer (Bruker NPFLEX optical profiling system).	60
Figure 3.15: Trace positions for roughness analysis on the small scale disc brake rotor.	60
Figure 3.16: Kemco 400 CNC coordinate measurement (CMM) machine.	61
Figure 4.1: The three modes of heat transfer [102].	64
Figure 4.2: Heat flux distribution between the disc and pad.	69
Figure 4.3: One dimensional thermal model for a brake disc.	70
Figure 4.4: One dimensional thermal model for a coated brake disc.	73
Figure 4.5: The overall Matlab model structure.	80
Figure 4.6: Sensitivity analysis simulation.	81
Figure 4.7: One dimensional FE model of brake disc in Abaqus.	83
Figure 4.8: The overall Abaqus model structure.	84

Figure 4.9: Mesh density sensitivity analysis for 1D Abaqus model.....	86
Figure 4.10: Disc surface temperature comparison between the current model and Newcomb [10].....	87
Figure 4.11: Validation of the Matlab numerical model with the Abaqus model.....	88
Figure 4.12: One dimensional transient models.....	89
Figure 4.13: Temperature distribution across the disc and pad without tuning.	91
Figure 4.14: Temperature distribution across the disc and pad with convection tuning.	92
Figure 4.15: Temperature across the disc and pad brake for different mesh density through the coating.....	93
Figure 4.16: Temperature between the disc and coating for different mesh density.	94
Figure 4.17: Global and local 1D thermal models of disc brake.	95
Figure 4.18: Temperature distribution of the global 1D thermal models at $t=4s$	96
Figure 4.19: Temperature distribution of the local coating thermal models at $t=4s$	97
Figure 4.20: Temperature distribution of the local substrate thermal models at $t=4s$	97
Figure 4.21: Temperature distribution of the local pad thermal models at $t=4s$	98
Figure 4.22: Temperature distribution of the local and global models at $t=4s$	98
Figure 4.23: The overall Matlab/Abaqus model structure.	100
Figure 4.24: Disc brake temperature distribution for different disc materials.	102
Figure 4.25: Disc brake temperature distribution for different convective heat transfer coefficients.	103
Figure 4.26: Disc brake temperature distribution for different disc thicknesses.	104
Figure 4.27: Disc brake temperature distribution for different pad materials.....	105

Figure 4.28: Disc brake temperature distribution for different initial velocities.	106
Figure 4.29: Disc brake temperature distribution for different vehicle masses.	107
Figure 4.30: Effect of rotating heat on the temperature distribution of the disc brake.	108
Figure 4.31: Effect of coating thickness on the temperature distribution of the disc brake.	109
Figure 5.1: Fiat Punto disc brake rotor geometry.	120
Figure 5.2: General layout of the small scale brake dynamometer.	124
Figure 5.3: Flywheel mass against scaling factor for different vehicle sizes.	125
Figure 5.4: Nexen L600 clutch unit schematic [116].	126
Figure 5.5: ACME Screw Linear Actuator (LMR 01) [117].	127
Figure 5.6: ACME Screw Linear Actuator (LMR 01) performance [117].	128
Figure 5.7: Main shaft layout	129
Figure 5.8: Wilwood PS1 caliper [119].	130
Figure 5.9: 3D model of PS1 Caliper support arrangement.	130
Figure 5.10: Wilwood brake pads [119].	131
Figure 5.11: Small scale brake pad geometry.	132
Figure 5.12: Wilwood master cylinder and support arrangement [119].	133
Figure 5.13: National instrument BNC-2090 adapter [120].	134
Figure 5.14: General data acquisition configuration of the small scale test rig.	134
Figure 5.15: Speed sensor configuration.	135
Figure 5.16: Pressure transducer setup.	136

Figure 5.17: Rubbing thermocouple configuration.....	137
Figure 5.18: Brake pad embedded thermocouple location.....	137
Figure 5.19: Brake pad with embedded thermocouples.....	138
Figure 5.20: Thermal imaging system configuration on the small scale rig.....	138
Figure 5.21: Load cell configuration.....	139
Figure 5.22: Linear actuator configuration.	140
Figure 5.23: Pneumatic clutch set-up configuration.	140
Figure 5.24: LabView user interface window.....	141
Figure 5.25: General layout of the full scale brake dynamometer.....	144
Figure 5.26: Full brake dynamometer.....	144
Figure 5.27: Small scale adaptor.....	145
Figure 5.28: Experimental setup of small scale brake dynamometer.	146
Figure 5.29: Full and small scale disc brake rotor thermocouple position.	147
Figure 5.30: Full scale brake pad geometry.	147
Figure 5.31: Full scale brake system configuration.	148
Figure 5.32: Experimental setup for small scale test rig.....	152
Figure 5.33: Experimental setup for full scale test rig.....	153
Figure 5.34: Manual mechanical press arrangement for compression loads.	155
Figure 5.35: Linear regression between output voltage and applied load for load cell calibration.....	156
Figure 5.36: Hydraulic dead weight tester for calibrating the pressure transducer.	157

Figure 5.37: Linear regression between output voltage and hydraulic pressure for pressure transducer calibration.....	158
Figure 5.38: Linear regression between output voltage and temperature for thermocouple calibration.....	159
Figure 5.39: Polynomial regression between actuator input voltage and brake line pressure for linear actuator.....	160
Figure 5.40: Position of the thermocouples on the bearings.....	162
Figure 5.41: Bearing surface temperature without braking condition at 1500 rpm.	162
Figure 5.42: CAD representation of the reduced scale disc brake.	163
Figure 6.1: Finite element model selection.	166
Figure 6.2: 2D axisymmetric thermal model setup and conditions.	167
Figure 6.3: 3D FE model assembly.....	171
Figure 6.4: Thermal boundary conditions.....	171
Figure 6.5: Disc and pad boundary condition before braking.....	172
Figure 6.6: Disc and pad boundary conditions during braking.....	173
Figure 6.7: 3D model steps overview.	174
Figure 6.8: Surface temperature at mean rubbing radius for different disc brake models.	177
Figure 6.9: 2D axisymmetric thermal model setup and conditions for full scale disc..	178
Figure 6.10: 2D axisymmetric thermal model setup and conditions for a coated small scale disc.	179
Figure 7.1: Overview of experimental work using brake dynamometer.	182

Figure 7.2: Uncoated aluminium alloy rotor after test showing degraded rubbing surface.	186
Figure 7.3: Temperature responses of the aluminium MMC disc.	187
Figure 7.4: Temperature responses of the coated aluminium MMC disc.	188
Figure 7.5: Temperature responses of the coated aluminium alloy disc.	189
Figure 7.6: Temperature responses of the GCI disc.	190
Figure 7.7: Temperature response of the coated aluminium alloy disc, Test 7.	191
Figure 7.8: Comparison between the sliding thermocouples and high speed thermal imaging system for coated wrought aluminium rotor (test 5).	192
Figure 7.9: Comparison between the sliding thermocouples and high speed thermal imaging system for grey cast iron rotor (test 9).	193
Figure 7.10: Temperature response of different disc brake materials.	194
Figure 7.11: Numerical and experimental temperature response for the GCI disc.	196
Figure 7.12: Numerical and experimental temperature response for the coated Al-MMC disc.	196
Figure 7.13: Measured disc surface temperature for the full scale disc brake rotor.	198
Figure 7.14: Coefficient of friction for the full scale Fiat Punto disc.	198
Figure 7.15: Temperature and COF response of the full scale disc brake.	199
Figure 7.16: Average coefficient of friction for the small scale disc brake rotor.	200
Figure 7.17: Temperature and COF response of the coated Al-alloy disc brake (test 9).	201
Figure 7.18: Temperature and COF response of the coated Al-MMC disc brake (test 9).	202

Figure 7.19: Surface appearance of the coated Al-alloy before the tests.....	203
Figure 7.20: Surface appearance of the coated aluminium alloy after testing showing a dark transfer layer.	203
Figure 7.21: Disc surface temperature for small scale and full scale discs for condition 1.....	205
Figure 7.22: Disc surface temperature for small scale and full scale discs under condition 2.....	205
Figure 7.23: Two dimensional axisymmetric finite element model for small scale discs.	206
Figure 7.24: Validation of the full disc surface temperature.	206
Figure 7.25: Numerical disc surface temperature for small and full scale discs during high drag braking.	207
Figure 7.26: Temperature distribution of the small scale disc at different time steps. .	208
Figure 7.27: Temperature distribution of the full scale disc at different time steps.	209
Figure 7.28: Temperature distribution of the coated wrought aluminium disc brake rotor before the catastrophic failure.....	210
Figure 7.29: Effect of vehicle mass on the maximum temperature of the disc brake...	211
Figure 8.1: Surface morphology of wrought aluminium alloy before braking tests.....	215
Figure 8.2: EDX analysis for wrought aluminium alloy before braking tests in three different regions (a), (b) and (c).....	216
Figure 8.3: SEM micrograph showing surface morphology of the aluminium metal matrix composite before braking tests.	218
Figure 8.4: Optical micrograph of the microstructure of the aluminium metal matrix composite before braking tests.....	218

Figure 8.5: EDX analysis for the aluminium metal matrix composite before braking tests in two different regions (a) and (b).	219
Figure 8.6: Surface morphology of PEO coating for the aluminium metal matrix composite substrate before braking tests.....	221
Figure 8.7: Surface morphology of PEO coating for the wrought aluminium alloy substrate before braking tests.	222
Figure 8.8: Cross sectional view for the coated wrought aluminium alloy substrate before braking tests: (a) SEM and (b) optical micrograph.....	223
Figure 8.9: Cross sectional view for the coated aluminium metal matrix composite substrate before braking tests.	224
Figure 8.10: EDX analysis for coated wrought aluminium (6082) substrate before braking tests in two different regions (a) and (b).	225
Figure 8.11: EDX analysis for the coated aluminium metal matrix composite substrate before braking tests in three different regions (a), (b) and (c).	226
Figure 8.12: EDX analysis for the brake pad before braking tests in three different regions (a), (b) and (c).	229
Figure 8.13: EDX analysis for the coated wrought aluminium substrate rubbing surface after braking tests in two different regions (a) and (b).	231
Figure 8.14: EDX map image of the coated aluminium alloy rubbing surface of disc brake rotor after testing.	233
Figure 8.15: EDX analysis for the coated aluminium metal matrix composite substrate rubbing surface after braking tests in two different regions (a) and (b).	234
Figure 8.16: EDX map image of the coated aluminium metal matrix composite rotor cross section after testing.	236
Figure 8.17: Micro-hardness tests of the materials surface.....	238

Figure 8.18: Roughness values for the discs before and after the braking tests.	239
Figure 8.19: SEM images of the coated aluminium alloy and aluminium MMC cross sections after the testing [132].	240
Figure 8.20: 3D profile of the disc brake rotor rubbing surface.	241
Figure 8.21: EDX map image of the coated aluminium alloy disc brake rotors after testing.	242
Figure 8.22: Coated wrought aluminium disc brake rotor after extreme braking condition.	243
Figure 8.23: SEM images of the failed coated aluminium alloy rubbing surface.	244
Figure 9.1: Temperature distribution at the end of the braking event for the Taguchi study for the uncoated disc brake rotor.	251
Figure 9.2: Main effects for the uncoated disc brake rotor.	253
Figure 9.3: Main effects for the coated disc brake rotor.	258
Figure 9.4: Building and validation points.	260
Figure 9.5: Response surface of maximum surface temperature of the coating for the two design variables.	261
Figure 9.6: Response surface of maximum temperature of the substrate for the two design variables.	262
Figure 9.7: Temperature distribution of the coated small scale disc brake rotor at the end of simulation for the Alpine descent.	264
Figure 9.8: Maximum temperature on the coating and substrate outer surfaces during the high g braking test.	264
Figure 9.9: Temperature distribution of the coated small scale disc brake rotor for the high rate constant g stop.	265

List of Tables

Table 2.1: Wrought aluminium alloy series features [64].	29
Table 2.2: Typical process parameters during Kernite PEO coating [29].	38
Table 3.1: Chemical composition of EN-GJL-250 grey cast iron [98].	46
Table 3.2: Chemical composition of 6082 aluminium alloy [99, 100].	47
Table 3.3: Chemical composition of aluminium metal matrix composite (AMC640XA) [99].	47
Table 3.4: Typical process parameters during Keronite PEO coating for AA6082 and AMC640XA.	48
Table 4.1: Thermal properties for different solid materials [13, 17, 25, 106, 107] at room temperature (20 °C).	75
Table 4.2: Initial conditions and parameters used for the simulation [13, 108].	75
Table 4.3: Initialization parameters used for the simulation.	76
Table 4.4: Mesh sensitivity analysis for the one dimensional Abaqus model.	85
Table 4.5: Parameters of automotive brake application [15, 17].	87
Table 4.6: Thermal properties for different pad materials [13, 15, 114].	105
Table 5.1: Scaling constant parameters [37].	117
Table 5.2: Scaling relations [37].	118
Table 5.3: Full scale parameters [115].	120
Table 5.4: Full and small scale parameters.	121
Table 5.5: Full and small scale comparison.	149
Table 5.6: Torque meter (TORQUEMASTER TM 213).	156

Table 6.1: 2D axisymmetric model mesh sensitivity analysis.	169
Table 6.2: Coupled 3D model mesh sensitivity analysis.	175
Table 6.3: CPU time for different thermal models.	177
Table 7.1: Test matrix for all brake rotors.	184
Table 8.1: Elemental composition (weight %) of wrought aluminium alloy 6082.....	217
Table 8.2: Elemental composition of the aluminium metal matrix composite (weight %).	219
Table 8.3: Elemental composition (weight %) of coated wrought aluminium alloy 6082.	225
Table 8.4: Elemental composition of the coated aluminium metal matrix composite (weight %).	227
Table 8.5: Elemental composition of the brake pad (weight %).	230
Table 8.6: Elemental composition of the coated wrought aluminium alloy rubbing surface after braking tests (weight %).	232
Table 8.7: Elemental composition of the coated aluminium metal matrix composite rubbing surface after braking test (weight %).	235
Table 8.8: Brake pad thickness variation before and after braking tests	237
Table 9.1: Factors selected for the Taguchi study with their maximum and minimum levels for the uncoated disc brake rotor.	249
Table 9.2: L ₈ Taguchi matrix.	249
Table 9.3: Results of the L ₈ Taguchi study of the uncoated disc brake rotor.	252
Table 9.4: S/N Ratio and main effects for the uncoated disc brake rotor.	253

Table 9.5: Factors selected for the Taguchi study with their maximum and minimum levels for the coated disc brake rotor.	255
Table 9.6: L_{12} Taguchi matrix	255
Table 9.7: Results of the L_{12} Taguchi study of the coated disc brake rotor.	256
Table 9.8: S/N Ratio and main effects for the coated disc brake rotor.	257
Table 9.9: Optimum and simulation results of the two design variables.	262

CHAPTER 1:

INTRODUCTION

1.1 Research overview and background

The foundation brake is one of the most important safety systems in a vehicle as it plays a major part in retarding its motion by converting the kinetic energy of the vehicle to heat energy that is dissipated through the disc brake and pads. To find an optimum design, the development process for disc brakes involves a number of steps and many aspects of the braking system need to be considered to ensure that it meets both legal and customer criteria.

Most of the road vehicles use grey cast iron or steel for manufacturing the disc brake rotor because of good friction, thermal properties and high melting point of ferrous materials. The main disadvantage of the conventional cast iron or steel disc is its weight which has an impact on fuel consumption and vehicle emissions. The automotive industry is under huge pressure to reduce vehicle emissions by an average of 10% by 2015 according to the European Federation for Transport and Environment [1] and this is encouraging automotive industry researchers to find a way to reduce vehicle weight by using lightweight materials. In order to meet legal limits, reduce fuel consumption and improve vehicle performance, efforts are needed to reduce the unsprung mass of the vehicle and one effective way to do this is by replacing the heavy cast iron disc with a lightweight alternative.

Many automotive brake engineers have introduced thermal modelling as a technique of evaluating system performance early in the development process while decreasing the level of complexity and time consuming for experimentation [2]. A selection of techniques have been used in the modelling of brake systems, each addressing some balance between accuracy and run time [3]. Overall, for wide-range of a braking event specification, a thermal model need to take into account for the effects of varying

friction coefficients at the pad-disc interface, vehicle geometry and inertia along with convective, conductive and radiative heat flows [4]. In order to account for all of these effects, studies in the literature generally combine and investigate a various range of engineering software to create complex, resource-heavy simulations [5, 6]. El-Sharkawy [4] explained that the main advantage of one-dimensional modelling lies in speedily highlighting issues early in the design process, after which more complex models can be used to examine the problem areas in greater detail.

The conventional design process using full scale dynamometer testing is expensive and time consuming because to achieve the desired goal there are complicated experimental procedures which need to be carried out. One key aspect of these procedures is to assess the maximum temperature reached by the brake discs and pads during critical braking events since these temperatures not only affect the friction performance of the system but also ultimately its structural integrity. Thermal modelling using theoretical considerations and finite element software is another method which can be used in the design process to save time and cost to investigate the thermal performance of disc brakes under different loading conditions [2, 3, 7, 8].

Different methods and approaches have been used to predict the temperature distribution in a disc brake. Newcomb [9, 10] was one of the earliest researchers to use the Laplace transformation to solve the one-dimensional governing equation in order to predict the temperature in the disc brake. More recently, many researchers have investigated the thermal analysis of disc brakes using different methods such as lumped parameter analysis, one dimensional analytical methods, two or three dimensional numerical models with different assumptions and comparing the numerical predictions with the corresponding experimental results [10-15]. Different studies in the literature utilise sophisticated finite element software such as Abaqus to create complex computationally intensive simulations [16-19].

Many researchers have also investigated the possibility of using lightweight disc brake rotors instead of the conventional grey cast iron or steel disc brake rotor [7, 17, 19-22]. Most research considers the use of aluminium alloy and metal or ceramic matrix composites as the material for the brake rotor. The reason for considering aluminium based materials is that they have tremendously encouraging properties. These include

relatively high specific heat capacity, low density and high thermal conductivity which make them favourable candidates for many engineering applications. On the other hand, aluminium alloys have disadvantages, namely low maximum operating temperatures and low wear resistance, which can limit their application. To overcome this problem, surface modification of the alloy, using processes like thermal spraying [23] and anodizing [24] can be applied. There are a few reports in the literature of using aluminium oxide coating on the rubbing surface of aluminium alloy brakes to provide a thermal barrier to protect the disc brake material [17, 20]. One type of aluminium oxide coating is plasma electrolytic oxidation (PEO) which provides a good thermal barrier because of its low thermal conductivity [25] and good wear resistance [26, 27]. This coating process has been developed by a UK Company, Keronite International Ltd [28] and showed good thermal and tribological properties. The ceramic coating prepared by the PEO process has several advantages such as significantly enhancing the wear and corrosion resistance of lightweight aluminium alloys [20, 27, 29, 30].

PEO, which is sometimes referred to as micro-plasma oxidation, plasma electrolytic anode treatment or spark/discharge anodic coating [31], is an electrochemical surface treatment process that generates an oxide coating on metal [32]. PEO coatings are formed by the oxidation of metal substrate in an aqueous electrolyte through a series of localized electrical discharge events [25, 31, 32]. The oxidation process takes place by passing a controlled electrical current through a path of electrolyte solution and then plasma discharge is formed around the desired component [33, 34]. The specified series of discharges allows oxide growth to form films on aluminium with a thickness of up to 100 μm [35]. The main advantages of the formed PEO coating are good wear resistance, good corrosion resistance and good thermal conductivity [25, 31, 33, 35]. Furthermore, the interfacial adhesion between the substrate and coating is excellent because substrate conversion is involved rather than simple deposition.

Although thermal modelling is useful at the design stage, the brake system ultimately needs to go through a series of vehicle or real road tests before it can be released as a commercial product. The main problem with vehicle testing is that it is time consuming, very expensive and subject to different road conditions and driving styles. Laboratory based brake dynamometer testing is the preferred way of assuring the friction and thermal performance of a disc brake which saves both time and cost. In addition, the

brake dynamometer is an excellent research platform as the test conditions and braking parameters can be carefully controlled. There are two major types of dynamometer: the inertial dynamometer and the CHASE dynamometer. The inertial dynamometer is used to evaluate full sized brakes but this is a very time consuming and expensive process. In contrast, the CHASE dynamometer uses a small amount of friction material rubbing against a drum and it requires shorter testing time than the inertial dynamometer [36].

A small scale test rig is another way to potentially reduce the cost and time of disc brake design [37]. A reduced scale testing system has been used in the past for different applications, such as screening for friction stability using the FAST machine, and monitoring drum lining material using the CHASE machine [38, 39]. These methods do not necessarily provide realistic values of the coefficient of friction because of the difficulty of replicating the real thermal operating conditions of a disc brake [36]. However, a reduced scale brake dynamometer, such as developed by Sanders et al. [37] based on constant energy density scaling, has the advantage that it can potentially reproduce operating conditions that are similar to those of a real braking system.

The main advantage of reduced scale testing is that it is more cost effective and involves lower material overheads than full scale testing which increases the potential for rapid back-to-back testing [40]. Furthermore, reduced scale testing can improve the accuracy and reproducibility of results by reducing spurious effects such as caliper and bracket deflection along with pressure fluctuation [37]. The simplification of the braking setup is an advantage but this can lead to a reduction in the relevance of the results when compared to the full scale brake. Moreover, one of the areas that needs to be considered carefully is convective cooling as the cooling rates of the reduced scale and full size configurations are not equivalent because of the different physical geometries [37]. Therefore, scaling is a complex process and careful tuning of the scaled parameters is needed in order to obtain comparable results [41].

A pin-on-disc type rig has been utilised as an experimental setup in the literature [41-44] to investigate friction materials. This uses a single pad pushed against one side of a rotating disc. Other studies use two brake pads attached 180 degrees from each other, again pressed against one side of a rotating disc [37, 40]. However, none of the previous small scale studies has tried to implement a caliper, thereby allowing the pads to be

applied to both sides of the disc simultaneously which represent the real world configuration of an automotive brake.

The main use of reduced scale brake dynamometers in industry is to produce a set of data describing the variation of the friction coefficient between friction materials and rubbing surfaces as a function of contact pressure, sliding velocity and temperature. This data is typically then utilised in the computer-aided engineering and design process [37] in order to validate the models afterward used to predict performance. Other industrial research applications include heat dissipation and thermal analysis [42, 45] and wear testing [43]. The range of applications of small scale brake dynamometers differs more commonly in the research community. The ability to accurately represent a full scale brake setup is potentially desirable and considerable effort has gone into the validation of test results obtained from reduced scale dynamometers [37, 46, 47].

Although the temperature distribution and the maximum working temperature of the conventional cast iron disc have been extensively studied, the thermal characterisation of lightweight disc brakes requires further investigation. To enable the automotive industry to widely use a lightweight disc brake in order to produce more economical and environmentally friendly vehicles, more research is needed to investigate its thermal behaviour.

Many researchers have investigated the thermal performance of lightweight disc brake rotors using different methods [5, 7, 12, 16-18, 20] but only a few of them have investigated their thermal performance based on an optimisation analysis approach [19]. Taguchi defined the design of experiment as the means to evaluate all possible methods of process or design to reach the desired objective, both efficiently and reliably. A Taguchi analysis has been used by Grieve et.al [19] to find the effects of various disc brake parameters on thermal performance. This result has then been used to optimise the design of lightweight disc brake rotor [19] to reduce its weight and improve thermal performance. In any optimisation problem, optimisation involves adjusting the input design variables annotated with a selected output response to locate the best possible combination [48]. It is too difficult to carry out numerical tests for every combination of design variable, so under these circumstances meta-modelling is used. This necessitates

carrying out simulation analyses at certain sample points in the design space and fitting a predictable response surface which is then utilised in the optimisation analysis [48].

In the present study, the assumptions underlying the scaling process are outlined before deriving the equations required to give equivalent thermal performance between the small and full scale brake. An existing full scale brake dynamometer is then described, followed by the derivation of the design parameters of the equivalent small scale system. Small scale solid brake rotors, machined from blocks of cast iron, wrought aluminium alloy and a 40% SiC reinforced aluminium metal matrix composite (Al-MMC), are used in the experimental analysis. Several of the wrought alloy and Al-MMC rotors were then subjected to a PEO coating process. The PEO coatings for both aluminium alloy and aluminium metal matrix composite were carried out by the Keronite Company. Both coated and uncoated rotors were subjected to a demanding series of brake applications using both small scale and full size brake dynamometers during which the maximum temperature on the surface of each rotor was measured with a rubbing thermocouple and high speed thermal camera.

Alongside these experimental studies, numerical simulations were also conducted to predict the sub-surface temperature distributions within the rotors. The thermal modelling of the disc brake rotor using different modelling approaches was investigated and validated with the experimental results obtained. Material characterisations of the coated disc brake rotors before and after the braking tests were conducted using different techniques to evaluate the coating durability and performance.

A Taguchi analysis was carried out for the small scale disc brake rotor to investigate the effect of various factors on the maximum surface temperature. A sensitivity analysis based on the Taguchi approach was conducted to investigate the effect of various parameters on the thermal performance of a typical disc brake. A genetic algorithm optimisation was subsequently performed for the selected coated aluminium disc brake rotor to find the optimum thickness of the coating and the substrate.

1.2 Research aim and objectives

1.2.1 Aim

The overall aim of this research is to investigate the possibility of replacing the conventional cast iron disc with a lightweight alternative effectively with short time and low cost.

1.2.2 Objectives

The above aim is realised through delivery of the following objectives:

1. To develop and validate a one dimensional thermal model with published and experimental results to help in understanding and designing small scale disc brake dynamometers.
2. To carry out a parametric study using the 1D numerical model to find the effect of various parameters on disc brake thermal performance.
3. To design, develop and commission a small scale brake dynamometer to complete a representative test matrix which assesses the thermal performance of lightweight disc brake rotors against the conventional grey cast iron.
4. To develop numerical models (2D and 3D) for the disc brake rotor using a finite element approach, validated against experimental results.
5. To characterise the surface of the brake rotor before and after typical braking cycles.
6. To simulate the effect of various disc brake parameters on thermal performance and so optimise the design of coated lightweight disc brake rotors.
7. To develop a representative finite element thermal model of the optimum design and undertake a quantitative analysis of the performance.

1.3 Structure of remainder of thesis

Chapter 2 provides a brief description of brake system fundamentals and thermal modelling in general. It also gives a review of literature relevant to the present study which covers thermal modelling, lightweight materials for disc brake rotors, coating techniques, disc brake thermal performance and characterisation of materials.

Chapter 3 describes the material characterisation methods used in the current study to analyse the coated lightweight materials before and after braking tests. The Chapter includes descriptions of all the equipment used to evaluate the disc brake substrate and coating.

Chapter 4 introduces one dimensional thermal modelling of disc brake rotors using different approaches. It includes the derivation of the one dimensional numerical equation used to evaluate the temperature across the thickness of the disc. Furthermore, coating modelling techniques are introduced in this Chapter along with a parametric study of disc brake rotors.

Chapter 5 presents the scaling methodology approaches used in the current research. The design of the small scale test rig is explained in detail with the description of the conventional brake dynamometer. In this Chapter all of the experimental equipment used for the braking tests is explained.

Chapter 6 presents the two and three dimensional finite element models for the transient heat transfer analysis of the small and full scale disc brake rotors using Abaqus software. The detailed boundary conditions and steps are explained. In addition, sensitivity analysis for each model was carried out to choose the optimum mesh size. A comparison between the two models (2D and 3D) is explained and presented.

Chapter 7 describes the representative test matrix which is based on appropriate SAE standards. Also, the general setup for the experiment, the equipment calibration and the commissioning procedure are explained for the small and full size test rigs. The experimental results for the various disc brake rotors are presented in detail using the developed test matrix.

Chapter 8 presents the material characterisation of the various disc brake rotors used in the braking tests before and after the tests. It provides an overview of the surface texture and the durability of coating. In addition, it reports the overall characteristics of the disc brake rotors after braking.

Chapter 9 describes the Taguchi analysis used to find the optimum coating and substrate thickness for lightweight coated disc brake rotors. A design of experiment

based on the Taguchi study is explained and used to find the best distribution of the design points.

Chapter 10 presents the main conclusions which can be drawn from the overall results of the research and also provides recommendations for future work.

CHAPTER 2:

LITERATURE REVIEW

2.1 Overview

The introduction of lightweight disc brakes has the potential to have an impact on the automotive industry. The main advantage of using, for instance, Al-MMC (aluminium metal matrix composite) instead of conventional cast iron, is that it reduces the weight of the vehicle. This will also reduce fuel consumption and emissions. In this Chapter, a number of different areas are investigated and studied in order to give the background necessary to achieve the aim of the research. These areas are as follows: Disc brake thermal analysis, design of experiment, optimisation analysis, coating technologies, scaling methodologies and disc brake materials. An overview of the literature review is shown in Figure 2.1.

A review is given of the methods used by researchers to investigate the thermal performance of a lightweight disc brake rotor with an appropriate coating. Different techniques and approaches were assessed and reviewed in order to help in the development of the future generation of lightweight disc brake rotors. Experimental approaches to validate the numerical modelling were investigated to find the best approach to assess the disc brake thermal performance. Finally, a summary of the findings from the literature are presented and explained.

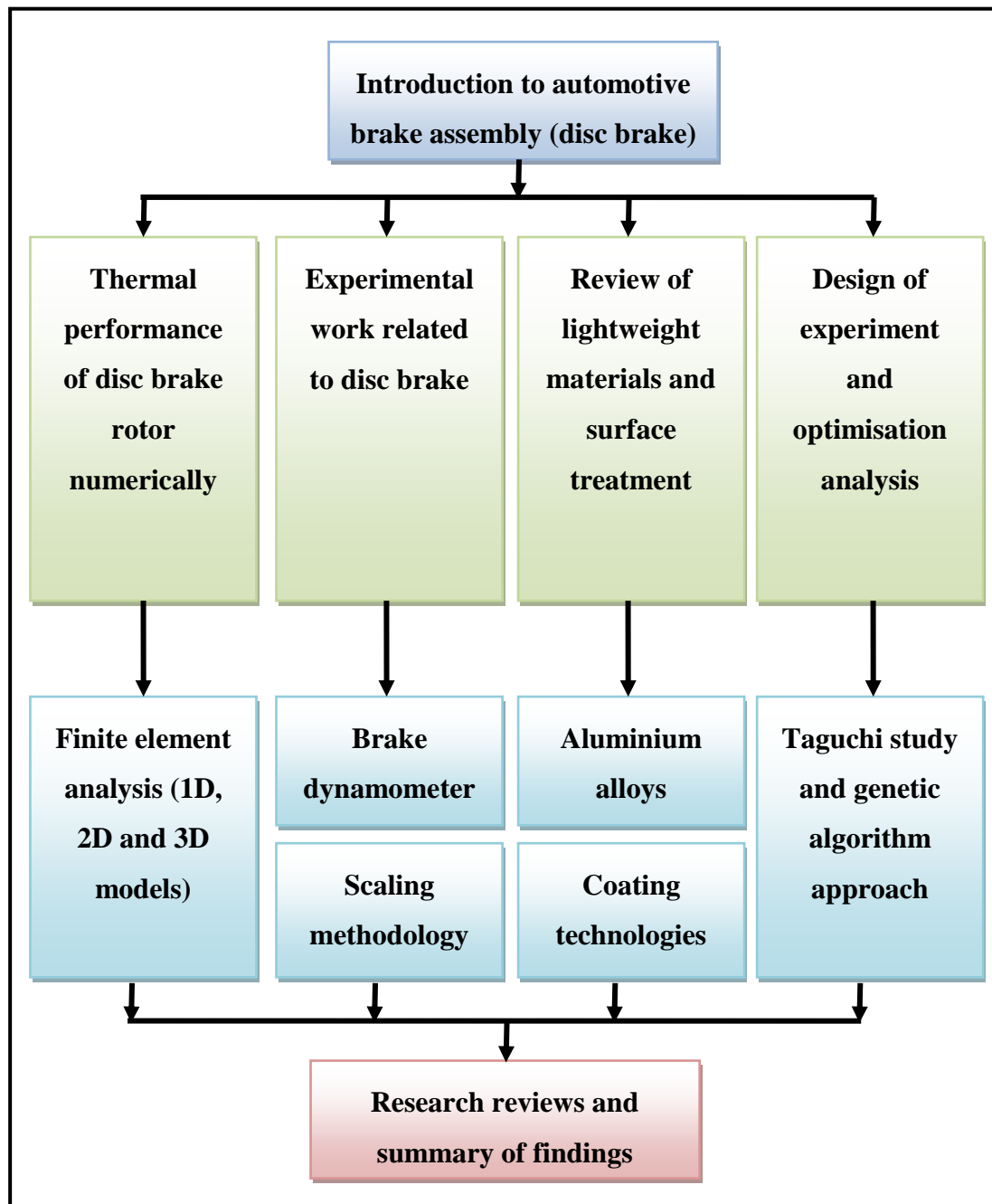


Figure 2.1: Literature review overview

2.2 Disc brake system overview

The first disc brake assembly was invented in 1902 by an English engineer named Frederick William Lanchester and used in Lanchester cars. Lanchester patented his invention and described his patent as a metal disc [49, 50]. This metal disc consisted of a rigid leaf of metal, attached to the back of each wheel of the vehicle, which was then pressed upon by a pair of claws in order to slow down the vehicle. In the period

between 1894 and 1896 an American inventor called Elmer Ambrose Sperry invented an electromagnetic disc. This system consists of a magnetic brake (disc) which is placed in contact with another disc to apply a braking torque. However, the first reliable disc brakes were developed in 1953 by the Dunlop Company.

There are many key criteria that should be met when either specifying or designing brake assembly materials. These are as follows: good strength, good corrosion strength, low noise, low weight, good thermal conductivity, long durability, low wear rate, steady friction and a reasonable cost ratio. Currently, within commercially available brake components there are more than 2000 types of material in use [49, 50].

The main purpose of a brake system is to slow or stop the wheels of a vehicle by engagement of friction at the rotor-stator interface. The brakes convert the kinetic energy of the vehicle, via rotation of the wheel, into heat energy which is dissipated in the brake. Numerous devices in modern vehicles have improved braking capability. In order to understand the brake system, and before looking at the individual components and construction of such a system, it is essential to understand its overall design and operation. The main components of any brake system are as follows: Brake pedal assembly, master cylinder, brake booster, brake lines, wheel brake assemblies and emergency or parking brake (see Figure 2.2 [51]):

The basic brake system operation is as follows: When an actuation force is applied to the brake pedal, this causes the lever action to push a rod into the brake booster and master cylinder which produces hydraulic pressure. The hydraulic pressure is transmitted through the brake lines into the brake assemblies which use the pressure to generate friction for braking. There are two common types of brake system: Disc brakes, in which uniform pads are compressed against a circular disc which is attached to the wheel and drum brakes in which rounded contact surfaces are pressed by force outwards against the internal diameter of a drum, see Figure 2.3. In this research, drum brakes will not be considered or discussed [51].

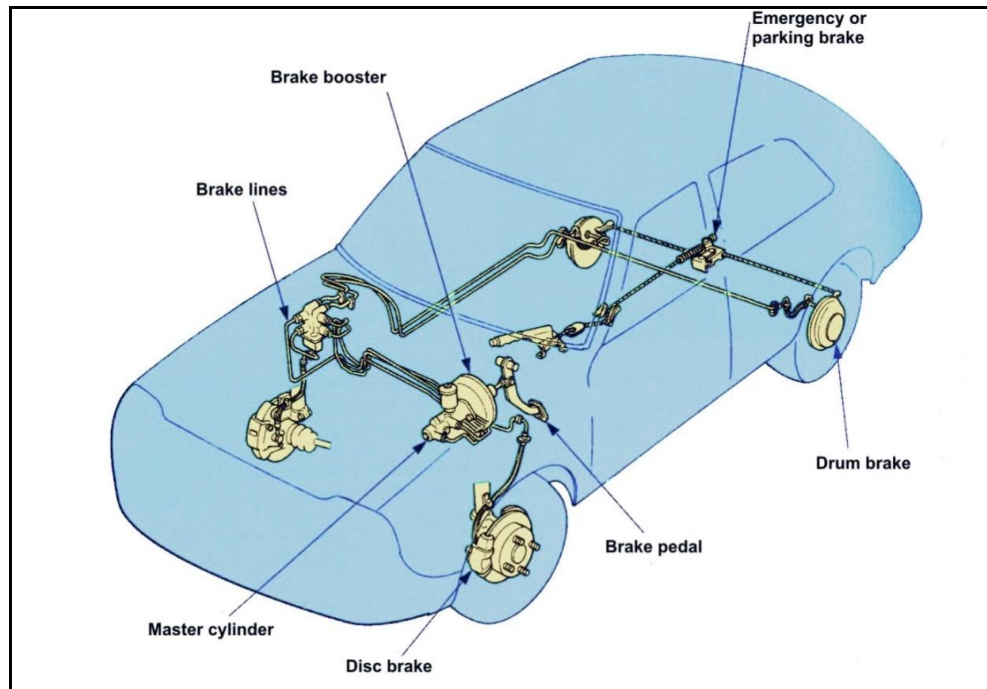


Figure 2.2: Basic components of an automotive brake system [51].

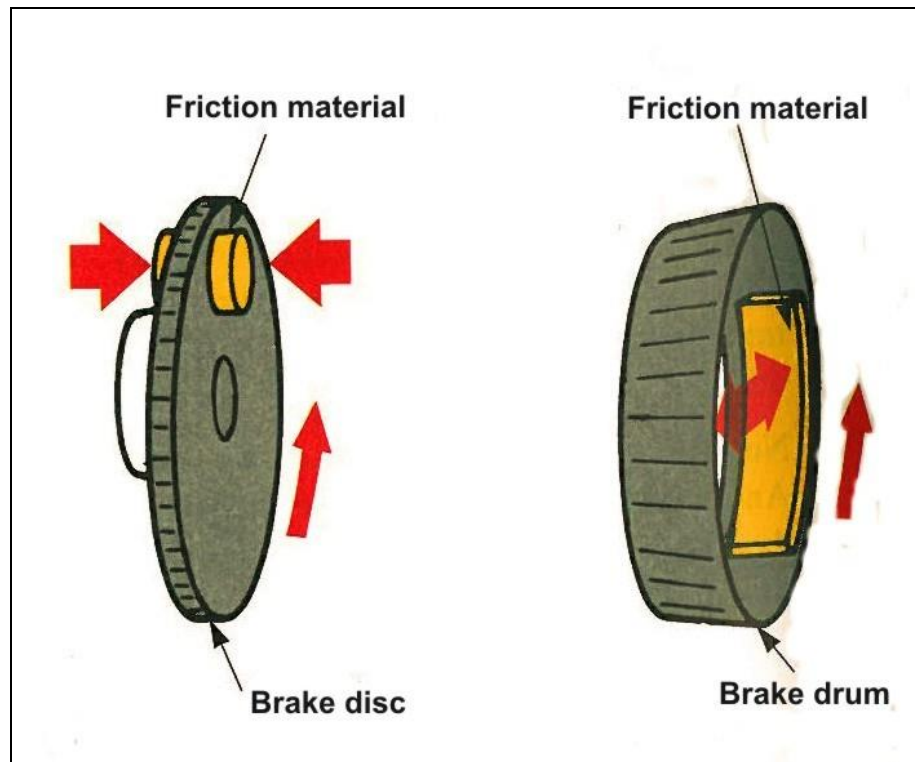


Figure 2.3: Schematic diagram of both disc and drum brakes [51].

The disc brake system is used in this research because of the many advantages that it has over the drum brake system, most notably its ability to generate a stable braking torque. Most disc brake rotors are made of cast iron, but with the development of government legislation, the automotive industry has tried to reduce the weight of the brake system by finding an alternative material for rotors which can tolerate severe service conditions, for example, high load, velocity, temperature and environment [51].

The main components of a disc brake are as follows:

- **Calliper:** The calliper structure is eventually part of a hydraulic clamp that provides the means through the pads and brake pistons are located relative to the disc. It has sufficient strength and rigidity to react all the applied loads including the in-plane friction force, generated at the rotor-pad interface, that is reacted through the pad backplate- calliper abutment.
- **Brake pads:** These comprise a steel backplate and friction material that is pushed against the disc due to the action of the piston, master cylinder and calliper cylinder.
- **Rotor (disc):** A metal disc, usually made of cast iron, that is used to stop or slow down the vehicle by means of friction. The rotor is attached to the wheel hub usually through some sort of “top-hat” arrangement.

2.3 Thermal analysis of rotors

During braking the kinetic energy of the vehicle is transformed into thermal energy due to frictional sliding. This energy transfer causes the disc and brake pad temperatures to rise due to the friction between the contact interfaces. Many studies have been conducted in the field of thermal analysis; these studies fall into two categories, either numerical analysis or experimental analysis. In this section the area of thermal analysis for disc brakes will be discussed and investigated in detail. A considerable amount of research work has been conducted in the area of disc brakes which deals with the thermal behaviour by developing different models that predict the temperature distribution through the brake system. These investigations provide a very comprehensive understanding of the disc brake thermal behaviour which helps in brake system design and material selection for the disc brake.

2.3.1 Simple one-dimensional analysis

Newcomb [9] studied the transient thermal analysis of a disc brake. The model was developed to predict the transient temperature at the friction surface of the disc brake, during constant deceleration braking. Experimental results were compared with the numerical results obtained from the 1D model. The experimental results were measured using a commercial infra-red radiation pyrometer. It was found that the calculated temperature was higher than the experimental temperature by about 15%, possibly attributable to the fact that the model did not take into account the cooling losses. In addition, Newcomb [10] investigated the thermal analysis of the disc to find the transient temperatures during braking at uniform deceleration. It was assumed that all the frictional heat flows into the disc. In this study both cooled and uncooled discs were considered and the numerical results obtained from the analysis were compared with the experimental results at the friction surface during a single brake application. In addition, a comparison was made between a disc and drum brake for repetitive braking at regular intervals under similar conditions. The results show a good agreement with only 15% difference of the surface temperature; this modelling could be improved in order to simulate real braking events and also to predict the exact temperature. Also the effects of radiation may be included which will have an effect on the surface temperature [9, 10].

Temperature distributions in the rubbing path and the mounting flange of a disc brake were calculated by Abbas et al. [11]. The calculated results were based on two cases of braking: the first case was a single brake application (transient temperature distribution) and the second case was a repeated brake application (steady state condition). The numerical equations were derived and the results were compared with experiment. The numerical results showed a very good agreement with the experimental results [11].

Rowson [52] derived the equations for the surface temperatures of the friction material and the disc brake in order to show how they are interrelated. The surface temperature rises were calculated for the bulk surface and for the real contact area by making some assumption regarding the heat generated during braking. The calculated results were compared with the observed results for both the bulk surface temperature and the temperature at the real contact area. Rowson found that the calculated results gave a

good agreement with the observed results. However the model could be improved in order to predict the surface temperature for different braking events. Rowson assumed that all the heat goes into the disc but in reality the heat is transferred to both the disc and the pad with a ratio that depends on the material properties of both the disc and pad [52].

The paths and amounts of heat flow have been determined experimentally by Yano and Murata [53]. Repeated braking was applied in this study until a quasi-saturation condition (stable condition) was reached. The authors were interested in the flow of heat under such conditions. They considered the following routes for heat transfer: Heat conduction through the pad and rotor flange, heat convection to the air from the friction area on both sides of the disc, heat convection from the top hat section of the rotor and finally heat convection from the ventilated parts. In this experiment a medium sized truck was used and the analysis was performed for the rear wheel brakes. It was found that 70% of the heat was transferred to the air from the rotor rubbing surface while 10% was transferred from the ventilated section. Finally, the authors suggested some modification to the fins and ventilation section air flow and the addition of a baffle plate which would improve brake cooling by 20% [53].

Sakamoto [54] investigated the heat convection from a disc brake using both theoretical and experimental approaches. Using the basic equation of heat convection with the measured flow volume and brake test data, the cooling efficiency of a ventilated disc was investigated. It was found that the cooling efficiency and the maximum temperature could be estimated from the cooling rate data. The disc design parameters, namely the heat convection area, heat transfer coefficient, disc mass, and specific heat, were used to derive the cooling coefficient. The maximum temperature calculated from the derived equation was in very good agreement with the experimental temperature. It was concluded that when designing brake discs the heat convection area is more important than the number or thickness of the fins [54].

In order to understand the convection through the brake rotor fins, Mcphee and Johnson [14] examined the validity of various numerical and experimental approaches. In the experimental approach two different aspects were studied: The first was the assessment of heat transfer and the second was the assessment of fluid motion. In this experiment it

was assumed that both conduction and radiation are negligible. Three different rotational speeds for the rotor were used: 342, 684 and 1025 rpm which give fin convection heat transfer coefficients of 27, 52.7 and $78.3\text{Wm}^{-2}\text{K}^{-1}$ respectively. It was found that the analytical results were very similar to the experiment results. This study gives a better understanding of the convection heat transfer coefficient and the potential for future developments to improve the overall performance by assessing the localised heat transfer [14].

Jun et al. [13] investigated the maximum temperature of disc brakes and brake fluid during the Alpine test. The Alpine test is carried out in this research to detect the temperature change in brake parts during a high mountain descent (see Figure 2.4). As a result of continuous or repetitive braking, the brake system experiences a rapid temperature change, which can lead to symptoms such as fade, thermal judder and thermal lock. In the study by Jun et al. [13], a numerical method for predicting the temperature change is proposed by using frictional heat division and one-dimensional heat transfer analysis. The Alpine test results were validated by comparison with reported experimental data and they showed very good agreement. The equation used to find the division ratio of the heat flux is not suitable for repetitive or continuous braking because of the following factors: Cooling by convective heat transfer and thermal contact resistance between the pad and the disc. This is why Jun et al. [13] present the heat flux correction factor which is an arbitrary calculated value. This study investigated the temperature change in various brake parts using a one-dimensional model, thus avoiding use of a more detailed model (three-dimensional model) which would have been time consuming. The results show a very good agreement with experimental data. However different braking events and materials need to be evaluated in order to fully validate the model [13].

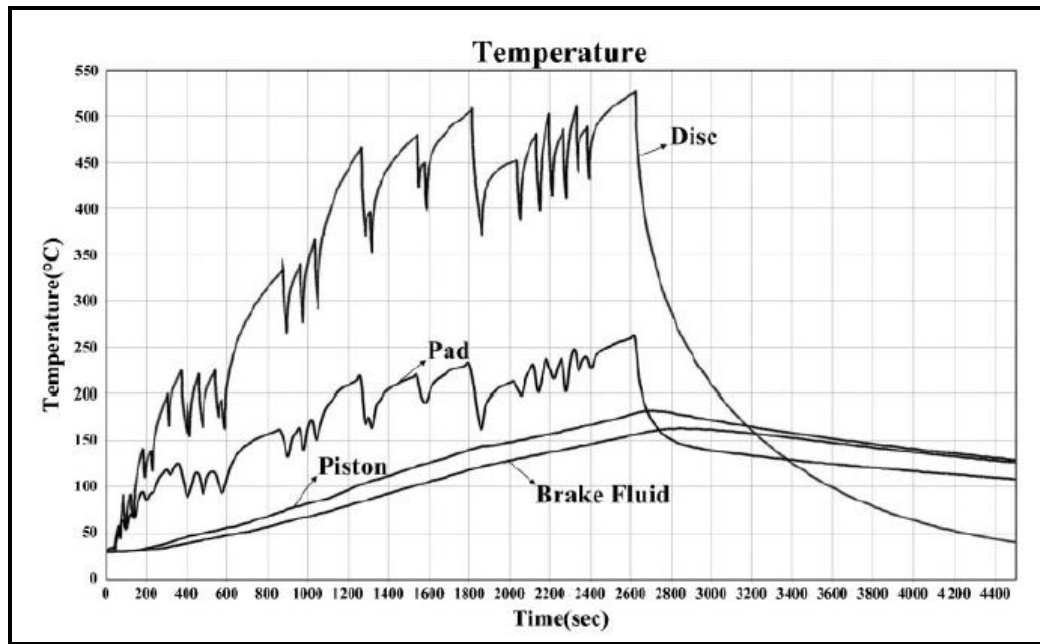


Figure 2.4: Calculated temperature rise of the brake components during the Alpine test [13].

An investigation into the thermal behaviour of both disc and pad was carried out by Talati and Jalalifar [15]. The governing transient heat equations were derived in terms of time and space. In their study many parameters were taken into account, such as vehicle velocity, duration of braking, geometry and dimensions of brake components, materials of both disc and pad and contact pressure distribution. It was found that in order to avoid a rise in temperature for different brake components and to avoid decreasing the friction coefficient between disc and pads, the heat generated should ideally be dissipated to the environment. In Talati and Jalalifar [15], the surface temperature was investigated for both disc and pad brakes. The model developed is capable of predicting the temperature in the radial direction for two different conditions, namely uniform pressure and uniform wear. It was found that the predicted temperatures have a very good agreement with the literature results, especially when assuming uniform wear. The results obtained from the model should be validated with experimental results different from the literature results in order to test the model, especially for the temperature distribution within the pads. Also, taking different braking events into account will give a better understanding of the temperature distribution during braking [15].

2.3.2 Finite element analysis

Day et al. [55] investigated the pressure distribution at the brake rubbing interface. The pressure distribution effects can be divided into bulk temperature effects and macroscopic thermal effects. The bulk temperature effects consist of thermal expansion, temperature and wear effects, while the macroscopic thermal effects relate to rotor surface damage and banding. Finite element methods were used in this research using a two-dimensional axisymmetric model. It was found that the interface pressure distribution has an effect on the friction interface temperature in brakes. Also the authors noticed that thermal problems occur when applying high amounts of frictional heat generation quickly to a cold friction pair. Finally, it was noted that there is much work still to be done in the area of interface contact, pressure distribution, frictional heat dissipation and generation of frictional heat [55].

Thermo-mechanical finite element model was developed by Brooks et al. [56] to investigate the brake judder. The interaction between the friction material and the rotor was studied as a function of time including the change in contact between the rubbing surfaces. In the finite element model, the rotating heat source was considered which is applying heat flux on the rotor surface node that underneath the pad and permit conduction of heat across the interface. Based on the fully coupled finite element model, the localised thermo-elastic instability at the interface of a disc brake friction pair has been successfully simulated.

Grieve et al. [19] investigated ways of reducing vehicle weight by using aluminium metal matrix composite brake discs instead of cast iron. However, aluminium metal matrix composites have a much lower maximum operating temperature compared to cast iron. A three dimensional finite element model was developed in this study for the existing design for both cast iron and an aluminium metal matrix composite in order to find the peak disc temperature during two different brake tests. The finite element models were developed using the Abaqus software package. Taguchi analysis was used to analyse all the critical design and material factors for an aluminium metal matrix composite. From the results, material combinations and suitable designs for a prototype front brake disc were defined that can be applied to small or medium passenger vehicles. It was found that using both finite element models and a Taguchi analysis

provide an excellent approach to finding an optimum Al-MMC brake disc. According to the Taguchi analysis it was found that the main factors in designing an optimum Al-MMC brake disc are: cooling rate to the disc surface, conductivity of disc material and cheek thickness. It was concluded by Grieve et al. [19] that Al-MMC brake discs can be used with appropriate modifications to the disc material and design.

Voller et al. [45] investigated disc brake cooling characteristics experimentally and numerically. As called spin rig was developed to obtain experimental results to compare with the numerical results obtained from the three dimensional finite element (FE) and computational fluid dynamics (CFD) models. In Voller et al. [45], conduction, convection and radiation heat transfer modes were all analysed. The effects of brake cooling parameters on disc brake temperature were investigated using the FE model. It was found that there is a slight change in the emissivity during the brake application. The spin rig was a very useful piece of equipment for investigating all modes of heat dissipation. However it was concluded that further investigation and improvement to the existing rig is needed to improve the brake disc heating system.

In order to study the thermal and mechanical interactions between the disc brake and pad during braking, a finite element analysis method was used by Eltoukhy et al. [57]. The temperature on the rubbing surface between the disc and the pads was predicted. In addition the thermo-elastic behaviour of the disc material properties was examined by comparing various types of brake disc material, namely grey cast iron, Al_2O_3 Al-MMC and SiC Al-MMC (ceramic brakes). It was found that the results attained from the finite element model were similar to the experimental results reported by Cueva et al. [57, 58].

Amin et al. [12] investigated the temperature distribution in disc brakes by using the method of order-of-magnitude analysis which was originally proposed by Ludwig Prandtl. The temperature distribution equations were developed for the disc brake radially, axially and circumferentially with respect to time in three dimensions. The temperature equations were analysed using the method of order-of-magnitude analysis in order to find the relative importance of the three directions in calculating the temperature variation. The results obtained from this approach were compared with the results obtained previously from the literature and found to have a very good agreement.

Thermal stress, thermal cracking and warping in disc brakes could all be included in the proposed approach. As a result, the order of magnitude analysis can be used to predict the essential directions of heat flow in a disc brake [12].

The brake system is one of the main and essential parts in any vehicle, and so, in order to improve brake system design, there are many safety and legal requirements to be met. Zaid et al. [8] investigated a ventilated disc brake rotor of a normal, fully loaded passenger vehicle. In order to predict the heat, temperature distribution and behaviour of the disc brake rotor, transient finite element analysis approaches were used. Overall, Zaid et al. [8] give a better understanding of disc brakes and of their thermal behaviour which could improve and optimise the design of effective disc brake rotors.

Zhu et al. [59] investigated the change in the temperature field for brake shoes under emergency braking conditions for a hoist. A three dimensional theoretical model was developed according to the law of energy distribution and transformation, the theory of heat conduction and operation condition of a mining hoist's emergency braking. In addition, by using the integral-transform method, an analytic solution for the temperature field was developed. The authors validated the results obtained by the proposed method with numerical simulation and experimental research. It was found that the simulation results displayed a good agreement with the experimental results which indicates that the integral-transform method is suitable for solving the theoretical model of three dimensional transient temperature fields [59].

Hwang and Wu [60] investigated thermal stress and temperature behaviour in a ventilated disc brake throughout single braking. Using a multi-body technique and a thermo-mechanical coupling boundary condition, a three-dimensional model was built which represented the ventilated pad-disc assembly. The braking test was carried out for constant deceleration until the disc velocity reached zero from a certain value. In order to validate the results the authors carried out an experimental investigation. It was found that, because of the thermal expansion, caused by the temperature field, a transient variation of contact pressure distribution occurs. Simulation results were seen to be in very good agreement with the experimental results [60].

Alsaif et al. [17] used a plasma electrolytic oxidation (PEO) technique to obtain a hard aluminium oxide coating on a lightweight aluminium alloy brake rotor. A full-size PEO treated aluminium metal matrix composite (70% AA6061, 30% SiC) vented brake rotor was investigated theoretically and experimentally. A simple one-dimensional theoretical approach and a detailed finite element analysis were used in order to investigate the heat flow from the friction interface into the rotor. A conventional grey cast iron rotor, an uncoated aluminium MMC rotor and a PEO-treated MMC rotor were investigated using back-to-back full-scale dynamometer tests. The three rotors had the same ventilated design. From the results it was noticed that the surface temperature of the PEO coated rotor rose more rapidly than either the uncoated MMC or the cast iron rotor, but it was found that the coated rotor was able to withstand a surface temperature of over 500°C without any loss of performance or surface deterioration. The study by Alsaif et al. [17], suggests that a lightweight alloy brake rotor could be more widely used in road vehicles as it was found that the PEO treatment gives a thermal resistant layer. Further investigations are required to optimise the pad composition to improve the friction performance. Also it is necessary to show the long-term durability and corrosion/wear resistance of the PEO treated rotor surface before a production prototype can be designed [17].

2.3.3 Experimental analysis

Lightweight material is the main target for the automotive industry in order to reduce the total weight of the vehicle, which will reduce fuel consumption. Recently, several pieces of research have been conducted in the field of lightweight disc brakes and the thermal performance of the materials. Different materials and coating techniques have been investigated by different researchers. Dahm et al. [20] used an environmentally friendly technique for applying an aluminium oxide (Al_2O_3) coating to lightweight disc brake rotors by using the plasma electrolytic oxidation (PEO) technique. The authors indicate that the PEO method is cheaper than using a thermal spray method. Two small scale aluminium alloy (AA6082 and AA7075-T6) rotors were PEO treated. Small scale dynamometer tests were performed on the small scale samples and compared with a standard cast iron rotor using standard non asbestos organic pads. It was found that the coefficient of friction (COF) for the AA6082 PEO treated rotor was 0.30-0.33 and for AA7075 was 0.25, compared to 0.50 for a standard grey cast iron rotor when sliding

against a standard non-asbestos organic friction material. The results show that the COF values for the PEO treated rotor were similar to the COF obtained for thermally sprayed Al_2O_3 . Also they show that all three surface engineered rotors have a very stable COF. According to these results the PEO technique is more appropriate for aluminium alloy disc brake rotors than the thermally sprayed Al_2O_3 coating [20].

Qu et al. [21] investigated the possibility of using an oxygen diffused titanium rotor instead of the conventional cast iron rotor. Titanium alloy has several advantages over the cast iron material which are as follows: Good strength, corrosion resistance, lighter than cast iron, also the titanium alloy friction and wear behaviour can be improved. Experiments have been done in order to compare the oxygen diffused titanium rotor with different materials using a sub-scale brake tester against a flat block of commercial brake lining. The treated titanium showed very good results compared with the untreated titanium, titanium based metal matrix composite and a thermal spray coated Ti alloy. The results showed that the treated titanium has a very good friction coefficient level with excellent fade resistance. Also the treated titanium had the best braking performance of all the different specimens. Finally the lining material used in this investigation was not designed for titanium rotors therefore the titanium rotors may not display their best performance. Qu et al. [21] investigated different titanium alloys without comparing the results with the conventional cast iron in order to have a better understanding and comparison. Small scale discs were used in this research without taking into account the effects of scaling.

2.4 Scaling methodologies

Testing is needed in order to evaluate the functionality of any brake system and to characterise different friction materials or designs. Brake dynamometers are widely used in the automotive industry to investigate and evaluate brake system design and components and reduced scale dynamometers are employed in order to save time and money. Full scale brake dynamometer testing is costly and time consuming. Using a reduced scale brake dynamometer is another way of testing the brake system which has many advantages over the full scale dynamometer, which are short time, lower cost and the production of more accurate results through the elimination of the full scale hardware effects. Attention to detail is required when carrying out the scaling process as

there are many parameters which may need to be tuned in order to generate accurate results.

A reduced scale dynamometer was developed by Sanders et al. [37] in order to find the frictional characteristics of lining material. It was assumed that the energy input per unit contact area is constant for both the full scale and reduced scale dynamometer. The scaling relation was chosen first in order to begin the scale dynamometer design. In order to obtain constant energy dissipation a scaling parameter by pad area was chosen. Some parameters, which were assumed to be similar for both full scale and a reduced scale, are sliding velocity, pad pressure and temperature. The friction coefficient was measured as a function of these parameters. The use of thermal mass scaling is very important in attaining equality for the temperature rise of the full scale and the reduced scale dynamometer. A comparison between the full and reduced scale dynamometers was made which showed a very good agreement in the results. It was found that the reduced scale dynamometer has the potential to become an important lining screening and design tool [37].

Kermc et al. [40] investigated brake friction material in order to determine brake system performance by using a reduced scale testing machine. The main goal in their research was to measure the friction coefficient as a function of pad pressure, sliding velocity and temperature, under the same conditions as real systems. This required that previous parameters were kept constant in the scaling in order to produce a one-to-one comparison. A reduced scale testing machine was designed and developed to replicate the same operating conditions as in a real braking event. The results generated from the reduced scale test machine were compared with the results obtained from a standard test machine and showed a very good agreement [40]. Furthermore, Kermc et al. [46] used a reduced scale testing machine that was designed and developed to investigate a ceramic based brake material. The new reduced scale test machine was capable of operating with different conditions. The operating parameters, such as pressure, speed, temperature and energy density, were equivalent to those in real braking events. Different material combinations investigated were a carbon ceramic composite against a metal matrix composite and conventional grey cast iron against a metal matrix composite. The reduced scale test results showed good agreement with the full scale testing machine results obtained previously.

Neis et al. [61] investigated the difference between temperatures measured by thermocouple and by infra-red thermography in order to define a relation between the two. In this research a reduced scale dynamometer was used which had the advantages of low cost and a shorter running time. The thermocouple was positioned 1mm inside the disc from the surface and a thermographic camera was used to find the gradient temperature on the contact surface. Two different materials were used for the friction material (pad) while the disc brake was made from conventional grey cast iron. The experiments were evaluated for different conditions of velocity and torque. The results showed that in the region of localized heating, with the heating rates recorded by the thermocouple, there was a good agreement between the thermographic images on the disc and the curves of temperature for the thermocouples. The occurrence of localised heating areas as identified by the thermographic images proved that there was irregular contact between the friction pair. From this study it should be noted that it is important to take special care when finding the final temperature of braking using thermocouples because of the presence of localised heating areas on the disc surface which may affect the result [61].

Various studies have been undertaken in the area of scaling methodologies. It was found that most of them use the same scaling process with some type of modification to suit their need. In the current research the process used by Sanders et al. [37] will be used with some modification to suit the existing test rig. Sanders et al. [37] suggest that a scaling factor of approximately 10 is suitable for cars and 15 for trucks. On the other hand, Kermc et al. [46] suggest that the scaling factor is dependent on the design simplicity, cost and practical concerns.

2.5 Investigation of disc brake rotor material

In designing and developing any brake system, the material selection plays a very important role as it defines the limits and performance of the brake system. The main parts in the brake system are the disc and pad. These parts are directly responsible for reducing the vehicle speed or stopping the vehicle. Many properties and parameters should be considered when choosing the pad and disc material. In this section the material selection process and an overview are presented in brief.

Three types of cast iron used in disc brake rotors (grey iron grade 250, high-carbon grey iron and titanium alloyed grey iron) were studied for wear resistance, and the results obtained were compared with a compact graphite iron (CGI) by Cueva et al. [58]. A pin-on-disc-wear-testing machine was used to carry out the wear tests. The discs were exposed to three different pressures, 0.7, 2 and 4MPa. The wear was assessed by measuring the weight of the disc before and after each test. It was found that, at any of the applied pressures, the CGI had a greater mass loss compared to the three cast iron discs. In addition, they found that with a lower applied pressure and the same friction force the CGI had the same performance as the cast iron discs [58].

A review of material modelling of different brake components was carried out by Barton [62]. In the review different aspects of brake system material were discussed. In the process of choosing a material for pad and disc, there are many issues that should be considered, namely high maximum operating temperature, resistance to the mechanical force, low thermal conductivity to minimise heat conduction, wear resistance, low cost, and ease of production. Most automotive industries still use grey cast iron for disc brakes. However, trials have taken place with lightweight materials, such as metal matrix composite (MMC) or ceramic matrix composite (CMC), in order to reduce the total weight of the vehicle. No existing pad friction material satisfies all the criteria and thermal properties, so this is why researchers use a complex composite which contains different particles, fibres, fillers and binders in order to meet the requirements. However, the process of friction material formulation is time consuming because it depends on trial and error, commonly referred to as 'black art'. Furthermore, some research has been conducted in order to understand and predict the thermal and mechanical properties of a composite. Some work was reported with regard to a coated MMC disc which showed potential for use as a lightweight disc of the future. It was concluded that micromechanical modelling material for a brake system is too difficult because of the complex non-linear thermo-mechanical interface which occurs at the rubbing interface [62].

Maleque and Rahman [63] developed a method for material selection in order to select the optimum lightweight material for disc brake application instead of the conventional cast iron disc. A digital logic method and cost per unit property were used for the selection of the materials. Different materials were analysed and evaluated, among them

cast iron, titanium alloy, aluminium alloy, ceramic and composites. During the material selection stages the key parameters used were compressive strength, wear resistance, friction coefficient, specific gravity, thermal conductivity and cost. As a result of this study it was found that the most suitable material for the brake disc system was the aluminium metal matrix composite [63].

2.6 Aluminium alloys

2.6.1 General background

Aluminium alloys are commonly used for components which require low weight materials with high strength. Different industries use aluminium alloys as alternatives for reducing weight with competitive cost [64]. Aluminium, as an element, forms about 8% of the earth's crust after oxygen and silicon [65, 66]. It was first discovered as a metal by Sir Humphrey Davy (1778-1829). It has been used widely in the industry, after steel, because of its lightness and good mechanical properties. Over the last 120 years, the production of aluminium has increased dramatically, as shown in Figure 2.5. The main limitation of aluminium alloys is their tribological behaviour which limits their more widespread use.

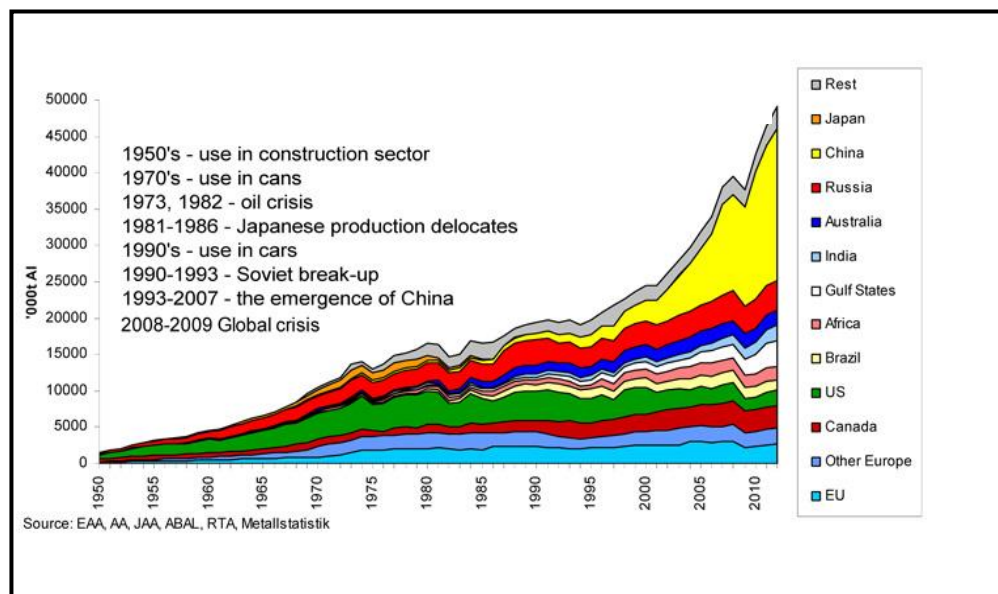


Figure 2.5: History of aluminium production in main countries and regions since 1950 [67].

2.6.2 Aluminium alloys classifications and properties

Based on the type of manufacturing process, aluminium alloys are classified into two main groups, which are wrought and cast aluminium alloys. The International Alloy Designation System (IADS), developed by the Aluminium Association in the USA, identifies aluminium alloys by a four digit number. There are eight aluminium alloy series that identify the type of aluminium, as shown in Figure 2.6. The main alloying elements and properties of each series are shown in Table 2.1 for the wrought aluminium alloys.

The best known characteristic of aluminium is its low mass density; aluminium metal has an atomic weight of 26.98 and a density of 2.7 g/cm^3 . This makes aluminium one third the mass of most other commonly used metals except titanium and magnesium. In addition, the thermal conductivity of pure aluminium is 244 W/mK for the temperature range $0\text{-}100^\circ\text{C}$, this is because of its low density. Moreover, aluminium has a higher resistance to corrosion because of the thin film of oxide which is always present due to oxygen in the atmosphere [68].

		Major alloying element	Atoms in solution	Work hardening	Precipitation hardening	
WROUGHT ALLOYS*) EN AW-	1XXX	None (min. 99.00% Al)		X		Non-heat treatable alloys
	3XXX	Mn	X	X		
	4XXX	Si	X	X		
	5XXX	Mg	X	X		
	2XXX	Cu	X	(X)	X	Heat treatable alloys
	6XXX	Mg + Si	X	(X)	X	
	7XXX	Zn	X	(X)	X	
	8XXX	Other	X	(X)	X	
CASTING ALLOYS*) EN AB- EN AC- EN AM-	1XXX0	None (min. 99.00% Al)				*) letters preceding the alloy numbers have the following meaning EN = European Standard A = Aluminium B = Ingot C = Cast Alloy M = Master Alloy W = Wrought Alloy
	2XXX0	Cu				
	4XXX0	Si				
	5XXX0	Mg				
	7XXX0	Zn				
	8XXX0	Sn				
	9XXX0	Master Alloys				

Sources: according to EN 573; prEN 1780

Figure 2.6: Aluminium alloy designation system [68].

Table 2.1: Wrought aluminium alloy series features [64].

Alloy series	General features
1XXX	<ul style="list-style-type: none"> - Non heat treatable - Low mechanical strength and high ductility - Excellent corrosion resistance - High electrical conductivity
2XXX	<ul style="list-style-type: none"> - Heat treatable - Very high mechanical strength - Low corrosion resistance
3XXX	<ul style="list-style-type: none"> - Non heat treatable - Moderate mechanical strength and high ductility - Excellent corrosion resistance
4XXX	<ul style="list-style-type: none"> - Non heat treatable - Used in architectural applications
5XXX	<ul style="list-style-type: none"> - Non heat treatable - Can be strengthened by cold work - Effectiveness of cold work hardening increased when magnesium content increased
6XXX	<ul style="list-style-type: none"> - Heat treatable - High mechanical strength and good formability - Good corrosion resistance
7XXX	<ul style="list-style-type: none"> - Heat treatable - Poor corrosion resistance - Cast properties are poor - Good machinability - Highest mechanical strength when heat treated - Good weldability and formability - Good dimensional stability
8XXX	<ul style="list-style-type: none"> - Heat treatable - High modulus of elasticity - Good weldability and high specific stiffness

The coefficient of thermal expansion of alloys depends on the nature of their composition; the presence of silicon and copper reduce the expansion while magnesium increases it. The melting point of pure aluminium at atmospheric pressure is 660°C. The addition of alloying elements reduces the melting temperature to around 500°C for some alloys [68].

2.6.3 Aluminium alloys applications

There are many advantages to using aluminium alloys in industry, due to their varied and attractive properties, such as low density (2.7 g/cm^3), ductility and tensile strength of around 90 MPa at 25°C . These shows that aluminium has a high resistance to failure. As explained earlier, since aluminium naturally has a thin oxide film on its surface, it has a good resistance to atmospheric corrosion. One of the important properties of aluminium is its high thermal and electrical conductivity which leads to its wide use in the building and construction industries. Figure 2.7 show the main applications of aluminium alloy. It shows that the main industry using aluminium alloys is transportation because of its properties, and particularly because of its lightweight.

Various industries are looking for alternatives to conventional materials especially in relation to the strong demand to tackle economic, safety and environmental issues. This implies a strong requirement to replace conventional steel and cast iron materials with lightweight alternatives. However, the properties of aluminium alloys cannot meet the demands of the automotive industry due to their low hardness value, low melting points and wear resistance. Therefore, surface treatments are very important in enhancing the surface of the aluminium alloy to withstand the rigours of various applications. Different coating technologies have been developed and improved to overcome these difficulties. The next section gives an overview of the main role of surface engineering in improving the aluminium alloy substrate.

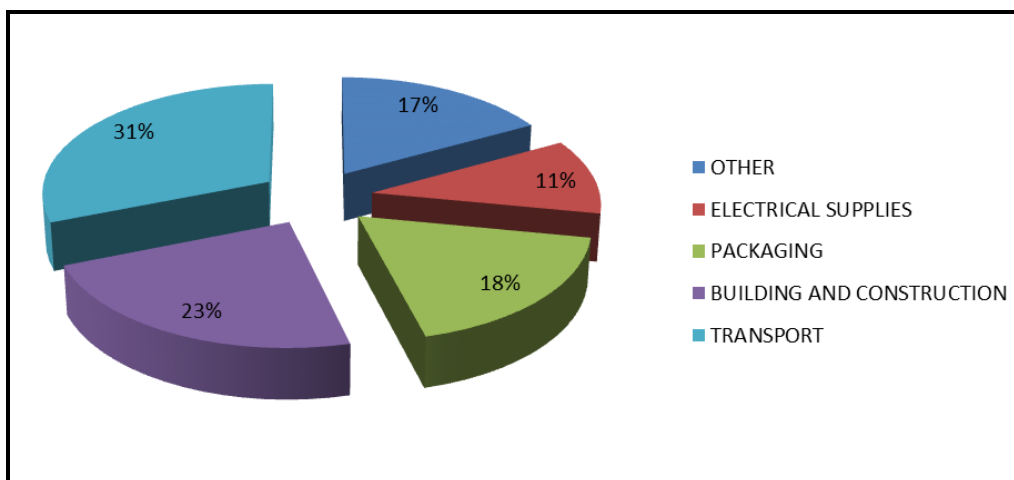


Figure 2.7: World consumption of aluminium by application [69].

2.6.4 Surface engineering on aluminium alloys and aluminium metal matrix composite

The term surface engineering is defined by the ASM handbook as the “treatment of the surface and near-surface regions of a material to allow the surface to perform functions that are distinct from those functions demanded from the bulk of the material” [70]. Many studies in the field of surface engineering have been carried out in order to enhance a material’s resistance to corrosion and wear. Statistics show that the surface engineering industry in the UK grew from £10 billion in 1995 to £21.3 billion in 2005 [71].

There are two main advantages to using surface engineering treatments for aluminium alloys. Firstly, it can improve the tribological performance of the component’s surface against the surrounding environment, which has an impact on service life and maintenance costs. Secondly, it makes available the option of selecting a cheaper substrate material for various applications with surface treatments [72].

There are various surface treatment techniques which can be used to improve the surface of the aluminium alloy. Each surface treatment (coating technique) has advantages and disadvantages as described in section 2.8.

2.7 Aluminium metal matrix composite

2.7.1 General background

Metal matrix composite (MMC) has been used commercially in the automotive industry for at least the past 20 years [73]. MMC is a composite with at least two components, one being a metal. It is made by dispersing a reinforcing material into a metal matrix. The reinforcing material has the advantage of improving the mechanical behaviour of the metal. As mentioned earlier, the automotive industry has used aluminium metal matrix composite (Al-MMC), which usually consists of aluminium reinforced with SiC particles, in many applications. Researchers have begun in the past 20 years to investigate the possibility of using Al-MMC materials in braking systems.

2.7.2 Aluminium metal matrix composite classifications and properties

The aluminium metal matrix composite classification and features depend on the aluminium alloy and the reinforced matrix used in the composition. The characteristics of the reinforced particles influence the mechanical and thermal behaviour of the MMC material. The American National Standards Institute (ANSI) standardised the aluminium metal matrix composite by the following [74]:

A / B/ CD – E

Where

A: Indicate the matrix alloy (four digit number)

B: Indicate the composition of the reinforced material (for example SiC)

C: Indicates the volume percentage of the reinforced material

D: Indicates the form of the reinforced material (p: particulate, w: whisker and f: fibre).

E: Indicates the temper designation of the matrix alloy.

In the current research, the aluminium metal matrix composite used is 6061/SiC/40p-T6. This indicates that the aluminium grade used in the matrix is 6061, the reinforced matrix is silicon carbon particles, the volume percentage of the silicon carbon particles is 40% and the temper designation of the aluminium is T6.

2.7.3 Aluminium metal matrix composite applications

There are many advantages to using aluminium metal matrix composites in industry, due to their varied and attractive properties, such as low density, ductility, high specific strength, excellent thermal conductivity and good tensile strength. Figure 2.8 shows the main applications of aluminium metal matrix composite. It shows that the main industries using aluminium metal matrix composite are transportation, aerospace and electronic because of its properties, and particularly because of its low density. MMCs are used in the field of automotive engineering for example in brake drums, pistons and cylinder blocks because of improved corrosion resistance and wear resistance [75, 76].

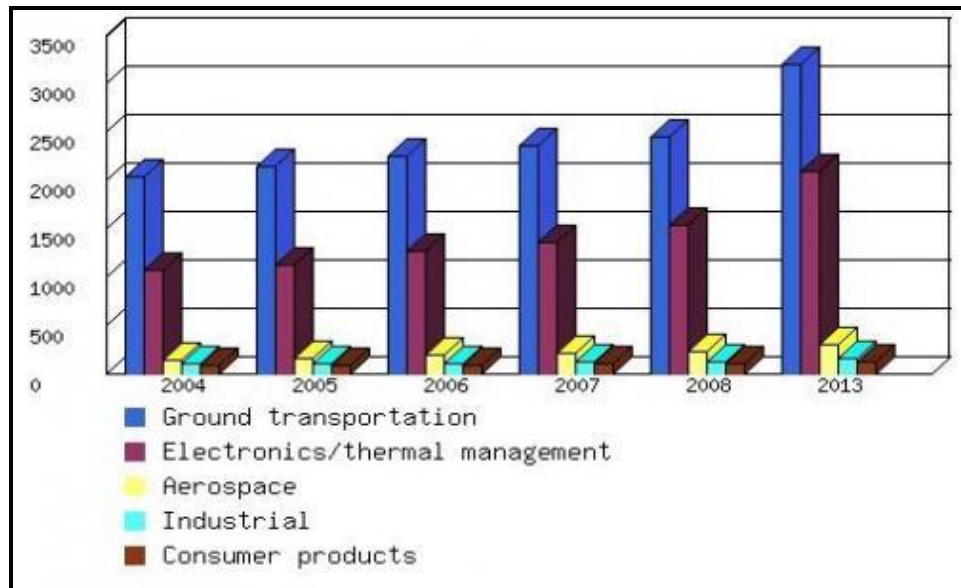


Figure 2.8: Global MMC outlook by application/segment, 2004-2013 KG 1,000S [77].

2.7.4 Surface engineering of aluminium metal matrix composite

Although the silicon carbon particles improve the properties of the aluminium alloy, surface engineering such as ceramic coating is often required to protect the surface of the Al-MMC. For example during an overruns braking test specifically the high surface temperatures might soften the aluminium alloy leaving the hard reinforced particles exposed on the surface. Coating the surface of the reinforced aluminium is a very important technique which can to improve the maximum operating temperature [78].

Alumina coated and uncoated aluminium metal matrix composite brake rotors were investigated by Rosso [79]. The results showed that the coated Al-MMC rotor showed better wear resistance than the plain disc without any significant difference in the performance. These results indicate the benefit of proper surface treatment in order to improve the thermal and wear performance of the plain Al-MMC. There are various surface treatment techniques which can be used to improve the surface properties of the Al-MMC. Each surface treatment has advantages and disadvantages as discussed below.

2.8 Coating technologies

In recent years, coating processes have been attracting much industrial attention especially from the automotive industry. In the future, different materials and coating

techniques will be investigated in order to achieve the standards set by government legislation and automotive industry expectations.

Plasma electrolytic oxidation (PEO), also known as ‘Microarc Discharge Oxidation’ (MDO), ‘Anodic Spark Deposition’ (ASD), or ‘Microarc Oxidation’ (MAO), is an environmentally friendly technique that is used to treat nonferrous alloys to create a hard aluminium oxide (Al_2O_3) coating. The main concept of this new technology is that it uses a low concentration alkaline solution (electrolyte) and a high voltage (V) to create a ceramic layer of different thicknesses (15-60 μm) on an alloy substrate. According to many researchers, the PEO coating layer improves the wear, corrosion and friction properties of the different components. Also, because it has a very low thermal conductivity, it provides a thermal barrier layer [17, 29, 80, 81].

Different areas of the PEO process were covered in a study by Yerokhim et al. [31] that included the physical and chemical fundamentals. It was found that using PEO coatings enhances the wear resistant layer, friction, corrosion and thermal properties. Also, as a result of the thick wear resistant layers, it provides excellent adhesion for the aluminium alloy components. Furthermore, the production cost of PEO coating is competitive compared with the conventional anodising process [31].

Shrestha et al. [30] investigated a black coating applied to aluminium (AA2219) using the Keronite PEO process. Coating characteristics and coating microstructures were investigated in this study and hardness, porosity, adhesion and phase composition were measured. In order to evaluate the PEO coating the results were compared with different coatings made using a normal black anodising process. Furthermore, friction behaviours and cold welding of the coated alloy were investigated in different environments. A pin-on-disc device was used in this study to test the coated disc. The pin was either coated with an aluminium alloy or AISI52100 bearing steel against a fixed flat disc (uncoated or coated aluminium alloy). It was found that the Keronite coating improved resistance to impact and fretting compared with the anodised coating. Also it was found that there was no damage to the Keronite coated layer under impact testing [30].

Furthermore, Curran and Clyne [81] studied both magnesium and aluminium substrates with plasma electrolytic coating. The thermal conductivity of the coating was measured

using a simple steady state method and it was found that the thermal conductivity was relatively low at 1W/mK. It was also found that the porosity levels were low so the low thermal conductivity was not due to the presence of pores. It was noted that with larger thicknesses, up to 100 μ m, low thermal conductivity coatings may work as a thermal barrier layer [81].

Cui et al. [80] used a plasma electrolytic technique protective coating on SiC_p/A356 composites. Both coated and uncoated SiC_p/A356 composites were tested in order to investigate the electrochemical corrosion behaviour by using a potentiodynamic polarization technique with low scanning test. It was found that, because of the PEO coating, the corrosion potential was shifted in the anodic direction and the corrosion density was much lower. Furthermore, a ring-on-ring wear tester was used in order to investigate the wear behaviour of the PEO coating and it was found that the PEO coating showed a low specific wear compared with bearing steel. Also, during the test, no fracture, cracking or collapse of coated SiC_p/A356 took place [80].

Various studies and programmes have been carried out in the last decade with regard to coating techniques and processes. These studies were concerned with finding the best possible methods for using lightweight instead of conventional materials. From various studies it has been shown that PEO can compete with anodising and thermal oxidation techniques. Also it has been found that PEO coating, instead of thermally sprayed Al₂O₃, is suitable for aluminium alloy. In addition, the PEO coating provides a cost effective solution for lightweight materials. Nowadays PEO coatings are the best candidate for various industrial applications because of their excellent friction, corrosion, wear and thermal properties [20, 31].

The main advantages of PEO coating are: its good wear and corrosion resistance [82]; it adheres well to the substrate [27, 30, 82]; the PEO process is environmentally friendly [83, 84]; it can be used to coat irregular shapes and complex geometries [85]; and there is no change in the chemical or mechanical properties of the substrate [82]. On the other hand, the main disadvantages of PEO coating are: the low growth rate [86] of the coating and its relatively high cost [87].

Demir et al. [88] investigated a coated disc brake rotor by using a number of surface treatments. Various thermal spraying techniques were used in this study with different aluminium discs. One disc was sprayed with NiCr as a bonding layer, one was coated with Al_2O_3 by plasma spraying and the last one was coated with NiCr- Cr_3C_2 by High Velocity Oxygen Fuel (HVOF) spraying. The three coated discs were tested using an inertia dynamometer, according to SAE's J2522 test procedure, and the results showed that the coefficient of friction of the disc coated with NiCr- Cr_3C_2 was higher by 6% than that of the original disc [88].

Dahm et al. [20] investigated the tribological characteristics of two aluminium alloy rotors (AA6082 and AA7075) using a dynamometer. Both rotors were PEO coated and the thickness of the coating layer was approximately $50\mu\text{m}$. A grey cast iron (GCI) rotor and an AA6082 alloy rotor coated by high velocity oxy-fuel (HVOF) spraying with a pure aluminium oxide were also tested. The test was carried out for the entire sample under the same conditions. It was found that the roughness of the PEO coated AA6082 was $0.46\mu\text{m}$ Ra which was lower than the roughness of the PEO coated AA7075 ($0.81\mu\text{m}$ Ra). Also it was found that the PEO coated AA6082 and the AA6082 coated with Al_2O_3 had a coefficient of friction (COF) of 0.3 to 0.33, on the other hand the PEO coated AA7075 had a COF of 0.25 while the cast iron had a COF of 0.5 [20].

2.8.1 Keronite PEO coating technology

Based on the literature review, the PEO process is the best candidate for improving the surface of aluminium alloy and aluminium metal matrix composite because of the advantages specified above [20, 88]. In addition, many studies have used PEO coating with aluminium alloy and it has shown very good tribological behaviour, especially in brake system applications. In this section the PEO coating process developed by the Keronite Company is explained as it was used to coat the lightweight rotors used in this research.

Keronite was established in 2000 in Cambridge and is one of the companies which specialises in surface technology, producing many coating products based on the PEO process for various applications. The company have improved the PEO process by developing the electrolyte formulation with electrical parameters in order to produce a

denser, more uniform coating, with greater hardness than anodised aluminium alloy [89]. The Keronite ceramic surface is created by converting the substrate metal surface into a dense, hard and highly adherent oxide layer by plasma discharge in a low concentration alkaline aqueous electrolyte [90]. The Keronite PEO process is shown in Figure 2.9 and involves the application of a controlled voltage to the object (anode) in an electrolytic bath (cathode), which is agitated using compressed air. The high voltage input is sufficient to develop intense plasma due to micro-arc generation at the material surface. This leads to oxidation of the material surface in addition to elemental co-deposition from the electrolyte solution to create a hard ceramic layer on the substrate alloy. A typical set of Keronite process parameters is illustrated in Table 2.2.

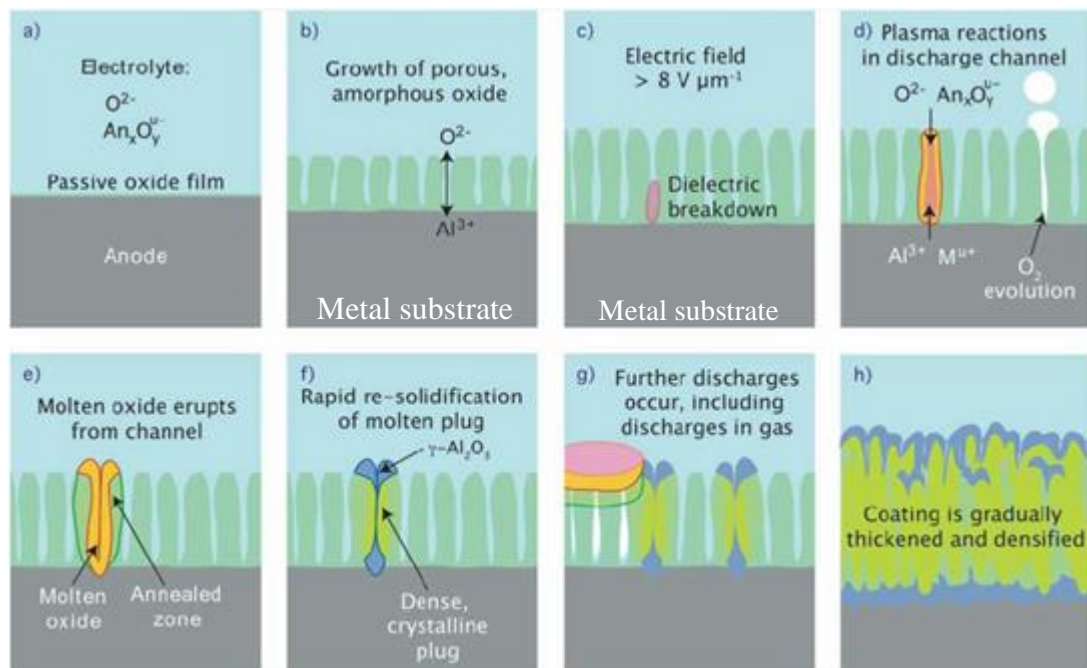


Figure 2.9: Keronite PEO process [90].

Table 2.2: Typical process parameters during Keronite PEO coating [29].

Parameter	Value
Aluminium alloy	7075
Pre-treatment	Degrease only
Electrolyte	Proprietary alkaline free of Cr, V or other heavy metals
Total salt content (%)	< 4
Typical pH	7-12
Nominal thickness (μm)	15-60
Coating rate ($\mu\text{m}/\text{min}$)	1 - 4
Voltage (V)	200 - 900
Process temp ($^{\circ}\text{C}$)	12 - 30
Coating formation method	Plasma oxidation
Surface appearance	Grey

Experimental analysis was carried out on an aluminium alloy, AA7075-T6, which was coated using the Keronite PEO process, to investigate the coating microstructure, roughness, hardness and phase structure. The results were compared with those for a hard anodised coating. The study showed that the Keronite coating had a crystalline structure composed of $\gamma\text{-Al}_2\text{O}_3$. On the other hand, the hard anodised coating had an amorphous alumina structure. The presence of the crystalline phase meant that the PEO coating was extremely hard (1620 $\text{HV}_{50\text{g}}$); in fact, four times harder than the anodised coating [89].

Keronite PEO coating was also applied to 2219 aluminium alloy in order to generate a dense, thin film on the substrate, as shown in Figure 2.10. It was found that the PEO coating microstructure mainly consisted of the $\alpha\text{-Al}_2\text{O}_3$ crystalline phase which improved the hardness value to around 1369 HV. Furthermore, other phases were also detected as shown in Figure 2.11 [30].

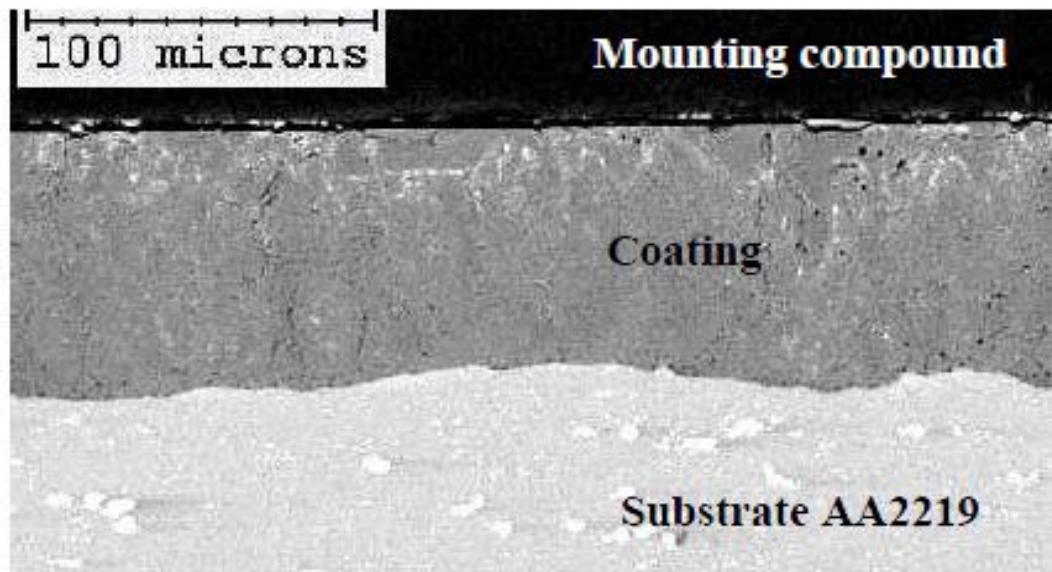


Figure 2.10: Cross-sectional BSEM image of Keronite coating on AA2219 alloy [30].

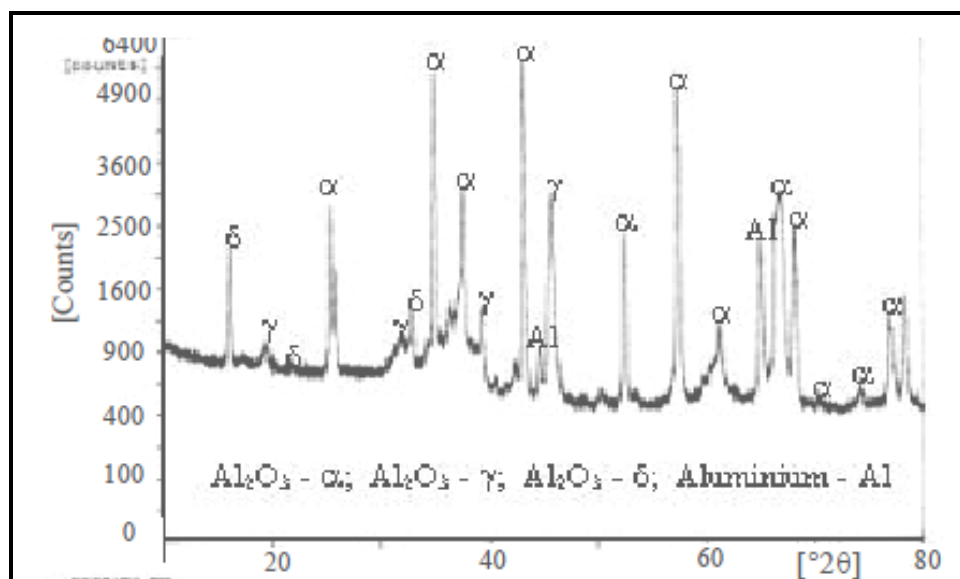


Figure 2.11: XRD analysis of Keronite coating on AA2219 alloy [30].

In addition, Al_2O_3 coating on AA6082 aluminium alloy, prepared by Keronite plasma electrolytic oxidation, was investigated and compared with a hard anodised coating on the same substrate. It was found that the hardness and elastic modulus values for the PEO coating were higher than for the hard anodised coating. Moreover, the adhesion of the PEO coating was better than that of the hard anodised coating based on a scratch test. The wear resistance of the PEO coating was much better than that of the hard

anodised coating which was directly influenced by the mechanical and structural properties [27].

2.9 Design of experiment (DoE) and optimisation analysis

Design of experiment and optimisation analysis provides the researcher with powerful tools for achieving a desired aim efficiently and reliably. Investigating every possible combination of the design parameters is a process which needs time and facilities. Using a Design of Experiment approach reduces the number of tests required to assess and investigate the design and find the main parameters that have an influence upon performance. Furthermore, utilisation of the optimisation techniques could improve the robustness of the design.

Taguchi analysis is a well-known technique used in the manufacturing and production process which improves quality by finding the best combination of factors that influence a product. Grieve et al. [19] used the Taguchi method of study to investigate the effect of various parameters on a lightweight disc brake rotor. The work produced optimised results which can be used for further investigation of the thermal performance of disc brake rotors. The study showed that the cheek thickness has the largest effect on the maximum temperature of the disc.

The Taguchi analysis defines the parameters that have the largest influence on the system which can then be used to optimise the design by finding the best combination that meets the main objective and constraints. Nowadays, optimisation plays an important role in improving the design of the product within the main objective and constraints. The automotive industry is investigating possible ways to reduce the weight of vehicles, as explained above, and one way would be to replace the conventional materials with lightweight alternatives. In addition, optimising the disc brake design could improve the thermal performance in addition to reducing the weight of the disc. Most researchers have used parametric studies to improve the design of their discs, which is a manual process [91]. The current design process can be difficult and time consuming for complex systems.

Aerodynamic shape optimisation of a disc brake was carried out by Qian [92] and it was found that there is great potential for computer based automatic design optimisation in

vehicle aerodynamic/thermal development. The optimisation analysis improved the cooling performance by 30%. Multi objective optimisation of a heavy truck disc brake system was investigated by Amouzgar et al. [93] using an iterative Latin hypercube sampling method. Three objectives were considered, namely: Minimising the maximum temperature, maximising the brake energy and reducing the mass of the back plate. A thermo-mechanical finite element model was developed and used in the optimisation analysis.

Researchers have investigated different ways to improve the thermal performance of disc brake rotors. Optimisation analysis is a very good approach to minimising the maximum temperature of the disc or to minimising the weight of the disc brake rotor with the same energy input [93, 94]. The Optimal Latin hypercube sampling method has been shown to be a good approach for use in the Design of Experiment and optimisation analysis.

Optimisation analysis requires a large number of simulations, which is time consuming. In order to reduce the computational cost, meta-models are used to replace the actual simulation models [95]. The first step is to use Design of Experiment to distribute the design variables in the design space. The defined design variables are then used to conduct the simulations based on the DoE. The output responses are used to obtain the best model that is fitted to the data. Finally, the candidate model (response) are used to find the optimum design variable using the appropriate optimisation technique [95].

Latin hypercube design (LHD), proposed by McKay et al. [96] and Iman and Conover [97], is a very popular DoE used in the area of design and analysis of computer experiments. The space filling qualities of the Latin hypercube are a very challenging problem. In the current research, optimal Latin hypercube design was used, which is based on the permutation genetic algorithm approach [48]. The proposed technique was used as it achieved good space filling and uniform distribution of the design variables in the space. In addition, it has the advantage of building and validation models which provide enhanced confidence in the fitted response.

2.10 Summary of the findings and implications for the current research

This Chapter has investigated in detail various aspects of disc brake knowledge in order to direct the current research towards achievement of its main aim and objectives. Many researchers have investigated the thermal behaviour of disc brakes using lumped, one-dimensional, two-dimensional and three-dimensional analysis. Most research studies evaluate the surface temperature of the disc brake assuming only one mode of heat transfer. Also most researchers used a constant heat flux or they assumed that most of the heat goes into the disc. However, the heat is transferred to both the disc and the pad with a ratio that depends on the material properties of both the disc and pad. This area needs more investigation and needs to be addressed in the numerical and finite element disc brake model. Accordingly many aspects need to be addressed in the current one-dimensional model, which are: the heat flux partitioning, radiation heat transfer, convection heat transfer, conduction heat transfer, rotating heat pulse (source), different materials and coatings.

Rotating heat pulse or source is defined as a technique of simulating the effects experienced in an actual life braking events. It applied the heat flux over the area of the brake pad to the area of the disc which is underneath. As the disc rotates the area alternate from being under the pad to being outside, this replicates the real world braking event. All these will be discussed in detail in the mathematical modelling Chapter. Most researchers investigate one mode of heat transfer in the one dimensional numerical model and neglect the effects of other modes such as convection and radiation. Although the radiation and the convection heat transfer have small effects on the temperature distribution of a disc brake, it is essential to develop a comprehensive model that can predict the temperature distribution in a disc brake and compare it with the experimental results.

In addition different studies have been done in the field of lightweight disc brakes and their thermal performance. They show that the aluminium composite material (Al-MMC) disc, with an appropriate coating, has the potential to replace the conventional cast iron disc in the future because of its characteristics and properties. This will lead to a reduction in the total weight of the vehicle. Further investigations need to be made in order for the Al-MMC disc to be used in the near future. Most researchers investigate

lightweight discs using experiments only, without validating the results with a numerical or finite element model which will give the potential for further investigation. Also, most researchers use a commercial pad material which might be a key factor, hence pad materials need to be investigated.

According to the previous research, it was concluded that material selection is a key factor in designing a disc brake or developing a brake system. Also it was found that many studies were concerned with replacing the conventional grey cast iron disc brake with a lighter material in order to reduce the overall weight of the vehicle, which has impacts on the performance and fuel consumption. Different materials have been investigated and studied for use in brake systems, especially disc brake systems, and it has been found that aluminium metal matrix composite and aluminium alloy is the best candidate for this application because of its various properties, which include high specific capacity, good static strengths, good fatigue strengths, low density, high thermal conductivity and high tensile modulus (almost double that of the parent alloy for Al-MMC). As a result, aluminium metal matrix composite disc brakes will be investigated in this research.

It was noticed that lightweight disc brakes need more investigation as most of the research is concerned with investigating the thermal performance of the current disc brake material, which is cast iron. Furthermore, few researchers have investigated, numerically or experimentally, the thermal performance of lightweight material such as wrought aluminium with an alumina coating. From various studies it was found that plasma electrolytic oxidation (PEO) can compete with anodising and thermal oxidation as a coating technique for aluminium alloy and MMCs.

It was reported in the literature that the small scale test rig has many advantages over the full scale test rig which make it a sensible or favourable candidate for the current research. It is clear from the literature that a formal scaling methodology should be followed in order to develop a small scale test rig as required to suit the current research need.

According to numerous studies, finite element models are essential to investigate the thermal performance of a disc brake and also to give some guidelines in designing the future generation of lightweight disc brakes.

There are a limited number of studies in the literature which look at the use of lightweight material in disc brakes. In addition, no research has been found that critically evaluates the performance of PEO coated disc brake rotors under a wide range of test conditions.

It was found that Design of Experiment and optimisation analysis offer an efficient approach to investigating the effect of various parameters on disc brake thermal performance and to finding the optimum lightweight disc brake rotor.

This research will investigate the effectiveness of PEO coating in enhancing the aluminium alloy and aluminium metal matrix composite surfaces under different braking conditions using both experimental and numerical approaches.

CHAPTER 3:

MATERIAL AND CHARACTERISATION

METHOD

3.1 Introduction

The experimental techniques used in the current research as well as the materials for the various disc brake rotors are explained and described in detail in this Chapter. The general properties and composition of the materials used in the tests were categorised for the purposes of investigating the surface damage after the braking tests. The sample preparation procedures and equipment used to investigate and analyse the material are explained. In addition, the metallographic preparation of the sample is covered in this Chapter based on the available standards and procedures. Different material characterisation techniques and equipment were used to analyse the lightweight brake rotors before and after the tests, which were as follows: Optical microscopy of materials, Scanning Electron Microscopy (SEM), Energy-Dispersive X-ray Analysis (EDX), micro-hardness tests, roughness analysis, and dimensional measurement of the rotors. These techniques and procedures were used for the lightweight disc brake rotors before and after the braking test with the results presented in Chapter 8.

3.2 Materials

Five types of material were investigated in this project, namely: 1. Grey cast iron; 2. forged aluminium alloy (6082); 3. The same 6082 alloy but with an alumina surface layer applied by plasma electrolytic oxidation (PEO); 4. Cast aluminium MMC (AMC640XA); and 5. The same MMC again but with a PEO alumina surface layer. The standard grey cast iron (EN-GJL-250) was used to provide a benchmark for the other materials as it is the standard material for disc brake rotors. The particulars of these materials are given in the following sub-sections.

3.2.1 Grey cast iron

Grey cast iron is a cast material which is based on iron and carbon. Carbon is present in the form of lamellar graphite particles (flake graphite). The properties of the material depend on the shape, amount and distribution of the graphite in the metallic matrix. The main components of cast iron alloy are iron and five main attendant elements; C, Si, Mn, P and S. Table 3.1 shows the chemical composition of the grey cast iron used in this study (referred to throughout this thesis as GCI) which is known commercially as EN-GJL-250. The main elements in grey cast iron are silicon, manganese and carbon. The carbon and silicon elements have the greatest impact on the hardness and tensile strength of the alloy.

Table 3.1: Chemical composition of EN-GJL-250 grey cast iron [98].

Element (wt.%)	C	Si	Mn	P	S	Fe
	3.20 – 3.40	1.60 – 2.40	0.60 – 0.90	max. 0.20	max. 0.08	Balance

3.2.2 Aluminium alloy

Aluminium alloys have been used widely in engineering applications and specifically in the automotive industry. In the current study, aluminium alloy 6082-T6 was used as a lightweight brake rotor. It has medium strength with excellent corrosion resistance and its chemical composition is shown in Table 3.2. It will be referred to throughout this thesis as Al-alloy.

The main elements of 6082 aluminium alloy are silicon, magnesium, manganese and other elements as shown in Table 3.2. T6 is the temper number which indicates that the alloy has been heat-treated and artificially aged.

Table 3.2: Chemical composition of 6082 aluminium alloy [99, 100].

Element (wt.%)	Si	Mg	Mn	Fe	Cr	Cu	Zn	Ti	Al
	0.70-1.30	0.60-1.20	0.40-1.00	0.50	0.25	0.10	0.20	0.10	Balance

3.2.3 Aluminium metal matrix composite

The aluminium metal matrix composite AMC640XA is a high quality aluminium alloy (AA6061) reinforced by 40% silicon carbide particles. The presence of the silicon carbide particles improves the corrosion resistance and material strength at elevated temperatures. The chemical composition of AMC640XA is shown in Table 3.3. In the current study, it will be referred to as (Al-MMC). Its main elements are silicon, carbon, magnesium and those shown in Table 3.3.

Table 3.3: Chemical composition of aluminium metal matrix composite (AMC640XA) [99].

Element (wt.%)	Si	Mg	Mn	Fe	Cr	Cu	Zn	Ti	SiC	Al
	0.40-0.80	0.80-1.20	Max. 0.15	Max. 0.70	0.04-0.35	0.15-0.40	Max. 0.25	Max. 0.15	40 Vol.%	Balance

3.2.4 PEO coating

The PEO coating for all disc brake rotors was carried out by Keronite International Ltd. The disc specimens, of $\phi 125\text{mm} \times 14\text{mm}$ thickness, were machined by turning a lathe from AA6082 alloy and Al-MMC (AMC640XA). Prior to coating deposition, the disc specimens were degreased with acetone, then coated using the Keronite processing system which involved a 160 kW pulsed bipolar AC power source and an alkaline electrolyte bath. General parameters of the PEO process are presented in Table 3.4. The PEO coating was applied for both materials to a nominal thickness of 30-50 μm which was confirmed using an induction thickness gauge and optical microscope.

Table 3.4: Typical process parameters during Keronite PEO coating for AA6082 and AMC640XA.

Parameter	PEO process	Parameter	PEO process
Pre-treatment	Degrease only	Coating rate ($\mu\text{m}/\text{min}$)	1-4
Electrolyte	Proprietary alkaline free of Cr, V or other heavy metals	Voltage (V)	200-900
Total salt content (%)	<4	Process temp ($^{\circ}\text{C}$)	12-30
Typical pH	7-12	Coating formation method	Plasma oxidation
Nominal thickness (μm)	15-60	Surface appearance	Grey to charcoal black

3.2.5 Brake pad material

All rotor materials were tested against a proprietary pad material manufactured by TMD Friction. This pad material was developed specifically to rub against an alumina coating but was also found to produce acceptable levels of friction performance against the standard cast iron and uncoated aluminium rotor brakes. The main elements in the brake pads are carbon, iron, copper magnesium and other elements in the form of particles, fibers and binder material as discussed in detail in Chapter 8. Figure 3.1 shows a Scanning Electron Microscopy (SEM) image of the surface of the brake pad used in the current study.

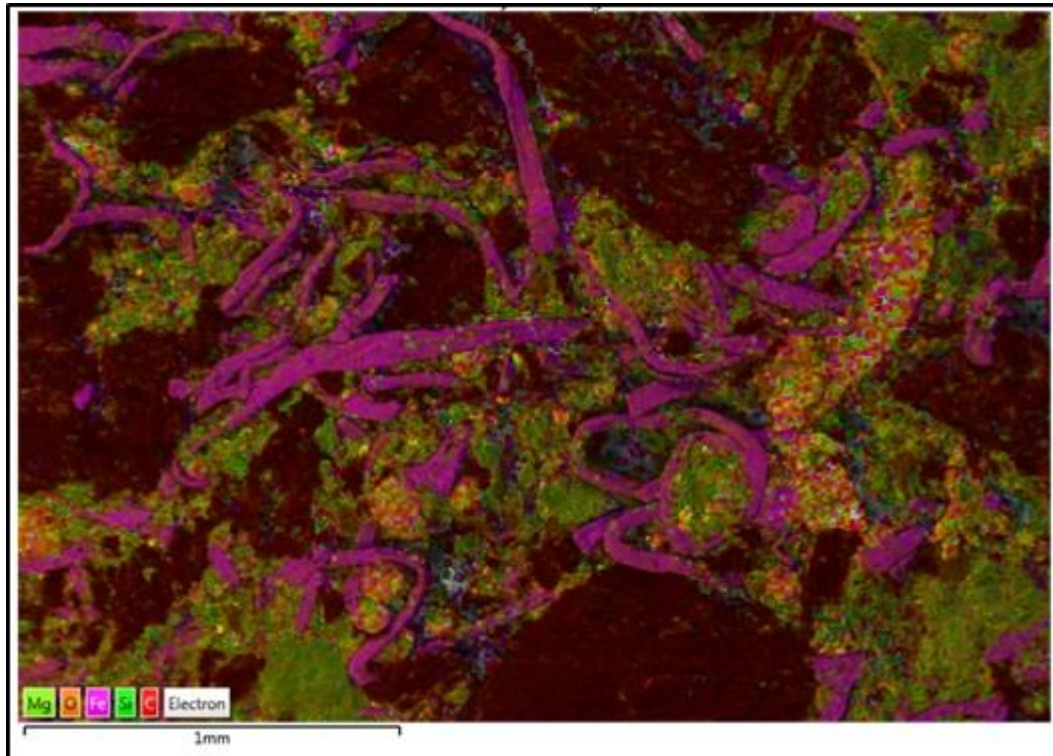


Figure 3.1: EDX image of the brake pad before the brake testing.

3.3 Sample preparation and metallographic preparation of samples

The coating surface and cross sectional view of the samples was prepared by cutting a specified section of the disc after the brake testing was finished and then using the automatic press machine (Figure 3.2) to mount the sample in Bakelite resin. The automatic press machine was used to avoid any gaps between the coating, the resin and the sample (Figure 3.3), and also to help in grinding and polishing the sample so that it would be easy to analyse using the microscope.



Figure 3.2: Automatic mounting press machine.

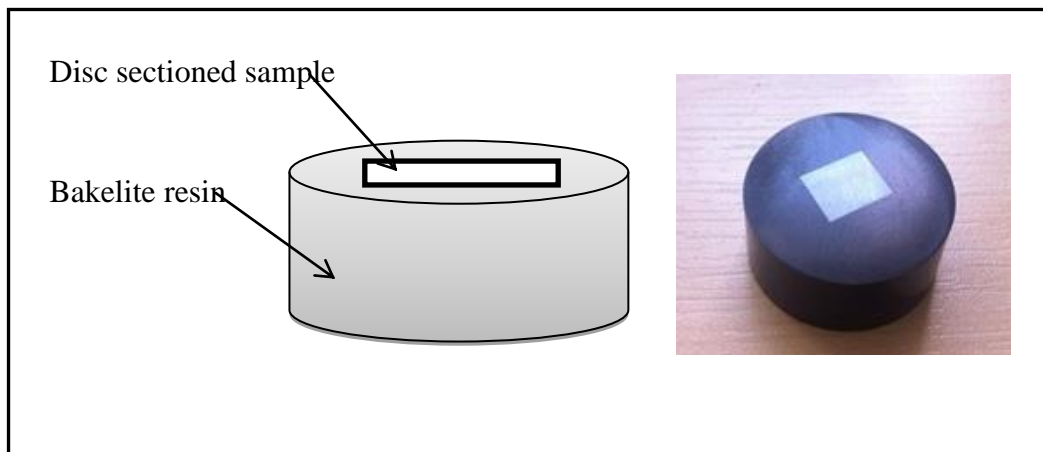


Figure 3.3: Preparing the coating and cross-sectional view samples.

On the other hand, the disc brake rotor rubbing surface was prepared by using a hack saw to cut the disc in order to avoid any contamination from the cooling fluids in the cutting machines. Figure 3.4 shows how the disc brake rotors were cut after the braking test. Each quarter was then used in the various material characterisation tests, without applying anything to the rubbing surface, in order to analyse the transfer layer and the ‘as worn’ surface texture.

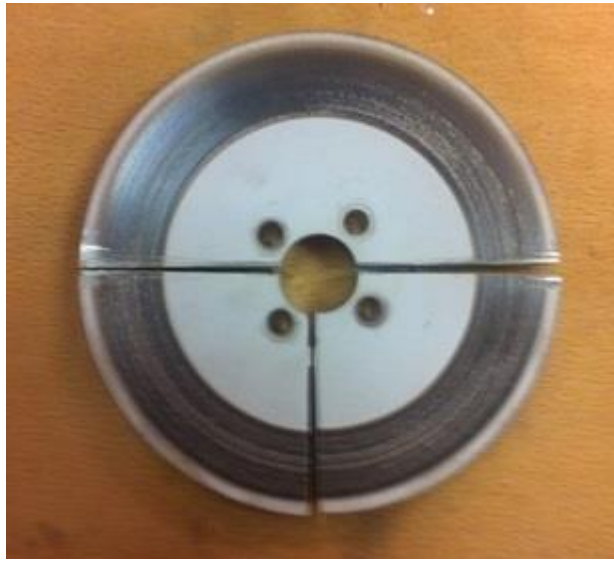


Figure 3.4: Preparing the small scale brake rotor rubbing surface samples for material characterisation analysis.

Metallographic processes (mechanical grinding and polishing) were carried out for the cross sectional surface only. The coating samples did not go through the metallographic processes, so as to avoid any damage to the coating surfaces. The cross sectional sample was ground using SiC paper with gradually decreasing grain size, beginning at paper 240 and ending with grade 1200. The grinding rotation speed was kept constant, at 300 rpm, for all paper grades and the sample was rotated 90° after each paper type. After grinding, the sample went through a polishing process where 3 µm pile based diamond suspension was used until a mirror-like surface was obtained. This procedure was achieved in accordance with guidelines given in Metallographic Techniques for Aluminium and its Alloys [101]. Figure 3.5 shows the complete procedure adopted to prepare the samples.

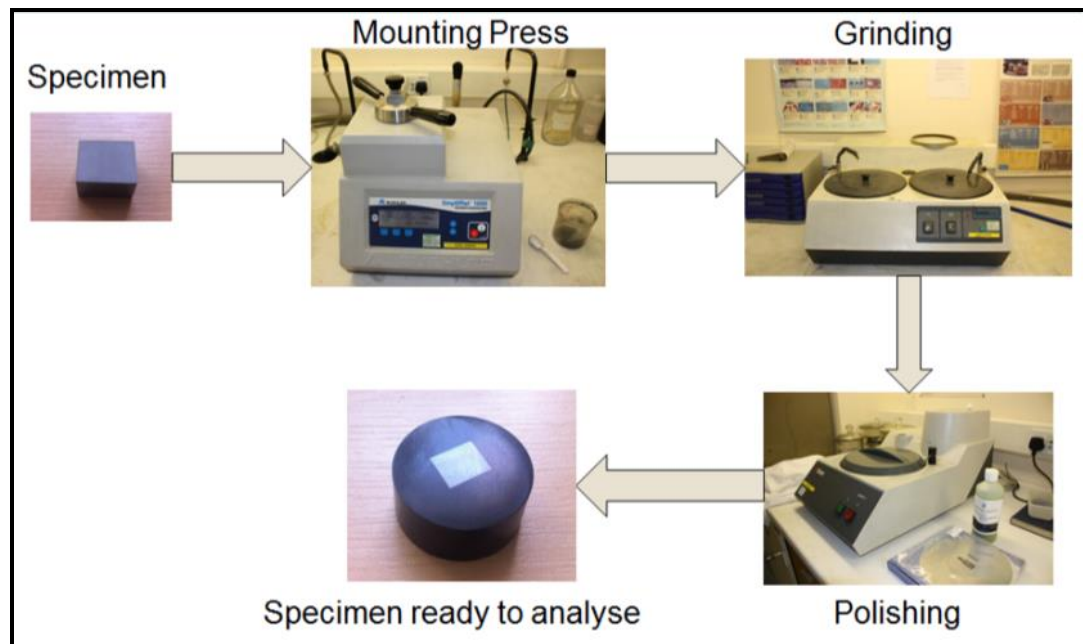


Figure 3.5: Complete procedure used to prepare the sample.

3.4 Experimental techniques

This section explains how various experimental techniques and machines were used to characterise the disc and brake pads before and after the braking test. The experiments are explained in detail, including the set-up, procedures, parameters and machines used to carry out the tests. The structure of the substrate and coating were investigated using Scanning Electron Microscopy (SEM) and optical microscopic analysis. In addition, the elemental composition was evaluated using Energy-Dispersive X-ray Analysis (EDX). The mechanical properties of the coating and substrate were obtained using micro indentation analysis, as explained in this section. Furthermore, the roughness analysis of the disc brake rubbing surface was evaluated using an optical interferometer. Finally, the overall geometry of the disc brake rotors was measured using a CNC coordinate measurement machine in order to evaluate the wear volume after the braking test.

3.4.1 Optical microscopy of materials

The surface morphologies and their structures were investigated by using a Leica microscope (LEICA CTR6000 and LEICA DM600M), as shown in Figure 3.6. Optical images were captured for all samples, which include the PEO coating and the brake rotor substrates, before and after the braking tests. Also, cross sectional images of the discs were taken to study the structure, coating thickness and uniformity of the coating. Furthermore, the optical images were used to investigate the level of porosity inside the coating in order to evaluate the coating adhesion and durability.



Figure 3.6: Leica microscope (LEICA CTR6000 and LEICA DM600M).

3.4.2 Scanning Electron Microscopy (SEM) and Energy-Dispersive X-ray analysis (EDX)

3.4.2.1 SEM and EDX fundamentals

Scanning Electron Microscopy (SEM) provides high resolution images of the desired sample by using a focused beam of electrons across the surface of the sample to scan the surface topography. The images are produced due to the interactions of the electrons

with the sample surface. The detailed microstructure of the materials can be investigated using the SEM technique with high magnification of up to 500,000 times. In addition, the elemental chemical composition of the material can be obtained using Energy-Dispersive X-ray analysis (EDX) which involves the interaction of the X-ray beam and the targeted sample. SEM analysis can be used for different applications and analyses such as obtaining high resolution images, identifying chemical compositions of materials, characterisation of materials, examining grain structures and measuring coating thicknesses by using polished cross sections.

In the current research, SEM was used to investigate the aluminium substrates and the PEO coatings. All of the SEM and EDX analyses were undertaken in the Electron Microscopy and Spectroscopy centre at Leeds University. The equipment used for the current analyses was the Carl Zeiss EVO MA15 SEM machine with integrated Oxford Instrument INCA 250 EDX system, as shown in Figure 3.7. Different samples were used in the SEM and EDX analysis which are as follows: cross sectional sample Figure 3.8a and disc brake rotor section Figure 3.8b.

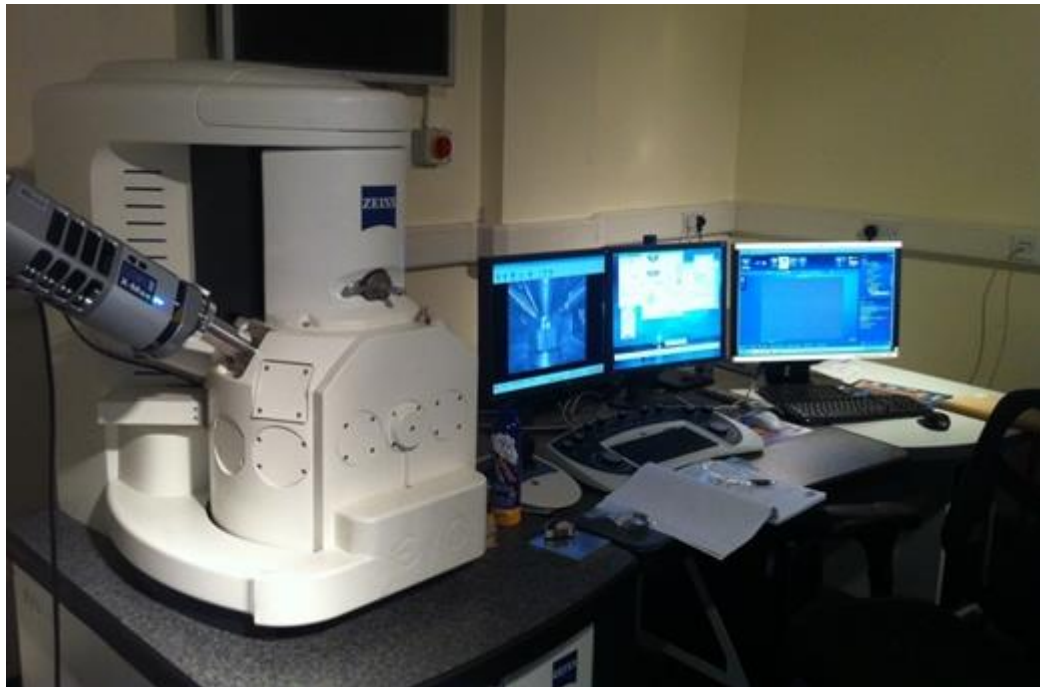


Figure 3.7: The Scanning Electron Microscopy machine with the integrated Energy-Dispersive X-ray system (Carl Zeiss EVO MA15 SEM machine with integrated Oxford Instrument INCA 250 EDX system).

3.4.2.2 SEM and EDX sample preparation

In the current study, various techniques and procedures were needed in order to capture images using SEM techniques. The surface of the sample should be conductive, so in the case of ceramic layers the coating surface needs to be coated with a conductive material such as carbon or gold. In this section the detailed procedure for preparing the sample for SEM analysis is explained.

There were two types of sample used in the SEM and EDX analysis; the first using resin to hold the sample, as shown in Figure 3.8a, and the second using the sample from the brake disc rotor without resin, as shown in Figure 3.8b. The reason for using the second type of sample was to make sure that the rubbing surface would not be damaged by the preparation process and the transfer layer could be identified correctly. Both types of sample should be kept completely dry (meaning that it should not outgas) before commencing SEM analysis.

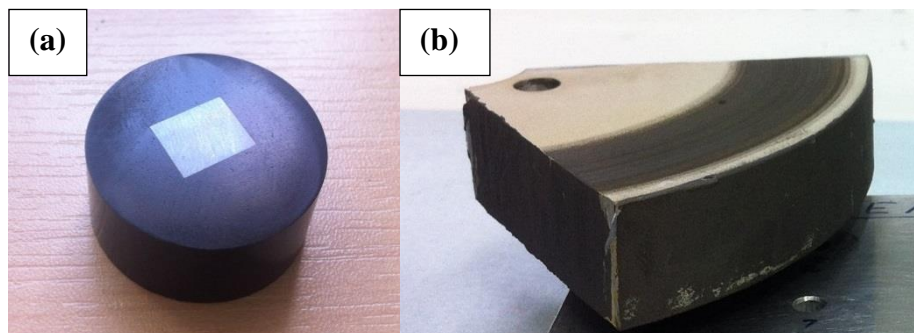


Figure 3.8: Types of sample used in the SEM analysis.

To perform the SEM analysis, each sample should be mounted into a sample holder. In this project double coated conductive carbon tape was used to mount the samples and sometimes two pieces were used for bigger samples. Double coated conductive tape is commonly used to mount samples to the holder. Carbon paint was then applied to the contact area between the sample and holder, and also to the Bakelite resin to make sure it was conductive, as Bakelite resin is a non-conductive material. Figure 3.9 shows the various components used in preparing the sample for the SEM analysis. In this case, the sample does not have Bakelite resin, and carbon paint is applied to the edge of the material.

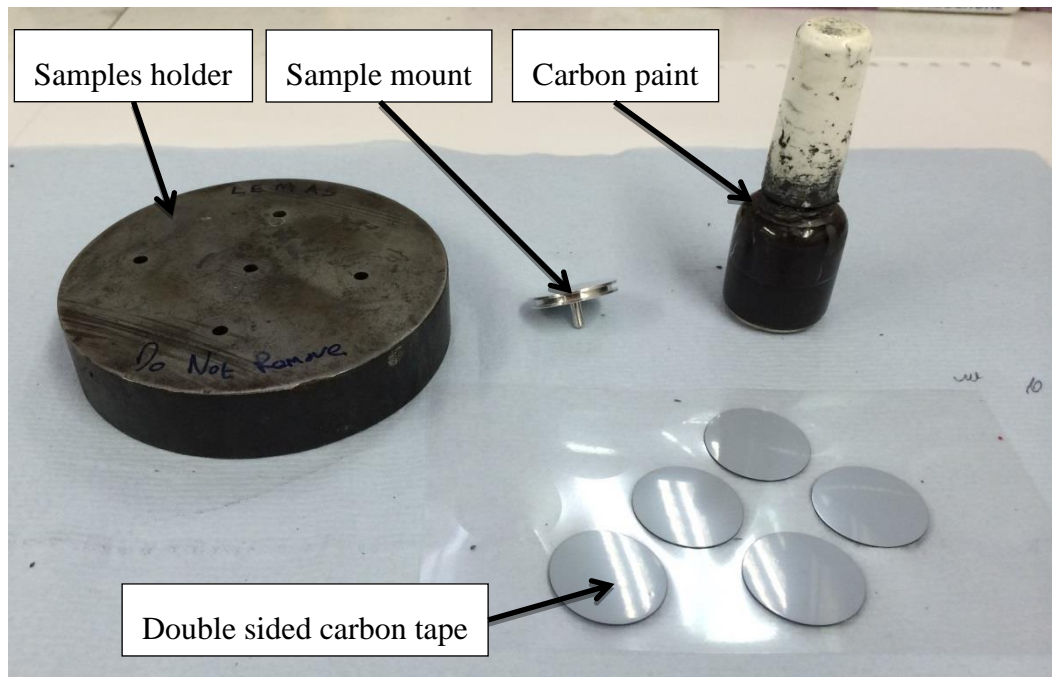


Figure 3.9: Main components used in preparing the sample for the SEM analysis.

As explained previously, the sample surface should be conductive in order to perform the SEM analysis. In this project both gold coating and carbon coating were used to coat the samples in order to make sure that the surface of the sample was conductive. The gold coating was used to obtain good SEM images, and also for the aluminium metal matrix composite since this contained carbon and so was too difficult to perform a reliable EDX analysis with a carbon coating. The carbon coating was used mainly to analyse the chemical composition of the material. In addition, the cross sectional sample was coated with gold in order to measure the coating thickness and find the level of porosity. The carbon coating was applied using the EMSCOPE TB500 SEM Carbon Coater shown in Figure 3.10 and the gold coating was applied using the EMSCOPE SC500 Gold Sputter Coater shown in Figure 3.11. The surface of a sample before and after coating is shown in Figure 3.12. After the sample has been coated it is ready for SEM and EDX analysis. In the current study most of the samples were coated, even the conductive materials.



Figure 3.10: EMSCOPE TB500 SEM Carbon Coater.



Figure 3.11: EMSCOPE SC500 Gold Sputter Coater.

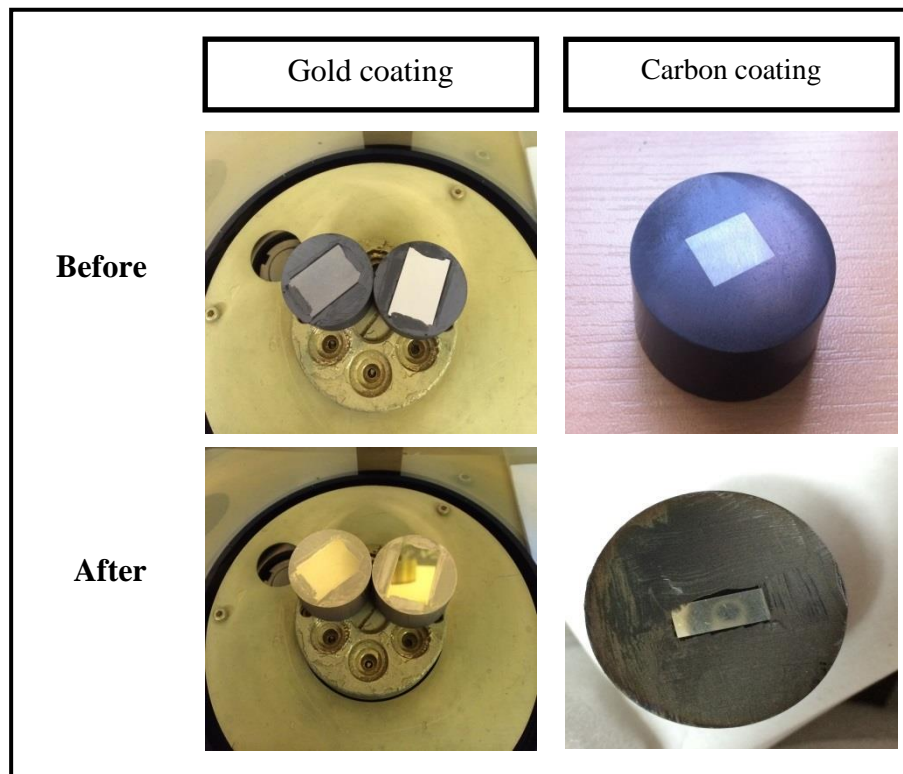


Figure 3.12: Sample surface before and after coating.

3.4.3 Micro-Hardness tests

A Micro Vickers Hardness Test machine (Mitutoyo HM-122 Hardness testing machine), Figure 3.13, was used to obtain the mechanical properties of the disc brake rotor substrates and coatings. The test was carried out in a controlled environment using Vickers indenter at a load of 1 kg. The hardness value of the coating and substrate was evaluated using the current analysis and the measurements were taken from different places of the tested surface. The coating surface was polished in order to evaluate the hardness and to see the indentation on the surface. In this analysis, the samples were clamp by resin in order to make sure that it will not move and also to make sure that the surface is horizontal. The test machine was calibrated before testing using the calibration kit with well-known hardness. The micro hardness of the coating and substrate was evaluated using standard analysis technique and the measurements were taken from at least four different places on the tested surface. The variation of the hardness value was evaluated using standard deviation analysis, which measures the amount of variation of the hardness value from the average value for each material.

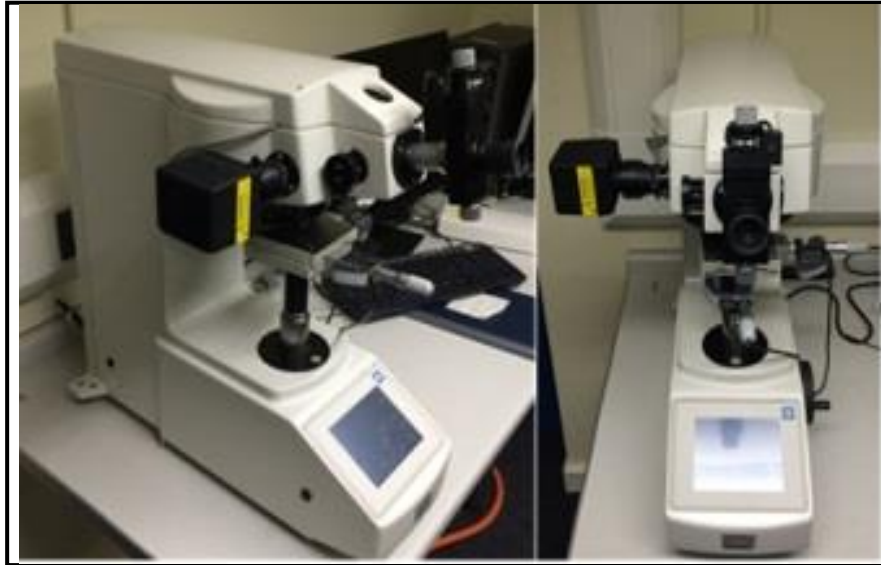


Figure 3.13: Micro Vickers Hardness Testing Machine (Mitutoyo HM-122 Hardness testing machine).

3.4.4 Roughness analysis

The roughness, wear profile and transfer layer thickness of the discs were measured and analysed using an NP Flex optical interferometer (Bruker NPFLEX optical profiling system), as shown in Figure 3.14. The texture of a surface is defined by its roughness parameters and this test was carried out in order to evaluate the effect of surface roughness on the friction behaviour. In addition, the same equipment was used to measure the transfer layer thickness and the wear profile of the rubbing surface after the braking test. The test parameters used for scanning the samples will be explained in Chapter 8. The current test does not require any special preparation for the sample.

The roughness analysis was carried out in order to evaluate the Ra value at four different positions across the wear scar as shown in Figure 3.15. The trace length was 22mm across wear scar at position 1, 2, 3 and 4. The analysis was performed using GUASSIAN Filter with 0.8mm cut OFF and 100:1 Band Width Least Squares Fit: L.S. line. The variation of the Ra value was evaluated using standard deviation analysis, which measures the amount of variation of the roughness value (Ra) from the average measured value for each line profile.



Figure 3.14: NP Flex optical interferometer (Bruker NPFLEX optical profiling system).

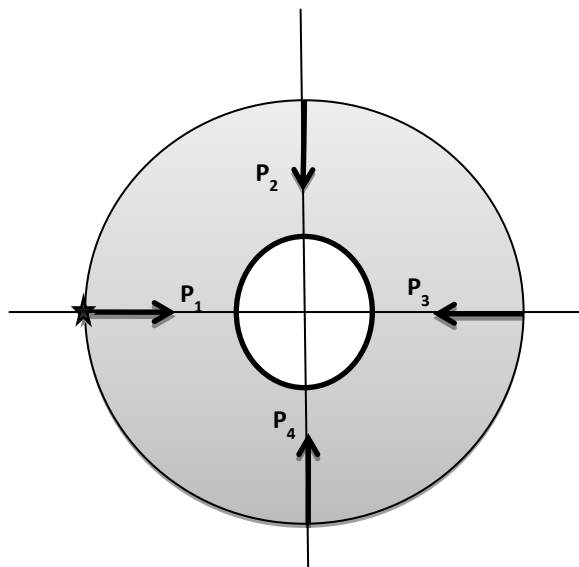


Figure 3.15: Trace positions for roughness analysis on the small scale disc brake rotor.

3.4.5 Geometry measurement

The three dimensional geometry of the brake rotors was determined before and after the braking test using a coordinate measurement machine (CMM; Kemco 400), as shown in Figure 3.16. The measurements of disc brake geometry were taken to help evaluate the wear volumes and also the variation in disc brake thickness after the tests. The CMM

machine was set up to measure the geometry of the solid disc brake rotors; a reference point was selected on the disc brake in order to perform the measurement in the same way before and after the braking tests. The machine resolution is 0.001 mm which is sufficiently accurate for the current application. The machine was calibrated before use in order to minimise any errors in the measurement.



Figure 3.16: Kemco 400 CNC coordinate measurement (CMM) machine.

3.5 Summary

This Chapter has outlined the experimental methodology for the material characterisation analysis. It explains the test set-up, the procedure, the test equipment and the test parameters. Overall descriptions of sample preparation for each analysis were given followed by descriptions of the various tests performed in order to evaluate and characterise the disc brake rotors before and after the braking tests.

The material characterisation of the substrates and coatings were performed using SEM and optical microscopic examination and their elemental compositions were evaluated using EDX techniques. The mechanical properties of the substrate and coating were measured using micro indentation analysis as outlined in this Chapter. The overall geometries of the disc brake rotors before and after the braking test were evaluated using a CNC coordinate measurement machine. The experimental results of the material characterisation analysis performed on the prepared samples, before and after the braking tests, are described in Chapter 8.

CHAPTER 4:

ONE-DIMENSIONAL THERMAL MODELS

4.1 Introduction

The theories and principles of methods for the one dimensional models that have been used in this research are explained and presented in this Chapter. A detailed one dimensional heat transfer model was constructed using Matlab to provide a powerful tool to predict the thermal performance of disc brakes during various braking tests. The comprehensive one dimensional model is capable of predicting the temperature distribution for the disc and pad brake with different material properties, braking conditions and coating layers. In addition, rotating heat source, radiation and convection effects are explained and addressed in the one-dimensional model in order to simulate a real braking event. The one-dimensional Matlab model is investigated and validated with an Abaqus 1D finite element model and literature results.

In order to achieve the main aim of replacing the cast iron disc with a lightweight alternatives (e.g. coated aluminium alloy, carbon/carbon and carbon reinforced ceramic), there are many issues to resolve. One of the issues is modelling the thin coating layer in the Abaqus finite elements software; this issue was investigated by using the thermal resistance approach, including a mesh sensitivity study and sub-modelling technique which is explained in this Chapter. Furthermore, a novel approach to the execution of disc brake finite element models using both Abaqus and Matlab software for different braking events is presented. This approach gives the user the power of using the Matlab optimisation toolbox in conjunction with the Abaqus solver. Also it reduces the computation time and memory required for such an analysis. Finally, the effects of various parameters on disc brake thermal behaviour were investigated in order to understand the thermal performance of the disc brake.

4.2 Background and theories

Heat transfer can be defined as any change in the temperature distribution in the form of thermal energy transfer. There are three different modes of heat transfer which are as follows: conduction, convection and radiation, see Figure 4.1. The first mode is conduction which is the transfer of heat through material at different temperatures, in a stationary medium whether solid or fluid. The second mode is convection which is defined as the heat transfer between fluid and a solid surface when they are at different temperatures. The last mode is radiation which is defined as heat transfer due to electromagnetic radiation. The thermal analysis presented in this Chapter was carried out included all three modes with reference to Incropera et al. [102] and Limpert [103].

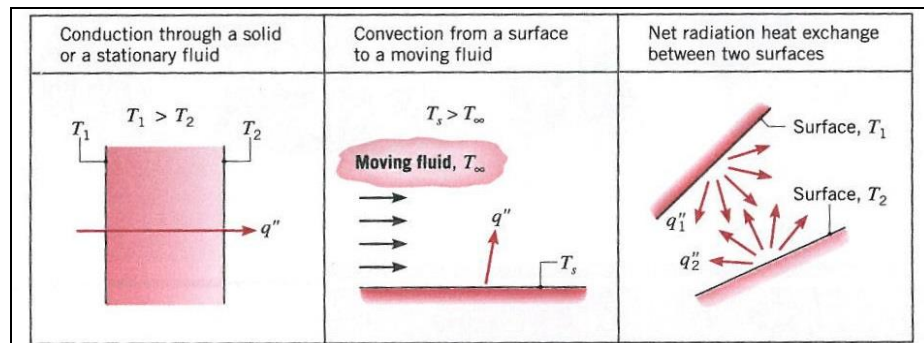


Figure 4.1: The three modes of heat transfer [102].

4.2.1 Fourier's law for heat conduction

It was explained above that heat transfer by conduction involves heat transfer between solids or stationary fluids: in this research the solid is the rotor and pads of the brake. The rate equation is used to compute the amount of energy transferred per unit time which is the well-known Fourier's law for heat conduction. The Fourier rate equation for one-dimensional steady state conditions is defined as:

$$q_x'' = -k \frac{dT}{dx} \quad (4.1)$$

where q_x'' is the heat flux per unit area in W/m^2 , $\frac{dT}{dx}$ is the temperature gradient and k is the thermal conductivity in $W/m.K$.

4.2.2 Newton's law of cooling

As explained in section 4.2, heat transfer between a surface and moving fluid is called heat transfer by convection, as shown in Figure 4.1. The rate equation for convective heat transfer is defined as:

$$q''_{conv} = h(T_s - T_\infty) \quad (4.2)$$

where q''_{conv} is the convective heat flux in W/m^2 , T_s is the surface temperature, T_∞ is the fluid temperature (in this research the fluid is air) and h is the convective heat transfer coefficient in $W/m^2.K$. This equation is known as Newton's law of cooling. The heat transfer coefficient for a solid disc in an air flow parallel to the surface of the disc may be approximated as follows:

$$h_R = \begin{cases} 0.7 \left(\frac{k_a}{d_o} \right) Re^{0.55} & \text{For } Re \leq 2.4 \times 10^5 \text{ (laminar flow)} \\ 0.04 \left(\frac{k_a}{d_o} \right) Re^{0.8} & \text{For } Re > 2.4 \times 10^5 \text{ (turbulent flow)} \end{cases} \quad (4.3)$$

where d_o is the outer diameter of the disc, k_a is the thermal conductivity of the air in $W/m.K$ and Re is the Reynolds number:

$$Re = \frac{V\rho_a l}{\mu_a} \quad (4.4)$$

where V is the vehicle speed in m/s , ρ_a is the density of the air in kg/m^3 , l is the characteristic surface length (assumed to be the diameter of the disc) and μ_a is the viscosity of the air in $kg/m.s$. All the air properties are assumed to be at ambient temperature in the present work.

4.2.3 Radiation heat transfer

As discussed in section 4.2, the last mode of heat transfer is radiation, as shown in Figure 4.1. The rate of radiation heat transfer from the surface per unit area is as follows:

$$q''_{rad} = \varepsilon \sigma (T_{sur}^4 - T_{\infty}^4) \quad (4.5)$$

where q''_{rad} is the heat transfer rate by radiation, ε is the emissivity of the surface, σ is the Stefan-Boltzmann constant $= 5.67 \times 10^{-8} \text{ W / m}^2 \text{ K}^4$, T_{sur} is the absolute temperature of the surface in $^{\circ} \text{C}$ and T_{∞} is the ambient temperature in $^{\circ} \text{C}$.

4.2.4 Thermal contact resistance

There have been many studies regarding thermal contact resistance (TCR). TCR occurs between any two faces in contact because the real contact surface is just a small proportion of the actual contact area [104, 105]. This occurs because of the roughness of the two surfaces which can only be seen on the microscopic scale. Contact pressure has a large effect on thermal contact resistance; TCR is reduced with increased surface contact pressure [104]. The resistance to conductive heat transfer through the interface of two solid surfaces in contact is known as the thermal contact resistance (R_{cond}). TCR is suitable for describing the phenomena but in order to calculate the conductive heat transfer, the thermal contact conductance (h_{cond}) is more appropriate. The thermal contact conductance is the inverse of thermal contact resistance which is defined as follows [104]:

$$h_{cond} = \frac{1}{R_{cond}} \quad (4.6)$$

4.2.5 Braking energy and power of the vehicle

The potential and kinetic energy of a moving vehicle is transferred to thermal energy by frictional work during braking. The braking energy E_b for a vehicle travelling from

velocity v_i to velocity v_f where there is no change in potential energy (ground height above sea level) is given by (tyre slip and air resistances were neglected):

$$E_b = \left(\frac{m}{2}\right)(v_i^2 - v_f^2) + \left(\frac{I}{2}\right)(\omega_i^2 - \omega_f^2) \quad (4.7)$$

where m is the vehicle mass in kg , I is the mass moment of inertia of rotating elements in the drive train in $kg.m^2$, ω_i is the angular velocity of rotating elements at the start of braking in rad/s , ω_f angular velocity of rotating objects at the end of braking in rad/s , v_i is the velocity at the start of braking in m/s , and v_f is the velocity at the end of braking in m/s . If the vehicle comes to a complete stop, which means $v_f = 0$ and $\omega_f = 0$, then equation (4.7) becomes:

$$E_b = \left(\frac{m}{2}\right)(v_i^2) + \left(\frac{I}{2}\right)(\omega_i^2) \quad (4.8)$$

When comparing the kinetic energy of the rotating elements with the kinetic energy of the whole vehicle, it was found that the former is very small compared with the latter, and the braking energy in equation (4.8) can then be written [103] :

$$E_b = \frac{Kmv_i^2}{2} \quad (4.9)$$

where K is the correction factor for rotating masses is given by:

$$K \approx 1 + \frac{I}{R^2m} \quad (4.10)$$

where R is the tyre radius in m . A typical value for the correction factor K for passenger cars is between 1.05 to 1.5 [103]. In order to study the thermal analysis for a single disc brake using equation (4.9), the braking energy for a single front wheel station is given by:

$$E_{b'} = \frac{x_f}{2} \frac{Kmv_i^2}{2} \quad (4.11)$$

where x_f is the ratio of braking energy on the front axle to the total braking energy of the vehicle. So the braking power $P_{b'}$ on a single front wheel of the vehicle can be derived by differentiating the braking energy for a single front wheel in equation (4.11)

with respect to time, i.e. $P_b = \frac{dE_b}{dt}$, and then:

$$P_{b'} = \frac{x_f}{2} Kmv_i a \quad (4.12)$$

where a is the deceleration of the vehicle in m/s^2 .

The previous derivation covered the braking power for a constant deceleration stop. In the case of a drag brake event or when there are changes in the potential energy, the same procedure can be used but with the adjustment of v_f and ω_f .

4.3 One-dimensional thermal model theory

The main aim of this Chapter is to develop an understanding of the thermal performance of the solid disc brake using a one dimensional thermal model. In this section the one dimensional thermal model was derived and developed. The derived equations were solved using Matlab software.

4.3.1 Assumption

In order to predict the temperature distribution of the brake disc and brake pad, the heat flux generated by friction between the pad and disc is required. The heat flux distribution between the disc and the pad is illustrated in Figure 4.2 In this study the thermal analysis is carried out according to the following assumptions:

- The kinetic energy changes to thermal energy without any other form of energy loss during braking.

- The frictional heat between the pad and the disc transfers uniformly to the friction surface during braking.
- The heat flux generated through friction between the pad and the disc is transferred from the friction interface to the brake parts by conduction.
- Heat transfer by radiation from the disc is included in this study along with heat transfer by convection and conduction.
- All brake parts are assumed to be at steady state conditions and constant temperature before braking.

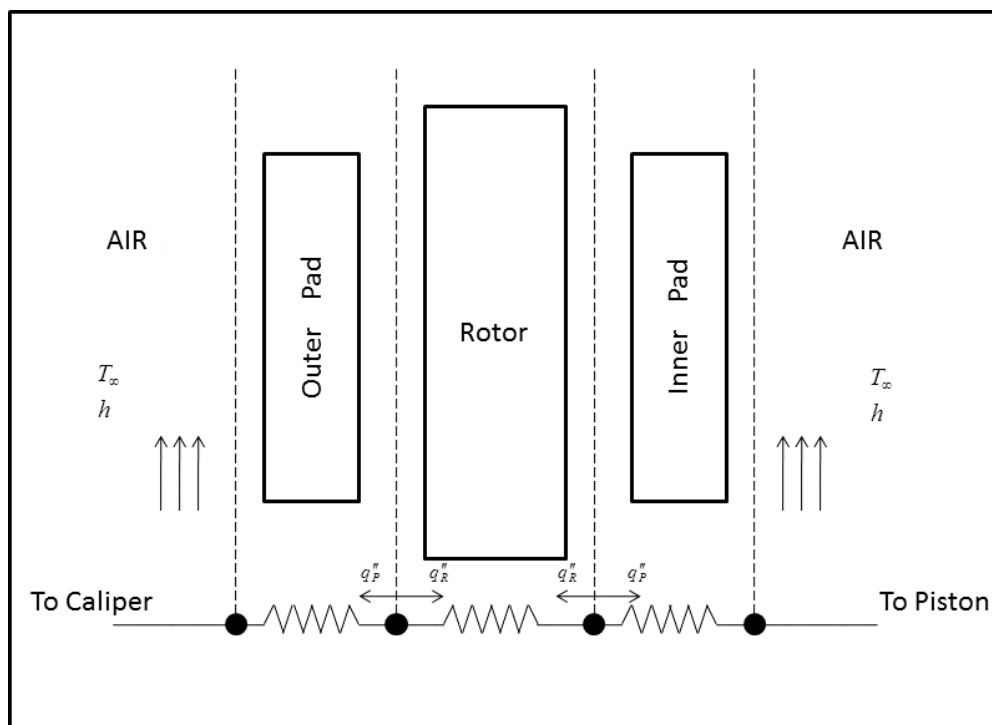


Figure 4.2: Heat flux distribution between the disc and pad.

4.3.2 Formulation

The one dimensional working layout model of the solid disc brake is illustrated in Figure 4.3. This model was used to derive the finite difference equation required to evaluate the thermal performance of a disc brake. There are two different approaches to defining the heat flux: the first approach assumes that the heat flux is distributed equally over the rubbing surfaces. The second approach is applying the heat flux on an arbitrary fixed point on the mean rubbing radius. This fixed point rotates with the disc and the heat flux is applied to that point.

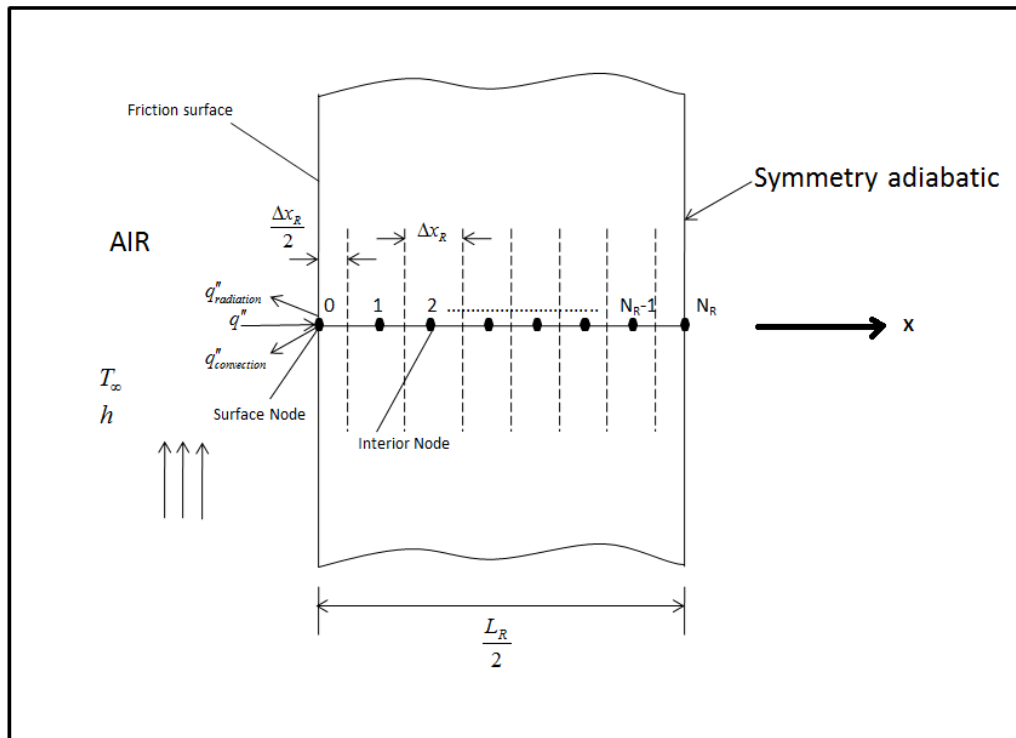


Figure 4.3: One dimensional thermal model for a brake disc.

The heat diffusion equation or heat equation with constant thermal conductivity is as follows:

$$\frac{\partial^2 T}{\partial x^2} + \frac{\partial^2 T}{\partial y^2} + \frac{\partial^2 T}{\partial z^2} + \frac{\dot{q}}{k} = \frac{1}{\alpha} \frac{\partial T}{\partial t} \quad (4.13)$$

where $\alpha = \frac{k}{\rho c_p}$ is known as the thermal diffusivity. This equation provides the temperature distribution $T(x, y, z)$ as a function of time, which will help in deriving the transient one dimensional numerical analysis for the brake. Considering the one dimensional system in Figure 4.3 under transient conditions with no internal heat generation and constant properties, Equation (4.13) becomes:

$$\frac{1}{\alpha} \frac{\partial T}{\partial t} = \frac{\partial^2 T}{\partial x^2} \quad (4.14)$$

The central difference approximation to the spatial derivative is as follows:

$$\frac{\partial^2 T}{\partial x^2} \Big|_{m,n} \approx \frac{T_{m+1,n} + T_{m-1,n} - 2T_{m,n}}{\Delta x^2} \quad (4.15)$$

Then by using the central difference approximation to the spatial derivative equation (4.15) and substituting it into equation (4.14), m is used to designate the location of the nodal point in x , the subscript n is used to designate the location of the nodal point in y and the superscript p is used to define the time dependence of T where:

$$t = p\Delta t \quad (4.16)$$

Then the equation for the finite difference approximation to time derivative in equation (4.15) can be expressed as:

$$\frac{\partial T}{\partial t} \Big|_m \approx \frac{T_m^{p+1} - T_m^p}{\Delta t} \quad (4.17)$$

Utilizing equation (4.17) and (4.15) in equation (4.14):

$$T_m^{p+1} = \frac{1}{M} (T_{m+1}^p + T_{m-1}^p) + \left(1 - \frac{2}{M}\right) T_m^p \quad (4.18)$$

where

$$M = \frac{\Delta x^2}{\alpha \Delta t} \quad \text{and} \quad N = \frac{h \Delta x}{k}$$

Equation (4.18) is valid for the interior nodes. This equation may be used for the node on the symmetry adiabatic, with $T_{m+1}^p = T_{m-1}^p$.

$$T_N^{p+1} = \frac{1}{M} \left(2T_{N-1}^p \right) + \left(1 - \frac{2}{M} \right) T_N^p \quad (4.19)$$

For the surface node with convection and radiation heat loss, the numerical analysis can be derived using the energy equation as follows:

$$\dot{E}_{in} + \dot{E}_g - \dot{E}_{out} = \dot{E}_{st}$$

$$hA(T_\infty - T_0^p) + \frac{kA}{\Delta x} (T_1^p - T_0^p) + q''A - q''_{rad}A = \rho cA \frac{T_0^{p+1} - T_0^p}{\Delta t} \quad (4.20)$$

where \dot{E}_{st} is the rate of stored energy (mechanical and thermal), \dot{E}_g is the rate of the thermal energy generation and \dot{E}_{in} and \dot{E}_{out} are the rates of the energy entering and leaving the control surface (inflow and outflow energy). Rearranging equation (4.20) for T_0^{p+1} :

$$T_0^{p+1} = \left(1 - \frac{2N+2}{M} \right) T_0^p + \frac{2NT_\infty}{M} + \frac{2T_1^p}{M} + \frac{2\Delta x q''}{kM} - \frac{2\Delta x q''_{rad}}{kM} \quad (4.21)$$

The mathematical stability condition should be satisfied in order to have a stable system, which requires choosing M to satisfy the following condition:

$$M \geq 2N + 2 \quad (4.22)$$

The above equations are valid for a solid disc brake. In the case of coated solid disc brakes the same procedure was carried out. Figure 4.4 represents the one dimensional thermal model of the coated brake disc.

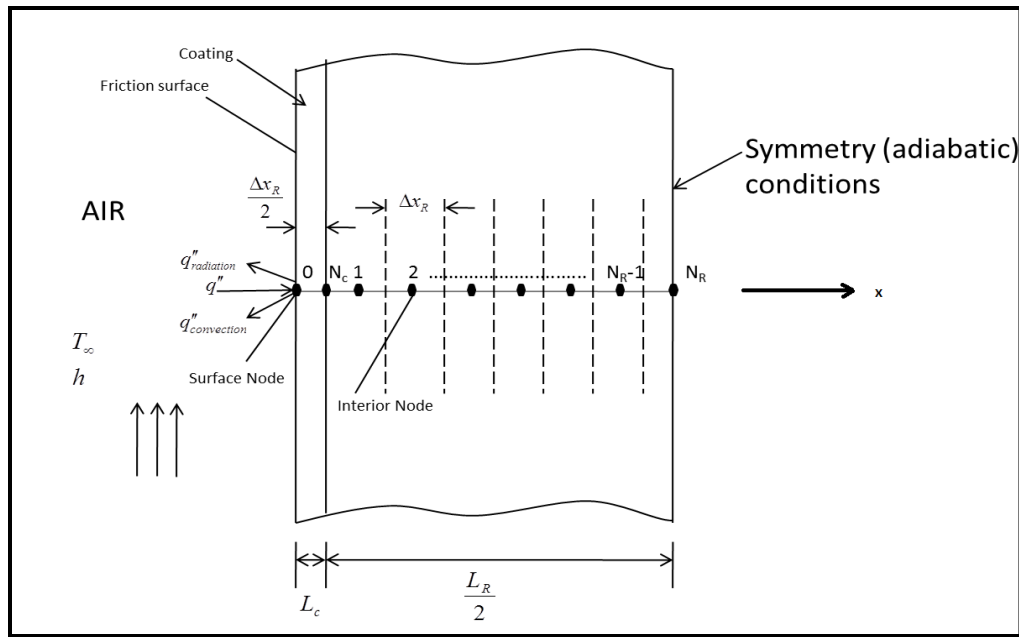


Figure 4.4: One dimensional thermal model for a coated brake disc.

The finite difference equations for the coated disc can be written as follows:

For the interior node of the disc and coating, the temperature is defined as follows:

For the disc:

$$T_m^{p+1} = \frac{1}{M_R} (T_{m+1}^p + T_{m-1}^p) + \left(1 - \frac{2}{M_R}\right) T_m^p \quad (4.23)$$

For the coating:

$$T_m^{p+1} = \frac{1}{M_C} (T_{m+1}^p + T_{m-1}^p) + \left(1 - \frac{2}{M_C}\right) T_m^p \quad (4.24)$$

For the centre point where the symmetry line is:

$$T_{N_R}^{p+1} = \frac{1}{M_R} (2T_{N-1}^p) + \left(1 - \frac{2}{M_R}\right) T_{N_R}^p \quad (4.25)$$

For the point between the coated material and the substrate (disc), the temperature is defined as follows:

$$T_{N_C}^{p+1} = \frac{(k_C \rho_C c_C)^{1/2} T_{N_C-1}^p + (k_R \rho_R c_R)^{1/2} T_{N_C+1}^p}{(k_C \rho_C c_C)^{1/2} + (k_R \rho_R c_R)^{1/2}} \quad (4.26)$$

For the disc surface node (coating surface):

$$T_0^{p+1} = \left(1 - \frac{2N_C + 2}{M_C}\right) T_0^p + \frac{2N_C T_\infty}{M_C} + \frac{2T_1^p}{M_C} + \frac{2\Delta x_C q_C''}{k_C M_C} - \frac{2\Delta x_C q_{radC}''}{k_C M_C} \quad (4.27)$$

where

$$M_R = \frac{\Delta x_R^2}{\alpha_R \Delta t}, \quad N_R = \frac{h_R \Delta x_R}{k_R}, \quad \alpha_R = \frac{k_R}{\rho_R c_{pR}}$$

$$M_R \geq 2N_R + 2$$

$$M_C = \frac{\Delta x_C^2}{\alpha_C \Delta t}, \quad N_C = \frac{h_C \Delta x_C}{k_C}, \quad \alpha_C = \frac{k_C}{\rho_C c_{pC}}$$

$$M_C \geq 2N_C + 2$$

4.3.3 Initial condition parameters and initialization

The one-dimensional Matlab model was simulated for different disc brake materials as presented in Table 4.1. In addition, the initial conditions and parameters used in simulations are presented in Table 4.2, unless otherwise specified. The partition ratio for most of the simulations was assumed constant as shown in Table 4.2, but in reality this value depends on the material of the brake and pads as described in section 4.3.4.2.

Table 4.1: Thermal properties for different solid materials [13, 17, 25, 106, 107] at room temperature (20 °C).

Materials	Density ρ [kg/m ³]	Specific heat c_p [J/kg.K]	Conductivity k [W/m.K]
Aluminium Alloy (6082-T6)	2700	895	180
Steel	7854	434	60.5
Grey Cast Iron (GCI)	7200	649	53
Al-MMC (AMC640XA)	2900	800	130
Alumina coating	3030	828	1.6
Pad Material	2596	827	0.736

Table 4.2: Initial conditions and parameters used for the simulation [13, 108].

Parameter	Value	Parameter	Value
Disc thickness, t_s	0.02 m	Proportion of braking at front axle, x_f	0.7
Rate of deceleration, d	0.7 g	Pad area, A	4100 mm ²
Number of nodes	100	Pad arc angle, θ_p	60°
Heat Partition ratio, p	0.17	Initial speed, v_i	100 km/h
Surrounding air temperature, T_∞	30 °C	Final speed, v_f	0 km/h
		Vehicle wheel diameter, d_t	0.6 m
Vehicle mass, m	1400 kg	Brake disc diameter, d_o	257 mm

In order to solve the finite difference approximation presented in the previous section, the following equations were used to calculate some quantities as shown in Table 4.3.

Table 4.3: Initialization parameters used for the simulation.

Parameter	Expression
Deceleration force (N)	$F = 9.82md$
Brake force at each front wheel (N)	$F_f = \frac{x_f F}{2}$
Stop time (s)	$t_s = \frac{v_i - v_f}{9.82d}$
Disc rotational speed (rad/s)	$\omega_{i/f} = \frac{2v_{i/f}}{d_t}$
Average angular deceleration of the disc (rad/s ²)	$\alpha_d = \frac{\omega_i - \omega_f}{t_s}$
Disc mean rubbing radius (m)	$r_d = \frac{d_o(1 + d_r)}{4}$
Disc circumference at mean rubbing radius (m)	$c_d = 2\pi r_d$
Circumferential distance covered by pad along mean rubbing radius (m)	$d_p = \frac{\theta_p c_d}{360}$
Radial pad thickness (m)	$w_p = \frac{d_o(1 + d_r)}{2}$
Number of nodal points	$N_n = \frac{\Delta x}{L}$

4.3.4 Solution procedure

In order to replicate the real braking scenario, a rotating heat source was addressed in the one-dimensional model. In the model, a fixed point was chosen at the disc surface in order to examine the different cases where the point is under the pad, or exposed to the environment. In the time where the point of interest rotates outside of the pad, then no heat goes into the disc which implies that the heat is transferred to the surroundings by convection and radiation. On the other hand, when the point of interest is underneath the pad, then the frictional heat generated will dissipate between the disc and the pad and there is no heat transfer by convection and radiation to the surroundings. In order to apply this method, the rotational speed of the specified point of interest is calculated and tracked at each time step. In addition, constant heat flux can be applied on the rubbing surface which eliminates the effect of convective heat loss between the rubbing surface and the environment where the point is under the pad.

The heat flux distribution and the portioning ratio were derived as presented later in order to solve the finite difference equations. The relation between the temperature and heat flux using the heat transfer formula for a semi-infinite solid is given by [109]:

$$T_j = \frac{2q_j \sqrt{k_j t}}{\alpha_j} \operatorname{ierfc} \left(\frac{x}{2\sqrt{k_j t}} \right) \quad (4.28)$$

where the function *ierfc* (integral of the complementary error function) is given by:

$$\begin{aligned} \operatorname{ierfc}(x) &= \frac{1}{\sqrt{\pi}} \left[\exp(-x^2) - x(1 - \operatorname{erf}(x)) \right] \\ \operatorname{erf}(x) &= \frac{2}{\sqrt{\pi}} \int_0^x e^{-\xi^2} d\xi \end{aligned} \quad (4.29)$$

Using equation (4.28) at $x=0$, the heat flux between the frictional surface of the pad and disc can be calculated, because the temperature on the frictional surface is the same for both surfaces:

$$T_R(0,t) = T_P(0,t) \quad (4.30)$$

where T_R is the temperature of the rotor and T_P is the temperature of the pad. Solving equations (4.28) and (4.29) with (4.30), the ratio of heat flux into the pad to the total heat flux can be defined as [103]:

$$\gamma = \frac{q_P''}{q_P'' + q_R''} = 1 - \frac{1}{1 + \sqrt{\frac{\rho_P c_P k_P}{\rho_R c_R k_R}}} \quad (4.31)$$

where γ is the ratio of heat flux into the pad to the total heat flux, q_P'' is the pad heat flux, q_R'' is the disc heat flux, c_P is the specific heat of the pad, c_R is the specific heat of the disc, k_P is the thermal conductivity of the pad, k_R is the thermal conductivity of the disc, ρ_P is the pad density, and ρ_R is the disc density. Utilising equations (4.28) and (4.31) and the frictional surface area A , the pad and disc heat flux can be defined as:

$$q_P'' = \gamma \frac{x_f Km}{2A} v_i a \quad (4.32)$$

$$q_R'' = (1 - \gamma) \frac{x_f Km}{2A} v_i a \quad (4.33)$$

Equations (4.32) and (4.33) are valid for short brake applications in the case of negligible cooling of the brake. In the case of repetitive or continuous braking, equations (4.31), (4.32) and (4.33) cannot be used because of the convective heat transfer and the thermal contact resistance between the pad and the disc at higher brake temperatures [103, 110]. This problem can be solved by using a heat flux correction factor ξ , which is the ratio of the real input heat flux into the brake system to the maximum total heat flux. Then equations (4.32) and (4.34) become [111]:

$$q_P'' = \xi \gamma \frac{x_f km}{2A} v_i a \quad (4.34)$$

$$q_R'' = \xi (1 - \gamma) \frac{x_f km}{2A} v_i a \quad (4.35)$$

Equations (4.34) and (4.35) are valid for repetitive or continuous braking, and are also valid for a single braking event.

4.3.5 Matlab model structure

The above equations were embedded within a bespoke Matlab m-file to investigate the temperature distribution through the disc brake. The overall Matlab model structure is shown in Figure 4.5. In the model, the first step is to calculate the time step and mesh size from the input parameter using the stability equation. Then the heat flux profile, convective heat transfer coefficient, radiation heat loss and rotational speed of the disc at each time step are calculated together. After that, the calculated parameters were utilized to solve the finite difference equations to find the temperature distribution through the disc at each time step. The rotational speed at each time step is required to evaluate the rotating heat source effect during each revolution of the disc. The temperature rise at the friction interface node and the other nodes are determined by the amount of energy dissipated at the surface.

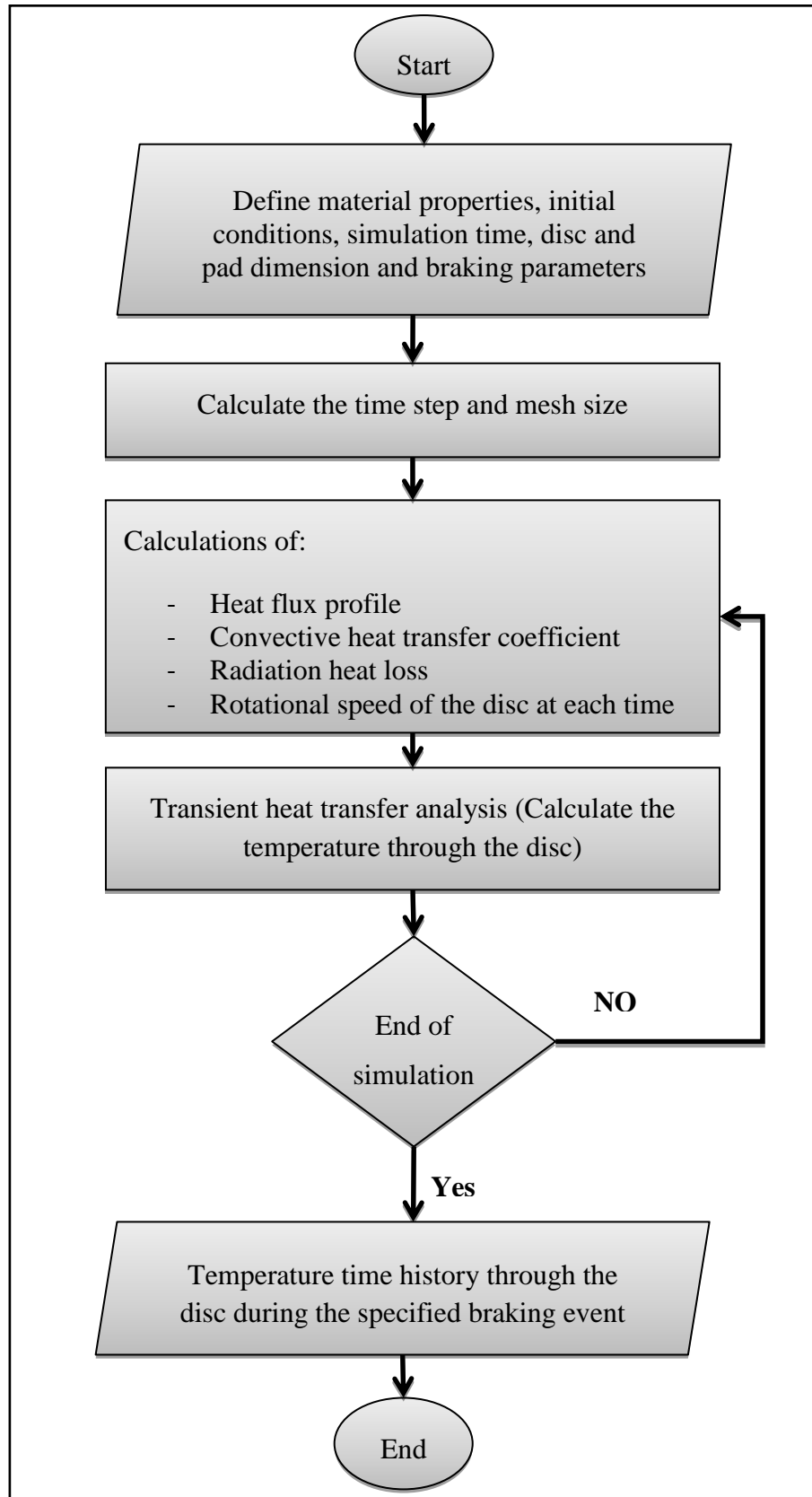


Figure 4.5: The overall Matlab model structure.

4.3.6 Sensitivity analysis

In order to have confidence in the results from the one-dimensional model, sensitivity analysis was carried out based on Fourier number stability condition (equation 4.22) to investigate the effect of the number of nodes on the accuracy of the results. In addition, the sensitivity analysis was carried out to investigate convergence of the governing equations. Using the material properties, initial conditions and parameters in Table 4.1 and Table 4.2, the maximum surface temperature difference versus number of nodes for a cast iron disc brake relative to a 100 nodes reference relative model is presented in Figure 4.5. It was found that, as the number of nodes increased, the temperature difference relative to the 100 nodes model decreased. Furthermore, Figure 4.6 shows that the number of nodes has significant effect on the surface temperature, especially when the number of nodes is below 60. As a result the 100 nodes model was chosen to carry out all the simulations in this study, except for the coating simulation as discussed below.

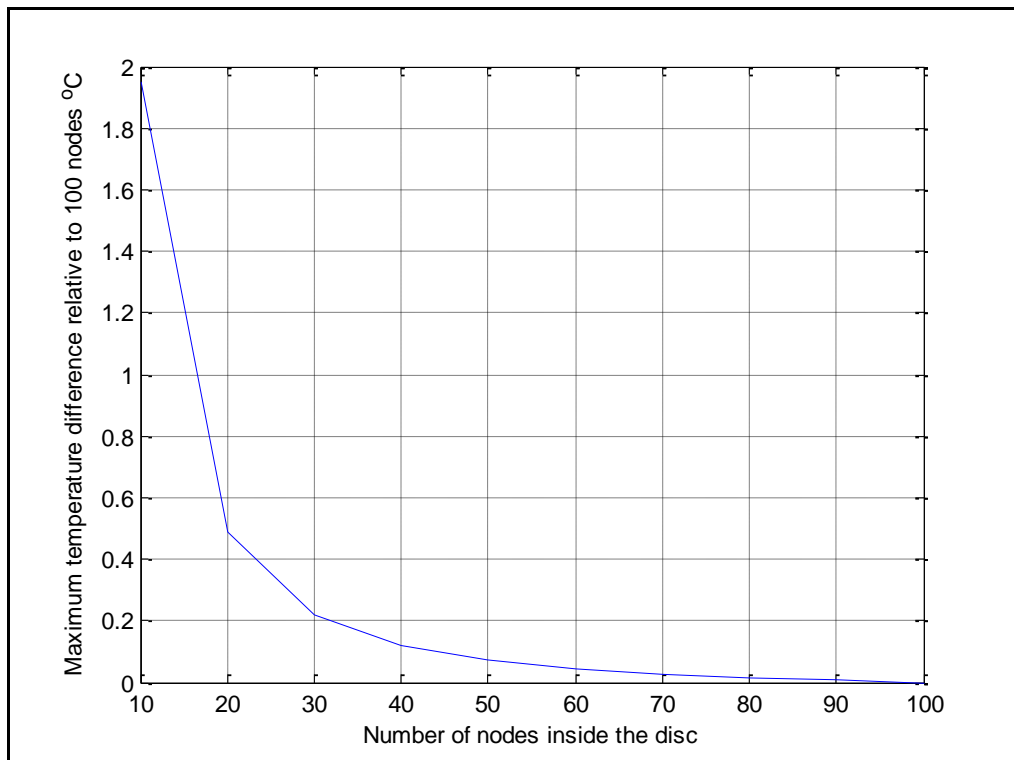


Figure 4.6: Sensitivity analysis simulation.

The above sensitivity analysis is valid for the normal disc without coating; in the case of a coated disc 100 nodes will not be sufficient to give an accurate result. According to the numerical equations in section 4.3.2, there are two stability conditions that should be met in order to have a stable system, which are as follows:

$$M_R \geq 2N_R + 2 \quad \text{and} \quad M_C \geq 2N_C + 2$$

In order to satisfy these two conditions, three parameters should be found, namely the number of nodes inside the disc, the number of nodes inside the coating and the time step; the time step should be constant for both cases. In order to find these three parameters, it is necessary to assume the number of nodes for the disc or the coating and then find the other two parameters. In the case of 100 nodes inside the disc, it was found that the number of nodes inside the coating is not an integer, which leads to an approximate value. The best way to solve this problem is to assume the number of nodes inside the coating and then to find the number of nodes inside the disc: it was found that for every 10 nodes inside the coating, 227 nodes were required inside the substrate to give accurate results. It was concluded that there is a trade-off between the number of nodes and the simulation run time. In the case of a coating disc, it was found that 10 nodes inside the coating give excellent results.

4.3.7 Limitations

There were some limitations due to assumptions which have an effect on the accuracy of the model results. These limitations could be reduced with the help of experimental results. One of the major assumptions made was the heat partitioning ratio between pad and disc. Most researchers in the literature used a constant partitioning ratio but a few researchers investigated the effect of partitioning ratio on the thermal performance of a disc brake. Experimental analysis of disc brakes could be the key to obtaining more accurate partitioning ratio. Furthermore, the convective heat transfer coefficient was estimated by assuming that the disc is a flat plate and air streams over the whole surface of the disc with a constant velocity. This assumption neglects the effect of interaction of the air flow with other components and surfaces, such as the wheel hub, caliper, wheel, and so on. Finally a number of parameters were taken from the literature or were estimated which may have a limited range of applicability and might affect the results.

4.4 Abaqus One Dimensional Model

The performance of the disc brake was also analysed using Abaqus finite element analysis (FEA) software. A 1D FEA model was first validated against the Matlab model and then used as a guide to develop the 2D and 3D FEA models. Also the 1D FEA model was used to investigate different approaches to including the effect of a coating layer with or without explicitly modelling it. The 1D transient heat transfer FEA model was meshed using 4-node linear axisymmetric heat transfer quadrilateral elements (DCAX4). The same boundary conditions as for the 1D Matlab model (see section 4.3) were applied in the 1D Abaqus model as shown in Figure 4.7. The overall Abaqus model structure is shown in Figure 4.8 [112].

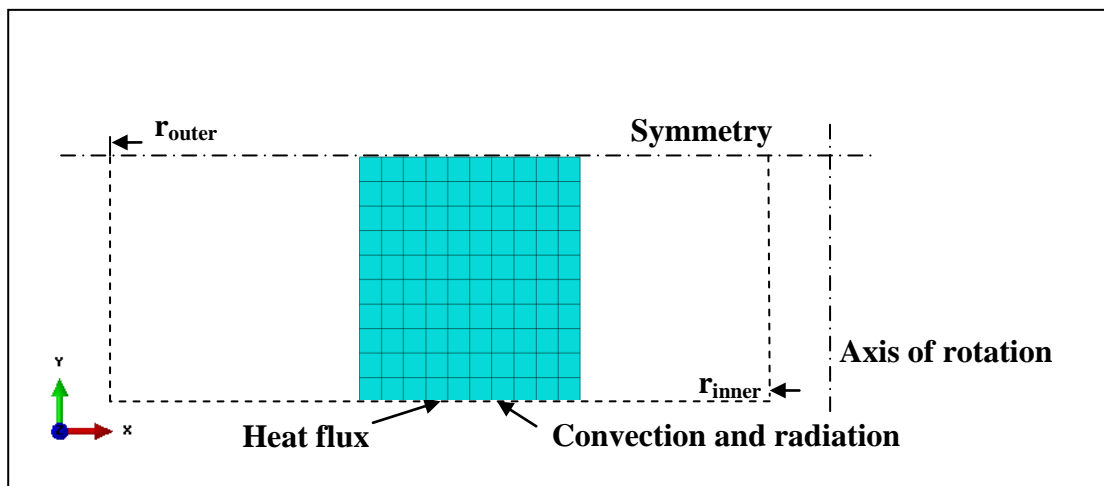


Figure 4.7: One dimensional FE model of brake disc in Abaqus.

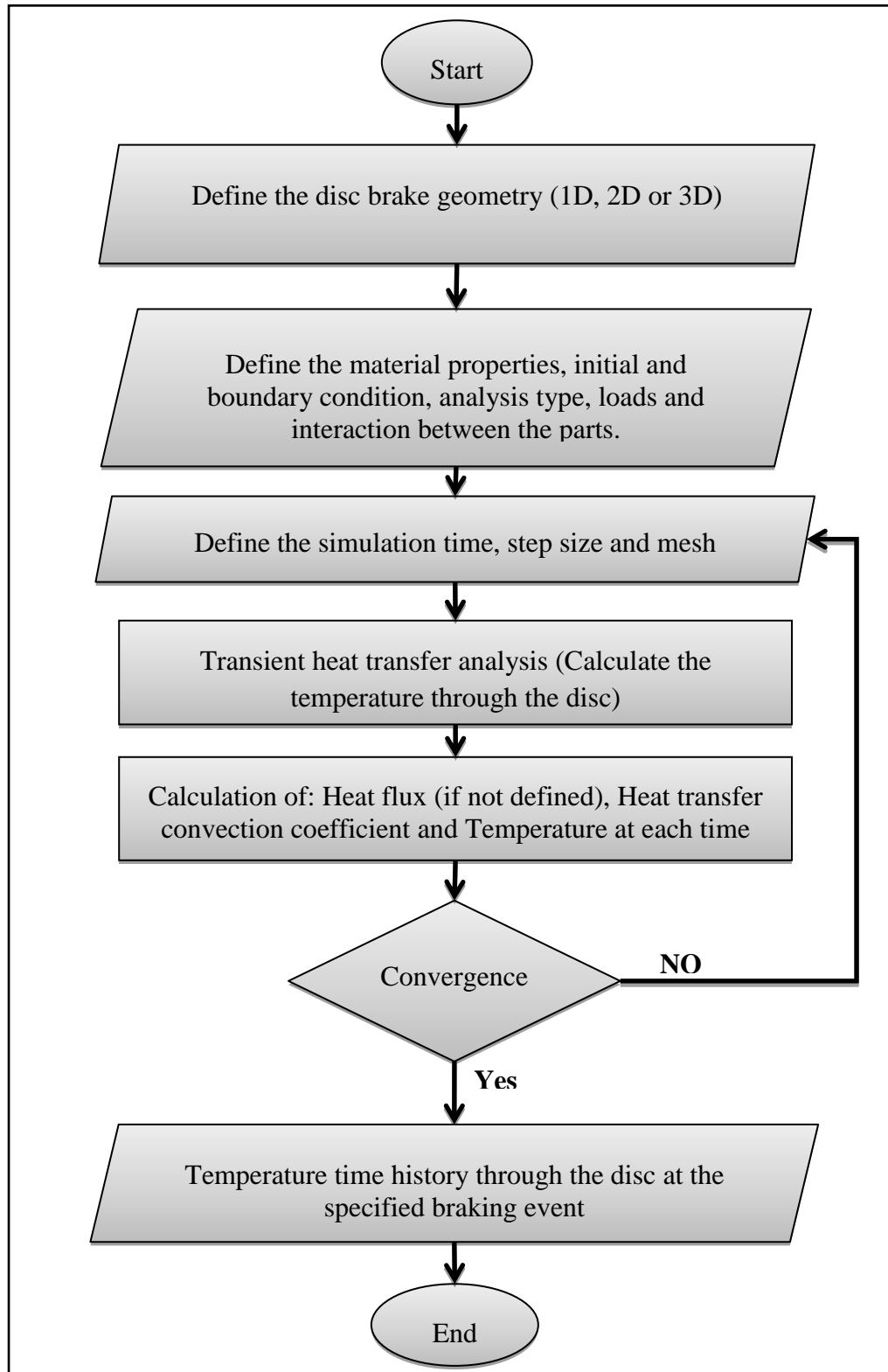


Figure 4.8: The overall Abaqus model structure.

In order to ensure an accurate temperature distribution across the disc brake in the 1D Abaqus model a mesh sensitivity analysis was conducted. It is very important to make

sure that the mesh is dense enough through the thickness of the disc to account for the changes in temperature in this dominant direction of heat conduction. The maximum temperatures at the surface and central nodes of the disc were compared for different mesh densities. As explained above, the 1D transient heat transfer model of the disc brake was meshed using 4-node linear axisymmetric heat transfer quadrilateral elements (DCAX4) with the same initial and boundary conditions as for the Matlab model. The material properties for the cast iron disc used in the mesh convergence study simulation are shown in Table 4.1 and the braking scenario parameters and conditions are shown in Table 4.2.

Table 4.4 and Figure 4.9 show the maximum temperatures at the disc surface and disc centre for different mesh densities (number of nodes). From the results it was concluded that the number of nodes has only a small effect on the temperature distribution. It was found that the maximum temperature of the disc was stable at 64 nodes. On the other hand, as the number of nodes increased beyond 64, the simulation time increased significantly so there is a trade-off between the mesh density and the simulation time. According to the mesh convergence study, 64 nodes will be sufficient for the 1D heat transfer model.

Table 4.4: Mesh sensitivity analysis for the one dimensional Abaqus model.

Nodes	Surface temp [°C]	Central temp [°C]
2	103.6	66.1
4	104.3	67.9
8	104.3	68.4
16	104.3	68.5
32	104.3	68.5
64	104.3	68.5
128	104.3	68.5

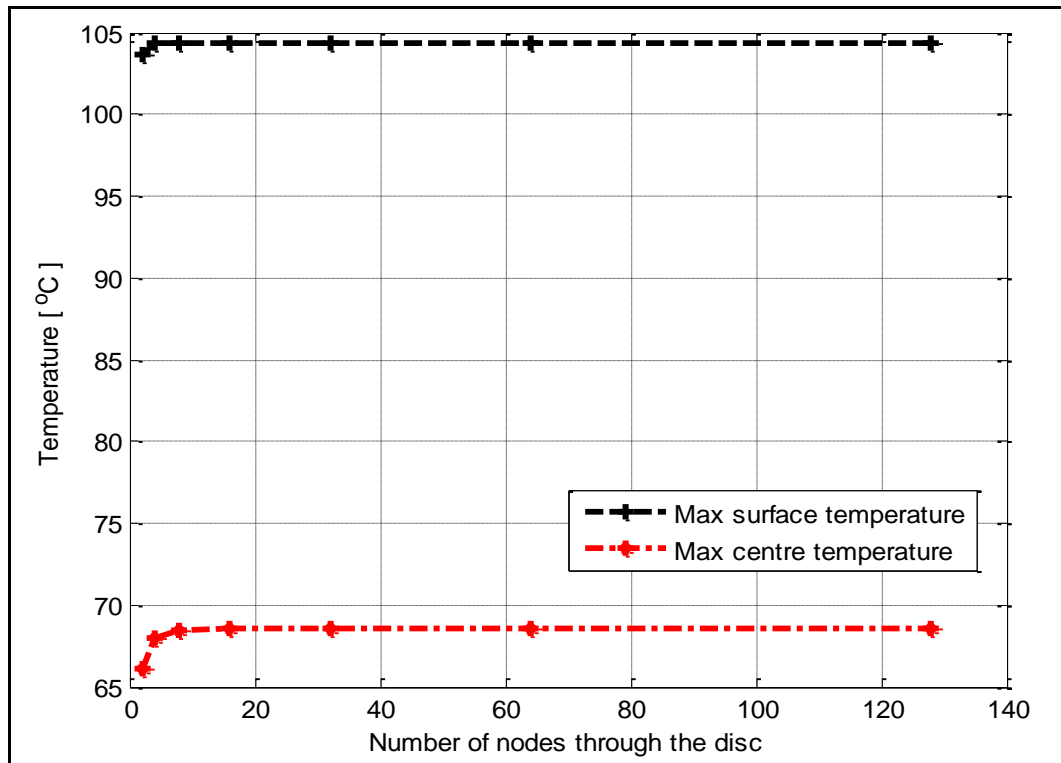


Figure 4.9: Mesh density sensitivity analysis for 1D Abaqus model.

4.5 Validation of the One-dimensional Matlab model

The 1D Matlab model was validated against the 1D Abaqus model and literature results in order to make sure that the 1D Matlab model is robust and can be used to carry out the investigation of various disc brake materials with different braking conditions.

4.5.1 Validation of the 1D model against literature

The one-dimensional Matlab model was validated against the results from the literature [10]. The material properties used in this simulation are for steel, as shown in the second line of Table 4.1. In addition, the specification of the disc brake modelled is presented in Table 4.5.

Table 4.5: Parameters of automotive brake application [15, 17].

Inner disc diameter	132 mm
Outer disc diameter	227 mm
Disc thickness	11 mm
Mean sliding radius	94.5 mm
Convection coefficient	$60 \text{ Wm}^{-2}\text{K}^{-1}$
Vehicle mass	1800 kg

Using the data in Table 4.1 and Table 4.5, the disc surface temperature was evaluated using the one dimensional Matlab thermal model, based on a braking duration of 4 seconds, an initial vehicle speed of 100 km/h and a constant deceleration of 7 m/s^2 . The results were compared with the published results (Newcomb, 1960) as shown in Figure 4.10. The calculated results show very good agreement with the published experimental results.

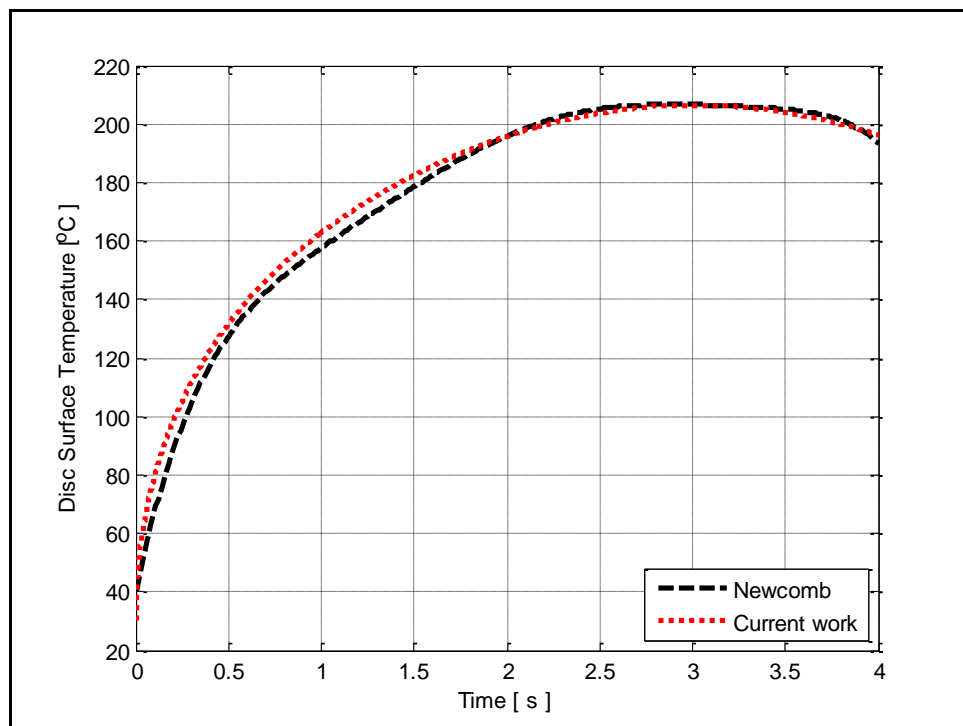


Figure 4.10: Disc surface temperature comparison between the current model and Newcomb [10].

4.5.2 Validation of the 1D Matlab model with 1D Abaqus model

The 1D Matlab model was validated against the 1D Abaqus cast iron disc model. The material properties, initial condition and braking parameters are shown in Table 4.1 and Table 4.2. The results derived from the Matlab show very good agreement with the results obtained from Abaqus model as shown in Figure 4.11.

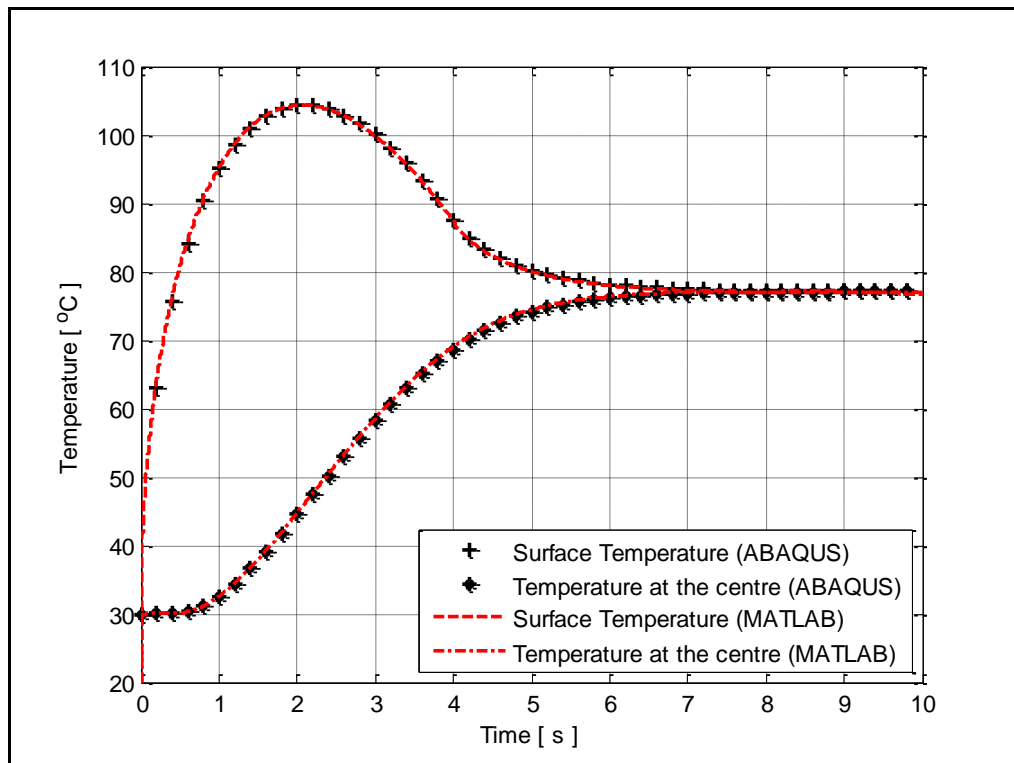


Figure 4.11: Validation of the Matlab numerical model with the Abaqus model.

4.6 Coating layer study

The main problem of modelling a thin coating layer on the surface of the brake disc in Abaqus using an explicit or implicit algorithm is the thickness of the coating which is typically in the order of μm ; this potentially requires a much denser mesh than for the substrate and causes high computation time. The thermal performance of a coated disc brake was therefore investigated using three different approaches: implicitly using a thermal contact resistance to regenerate the coating, explicitly modelling the coating with a very fine mesh and using sub modelling technique.

4.6.1 Thermal resistance modelling

The standard Abaqus software was used to solve two different transient one dimensional heat transfer models. The first model consists of two bodies directly in contact in the form of an aluminium metal matrix composite (Al-MMC) disc and pad brake modelled using 4 node heat transfer elements as shown in Figure 4.12a. The second model consists of the same two bodies but with an alumina coating layer explicitly modelled on the Al-MMC disc brake as shown in Figure 4.12b. The axial thickness of the disc is 7 mm which is the same as the radius in the 1D model. The radial width of the disc and pad included in the model is also 7 mm although this is arbitrarily chosen as no heat flow occurs in the radial direction in this 1D model. In reality the coating thickness is on the scale of μm [113] but, in order to investigate the heat flow and temperature distribution through the coating layer, it was assumed that the coating thickness was 0.25 mm. This coating thickness was chosen to reduce the model size and computational time. The material properties for the disc, pad and coating used in this analysis are shown in Table 4.1.

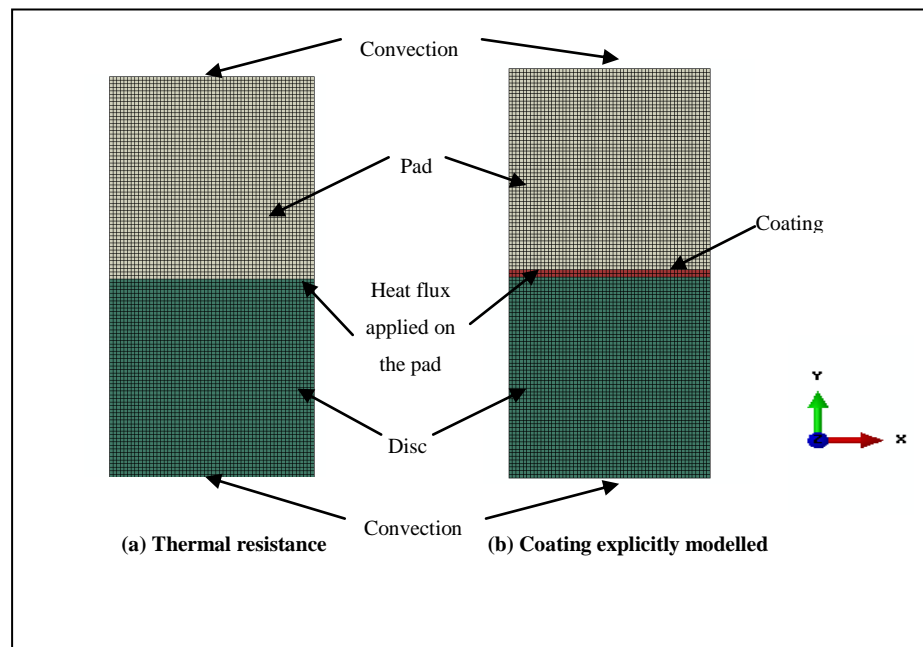


Figure 4.12: One dimensional transient models.

The two transient models were constructed and solved using Abaqus, one with the coating modelled as a thermal resistance on the disc rubbing surface (Figure 4.12a) and one with the coating modelled explicitly with finite elements (Figure 4.12b). A 4 second transient heat transfer analysis with 0.01 second time step was performed in both cases, using a 4 node heat transfer element (DC2D4). At the contact interfaces, surface contact with small sliding motion was chosen. The mesh size was chosen so that the distance between the nodes is 0.125 mm in the heat flow direction. A heat flux of either $1 \times 10^5 \text{ W/m}^2$ or $5 \times 10^5 \text{ W/m}^2$ was applied on the rubbing surface to represent both moderate and extreme braking events. Heat transfer by convection was considered from the non-conductive surfaces of the models with a heat transfer convection coefficient of $30 \text{ W/m}^2\text{K}$ for both models, and the component initial temperature was set to 20°C .

In the thermal resistance models Figure 4.12a, thermal resistance or conductance needs to be defined between the different bodies. The highest thermal conductance allowed by Abaqus, which is $1 \times 10^{15} \text{ W/m}^2\text{K}$, was used when there is no gap between the surfaces, in order to exclude the effect of thermal contact resistance between the physical coating layer and the disc and pad bodies in model Figure 4.12b. This procedure produced a zero contact resistance between the surfaces which is essential when aiming to focus on the effect of coating and avoid any other type of losses. The thermal resistance for the implicit coating model shown in Figure 4.12a was obtained using the thermal conductivity, thickness and cross-sectional area of the coating as follows:

$$R_{cond} = \frac{\delta x}{kA} = \frac{0.00025}{1.6} = 0.000156 \text{ m}^2\text{K/W} \quad (4.36)$$

Abaqus uses a thermal conductance rather than a resistance, which is equal to $1/R_{cond} = 6400 \text{ W/m}^2\text{K}$, and this was applied to the rubbing surface of the brake disc.

A heat flux of $5 \times 10^5 \text{ W/m}^2$ was used to evaluate the temperature across the disc and pad for both models. The temperature distribution at the end of the simulation ($t=4 \text{ s}$) is shown in Figure 4.13. The x-axis shows the distance from the bottom block (disc) to the top block (pad). In order to compare both results the temperature distribution of the thermal resistance model should be shifted by 0.25 mm to the right (coating thickness).

The results in Figure 4.13 show that the thermal resistance approach can be used to model the effect of the coating layer with some limitations, the maximum surface temperatures for both models are similar but there is a relatively small difference in the temperature across the disc itself with the temperatures being around 5°C higher for the thermal resistance model. This is because the higher thermal inertia (ρc_p) of the coating compared to the substrate is not included in the thermal resistance model. The effect of this is to cause a lower proportion of the frictionally-generated heat to be transferred to the disc as can be seen from the simple heat partition equation (4.31):

$$\gamma = \frac{q_P''}{q_P'' + q_R''} = 1 - \frac{1}{1 + \sqrt{\frac{\rho_P c_P k_P}{\rho_R c_R k_R}}}$$

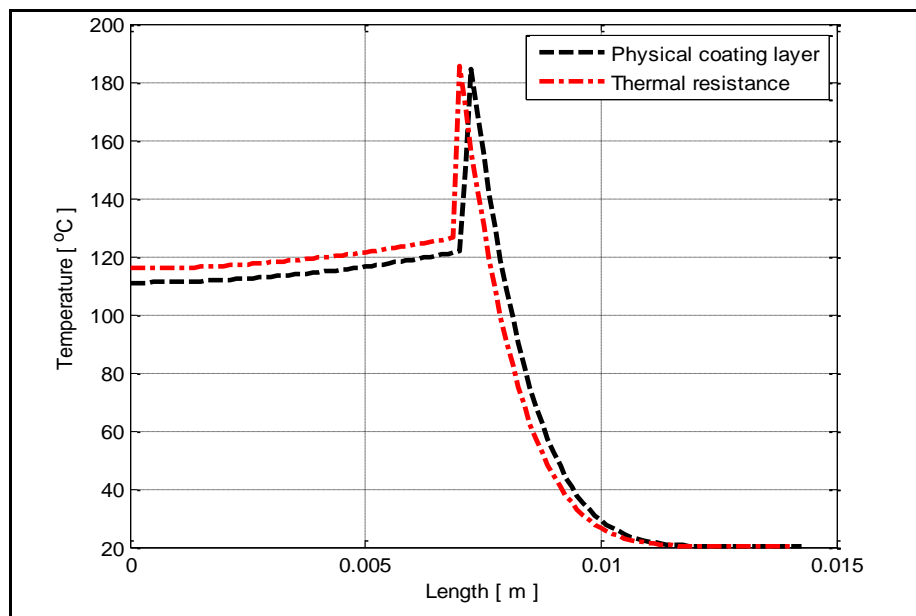


Figure 4.13: Temperature distribution across the disc and pad without tuning.

The thermal resistance model was then tuned through a trial and error process by raising the convection coefficient on the disc exposed surface. This increased the amount of heat that is transferred to the disc. Figure 4.14 shows the temperature across the disc, coating and brake pad for the two different models after tuning of the thermal resistance model at the end of simulation ($t=4$ sec). Again the x-axis shows the distance from the bottom block (disc) to the top block (pad). Note that in order to compare both results the temperature of the thermal resistance model should be shifted by 0.25 mm to the right to

account for the coating thickness. The results show that the use of the thermal resistance model instead of explicitly modelling the coating layer with finite elements can give good accuracy if the model is tuned to account for the higher thermal inertia of the coating.

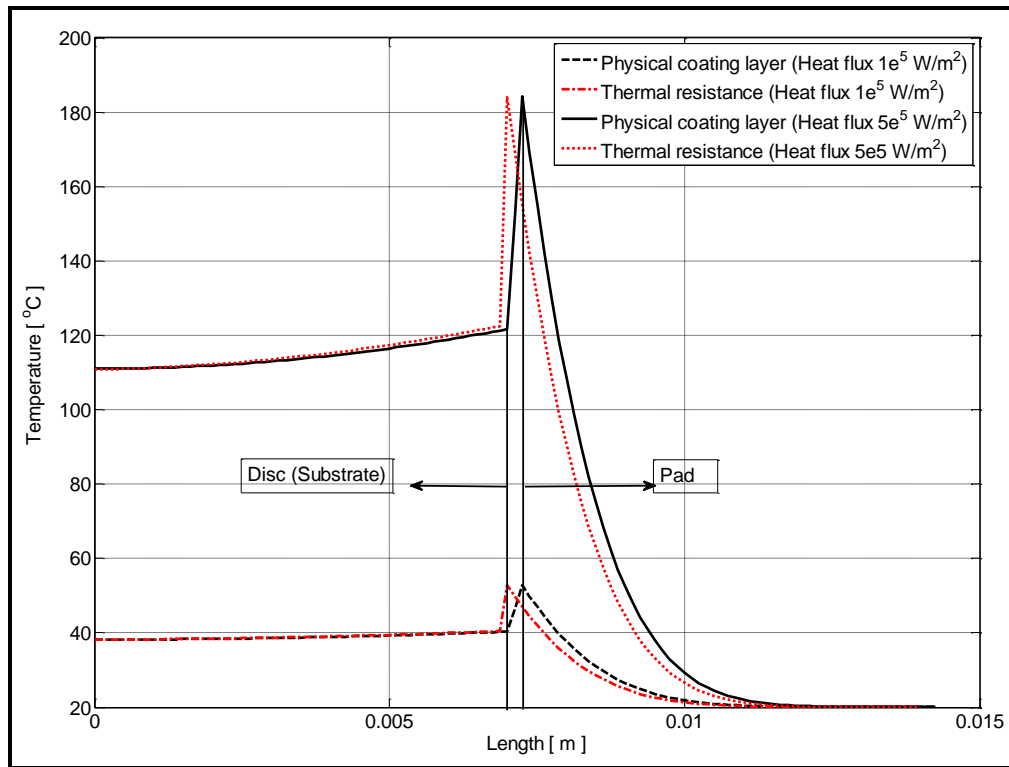


Figure 4.14: Temperature distribution across the disc and pad with convection tuning.

4.6.2 Mesh density analysis

In this section a mesh density study was carried out in order to find the effect of different numbers of nodes inside the coating with respect to the temperature distribution. The one dimensional finite element model shown in Figure 4.12b with the coating explicitly modelled was used in this analysis with the same conditions as explained in section 4.3. A heat flux of $5 \times 10^5 \text{ W/m}^2$ was applied on the rubbing surface. The 1D finite element models were solved for three different mesh densities through the coating, as follows: 1, 2, or 4 nodes respectively.

Figure 4.15 and Figure 4.16 show the spatial temperature distribution across the model and the temperature between the disc substrate and coating as a function of time

respectively. The results show that there is a negligible effect of the mesh density on the temperature distribution, which suggests the use of a smaller number of nodes inside the coating with good resolution results. In this study, one node inside the coating was chosen to carry out the subsequent simulations, which reduces the memory and time required to conduct such an analysis.

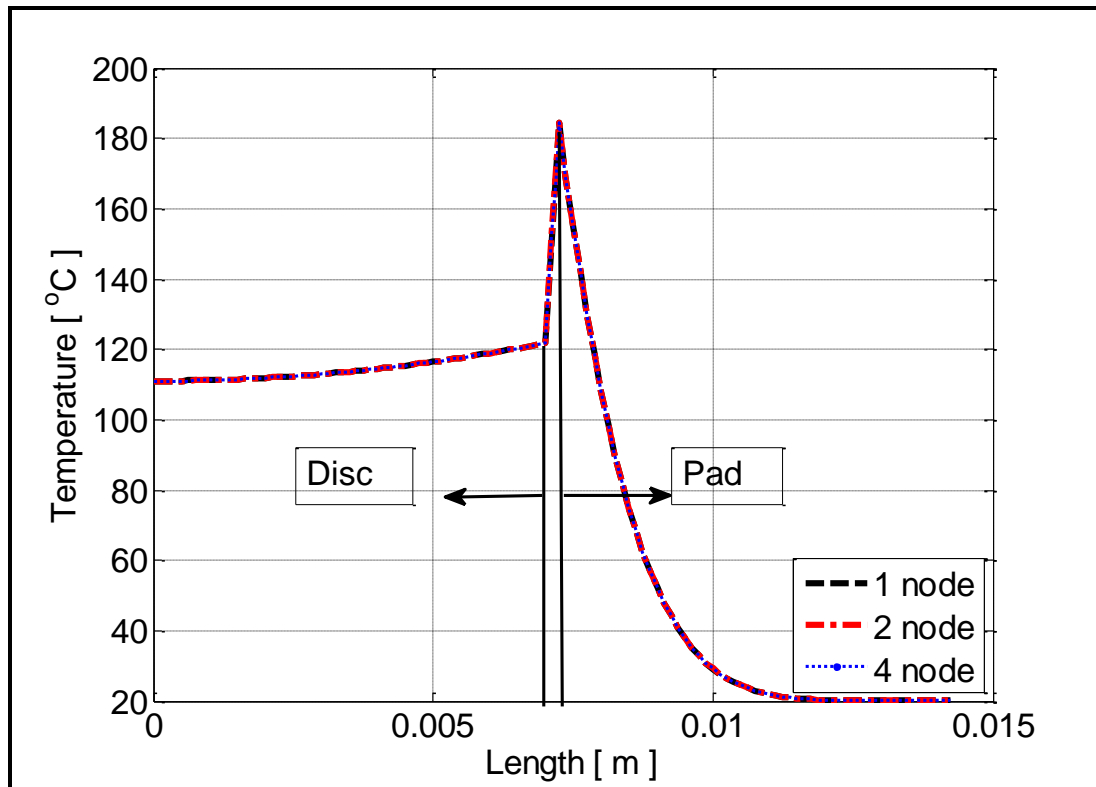


Figure 4.15: Temperature across the disc and pad brake for different mesh density through the coating.

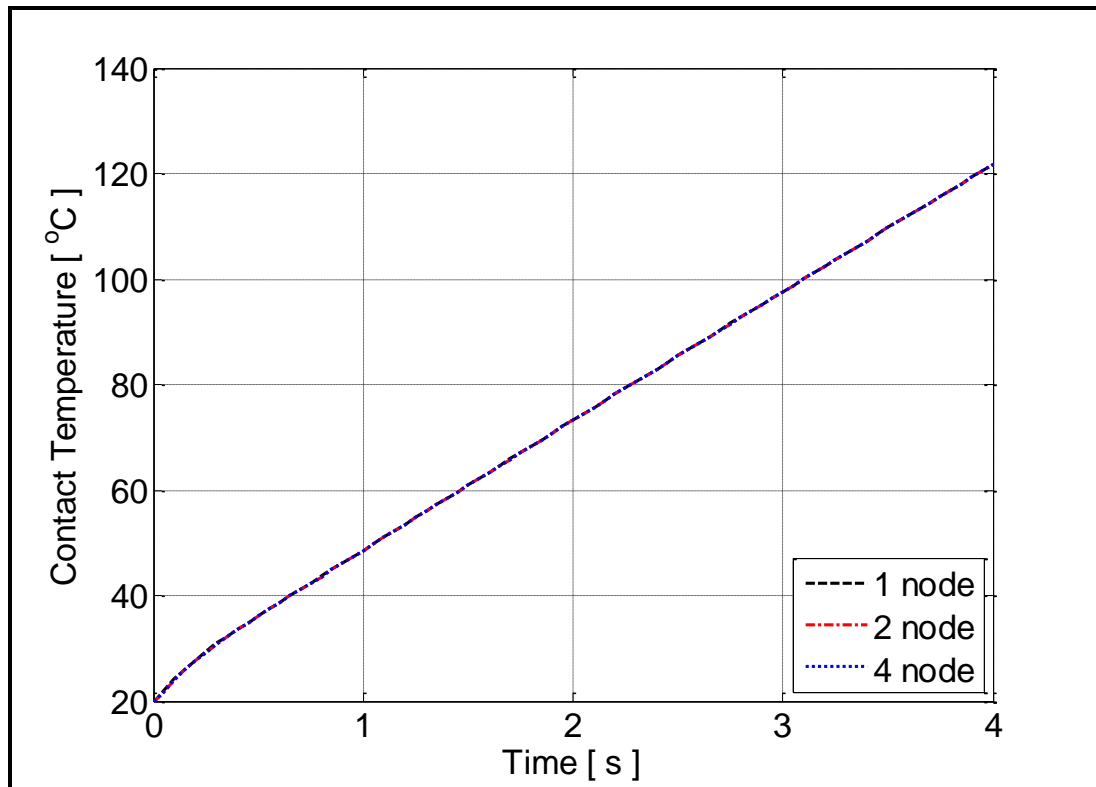


Figure 4.16: Temperature between the disc and coating for different mesh density.

4.6.3 Sub-modelling analysis

Sub-modelling is an effective technique used in Abaqus to analyse a local region with a refined mesh established by interpolation of the solution from an initial global model. In order to investigate the temperature distribution through the thin coating and disc substrate, a sub-modelling technique was used. The first step is to create the global model which is the complete 1D thermal model of the disc brake as shown in Figure 4.17. The global model was solved using Abaqus to create the input data and boundary condition for the sub-models, with no need for a fine mesh in the global model. Sub-models can subsequently be created and linked to the global model in order to define the various parameters such as heat flux, contact algorithm and partitioning ratio. In the sub-model a refined mesh was used in order to investigate the detailed temperature distribution across the model. In this section three different sub-models were investigated which are the pad, disc substrate and coating as shown in Figure 4.17.

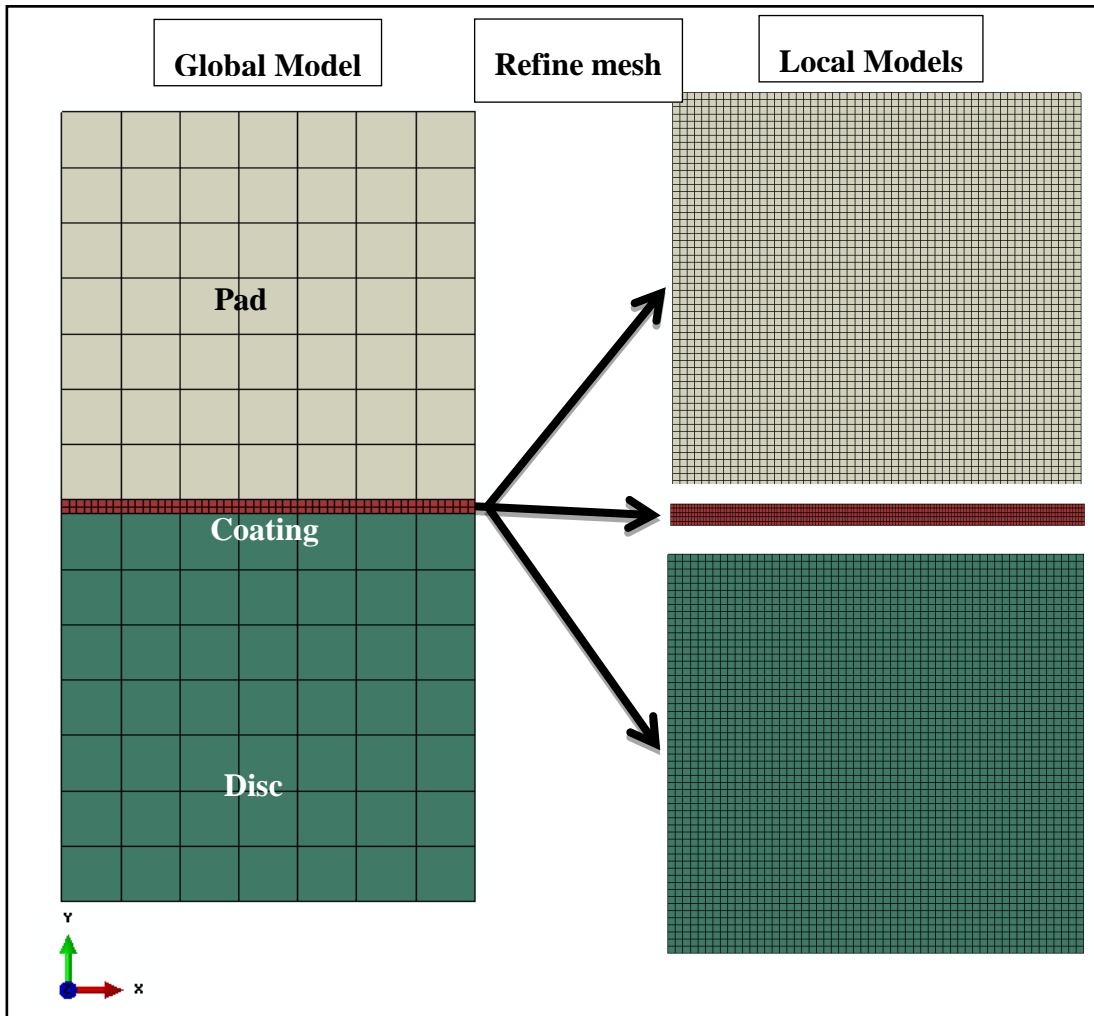


Figure 4.17: Global and local 1D thermal models of disc brake.

The same braking parameters, boundary conditions and materials properties used in section 4.6.1 was used in this analysis with heat flux of $5 \times 10^5 \text{ W/m}^2$. The global model used in this study is exactly the same model as described in section 4.6.1 with different mesh size as shown in Figure 4.18. The model was solved in Abaqus and the temperature distribution after 4 s is shown in Figure 4.18. The temperature distribution of the global model was compared with the temperature distribution of the same model with the fine mesh described in section 4.6.1. The comparison demonstrates that there is only a small difference between the results from the two models which also was shown in the mesh sensitivity study in section 4.6.2. Using the fine mesh to solve the global model will require large CPU time and memory.

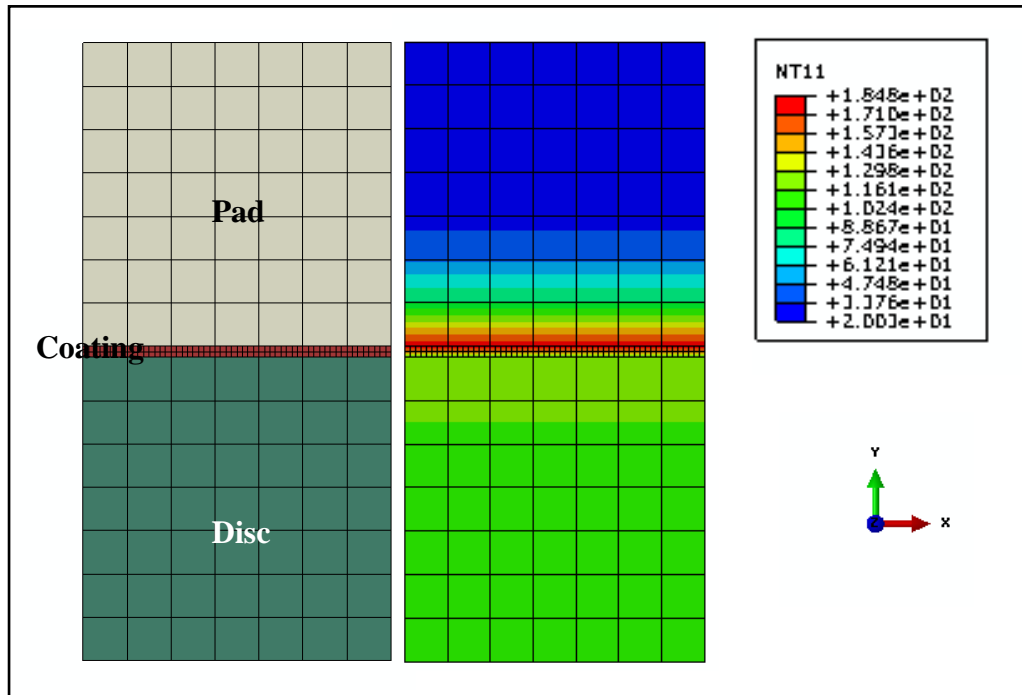


Figure 4.18: Temperature distribution of the global 1D thermal models at $t = 4\text{s}$.

The thermal distribution of the coating with a fine mesh was investigated using the sub-modelling technique as shown in Figure 4.19. The coating model was linked with the global model using two boundary conditions at the contact surfaces in order to define the contact algorithm and the thermal distribution. Furthermore, the same analysis was used to investigate the temperature distribution of the disc and pad 1D thermal model with the results as shown in Figure 4.20 and Figure 4.21 respectively.

Finally, the temperature distribution across the full model was compared for both global and local models as shown in Figure 4.22. The results show that there is a small improvement in the results using the sub-modelling technique; also it was found that using the sub-modelling technique can save CPU time and memory.

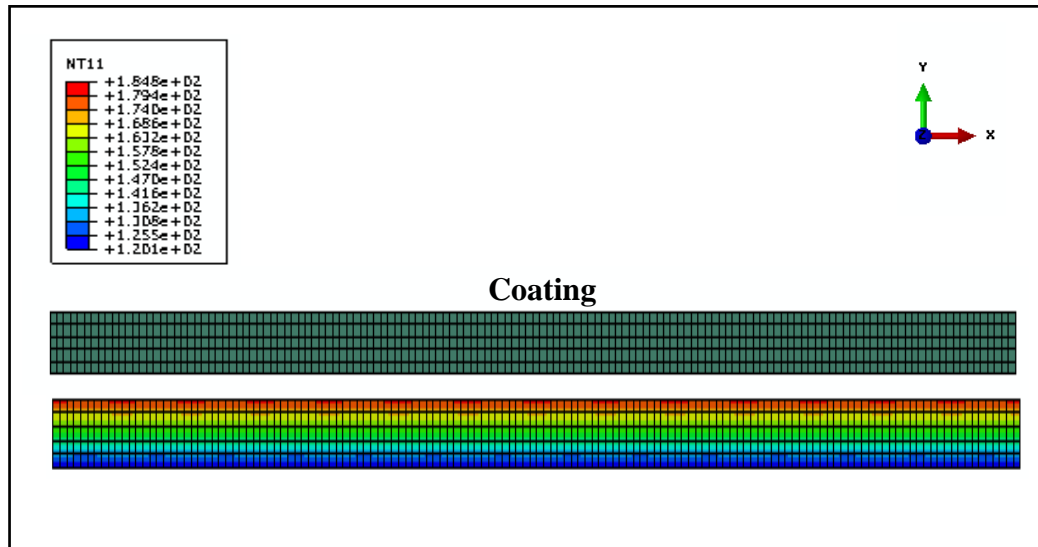


Figure 4.19: Temperature distribution of the local coating thermal models at $t=4s$.

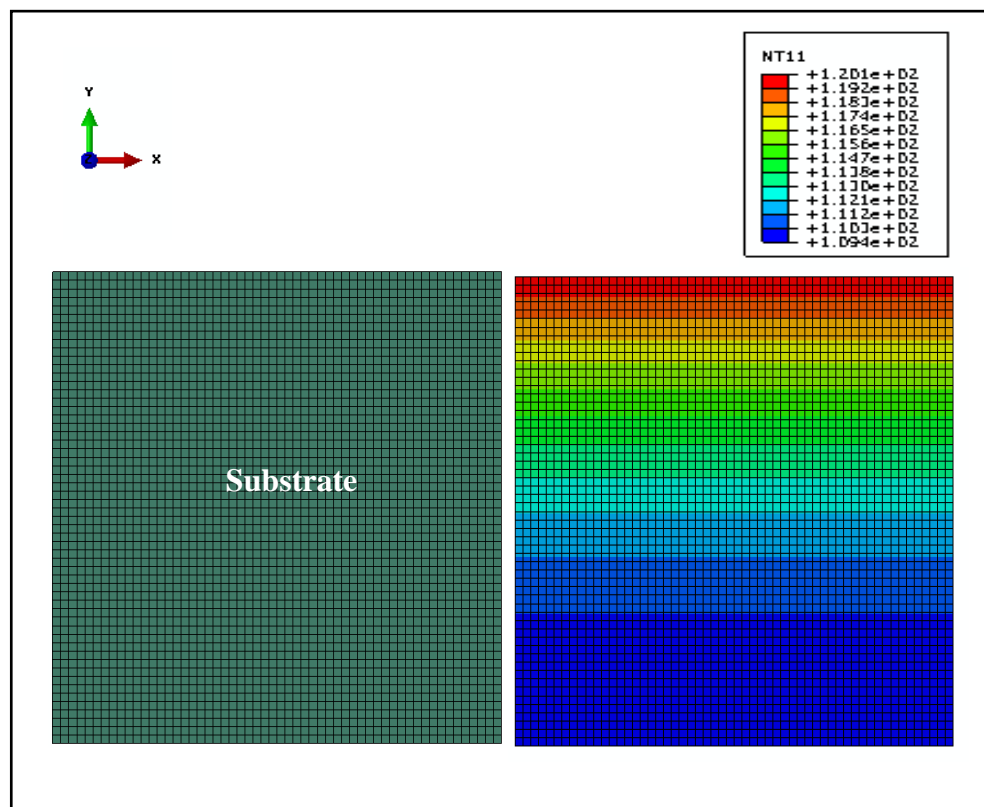


Figure 4.20: Temperature distribution of the local substrate thermal models at $t=4s$.

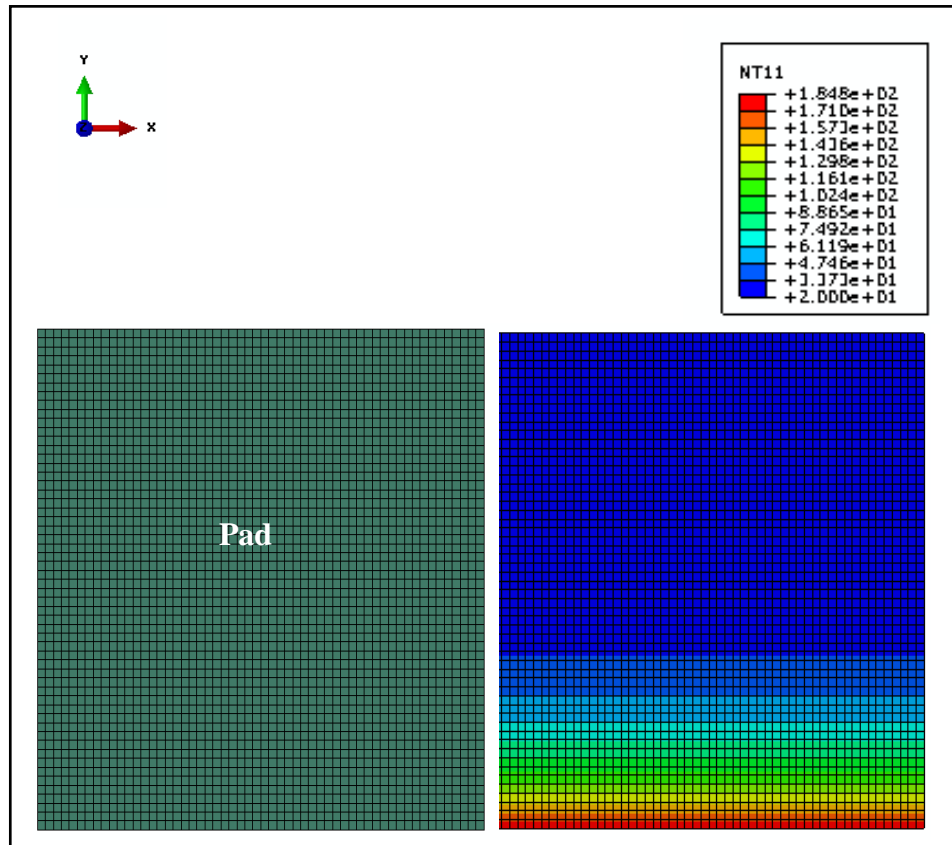


Figure 4.21: Temperature distribution of the local pad thermal models at $t = 4$ s.

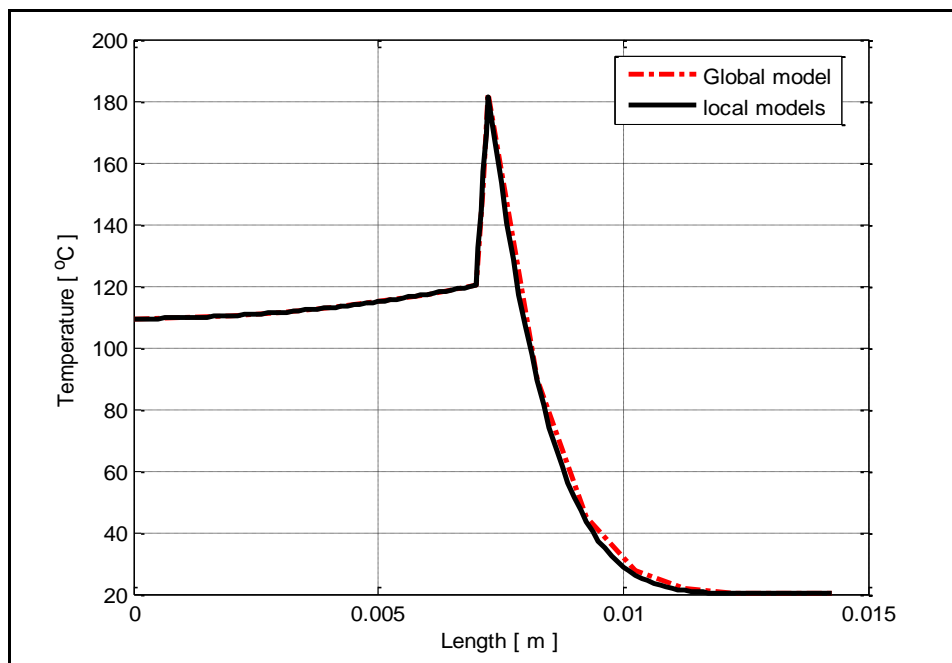


Figure 4.22: Temperature distribution of the local and global models at $t = 4$ s

4.7 Controlling the Abaqus model through Matlab code

4.7.1 Problem definition

Abaqus is a powerful finite element software with which to study and analyse the brake disc thermal problem. In the current research, disc brakes were investigated using both Matlab and Abaqus software. Matlab and Abaqus models showed very good agreement in the predicted temperature but with limitations. The main parameter in the braking event is the heat flux. Heat flux was calculated using both Matlab and Abaqus software, and it was found that Abaqus required long computational time and a great deal of memory to perform such calculations. The main problem associated with Abaqus was the time and memory usage for the Abaqus/Matlab coupled thermal analysis. In this section, Matlab code was developed to calculate the heat flux profile and then communicate with the Abaqus model to utilize a finite element solver inside Abaqus to perform thermal analysis. This then enables 2D axisymmetric and potentially even 3D analysis to be carried out.

4.7.2 Solution procedure

Both Matlab and Abaqus have their own advantages and disadvantages. In this research, in order to investigate the thermal performance of solid disc brakes for different braking scenarios, both Abaqus and Matlab were utilized to carry out the analysis. The main problem with Abaqus modelling was the time and memory usage for coupled thermal analysis. This problem was solved by using uncoupled analysis with the help of Matlab code in order to calculate the heat flux profile (braking scenario). Figure 4.23 shows the overall structure of the code used to interact between Abaqus and Matlab. Another advantage of using this code is the potential to utilize the optimization toolbox in Matlab with Abaqus modelling power.

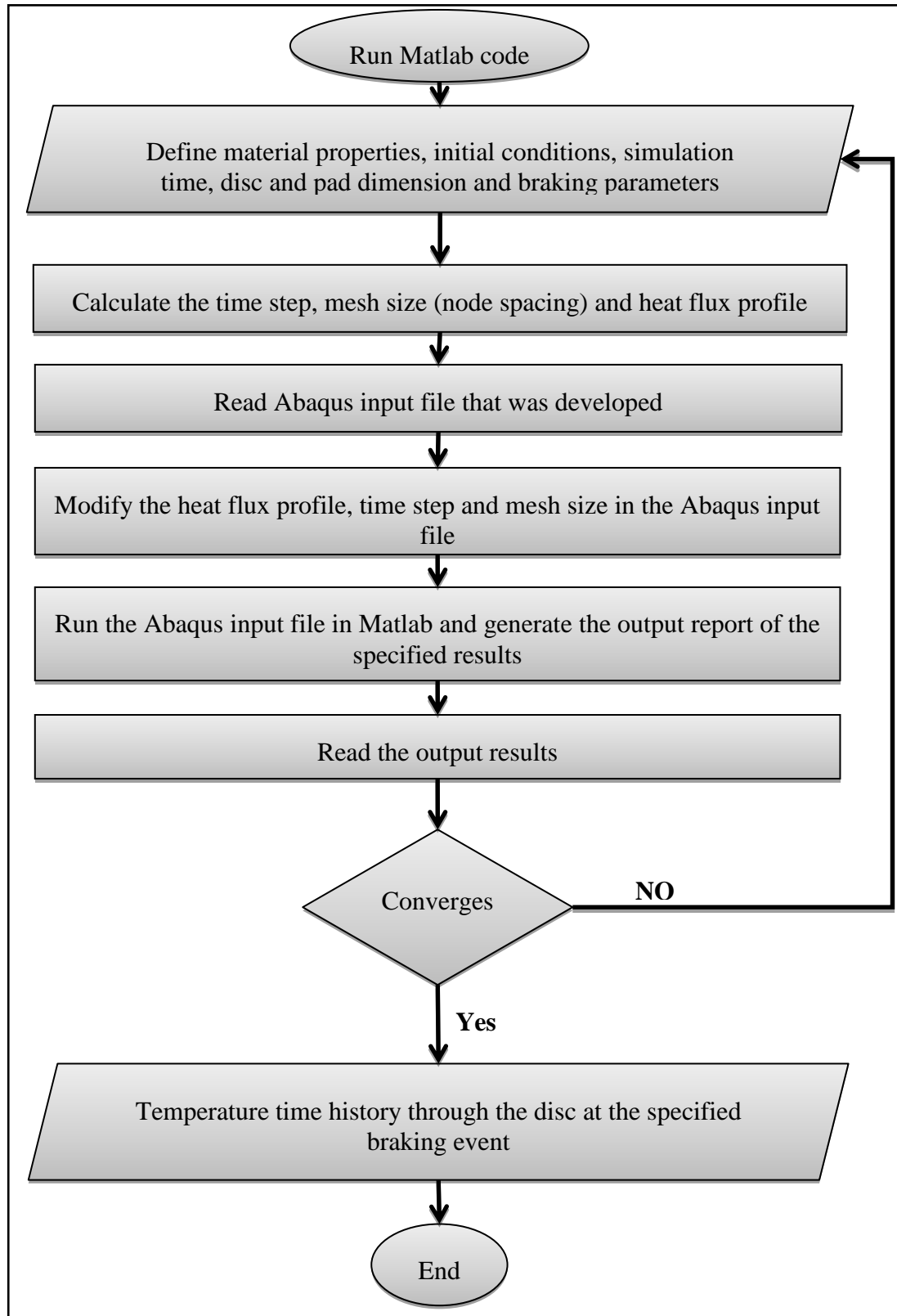


Figure 4.23: The overall Matlab/Abaqus model structure.

4.7.3 Benefits

Controlling the Abaqus model using Matlab has many benefits, including the ability to:

- Carry out different braking scenarios such as: drag braking, repetitive brake application, Alpine test, and so on.
- Perform optimization on the disc brake by utilizing the optimization toolbox in Matlab.
- Investigate the wear rate in the disc brake by changing the surface profile of the disc and pad.
- Investigate the contact pressure between the disc and pad surfaces.
- Minimizing output volume of the results and better results processing.
- Direct control of input and output parameters via Matlab.

4.8 Parametric study

A parametric study is essential in analysing the different brake design parameters because it helps to: define the different parameters for evaluation, define the parameter range, identify the design constraints, and analyse the results for each parameter. In this section, the simulation results for the 1D transient heat transfer model are presented and discussed, as various model parameters are varied around their nominal values, as defined in section 4.3.3. The various parameters that are investigated in this section are the disc material, convection coefficient, disc thickness, pad materials, initial vehicle velocity, vehicle mass, rotating heat source and coating thickness. The braking parameters, material properties and conditions used in these simulations are shown in Table 4.1 and Table 4.2 unless otherwise specified.

4.8.1 Effects of disc materials

Material thermal properties are very important factors that have an impact on the thermal performance of disc brakes. Although it is easy to find the optimum thermal properties for any desired application, it is hard to design and produce the optimum material. In this section three different materials were investigated. These are: grey cast iron (GCI), aluminium alloy (Al-Alloy, 6082-T6) and aluminium metal matrix composite (Al-MMC, AMC640XA).

Figure 4.24 shows the temperature distribution through the disc for different disc brake materials. It was found that both Al-Alloy and Al-MMC experience higher temperatures than the GCI disc, which was expected based on the thermal properties of the discs shown in Table 4.1. Furthermore, the temperature of the Al-MMC is higher than that of the Al-alloy which also was expected because Al-alloy has a higher thermal inertia than the Al-MMC.

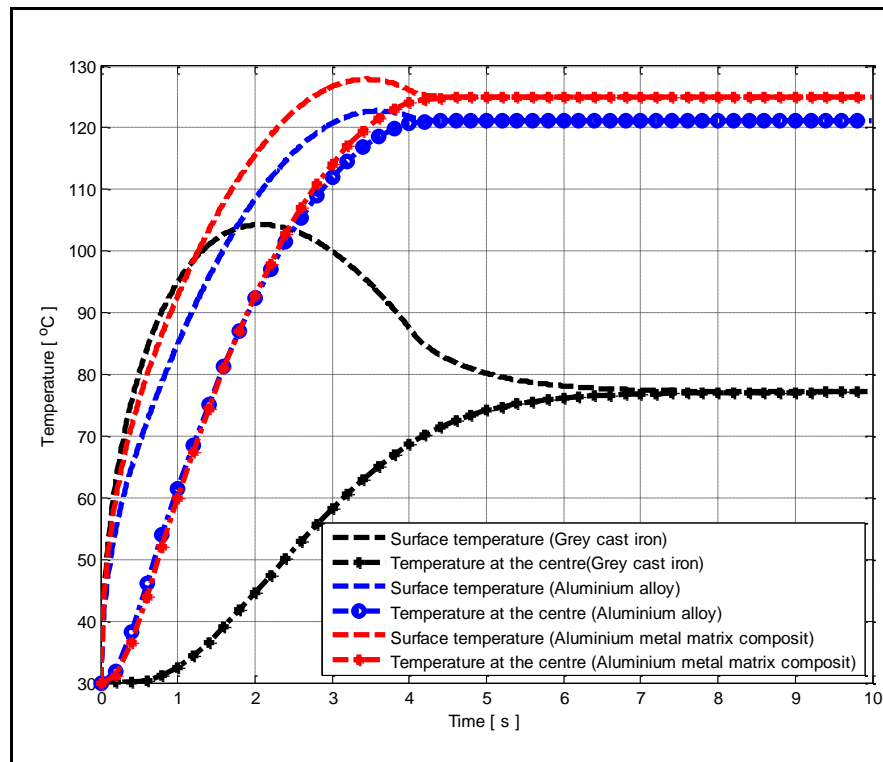


Figure 4.24: Disc brake temperature distribution for different disc materials.

4.8.2 Effects of convective heat loss

At the beginning of this Chapter, heat transfer by convection was explained; in order to find the effect of convection heat loss on the disc brake temperature, different convection coefficients were used with the results simulated as shown in Figure 4.25. It was demonstrated that the convection coefficients have a very small effect on the temperature distribution for this particular braking event. The effect may be more significant for larger duration event such as Alpine decent.

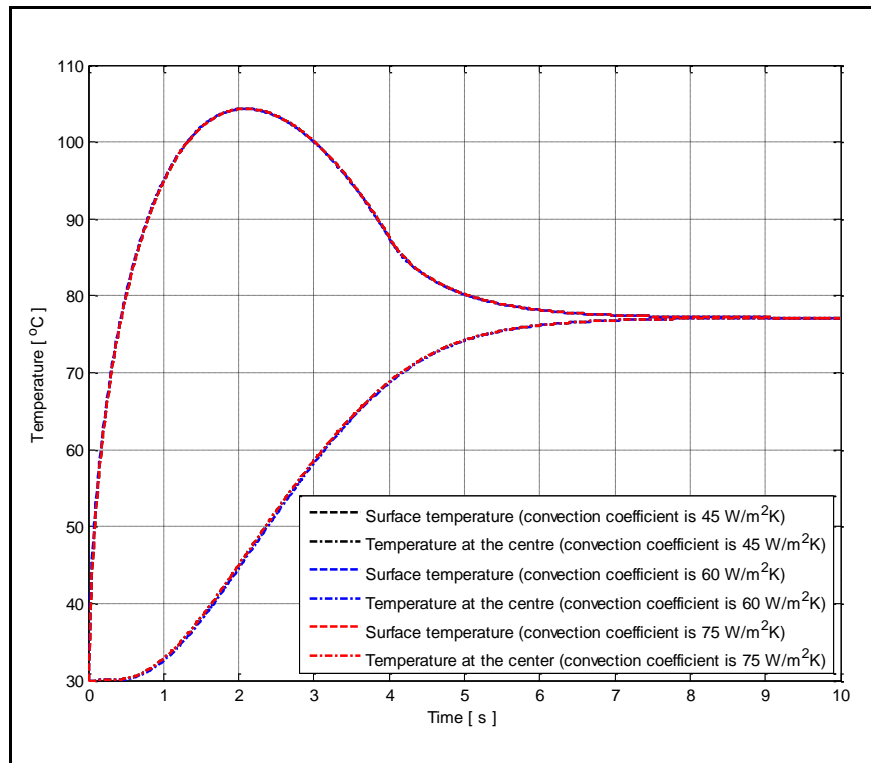


Figure 4.25: Disc brake temperature distribution for different convective heat transfer coefficients.

4.8.3 Effects of disc thickness

The weight of the disc depends on the disc geometry and material density. One of the parameters that influence disc geometry is the disc thickness, which also has an impact on the total weight of the disc. Various studies have been made in the area of reducing the weight of disc brakes in order to reduce emissions and fuel consumption [18-20].

In this section, temperature distribution through a GCI disc brake for different disc brake thicknesses was simulated, as shown in Figure 4.26. It was concluded that the disc thickness has only a small effect on the surface temperature, but has a large effect on the central plane temperature.

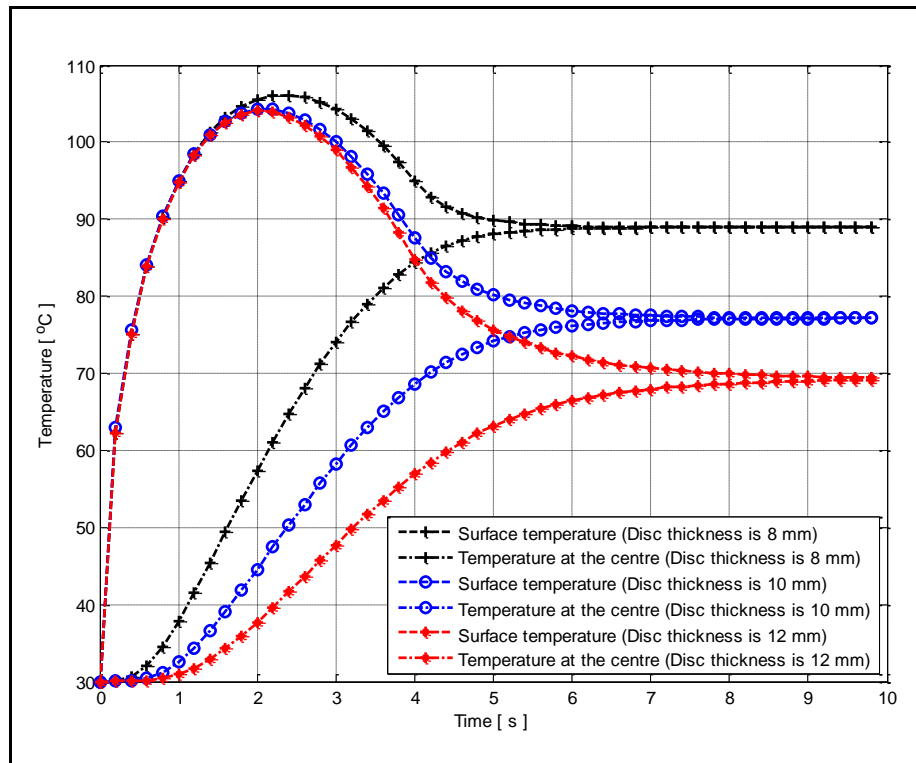


Figure 4.26: Disc brake temperature distribution for different disc thicknesses.

4.8.4 Effects of pad material

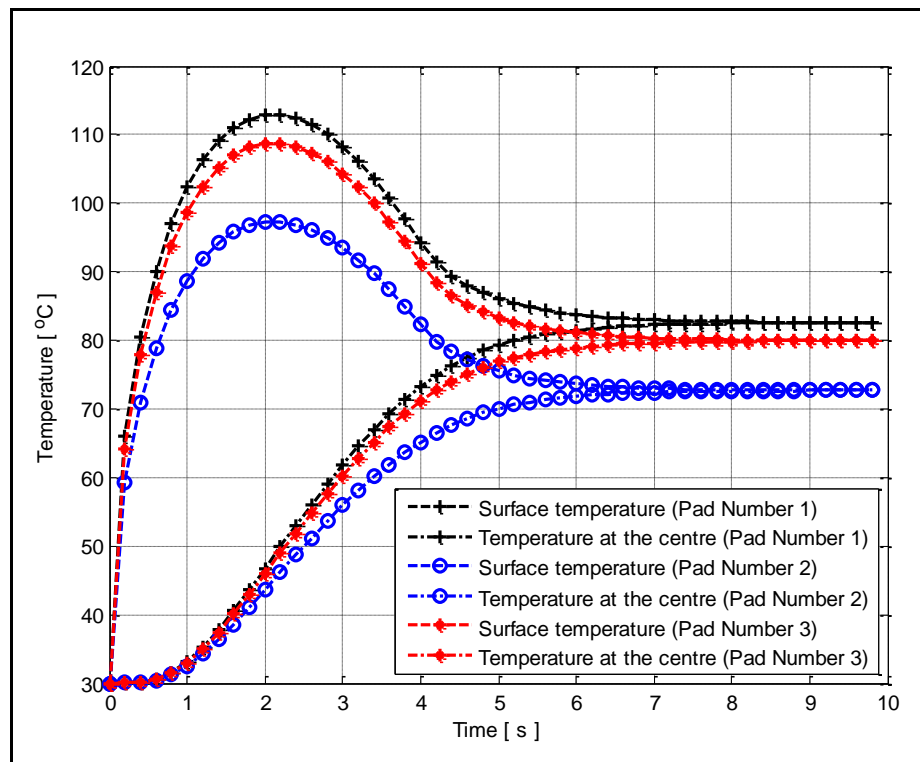
Automotive industries have investigated and developed different pad materials in order to improve the performance of braking systems. Pad materials properties may have large effects on the thermal performance of braking systems, because they have an influence on the proportion of the frictionally-generated heat to be transferred to the disc as can be seen from the simple heat partition equation (4.31):

$$\gamma = \frac{q_P''}{q_P'' + q_R''} = 1 - \frac{1}{1 + \sqrt{\frac{\rho_P c_P k_P}{\rho_R c_R k_R}}}$$

In this section different pad materials were specified as shown in Table 3.6, to investigate the effect of pad material on the thermal performance of solid cast iron disc as shown in Figure 4.27. It was found that the pad materials do indeed have large effects on the temperature distribution of the disc brake, as expected. The temperature distribution depends on the partition ratio as shown in Table 4.6; it was found that the disc with the lower partition ratio has the highest temperature, as expected.

Table 4.6: Thermal properties for different pad materials [13, 15, 114].

Pad Number	Density ρ [kg/m ³]	Specific heat c_p [J/kg.K]	Conductivity k [W/m.K]	Partition ratio (Pad:Disc), p
1	2596	827	0.736	0.0740
2	2500	900	12	0.2482
3	2595	1465	1.212	0.1200

**Figure 4.27: Disc brake temperature distribution for different pad materials.**

4.8.5 Effects of initial vehicle velocity

In order to investigate and understand disc brake thermal performance, initial vehicle velocity was investigated. Three different initial vehicle velocities were used to investigate the thermal performance of grey cast iron discs as shown in Figure 4.28. It

was concluded that as the initial vehicle velocity increased the disc temperature increased. This trend was expected because as the initial vehicle velocity increases the power required to stop the vehicle also increases which causes more heat to be generated and transferred to both the disc and pad.

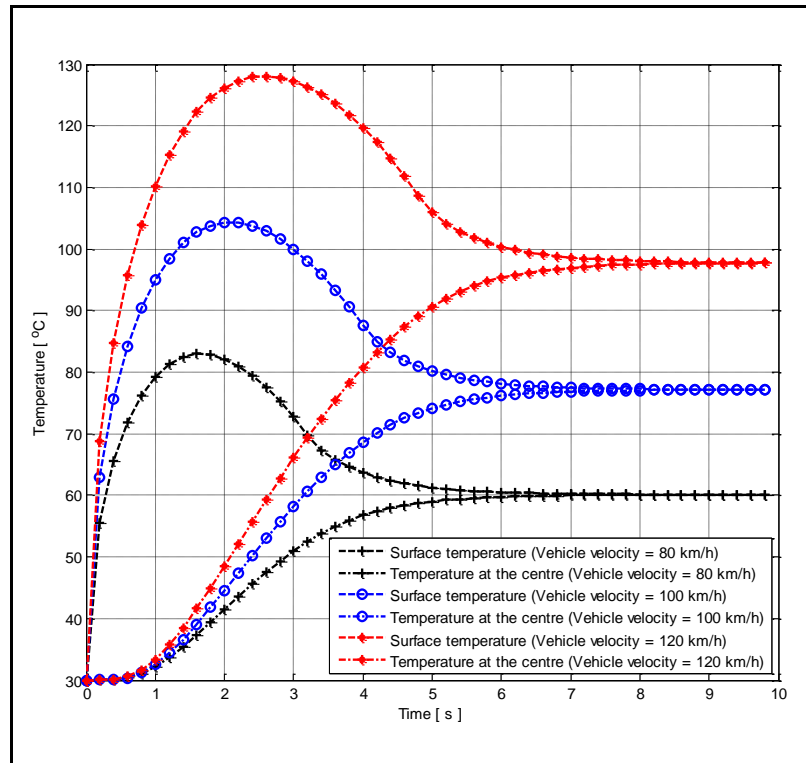


Figure 4.28: Disc brake temperature distribution for different initial velocities.

4.8.6 Effects of vehicle mass

The weight of the vehicle is influenced by many factors: passengers, fuel, cargo, etc. The automotive industry uses the gross vehicle mass (GVM), which is the maximum operating mass of a vehicle, to investigate the thermal performance of disc brakes. In this study, the thermal performance of a solid grey cast iron disc was carried out using different vehicle masses in order to understand the effect of vehicle mass on the thermal performance of disc brakes.

The results in Figure 4.29 show that the vehicle mass has a large effect on the disc temperature. It shows that as the vehicle mass increases the temperature significantly increases, which was expected.

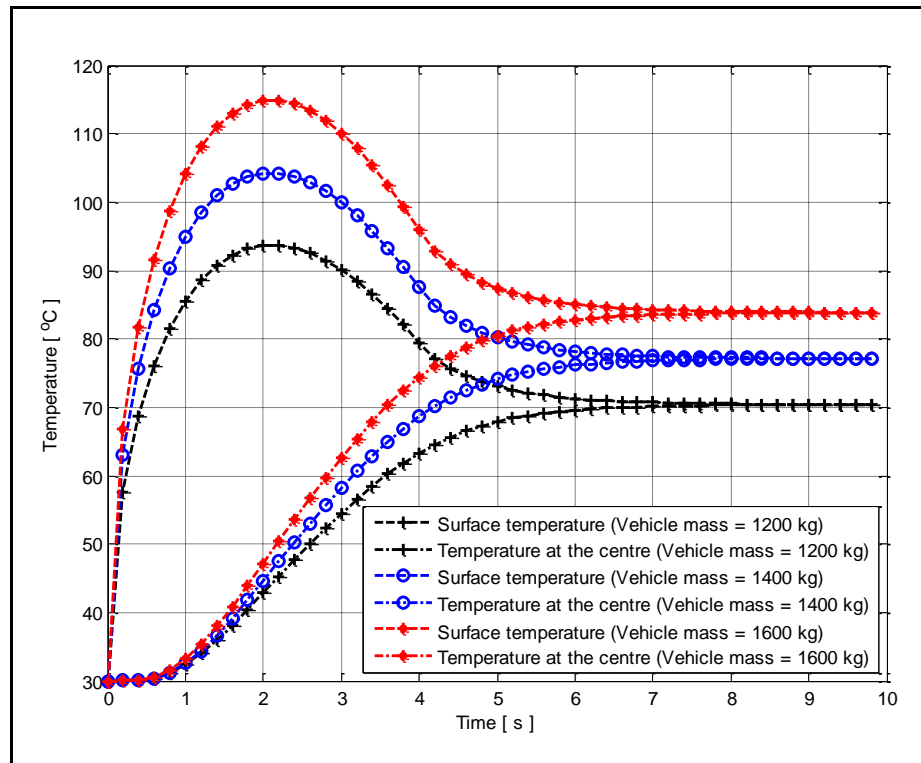


Figure 4.29: Disc brake temperature distribution for different vehicle masses.

4.8.7 Effect of rotating heat source

Many researchers assume that the heat flux is distributed uniformly over the rubbing surface of the disc which neglects the effect of convection. In this section, a rotating heat was addressed in order to find the effect of this more accurate method of evaluating the thermal performance of disc brakes.

Figure 4.30 shows the effect of a rotating heat source on solid cast iron disc temperatures. It was found that the rotating heat has an effect on the surface temperature of the disc only, as the temperature at the centre of the disc is almost unaffected. According to the results, the mean surface temperature with rotating heat follows approximately the surface temperature with heat flux distributed over the rubbing surface. However the maximum temperature reached in each revolution are higher by about 20°C.

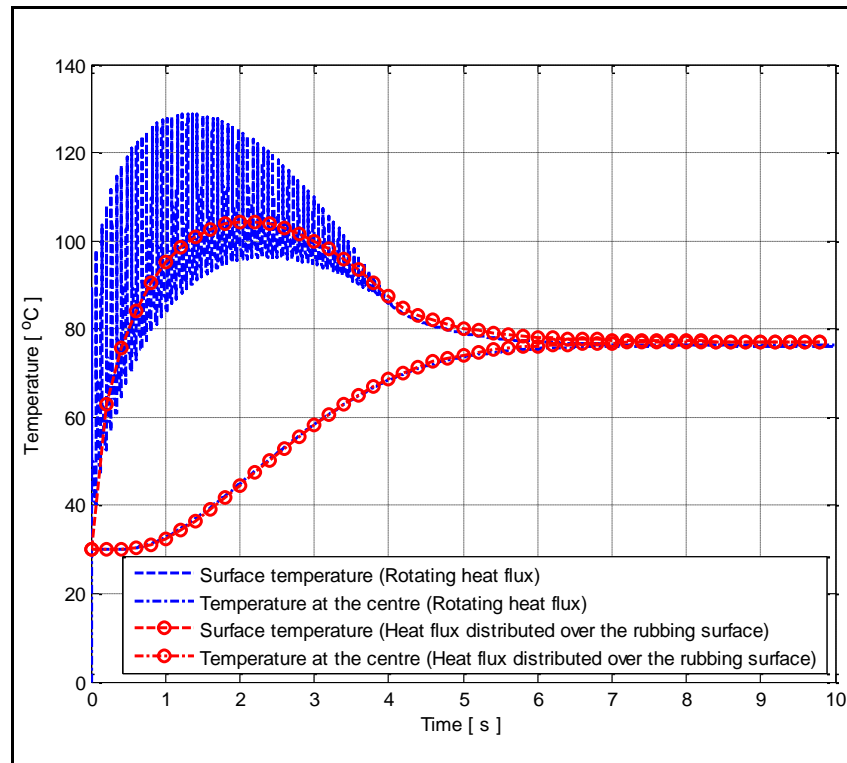


Figure 4.30: Effect of rotating heat on the temperature distribution of the disc brake.

4.8.8 Effect of coating thickness

In the current research the main aim is to replace the conventional cast iron disc with lighter materials and one of the best candidates is Al-MMC. Although Al-MMC has very good thermal properties, the main problem is its maximum operating temperature. In order to solve the maximum operating temperature problem, Plasma Electrolytic Oxidation (PEO) coating has been proposed in the literature to protect the disc from the high operating temperature and to work as a thermal barrier.

Using data contained in Table 4.1 and Table 4.2, the effect of coating thickness on the temperature distribution within an Al-MMC disc was predicted using the 1D Matlab thermal model (see Figure 4.31). As the coating thickness increased, the temperature at the surface increased because of the increased thermal barrier effect. Conversely, the temperature at the centre of the disc and between the coating and the substrate decreased. The increase in the surface temperature is much higher than the decrease at the centre of the disc and between the coating and substrate. It was concluded that

higher coating thickness can cause problems for the pad material as it has a large effect on the surface temperature of the coating. On the other hand, a thickness of 0.1 mm or less does not cause a very significant increase in disc surface temperature. These results provide the basis from which to develop guidelines for the selection of coating thickness in the future.

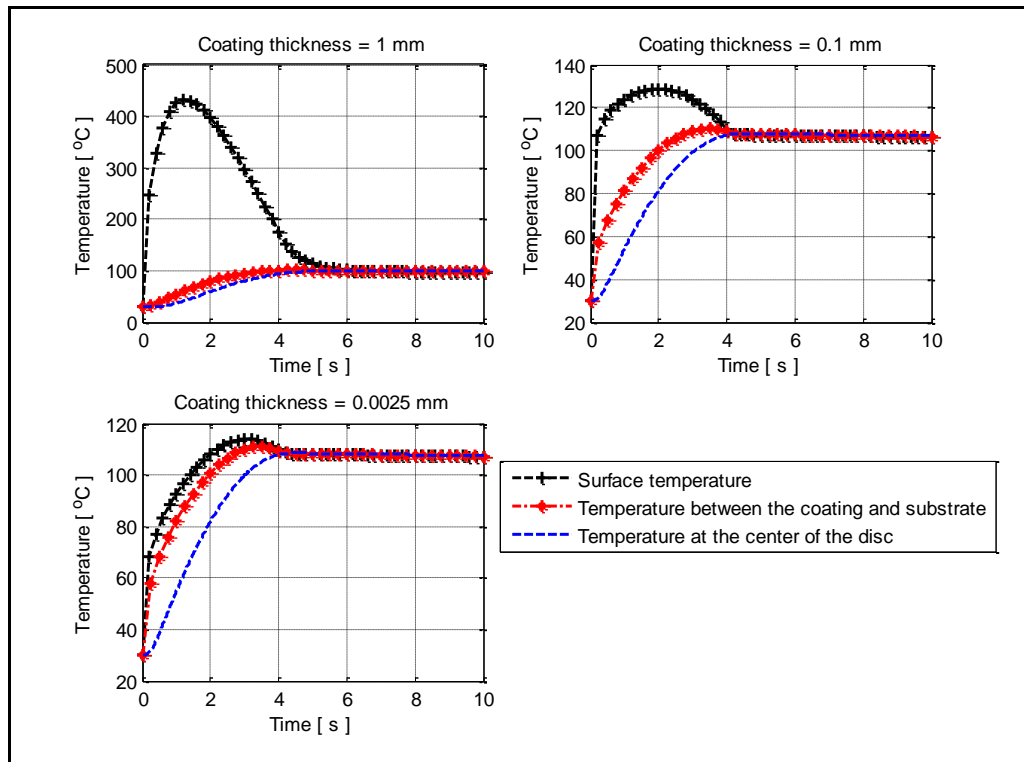


Figure 4.31: Effect of coating thickness on the temperature distribution of the disc brake.

4.9 Summary

In this Chapter, the derivation of detailed one dimensional heat transfer models was presented. One dimensional thermal models of an automotive disc brake were developed using both Matlab and Abaqus. The 1D Matlab thermal models were validated and compared with the results obtained from the literature and Abaqus. Overall it was found that the Matlab results showed good agreement with Abaqus and the experimental literature results. Abaqus was also used to model the coating layer in different ways. The thermal resistance modelling approach without explicitly modelling the thin coating layer reduces the analysis time by up to 20-25% and also reduces the

computer memory needed for such analysis. This approach could be of importance when modelling a coated three dimensional disc in Abaqus because it will save much time and reduce the model size. Despite the thermal resistance approach to modelling a thin coating layer giving very good results, particularly when using convection tuning, it needs more investigation before it can be implemented with confidence. The mesh study analysis was carried out to find the effect of the coating mesh density on the temperature distribution; it was found that there is a small effect of coating mesh on the temperature distribution. In addition, sub-modelling technique was used to investigate the temperature distribution through the disc, pad and coating. It was noticed that using sub-modelling could improve the temperature distribution and also save the CPU time and memory usage. This technique will be very valuable when dealing with 2D and 3D models.

Furthermore, the Abaqus\Matlab interaction approach for solving the disc brake thermal performance was developed which has several advantages. For example, the new approach to analysis is significantly faster. The time required to perform a typical brake disc analysis has been reduced by up to 60-65%. The capabilities of modelling various braking events, such as drag braking, repetitive braking, Alpine test... etc, are apparent with the combined approach. In addition the interaction approach will be used in future to perform optimization analysis utilizing the optimization toolbox in Matlab. Furthermore, different braking analysis will be carried out using different disc and pad materials in order to investigate the possibility of replacing the conventional cast iron with a lighter disc material. Finally, parametric studies were carried out to investigate the effect of different parameters on the thermal performance of solid disc brakes. This approach will help to progress the design of experiments and subsequent sensitivity analyses.

CHAPTER 5:

SCALING METHODOLOGIES AND TEST RIG DESIGN

5.1 Introduction

The thermal behaviour of disc brakes is a critical factor that demands to be consideration in the design phase. Although thermal modelling is useful at this stage, the brake system ultimately needs to go through a series of vehicle or real road tests before it can be released as a commercial product. Most researchers utilise the full brake dynamometer or the pin-on-disc rig to evaluate the performance of a disc brake. In this Chapter, a scaling methodology is proposed, to evaluate the thermal performance of a disc brake using a small scale brake dynamometer which is capable of replicating the same braking conditions and scenarios as the full brake dynamometer (real conditions). The small scale rig has the advantages of low cost and short operating time. The design detail and practical considerations of the small scale test rig are discussed and presented in detail and include the selection of various components that control and monitor the test rig. The small scale test rig was designed using scaling methodology proposed in the current Chapter. The selection of the small scale disc brake geometry and materials that will be used in the experiment and numerical analysis are also presented. An existing full scale brake dynamometer was used in the current research in order to validate the scaling methodology and investigate the thermal behaviour of the lightweight brake rotor under different braking conditions. A description of the full scale brake dynamometer is given. A comparison is made between the full and small scale brake dynamometers. The procedure used to calibrate the sensors and actuator for both rigs is explained. The commissioning of the newly developed small scale dynamometer is also explained in this Chapter. The experimental results and the test matrix which was used with the test rigs are presented in Chapter 7.

5.2 Scaling methodologies

5.2.1 Scaling method

The main aim of the scaling methodology is to develop a small scale rig that can replicate real world conditions accurately. There are many different parameters that need to be monitored and measured during the tests. One of the main parameters to be measured is the friction coefficient as a function of temperature, brake pressure and sliding velocity and it is very important to ‘maintain the one-to-one relationship between these parameters when comparing the small and full scale dynamometers. One way to achieve the desired goal is to scale the parameters by the pad area and maintain a constant relationship, including constant energy density.

5.2.2 Scaling principle

The scaling factor is the fundamental quantity used to develop the scaling methodology. The physical specification of the small scale test rig was developed by applying the scaling factor to the full scale rotational inertia and disc mass as explained below. The sliding velocity at the interface is preserved between the full and small scale rotors. In the following sections the detailed derivation of the scaling methodology used to develop a small scale test rig which is capable of replicating real world braking conditions is presented.

5.2.2.1 Rotational inertia

The main parameter for the proposed scaling process is the scaling factor (S), which is defined as the ratio between the full scale and small scale pad areas. If full scale parameters are denoted by a subscript F and small scale parameters are denoted by a subscript S , then:

$$S = \frac{A_F}{A_S} \quad (5.1)$$

where A_F is the full scale pad area and A_S is the small scale pad area.

The vehicle corner inertia (I_F) for full scale is defined as:

$$I_F = M_F R_{GF}^2 \quad (5.2)$$

where M_F is the vehicle corner mass for the full scale case and R_{GF} is the radius of gyration for the full scale case. Assuming that the energy density (energy per unit area) at the pad-disc interface is constant between the small scale case and the full scale case leads to finding the scaling of the rotational inertia. The energy per unit area is defined as:

$$E_F = \frac{1}{2A_F} M_F v_s^2 \quad (5.3)$$

where E_F is the total energy for the full scale case and v_s is the sliding velocity which is assumed to be the same for both full and small scale. Substituting M_F from equation (5.2) into equation (5.3) leads to:

$$E_F = \frac{I_F}{2A_F} \left(\frac{v_s}{R_{GF}} \right)^2 \quad (5.4)$$

The corresponding energy density for the small scale case is similarly defined as:

$$E_S = \frac{I_S}{2A_S} \left(\frac{v_s}{R_{GS}} \right)^2 \quad (5.5)$$

where E_S is the total energy for the small scale case, R_{GS} is the corresponding radius of gyration and I_S is the equivalent vehicle corner inertia. Equating the full scale energy density equation (5.4) with the small scale density equation (5.5) and simplifying the relation for the inertial ratio leads to:

$$\frac{I_F}{I_S} = \frac{A_F}{A_S} \left(\frac{R_{GF}}{R_{GS}} \right)^2 \quad (5.6)$$

The radius of gyration is a linear quantity and thus scales with $S^{0.5}$. Substituting the scaling factor equation (5.1) and the radius of gyration scaling factor in equation (5.6) leads to:

$$\frac{I_F}{I_S} = S^2 \quad (5.7)$$

5.2.2.2 Disc mass

The disc mass was scaled by using the energy balance equation as follows:

$$Q = m_d c_p \Delta T \quad (5.8)$$

where Q is the heat flow from or to the disc, m_d is the disc mass, c_p is the specific heat and ΔT is the difference between the final and initial temperatures. As it was assumed earlier that the energy density in the full and small scale cases should be equal, this leads to:

$$\frac{Q_F}{A_F} = \frac{Q_S}{A_S} \Rightarrow \frac{Q_F}{Q_S} = \frac{A_F}{A_S} = S \quad (5.9)$$

Substituting equation (5.8) into equation (5.9) leads to:

$$\frac{(m_d c_p \Delta T)_F}{(m_d c_p \Delta T)_S} = S \quad (5.10)$$

One of the main aims of the small scale test rig is to replicate the same conditions as for the full scale case and this means that ΔT should remain constant. Then equation (5.10) reduces to:

$$\frac{(m_d c_p)_F}{(m_d c_p)_S} = S \quad (5.11)$$

5.2.2.3 Brake torque

The brake torque was calculated using the following equation:

$$\tau = F_t r_d \quad (5.12)$$

where F_t is the tangential force at mean rubbing radius r_d . The contact pressure for small and full scale was assumed constant in the current scaling methodology, which can be defined as follows:

$$P_F = P_S \Rightarrow \frac{F_{nF}}{A_F} = \frac{F_{nS}}{A_S} \quad (5.13)$$

where F_{nF} is the normal force for the full scale pad and F_{nS} is the normal force for the small scale pad. The normal force for the small and full scale is given by:

$$F_{nF/S} = \mu F_{tF/S} \quad (5.14)$$

where μ is the coefficient of friction. Substituting equation (5.14) and (5.12) into equation (5.13) leads to:

$$\frac{\tau_F}{A_F r_{dF}} = \frac{\tau_S}{A_S r_{dS}} \quad (5.15)$$

Substituting the scaling factor in equation (5.1) and the mean rubbing radius in equation (5.15) leads to:

$$\tau_F = S^{3/2} \tau_S \quad (5.16)$$

5.2.2.4 Functional parameter

In order to find the small scale rig rotational speed, the full scale sliding velocity is required as follows:

$$v_{sF} = r_{dF} \frac{2v_i}{d_t} \quad (5.17)$$

where r_{dF} is the full scale mean rubbing radius, v_{sF} is the full scale sliding velocity, v_i the velocity initial forward speed and d_t is the road wheel rolling diameter. The rotational speed of the small scale rig is given by:

$$\omega_S = \frac{v_{sS}}{r_{dS}} \quad (5.18)$$

in which ω_S is the initial rig rotational speed, r_{dS} is the mean rubbing radius for the small scale case and v_{sS} is the sliding velocity for the small scale case. Equating the sliding velocity in equations (5.17) and (5.18), leads to:

$$\omega_S = \frac{2v_i}{d_t} \left(\frac{r_{dF}}{r_{dS}} \right) \quad (5.19)$$

Equation (5.19) defines the initial rig rotational speed as a function of the vehicle wheel rolling diameter, initial vehicle speed and mean rubbing radius for small and full scale rigs. In the conventional braking system the contact pressure is a function of hydraulic pressure on the brake calliper piston, or is the load on the master cylinder. In order to maintain the contact pressure at the pad-disc interface, it is necessary to derive the relationship between the load on the master cylinder and the contact pressure, taking into account the various parameters. Assuming that the full scale contact pressure is

known and equal to P_F , then the hydraulic pressure in the small scale case is defined as follows:

$$P_S = \frac{P_F A_S}{A_{piston}} \quad (5.20)$$

where P_S is the small scale hydraulic pressure, A_{piston} is the calliper piston cross-sectional area and A_S is the small scale pad area. Therefore, the force required on the master cylinder is defined as:

$$F_{cyl} = P_F A_S \left(\frac{A_{cyl}}{A_{piston}} \right) \quad (5.21)$$

where A_{cyl} is the master cylinder cross-sectional area and F_{cyl} is the master cylinder force. Equations (5.20) and (5.21) are used to find the force required at the master cylinder. Finally, Table 5.1 and Table 5.2 summarize the constant parameters and the scaling relations respectively.

Table 5.1: Scaling constant parameters [37].

Variable	Symbol
Sliding velocity	v_s
Deceleration	g
Pad pressure	P
Energy density	E_a
Disc temperature	T
Stop time	t_s

Table 5.2: Scaling relations [37].

Variable	Symbol
Pad area	$A_F = A_S S$
Effective radius	$r_{eF} = r_{eS} S^{1/2}$
Rolling radius	$R_{rF} = R_{rS} S^{1/2}$
Linear velocity	$V_F = V_S S^{1/2}$
Torque	$\tau_F = \tau_S S^{3/2}$
Inertia	$I_F = I_S S^2$

The proposed scaling methodology was developed based on the constant energy density. There are a number of factors that were not considered in the development of the current methodology which might have an impact on the results. Some of these factors are as follows:

- Convective cooling was not considered in the scaling methodology which will have an effect on the overall thermal performance of the disc brake especially in the repeated constant G stop.
- The brake pad geometry (aspect ratio) was not included in the current model but needs to be investigated in order to identify its influence on the overall thermal performance of small scale discs.
- The full scale disc brake rotor geometry was not considered in the current scaling methodology as the thermal mass was scaled based on the scaling factor. This needs to be investigated as different brake geometries will also affect the convective cooling efficiency.
- The coating thickness was not considered in the scaling methodology for the lightweight disc brake rotor which might influence the overall thermal performance of the disc brake rotor.

5.2.3 Selection of vehicle for scaling

The thermal performance analysis of a lightweight brake rotor, using the proposed scaling methodology, was carried out on a Fiat Punto 188 1.4 hatchback for the following reasons:

- The main problem with lightweight aluminium-based brake rotors is the low melting temperature which is of the order of 450°C. A small sized vehicle is best for investigating the possibility of using lightweight disc brake rotors in passenger vehicles as the small sized vehicle generates less energy input to the disc brake. On the other hand, using a medium or large sized vehicle will generate high energy input to the disc brake which might be too aggressive for the lightweight disc brake rotor.
- The Fiat Punto 188 1.4 hatchback vehicle has solid disc brakes which are easier to investigate than ventilated disc brakes which are more complex to produce and more problematic from a scaling prospective.
- In addition, the automotive industry needs to meet 2015 EU vehicle emission standards which means that they are required to reduce vehicle emissions by an average of 10% [1].

In this study the main motivation was to investigate the possibility of replacing the conventional disc brake rotor with a lightweight disc brake rotor beginning with an easy to work with, small sized vehicle, as explained above. The disc brake geometry for the selected vehicle is shown in Figure 5.1. In addition, the Fiat Punto specifications and parameters are shown in Table 5.3.

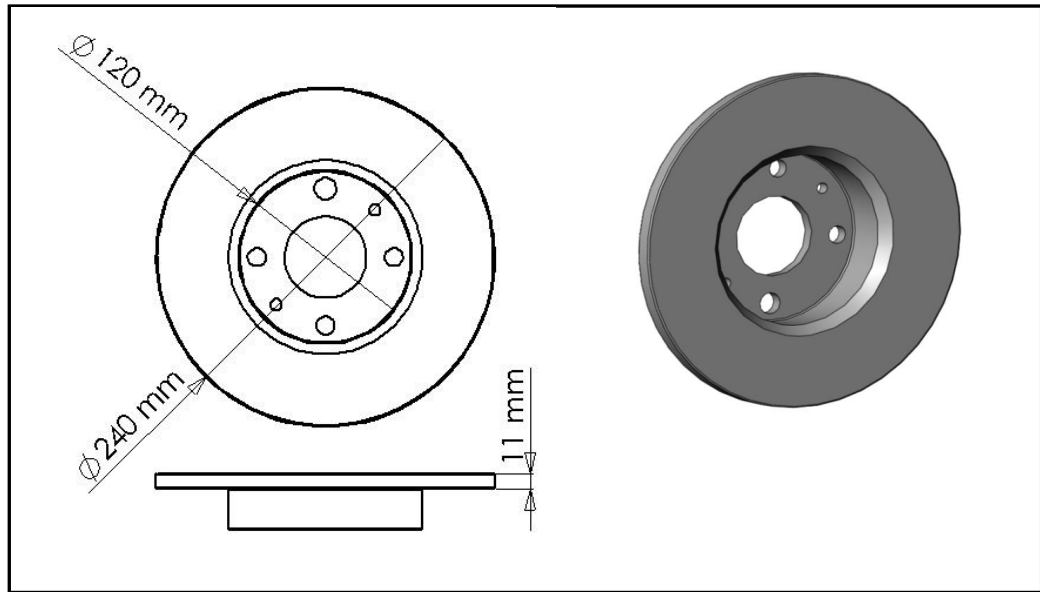


Figure 5.1: Fiat Punto disc brake rotor geometry.

Table 5.3: Full scale parameters [115].

Vehicle Parameter	Value	Vehicle Parameter	Value
Pad area (mm ²)	2736	Maximum speed (km/h)	205
Mean rubbing radius (mm)	95	Disc inside diameter (mm)	120
Disc outside diameter (mm)	240	Wheel rims size (mm)	R15
Disc mass (kg)	3.57	Acceleration from standstill to 100 km/h	13.2 s
Disc thickness (mm)	11	Vehicle weight (kg)	1400

5.2.4 Scaling summary

The scaling process can be completed over a series of steps which provide a small scale brake test for a given set of data and vehicle parameters. In order to quantify the scaling

parameters the following full scale parameters are required: pad area, vehicle mass, material heat capacity, disc brake mass, initial vehicle speed, wheel rolling diameter, mean rubbing radius and pad contact pressure. Then the scaling parameters can be derived using the scaling methodology equations in section 5.2.2. In this section, the scaling methodology was applied to the selected vehicle, which was a Fiat Punto. Using the scaling methodology proposed, the scaled parameters are as shown in Table 5.4.

Table 5.4: Full and small scale parameters.

Vehicle parameter	Full scale	Small scale	Relation
Scaling factor	1	3	$S = \frac{A_F}{A_S}$
Pad area (mm ²)	2736	900	
Mean rubbing radius (mm)	95	54	$r_{dF} = r_{dS} S^{1/2}$
Inertia (kg m ²)	44.1	4.9	$I_F = I_S S^2$
Disc outside diameter (mm)	240	125	$\frac{(mc_p)_F}{(mc_p)_S} = S$
Disc mass (kg)	3.57	1.2	
Disc thickness, t _s (mm)	11	14	
Corner weight (kg)	490	163	$M_S = \frac{M_F}{S}$
Rotational speed (rpm)	350	620	$\frac{\omega_f}{\omega_s} = S^{-0.5}$

5.3 Test rig design and development

The brake dynamometer is one of the most important pieces of equipment in the design process of any disc brake. It is used to find the optimum disc brake design that meets the desired objectives. In the current research two brake dynamometers were used to investigate the thermal performance of a lightweight brake rotor and to validate the scaling methodology. The first was an existing full scale brake dynamometer and the second a small scale one which was developed based on the scaling methodology proposed in this Chapter. In this section the general layout and specification of both full and small scale brake dynamometers are discussed and presented. In addition, the design and selection of various components for the small scale brake dynamometers are explained. The data acquisition and sensor set-up for both dynamometers are explained in detail. Finally, comparisons between the results from the full and small brake dynamometers are presented.

5.3.1 Small scale brake dynamometer

The small scale brake dynamometer was developed based on the scaling methodology presented above and the understanding from the one dimensional thermal model in Chapter 4. The general design and layout of the developed rig was based on an existing small scale dynamometer which was available in the lab at the University of Leeds. The main reasons for developing a new small scale dynamometer and not using the existing rig were as follows:

- The existing rig design was found to conflict with the scaling methodology that was based on constant energy density.
- There was no information available about the theoretical foundations and practical operation of the existing rig.
- The existing rig used dead weight to apply the braking pressure which limits the braking condition to drag braking only, and made it too difficult to apply constant g stopping or repetitive braking conditions.
- The overall setup of the existing rig is similar to a pin-on-disc configuration and this is not the same loading arrangement as for a real brake caliper.

For the above reasons it was essential to develop a new test rig that is capable of replicating full scale vehicle and real world conditions. Also it was important to have full control over the test rig and to be able to apply different braking conditions such as constant g stops and drag braking.

5.3.1.1 General layout

The general layout of the new small scale rig was based on, and used various components which were available in, the existing rig'. A number of design guidelines were considered in the new rig which were as follows:

- Using the existing 2 kW DC motor.
- Utilizing the same base (support table) as the original rig.
- Limiting shaft misalignment by using two bearings.
- Restricting the disc brake location to the end of the rig to simplify the assembly and to allow the use of thermal imaging.
- Minimizing the axial distance between the disc and flywheel in order to eliminate the deformation of the shaft under high load.
- Positioning the bearings as close as possible to the main loads, such as the flywheel and clutch unit, to minimize the stress on the shaft.
- Using an automated system to control the test rig especially the brake pressure.

According to these general design guidelines, the layout of the developed small scale rig consists of a DC motor driving a main shaft through a shaft mounted clutch unit with the brake disc located at the end of the shaft as shown in Figure 5.2. In addition, two bearings were placed close to the flywheel in order to limit the stress magnitude on the main shaft and to provide stability. The design and selection of the main components of the rig are covered in subsequent sections.

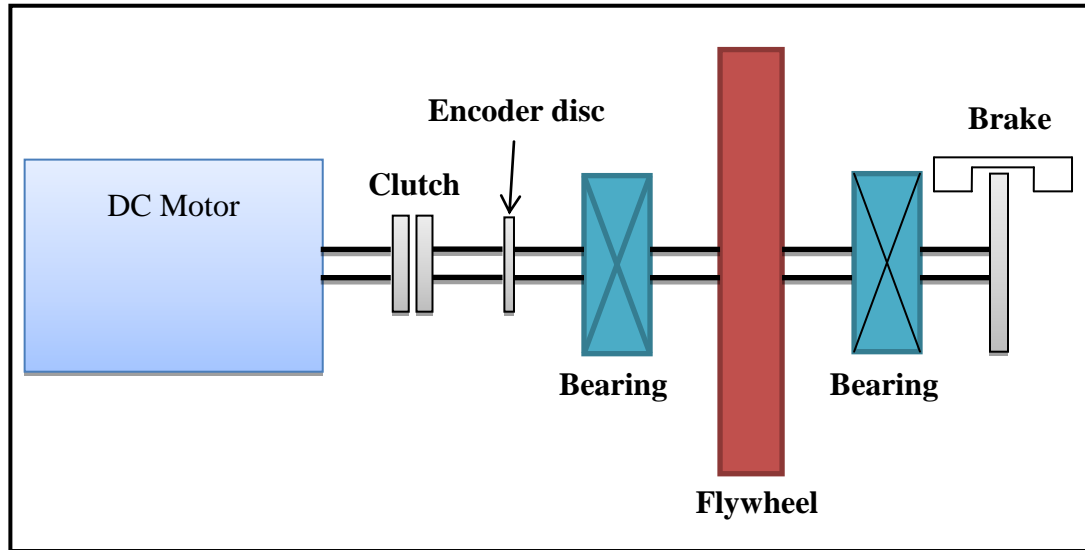


Figure 5.2: General layout of the small scale brake dynamometer.

5.3.1.2 Load calculations and design

The design and selection of various components for the small scale test rig needed to be carefully considered. Identifying the major loads on the system was key to commencing the design and to selecting the major components of the test rig. The major loading magnitudes in the proposed layout are: motor drive torque, brake torque and flywheel weight.

The existing DC motor was used for the developed rig as mentioned above, and the motor specifications were as follows: Maximum rotational speed of 4000 rpm and power of 2 kW. According to the motor specification the torque was calculated for 2 kW power at 4000 rpm which indicates a torque of 4.8 Nm. The motor was modified so that the user could control it by varying the voltage through LabView software. The detailed control of the DC motor is explained in the data acquisition section. In the current study, a Fiat Punto was chosen for the scaling methodology and to test the thermal performance of a lightweight disc brake rotor, but the developed small scale rig will be used for different vehicles in the future. The brake torque was calculated for the worst case scenario: a Range Rover III 4.4 (05/05-) was chosen for calculating the maximum brake torque. The Range Rover data is as follows: mass approximately 2500 kg slowing from 160 km/h at 0.9 g, a brake disc diameter of 360 mm, pad height of 58mm and a tyre size of 255/60R18. The brake torque was calculated based on the

available data and the maximum brake torque for the test rig which was in the order of 290 Nm.

The last loading factor is the flywheel weight, and according to the scaling methodology the moment of inertia of the small scale rig depends on the moment of inertia of the real vehicle (Full scale) and the scaling factor. In order to calculate the maximum weight of the flywheel, the inertia of different vehicles with different scaling factors needed to be investigated. The vehicle corner masses for typical passenger vehicles are in the range 250 to 800 kg. The existing flywheel weight is 26.7 kg, the diameter and thickness of the existing flywheel are 325 mm and 43.5 mm respectively. The flywheel mass against vehicle corner mass was calculated for different scaling factors as shown in Figure 5.3. It shows that as the vehicle size increases (corner mass) the flywheel weight also increases, which was as expected. In addition, larger scaling factors will reduce the weight of the flywheel. In the current study, the existing flywheel was used in the small scale test rig in order to make sure that the rig was fully function before designing another flywheel, but the design of the test rig was based on a worst case flywheel mass of approximately 55 kg.

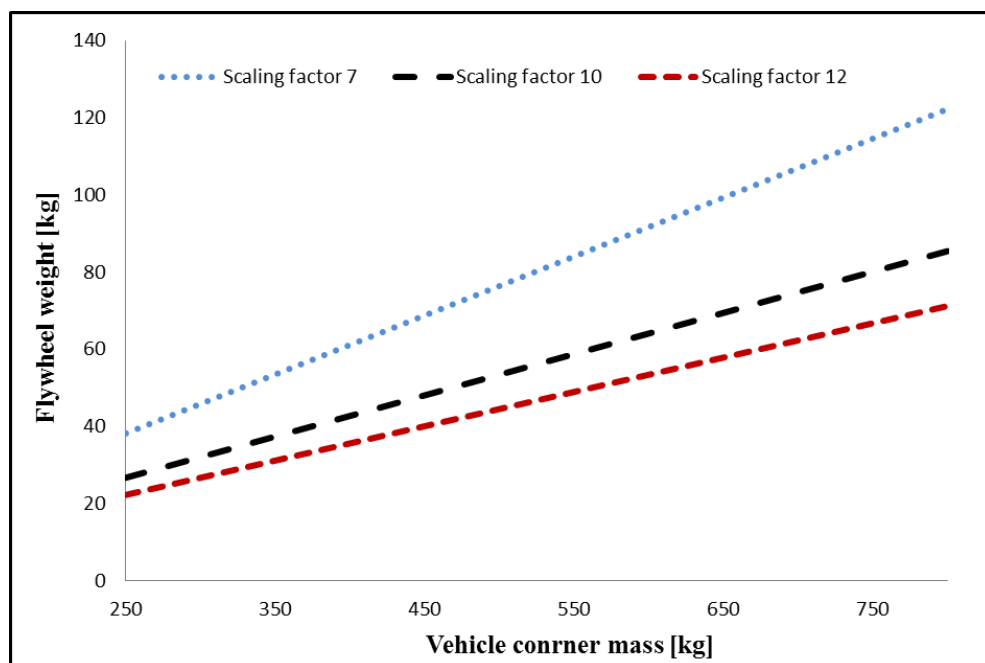


Figure 5.3: Flywheel mass against scaling factor for different vehicle sizes.

5.3.1.3 Clutch and actuator selection

In the design process of the small scale test rig, two important features were considered in order to assess the thermal performance of the small scale disc brake rotor under different braking conditions. The first feature was the ability to apply drag braking and the second feature was to apply the brake pressure as fast as possible using LabView software (constant g stop). In order to achieve the first goal it was necessary to find a mechanism that was capable of coupling the motor outlet to the main shaft. It was found that a shaft mounted clutch unit would be the best approach to achieving the desired goal. The selection of the clutch unit was based on the knowledge of the worst case design load from section 5.3.1.2. The general guidelines for clutch unit selection were as follows: electric or pneumatic actuation with decoupling mechanism, maximum torque of at least 10 Nm and bore diameter of 25 to 28 mm for main shaft and motor output shaft. In accordance with the general layout and guidelines, a pilot-mount clutch was selected as shown in Figure 5.4.

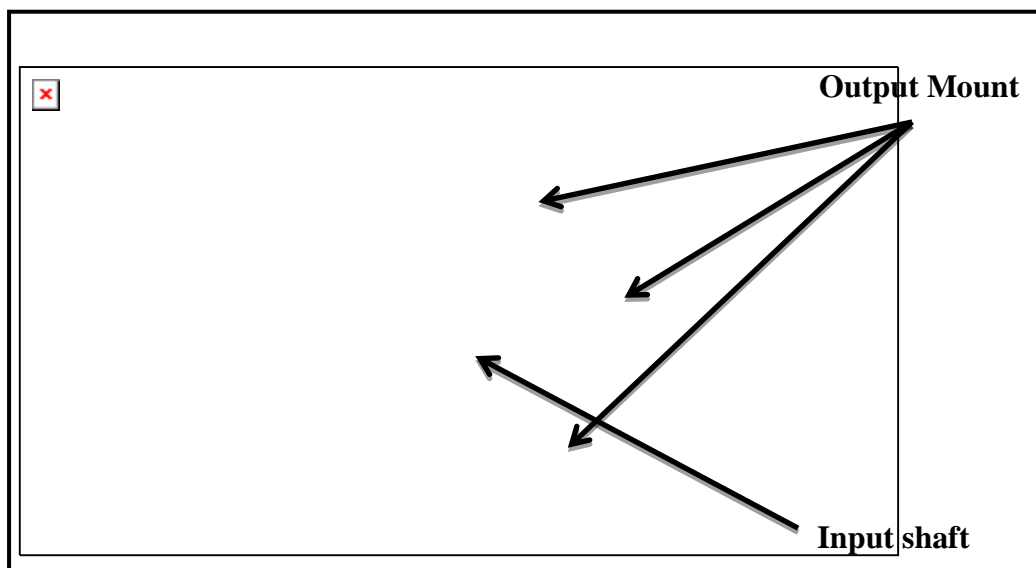


Figure 5.4: Nexen L600 clutch unit schematic [116].

The clutch unit was located on the main shaft and the jaw type coupling of the existing rig, which was driven by the motor, was coupled to the output mount by a developed adapter. The selected clutch unit was the Nexen L-600, catalogue number 950150 [116]. The main characteristics of the unit were: bore size 25 mm, maximum static torque 44

Nm, maximum rotational speed 3600 rpm, mass of 7 kg and the actuation/return by pneumatic/spring. The torque capacity of the chosen clutch unit was greater than the assumed load of 10 Nm which provides a safety factor against motor overload. The maximum rotational speed of the clutch unit was lower than the maximum speed of the existing DC motor (4000 rpm). Therefore, the maximum speed of the motor was limited to 3000 rpm to guarantee that the clutch unit would not be damaged.

The second main feature was to apply the brake pressure as fast as possible in order to achieve the constant g stop. The main guidelines for the selection of the brake pressure mechanism were: maximum load on the master cylinder 340 N, the speed of the actuation needed to be as fast as possible and controlled using LabView. In accordance with the general guidelines, a linear actuator was selected which was capable of applying the desired braking pressure at the fastest speed by using the existing data acquisition (LabView). The chosen linear actuator was the ACME Screw Linear Actuator (LMR 01) as shown in Figure 5.5 [117]. The main characteristics of the unit are: maximum load of 1300 N and linear speed up to 52 mm/s as shown in Figure 5.6.

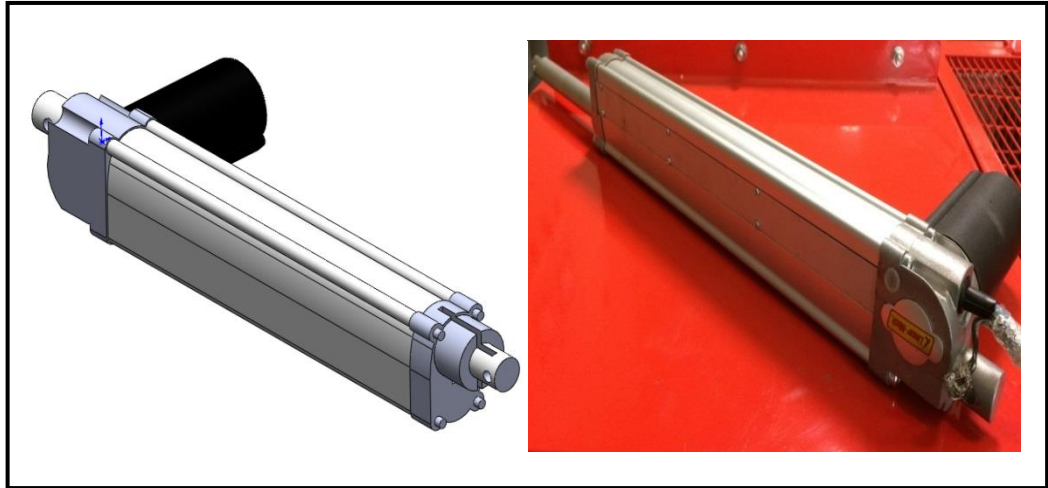


Figure 5.5: ACME Screw Linear Actuator (LMR 01) [117].

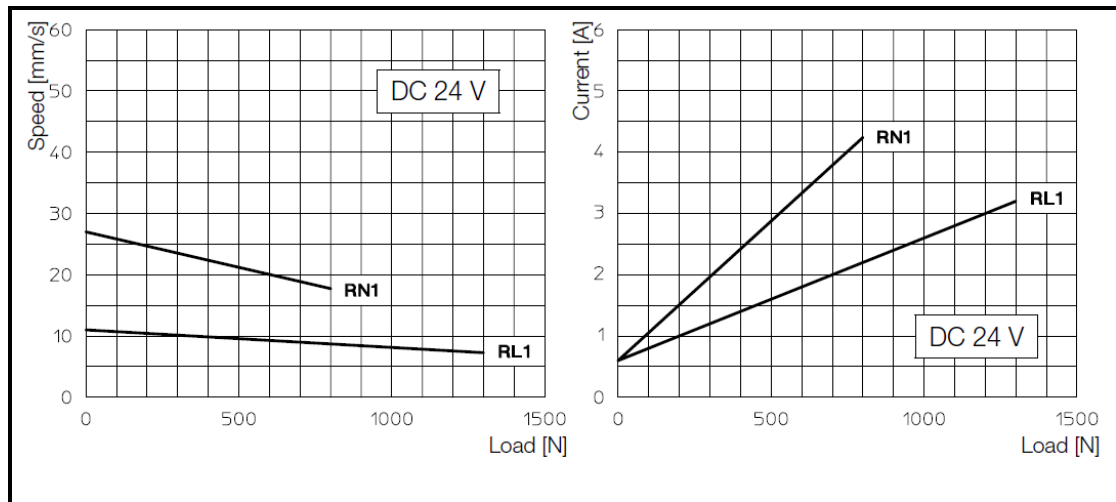


Figure 5.6: ACME Screw Linear Actuator (LMR 01) performance [117].

5.3.1.4 Main shaft design

The critical part in the new small scale test rig is the main shaft because it needs to withstand worst case dynamic loads and accommodate the different components while sustaining a series of practical and manufacturing considerations. The main guidelines for the main shaft were: ensure that practical and manufacturing considerations are satisfied at all times; provide sufficient static location and support for various components at rotational speed up to 3000 rpm; provide mounting point for bolt; and to offer appropriate keyways for transfer of drive torque and to make sure that the material yield stresses are not exceeded under the worst case loads. The detailed design of the main shaft was carried out by an MSc student at the University of Leeds, including the detailed stress analysis based on the worst case loads [118]. The final design of the main shaft is shown in Figure 5.7.

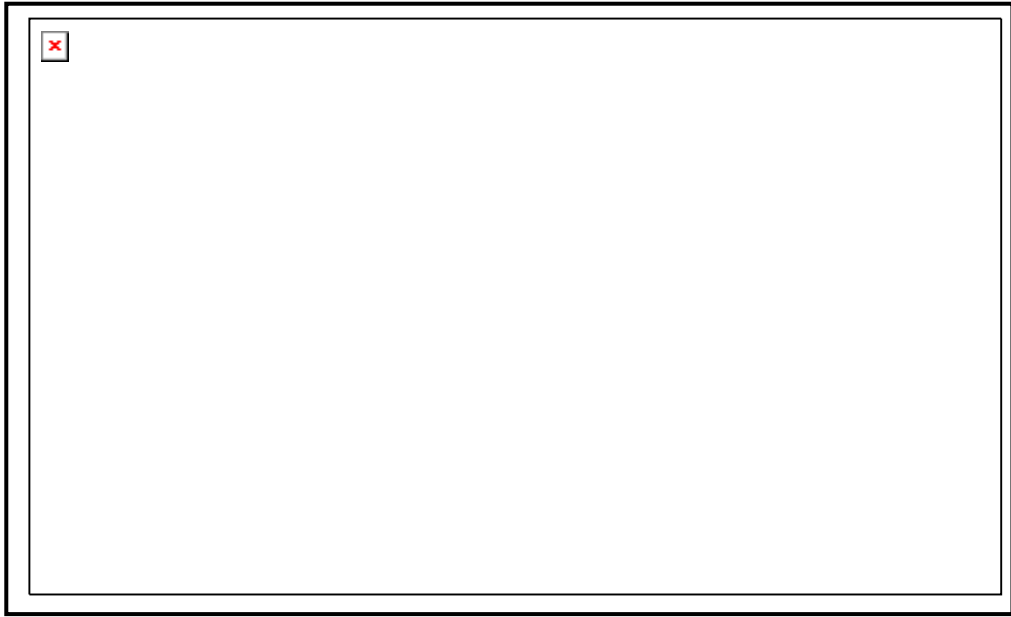


Figure 5.7: Main shaft layout

5.3.1.5 Brake system selection and design

One of the main advantages of the small scale test rig is that it allows us to use a real braking system in order to replicate real world conditions. The main problem was in finding a small scale caliper that would fit the selected small scale disc brake. It was discovered that the Wilwood PS1 brake caliper (part no. 120-8374) [119] would fit the small scale disc brake rotor and the small scale test rig. The PS1 caliper is lightweight and compact, made out of aluminium, as shown in Figure 5.8. The caliper consists of two opposed pistons with a diameter of 28.6 mm, and is designed to accept brake discs between 3.8 and 5 mm in thickness. In accordance with the scaling methodology the thickness of the small scale disc brake rotor was calculated and it varied up to 35 mm based on the scaling factor. The limitation of the disc thickness was overcome by designing a spacer to obtain the desired thickness; also the spacer was used to provide mounting points for a pivoted arm arrangement. The pivoted arm arrangement was designed to enable torque measurement using a conventional load cell (REP transducer, type TC4) as shown in Figure 5.9.

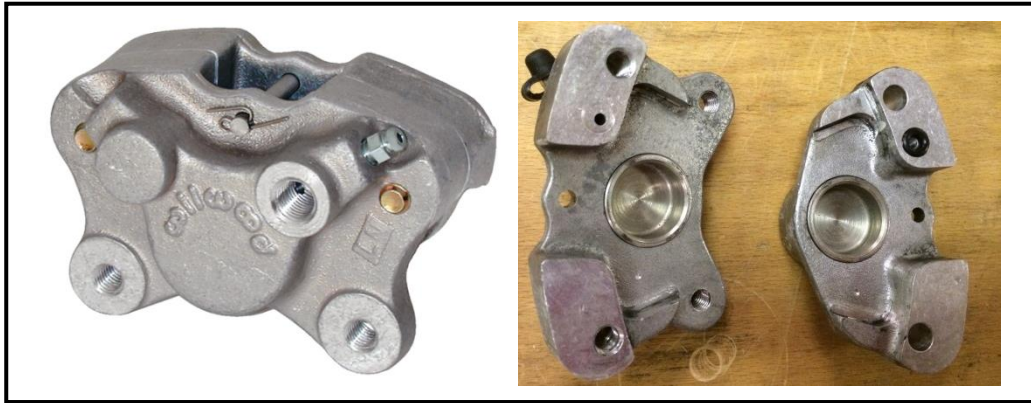


Figure 5.8: Wilwood PS1 caliper [119].

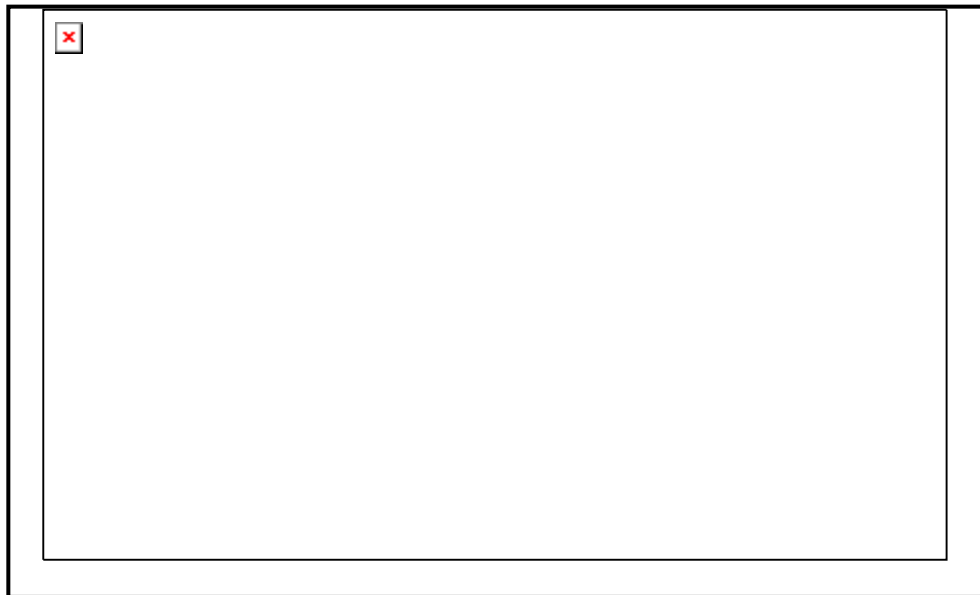


Figure 5.9: 3D model of PS1 Caliper support arrangement.

The stress analysis of the pivot arm arrangement was carried out based on the maximum brake torque. The support arm arrangement gave the user the ability to move the caliper in the vertical and horizontal directions in order to adjust the mean rubbing radius. The load cell was attached to the pivoted arm by using a tapered hole which allowed for fine adjustment of the vertical height.

A further attention in the brake system was the brake pads, and the Wilwood PS1 Caliper accepts Wilwood part no. 150-4091k brake pads as shown in Figure 5.10. The commercial Wilwood brake pads have a contact area of approximately 1260 mm^2 ,

whereas the pad area for the small scale pads are 575 mm^2 and 900 mm^2 as shown in Figure 5.11. The first area (575 mm^2) was used to investigate the thermal performance of the lightweight disc brake and the second area (900 mm^2) to validate the scaling methodology. There were two methods of achieving the desired brake pad areas: 1.) remove or cut away part of the pad material to achieve the desired area; or 2.) produce the back plate and design the pad material according to the required dimensions. The first approach was used to achieve the first pad area, and the second to produce the brake pads for the thermal performance analysis. The second approach was achieved with the help of TMDfriction Company as they provide pad material for specific areas with special compositions to suit the lightweight disc brake rotor.

The pad shape was designed based on the pad to disc rubbing surface area ratio while maintaining constant sliding velocity between the full and small scale disc brake rotors. In addition, the practicality of, removing or producing the pad shape was taken into consideration in the developed pad.

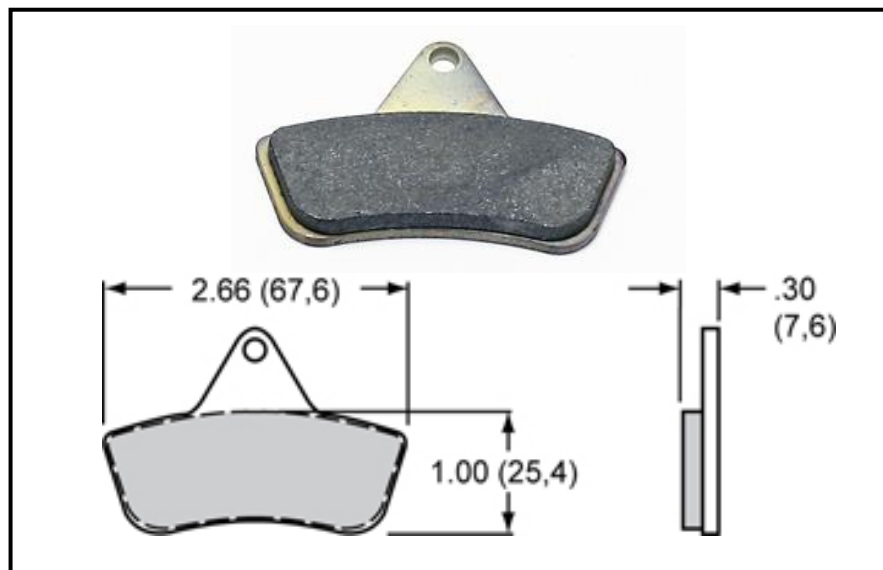


Figure 5.10: Wilwood brake pads [119].

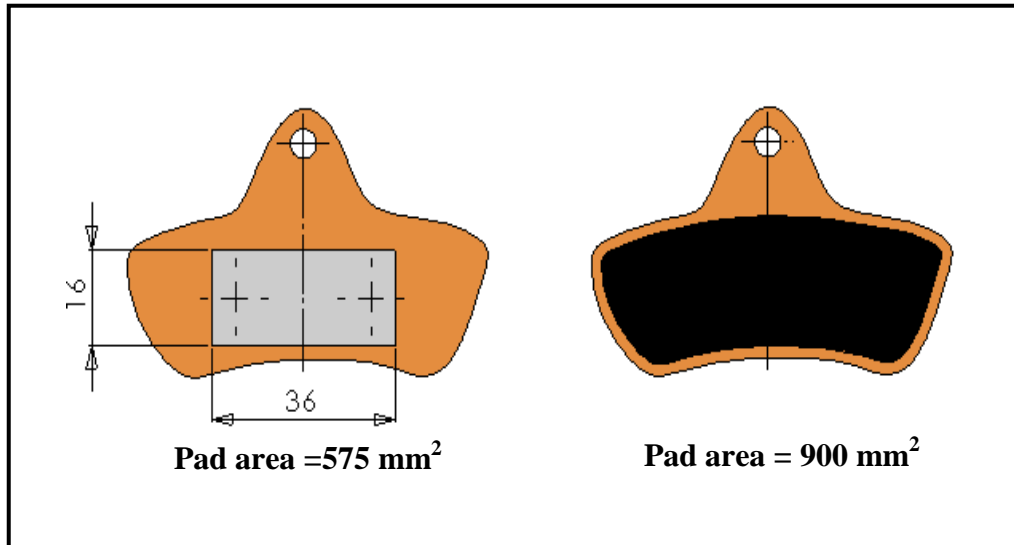


Figure 5.11: Small scale brake pad geometry.

The final consideration in the brake system design was the hydraulic pressure, which is required to actuate the caliper piston. The method of generating the required pressure is by using a master cylinder. The Wilwood Go Kart master cylinder (part no. 260-5520) [119], as shown in Figure 5.12, was chosen for the small scale brake system in order to generate the desired braking pressure. The Wilwood master cylinder was chosen due to its appropriateness for use with the PS1 caliper. A support bracket was designed to secure the master cylinder to the test rig bench as shown in Figure 5.12. The stress analysis was carried out for the developed design based on the maximum loads calculated.

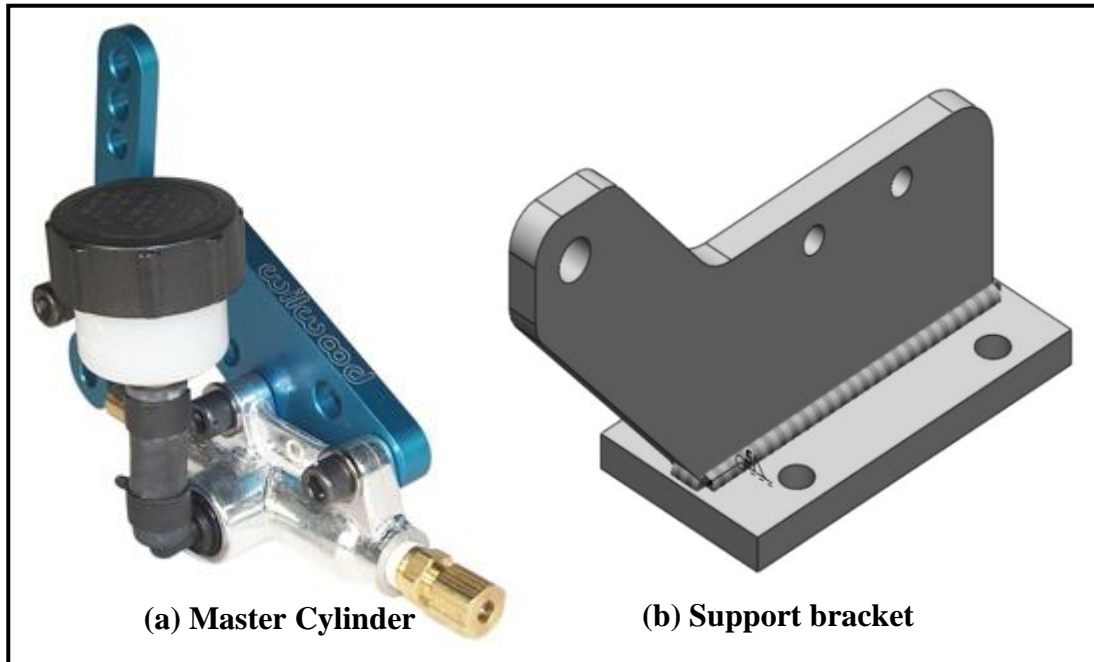


Figure 5.12: Wilwood master cylinder and support arrangement [119].

5.3.1.6 Data acquisition and sensors

One of the main objectives for the developed small scale test rig was to monitor and control the braking event remotely using LabView software. There were a number of variables which needed to be monitored and controlled during the test. These included:

- The rotational speed of the rig.
- The surface temperature of the disc brake rotor.
- The hydraulic pressure in the brake system.
- The disc brake surface temperature.
- Brake pad temperature.
- The brake torque generated during braking, and
- The linear actuator to control the brake hydraulic pressure.

The data acquisition system adopted was based on National Instrument hardware and software. The hardware used in the small scale test rig was the BNC-2090 adapter [120], shown in Figure 5.13, which consists of 22 BNC connectors for analog, digital and timing signals. In addition there are 28 spring terminals for digital and timing signals. The software used in the developed rig was LabView software which has the

ability to control and monitor the various components in the test rig and is compatible with the selected hardware.



Figure 5.13: National instrument BNC-2090 adapter [120].

The general data acquisition configuration of the small scale test rig is shown in Figure 5.14 which indicates that the user is in control of the braking pressure, motor speed and clutch unit while monitoring the temperature, braking pressure, motor speed and braking torque. LabView software can be modified to work with a different braking scenario depending on the user's requirements.

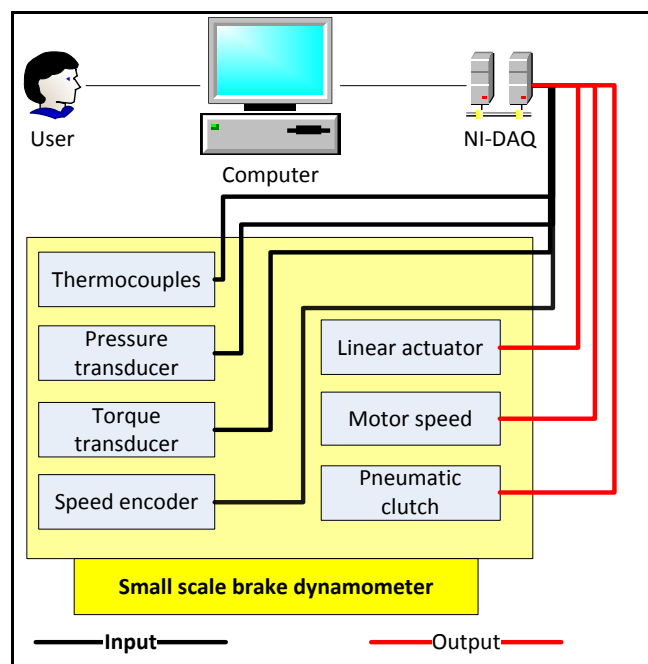


Figure 5.14: General data acquisition configuration of the small scale test rig.

The rotational speed of the small scale test rig was measured using the same configuration as the existing rig. The speed encoder system consists of a solid disc with

80 holes around its circumference located on the developed main shaft by a single grub screw and an infrared emitting diode facing an Optoschmitt detector encased in a black thermoplastic housing (HOA2001) [121], as shown in Figure 5.15. The HOA2001 sensor logic provides a high output when the optical path is clear, and a low output when the path is interrupted. The rotational speed of the test rig was calculated based on the knowledge of the number of holes in the disc and the output signal of the sensor.

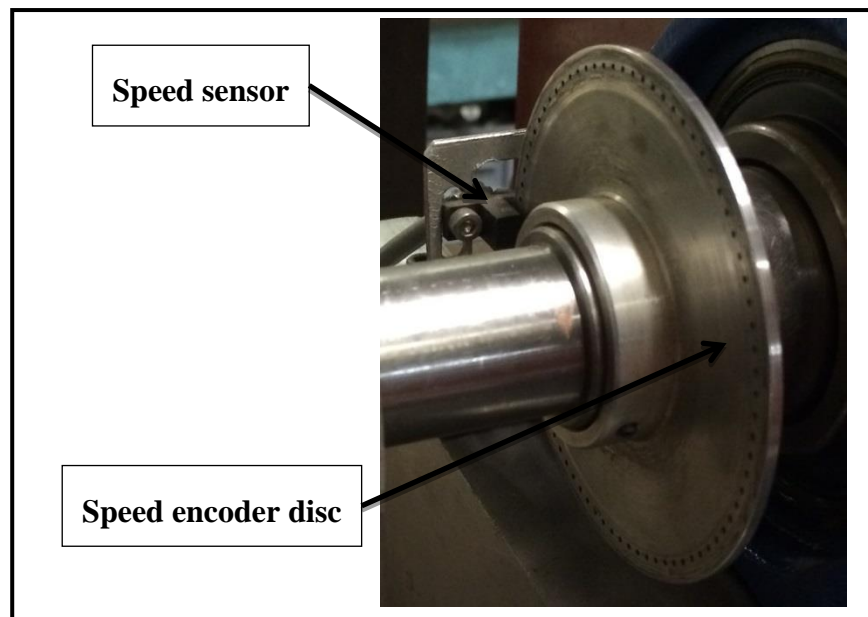


Figure 5.15: Speed sensor configuration.

The hydraulic pressure of the brake system was monitored during the test by using a pressure transducer (RS TYPE 461) [122]. The location of the pressure transducer was chosen to be as close as possible to the caliper in order to measure the actual pressure without any loss, as shown in Figure 5.16. The chosen pressure transducer can measure pressure up to 25 bar. Braided hose and Cupro- Nickel (Kunifer) pipe was used to connect the braking system together. The flexible braided hose was used to capture any movement of the caliper arm. In addition, the Kunifer pipe was used to make sure that the pressure was constant and the pipe will not expand with the time.

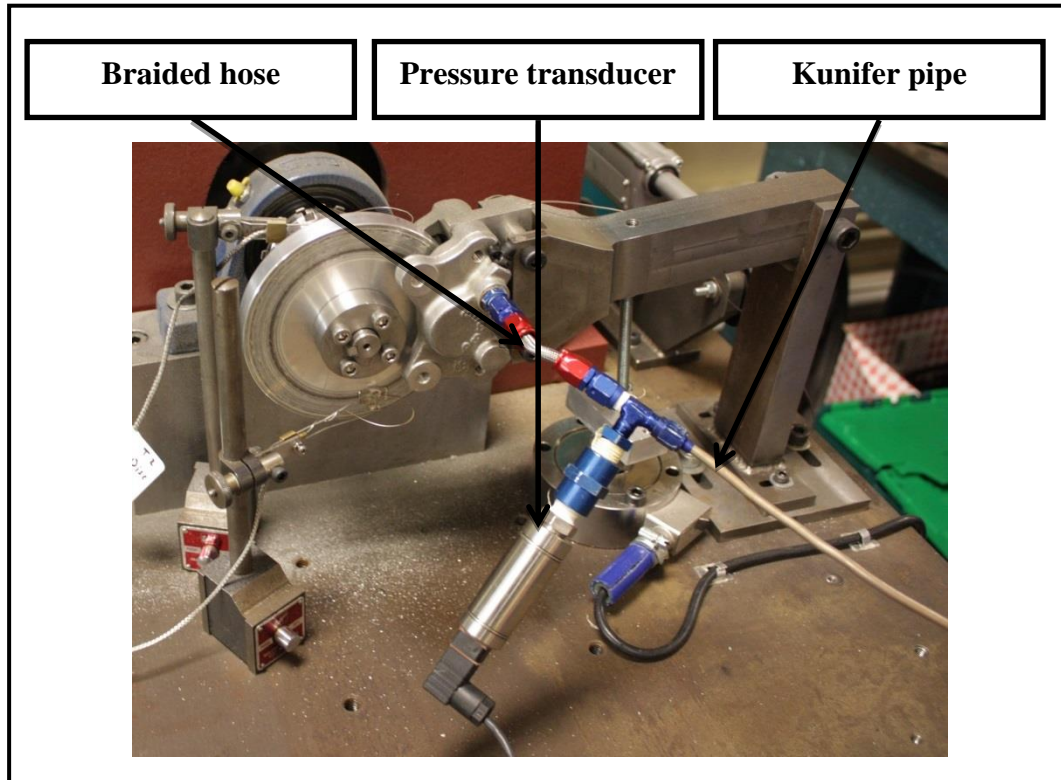


Figure 5.16: Pressure transducer setup.

One of the main parameters which needed to be monitored during the tests was the surface temperature of the disc brake rotor and the temperature of the brake pad. The surface temperature of the disc was monitored using a rubbing thermocouple (K type, HTA1001A) [123], the temperature range of which was between -40°C and 1200°C , with accuracy of 1.5°C . The configuration and location of the thermocouples is shown in Figure 5.17. The sliding thermocouple was placed before and after braking at the mean rubbing radius. The location of the rubbing thermocouples is very important in order to obtain good comparisons and for use in the numerical analysis. Furthermore, the location of the disc at the end of the shaft was planned to allow thermal imaging of the disc. In addition, an embedded thermocouple was used to monitor the temperature of the brake pad; it was located 3 mm from the rubbing surface of the brake pad, as shown in Figure 5.18.

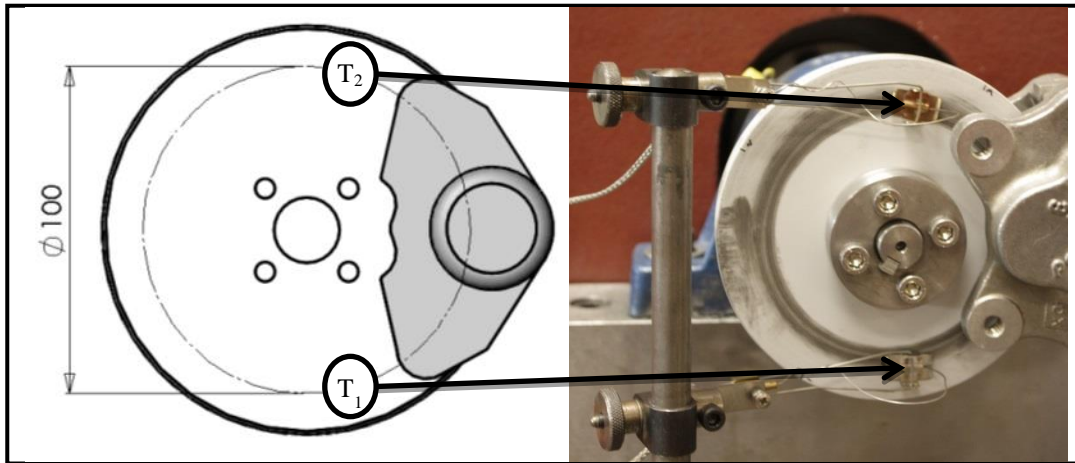


Figure 5.17: Rubbing thermocouple configuration.

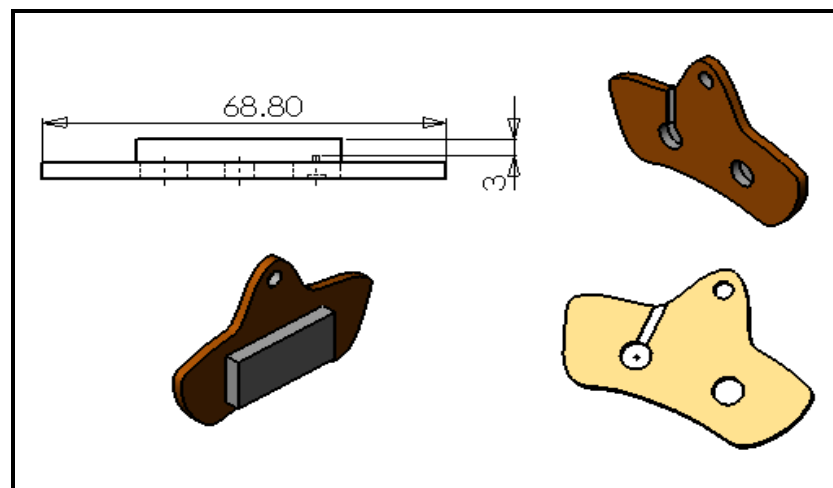


Figure 5.18: Brake pad embedded thermocouple location.

Figure 5.18 shows the location of the embedded thermocouple inside the brake pad. It was fixed using Epoxy structural adhesive which has a very good thermal conductivity and high temperature resistance. The surface of the back plate was ground to remove the excess Epoxy and to make sure that the back plate surface was flat, as shown in Figure 5.19.

The surface temperature of the rotor was also monitored by using a high speed thermal imaging system (FLIR X6540SC) as shown in Figure 5.20, which shows an overview of the set-up of the camera on the small scale rig. The main advantages of using such a system are to be able to assess the temperature distribution across the whole rubbing

surface and to obtain the temperature response as fast as possible. The main features of this thermal camera are: Fast frame rate up to 4300 Hz, high resolution $\pm 1^{\circ}C$, temperature range up to $3000^{\circ}C$, auto exposure, ultrasonic smart lenses, motorised filter wheel and configuration management.



Figure 5.19: Brake pad with embedded thermocouples.

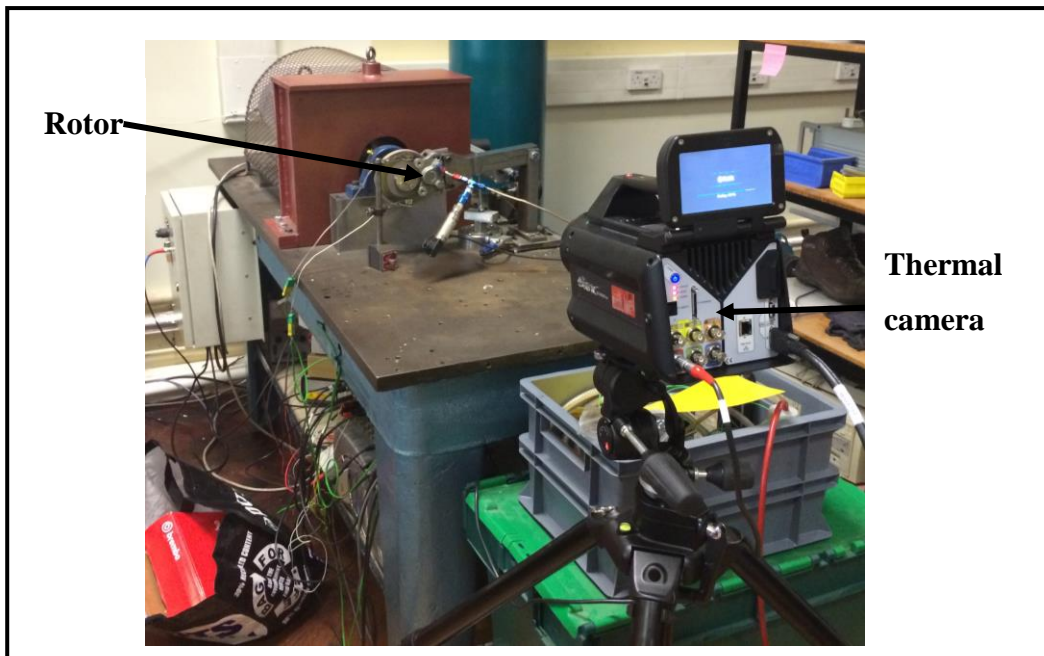


Figure 5.20: Thermal imaging system configuration on the small scale rig.

The brake torque is one of the important parameters that must be monitored during the test in order to calculate the heat flux input that is required in the numerical validation. Also, it was used to evaluate the coefficient of friction and the partition ratio which was used in the numerical simulations. The brake torque was measured using a conventional load cell (REP transducer, type TC4), and the brake torque hardware configuration is shown in Figure 5.21. The brake torque was calculated based on knowledge of the force at a known position.

The brake hydraulic pressure was controlled using the linear actuator chosen in section 5.3.1.3. The control of the hydraulic pressure is processed based on a closed loop feedback system that was developed in LabView. The control algorithm for the brake pressure was based on knowledge of the pressure inside the brake line which was measured using the pressure transducer. The linear actuator was attached at the far end of the master cylinder lever in order to make sure that the maximum load required was as low as possible; the linear actuator configuration is shown in Figure 5.22.

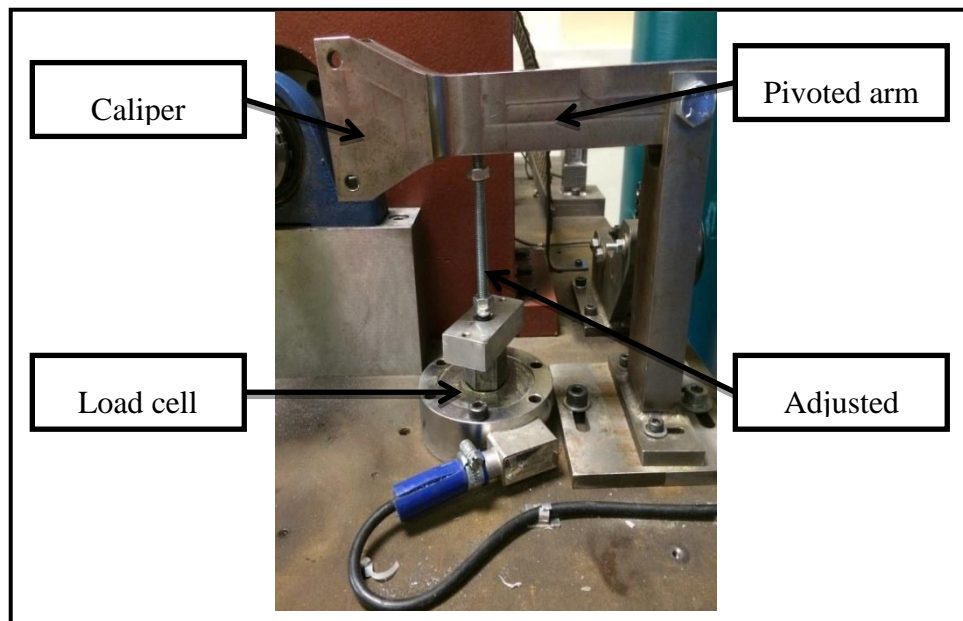


Figure 5.21: Load cell configuration.

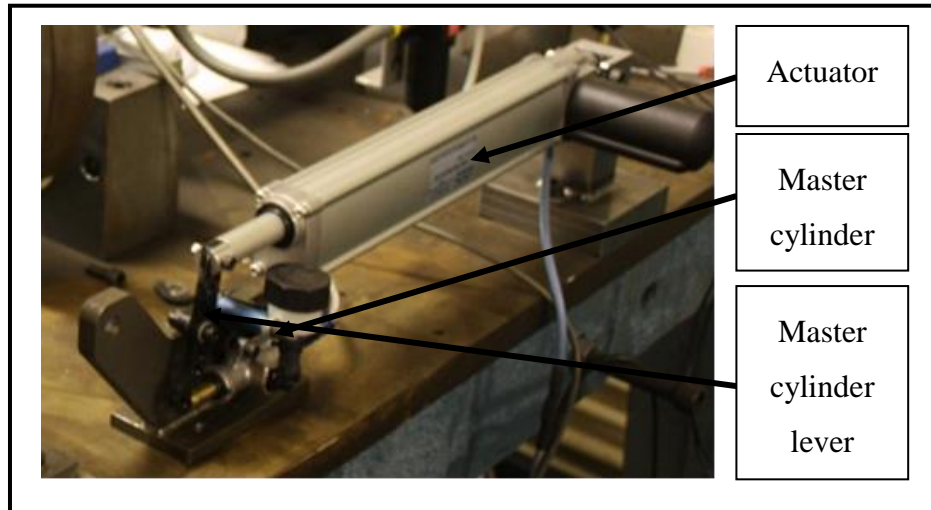


Figure 5.22: Linear actuator configuration.

The pneumatic actuated clutch unit was used to engage and disengage the motor output from the main shaft; the clutch unit was controlled using a control unit which consists of the following: Filter, regulator, 3 way valve, exhaust valve and lubricator, as shown in Figure 5.23. The clutch control unit was used to engage and disengage of the clutch unit through the 3 way valve. The actuation pressure of the air was between 1 and 5.5 bar.

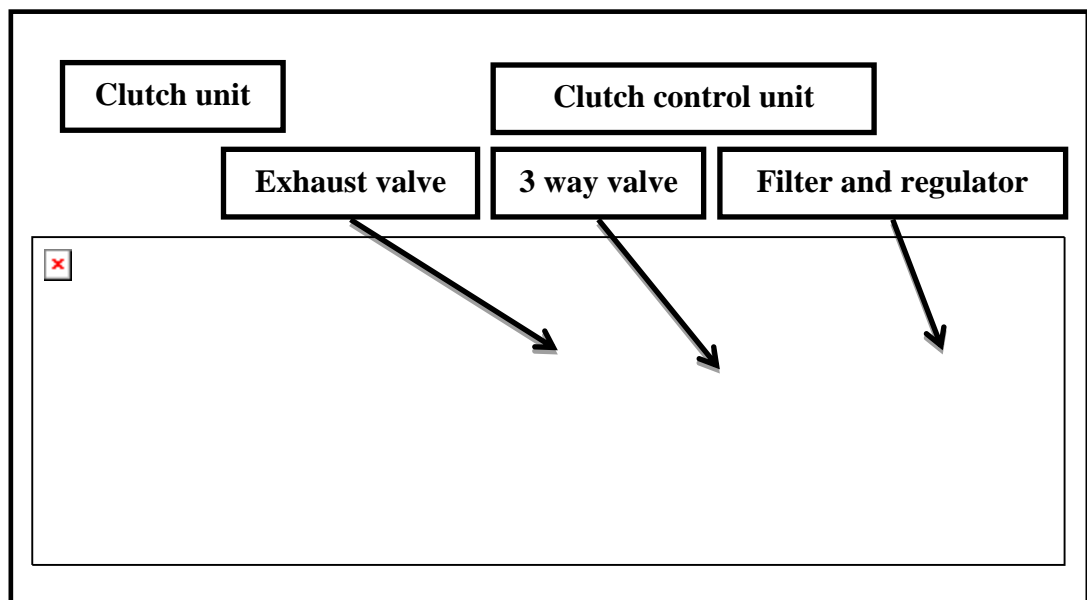


Figure 5.23: Pneumatic clutch set-up configuration.

LabView software was used to communicate between the user and the various components in the system. Also it was used to record all the required data in order to analyse the results and use the data for numerical validation. The LabView user interface window is shown in Figure 5.24. It provides the user with all the key parameters, including disc surface temperature, brake pressure, load cell force, motor speed and brake pad temperature. In addition, the user can change the following: the motor speed, the constant g stop brake pressure and the drag brake pressure. This code was developed to provide the desired output of data from the small scale test rig but it can be modified to work with any braking scenario.

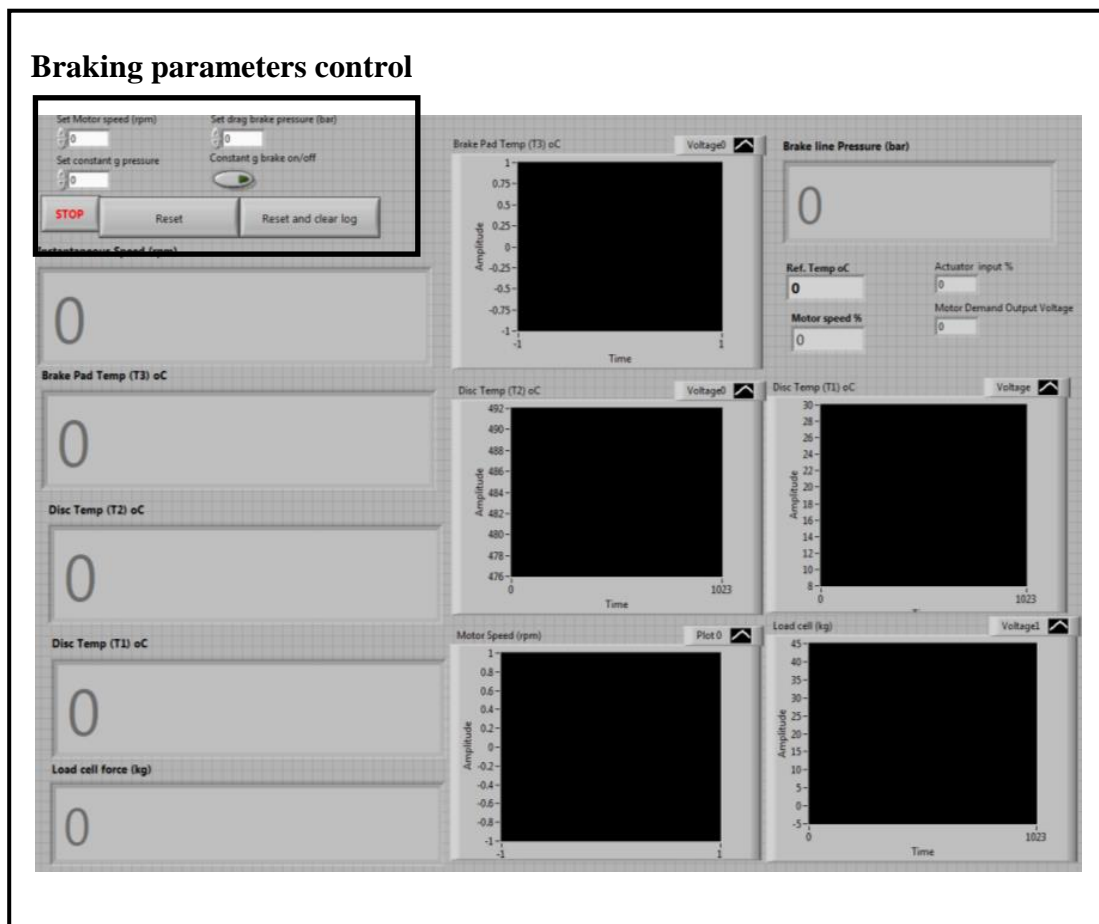


Figure 5.24: LabView user interface window.

5.3.1.7 Test rig specification and limitation

The small scale test rig was developed in order to investigate the scaling methodology and to investigate the thermal performance of lightweight brake rotors under different braking conditions. The developed test rig can replicate different braking conditions and scenarios. The major characteristics of the small scale test rig are listed below:

- Scaling factors 3-12 were chosen. A lower scaling factor would limit the use of constant g stopping because it would be difficult to replicate the required inertia. Scaling factors above 7 are preferable because they make it easy to replicate the desired inertia.
- Pad equivalent diameter: the value and shape of the pad depends on the scaling factor and the full scale pad area.
- Disc outer diameter 125 mm: the diameter of the disc was selected based on the brake system specification and the space limitation.
- Maximum flywheel thickness was 90 mm, based on the maximum load calculation and the space available. In addition, the maximum flywheel mass was estimated as 55 kg.
- A disc thickness of between 5 and 35 mm was considered in the design and selection of the braking system.
- The maximum rotational speed of the motor was limited to 3000 rpm which allows for a wide range of vehicle speeds.
- The maximum brake torque for the rig was calculated as 290 Nm.

The developed test rig met all the objectives but there were some limitations that need to be addressed in the future. One of the main limitations is the DC motor torque which is 2 kW; this torque would not be sufficient to apply a drag braking with high brake torque. The motor issues were solved by using the full scale dynamometer with an adapter as will be explained in the next section to take the small scale brake rotor. The full brake dynamometer is capable of performing a drag brake under high torque. The detailed design and configuration of the full scale brake dynamometer will be explained in the next section.

The calibration of the various components, namely load cell, thermocouples, pressure transducer, speed encoder and linear actuator, are presented in Chapter 7. In addition, the commissioning process of the small scale test rig is explained in detail in Chapter 7. The assembly and disassembly of the small scale rig are shown in Appendix A.

5.3.2 Full scale brake dynamometer

The University of Leeds full scale brake dynamometer was used to validate the scaling methodology and also to investigate the possibility of using the lightweight brake rotor in a passenger car. In this section the general layout of the existing full scale brake dynamometer is explained, also the main features and parameters of the current test rig are highlighted. Furthermore, the design of a small scale adaptor for use with the full scale brake dynamometer is presented in detail. Finally, the data acquisition configuration and test rig limitations are discussed in detail.

5.3.2.1 General layout

The general layout of the existing full scale rig consists of a high torque DC motor driving a main shaft through a drive belt unit with the brake disc located at the end of the shaft, as shown in Figure 5.25. The existing rig consists of two bearings which were placed as shown in Figure 5.25. The speed and torque sensors were placed between the two bearings.

The existing full scale brake dynamometer is capable of applying drag braking conditions only, as there is no inertia involved in the current setup. The full brake dynamometer has a 45 kW motor which is very important when applying a drag brake stop. The main components of the full scale brake dynamometer were as follows: motor, linear actuator, caliper, master cylinder, torque transducer, speed encoder and sliding thermocouples, as shown in Figure 5.26. The brake dynamometer was controlled and monitored using the LabView based data acquisition system.

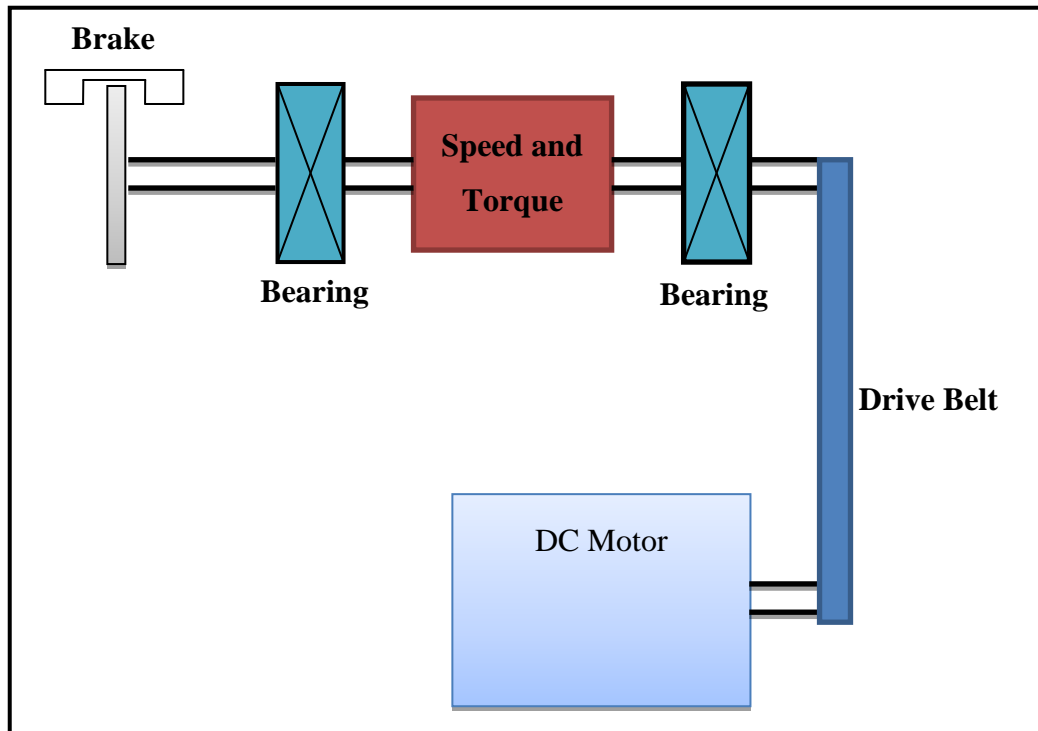


Figure 5.25: General layout of the full scale brake dynamometer.

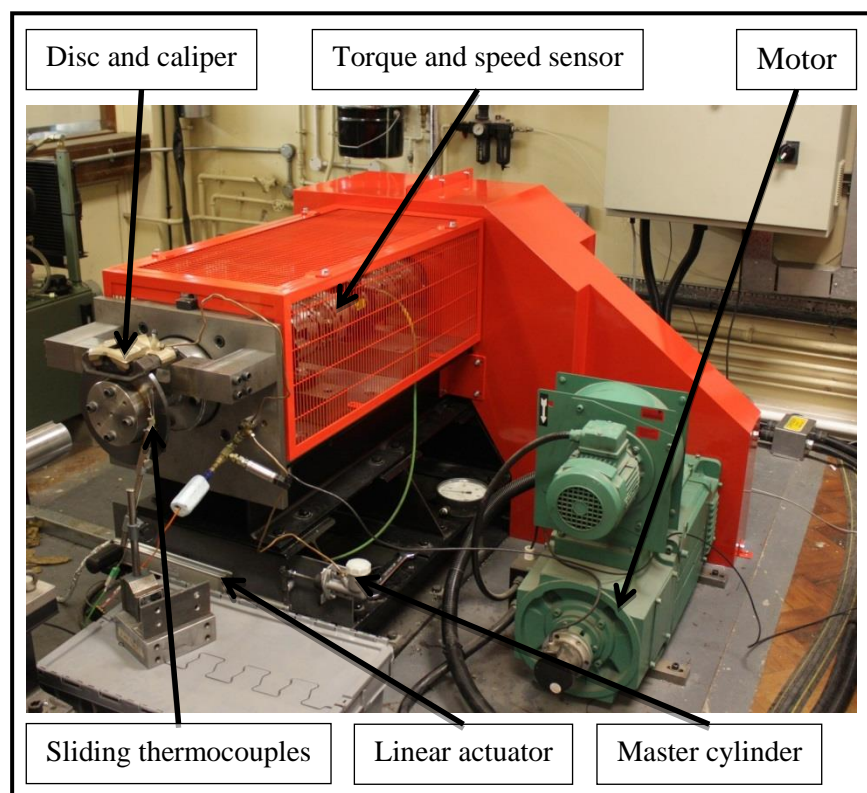


Figure 5.26: Full brake dynamometer.

5.3.2.2 Small scale disc adapter

In the development of the small scale test rig an issue was identified with the low torque DC motor and in order to overcome this problem it was decided to use the full scale brake dynamometer to carry on with drag brake scenarios for the small scale discs. The full scale brake dynamometer had a 45 kW motor which was more than enough to drive the small scale disc to its thermal limits. A special adapter was designed and developed to fit the small scale disc and brake system onto the full brake dynamometer, as shown in Figure 5.27. A stress analysis was carried out to make sure that the developed adapter was capable of taking the maximum desired torque.

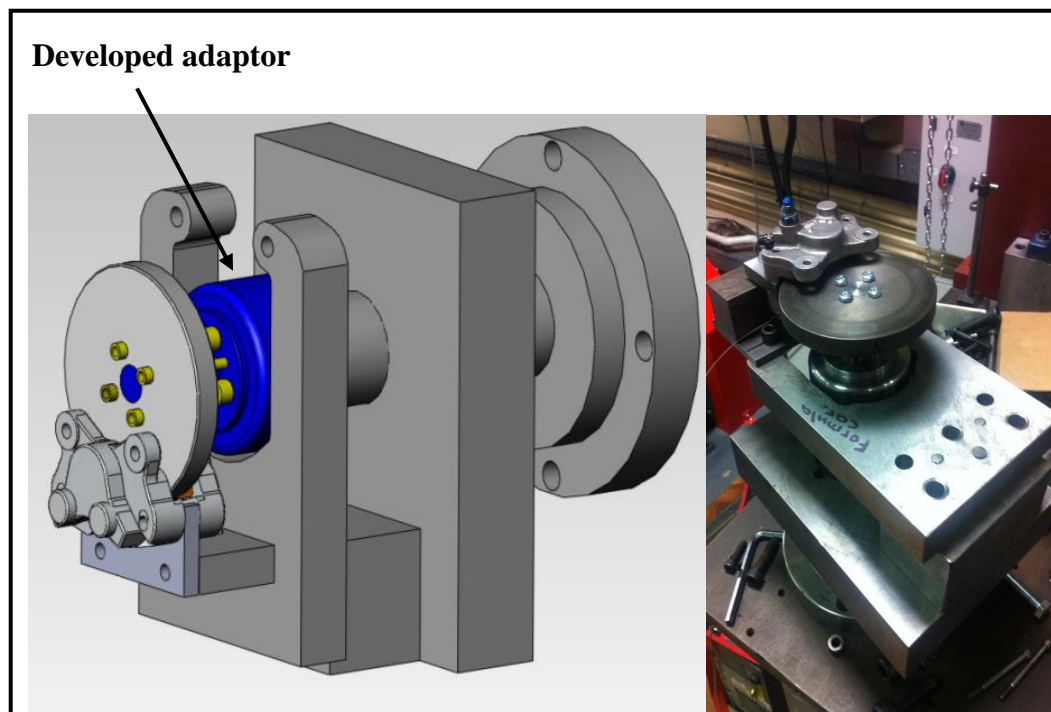


Figure 5.27: Small scale adaptor.

5.3.2.3 Data acquisition and sensors

The general hardware configurations of the full scale brake dynamometer for full and small scale dynamometer are shown in Figure 5.28. The user controls the test rig using in house LabView software that has been developed in order to give full control over the braking conditions. The user controls the braking pressure through the linear actuator and the speed of the motor while measuring the temperature of the disc and

pad, braking pressure, braking torque and motor speed. In addition, the LabView software can be modified to replicate different braking scenarios.

The surface temperature of the small and full scale disc brake rotor was monitored using sliding thermocouples, as shown in Figure 5.29. The location of the sliding thermocouples was fixed for both small and full scale discs in order to facilitate accurate comparison; also thermocouples results were used in the validation between the experimental and numerical results. The sliding thermocouples were placed, after braking, at the mean rubbing radius. The brake pad geometry for the full scale disc brake rotor is shown in Figure 5.30.

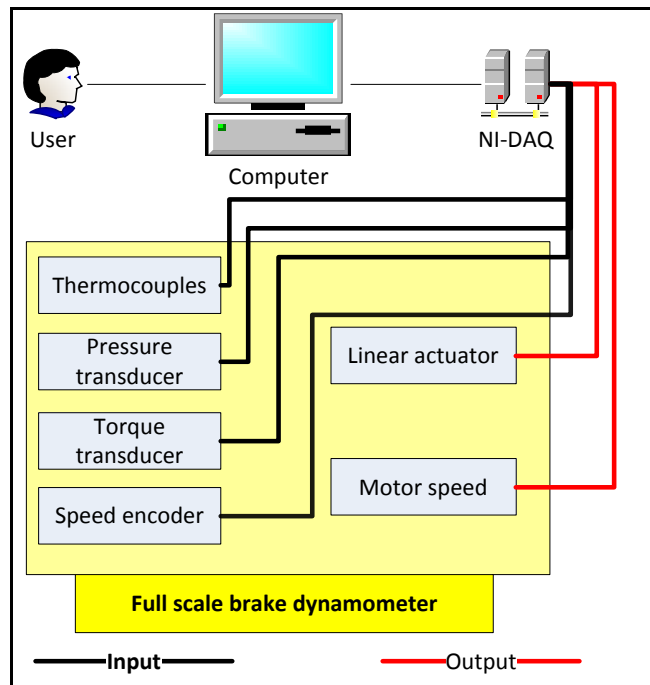


Figure 5.28: Experimental setup of small scale brake dynamometer.

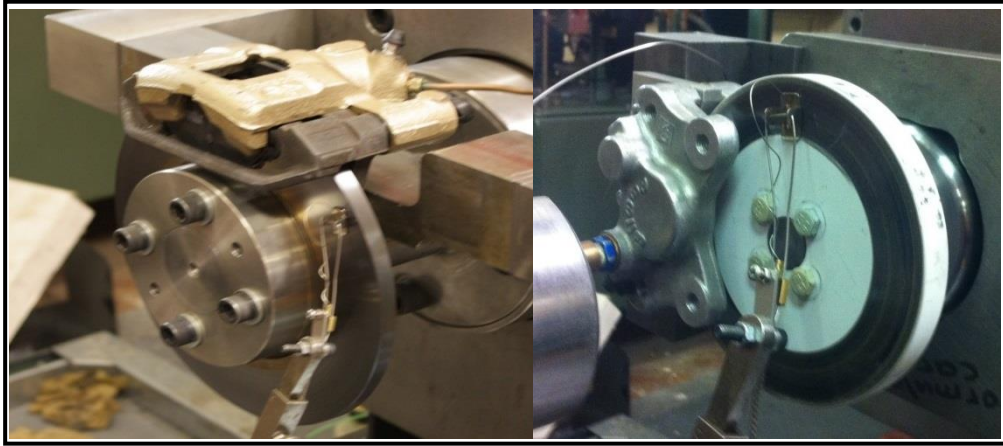


Figure 5.29: Full and small scale disc brake rotor thermocouple position.

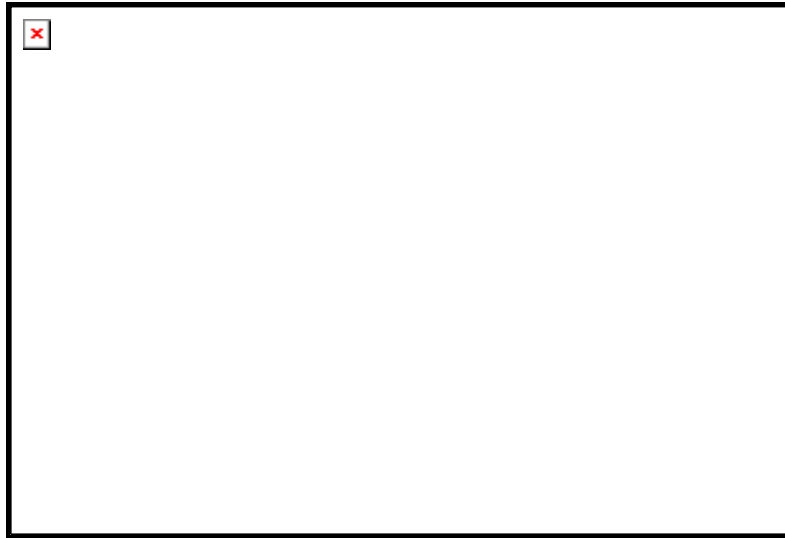


Figure 5.30: Full scale brake pad geometry.

The actuation system for the full brake dynamometer was modified in order to produce a quick response. The same linear actuator used in the small scale test rig was used for the full scale rig, the system configuration is shown in Figure 5.31. The pressure transducer was located as close as possible to the brake caliper as explained earlier in this Chapter. The maximum load required for the master cylinder was calculated to make sure that the linear actuator was suitable.

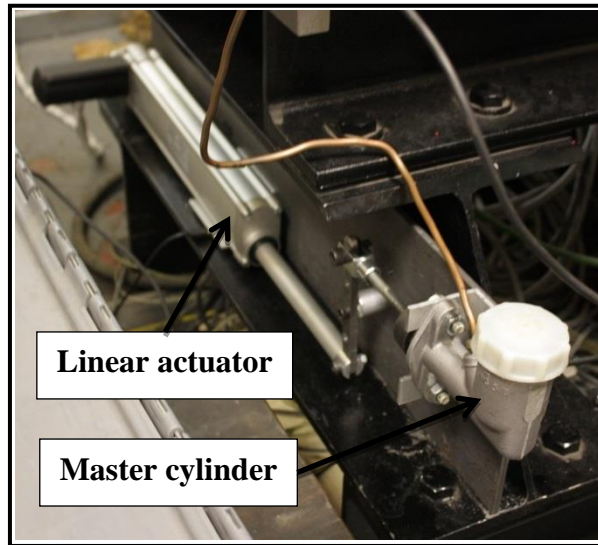


Figure 5.31: Full scale brake system configuration.

The in house LabView software for the full scale brake dynamometer is similar to the small scale software with minor modifications. The changes were the removal of the constant g stop control as the full scale rig cannot perform such an analysis and other changes regarding motor control and brake torque measurement.

5.3.2.4 Test rig specification and limitation

The existing full scale brake dynamometer is a powerful test rig for the evaluation of the thermal performance of disc brake rotors under different drag brake conditions. The high torque motor is one of the key components in the full test rig which provide a wide range of braking conditions. The general specification of the full brake dynamometer at the University of Leeds is as follows: direct drive no inertia; inline torque measurement up to 500 Nm; can hold both disc and drum brakes; 20:1 reduction gearbox; can mount small and full scale disc brake rotors; controlled by LabView. On the other hand, the main issue with the full scale rig is that it only executes drag brake tests which limits its application. The motor speed of the full rig is limited to 1500 rpm which also restricts the braking conditions it can simulate’.

5.3.3 Comparison between full and small scale rigs

The full and small scale test rigs are valuable testing machines that can be used to evaluate the thermal performance of disc brakes, both are controlled by in house

LabView software that can be modified to simulate the desired braking scenario. There are many advantages and disadvantages to the full and small scale test rigs which are summarised in Table 4.5. The main advantages of the small scale rig are as follows: it can conduct drag, constant g and repetitive braking stops while the full scale equipment can only replicate drag brake scenarios. The main advantage of the full scale rig is that it has a high torque motor which is capable of performing high torque drag braking. The maximum hydraulic pressure for both rigs was limited to 25 bar because of the limitation placed on the pressure transducer by the scaling calculation.

Table 5.5: Full and small scale comparison.

Parameter	Full scale	Small scale	Remark
Motor maximum speed (rpm)	1500	4000	
Motor maximum torque (kW)	45	2	
Inertia (kg.m²)	na	Up to 55 kg flywheel	
Maximum hydraulic pressure (bar)	25	25	Limited by the pressure
Constant g stop	No	Yes	
Drag brake	Yes	Yes	
Repetitive braking	No	Yes	

5.4 Calibration and commissioning of test rigs

The general layout and the design of the various components of the small scale dynamometer were explained in detail. In this section the small and full scale dynamometer configuration and set-up to complete the test matrix defined in section 7.2 are explained. The control software used to control and record the data is presented above. In addition, the safety procedure carried out to make sure that the tests were conducted in a safe environment is discussed. The commissioning and calibration of both small and full scale brake dynamometers, in order to make sure that the results from the experiment were accurate and representative, are explained in section 5.4.2 and 5.4.3. The commissioning of the test rigs to ensure that they were functioning as desired is also covered in this section. Finally, the outcome of the commissioning process is presented and discussed.

5.4.1 Test rig setup and configuration

The detailed design process for the small scale test rig was covered earlier. The test rig was fitted with various control and measurement instruments, as shown in Figure 5.32. The rig main shaft was driven by a 2 kW DC motor, controlled by LabView code which changed the input voltage to the motor driver in order to vary the shaft speed. The actuation of the pressure was controlled using a linear actuator which determined the movement of the piston within the master cylinder; the linear actuator itself was controlled by changing the input voltage to the system. A pneumatic clutch was used to connect the motor to the main shaft. The surface temperature of the disc was monitored using K-type sliding thermocouples and the pad temperature was measured with an embedded thermocouple; the thermocouple outputs was measured by a 4 channel signal conditioning unit. The speed of the main shaft was monitored and recorded during the test by using an optical shaft encoder system. In the new rig, a load cell was used to evaluate the braking torque by measuring the force acting on a specified point on the pivoted arm which is 17 cm away from the centre of the disc. In order to change the braking conditions, the brake line pressure was monitored and recorded during the test.

The brake pressure was measured using a pressure transducer which was connected to a 12 V power supply through a signal condition box.

The main features of the developed software were that both drag braking and constant g stop could be applied during any test. The user needed to specify the rotational speed of the motor, the drag brake pressure (if required) and the constant g stop pressure (if required). The rig was designed to accommodate different braking events and conditions in a safe environment.

The working area for both brake dynamometers consisted of two separate sections, the control area which contained the monitoring and control station, and the testing area which included the brake dynamometers themselves. The testing areas were separated by a safety door which had to be closed before performing any test. In addition, an electric stepper motor controller was available for turning off the motor in case of emergency.

The configuration of the full scale brake dynamometer allowed the user to simulate drag braking events only, while the small scale brake version was capable of simulating both drag braking and constant g stopping events. An overview of the full scale brake dynamometer setup and configuration is shown in Figure 5.33. The rig main shaft was driven by a 45 kW DC motor, the speed of which was controlled by changing the input voltage through LabView code. The brake pressure was controlled by using the same linear actuator system operating on the master cylinder as the small scale brake dynamometer. In addition, the surface temperature of the disc and the temperature of the pads were recorded using the k-type thermocouples previously mentioned. During each test, all controlled and measurement parameters were recorded for use in the analysis of the results. In the full scale brake dynamometer, the brake torque was recorded using an inline torque meter. The same torque meter was used to measure the speed of the motor as it had a built-in speed encoder.

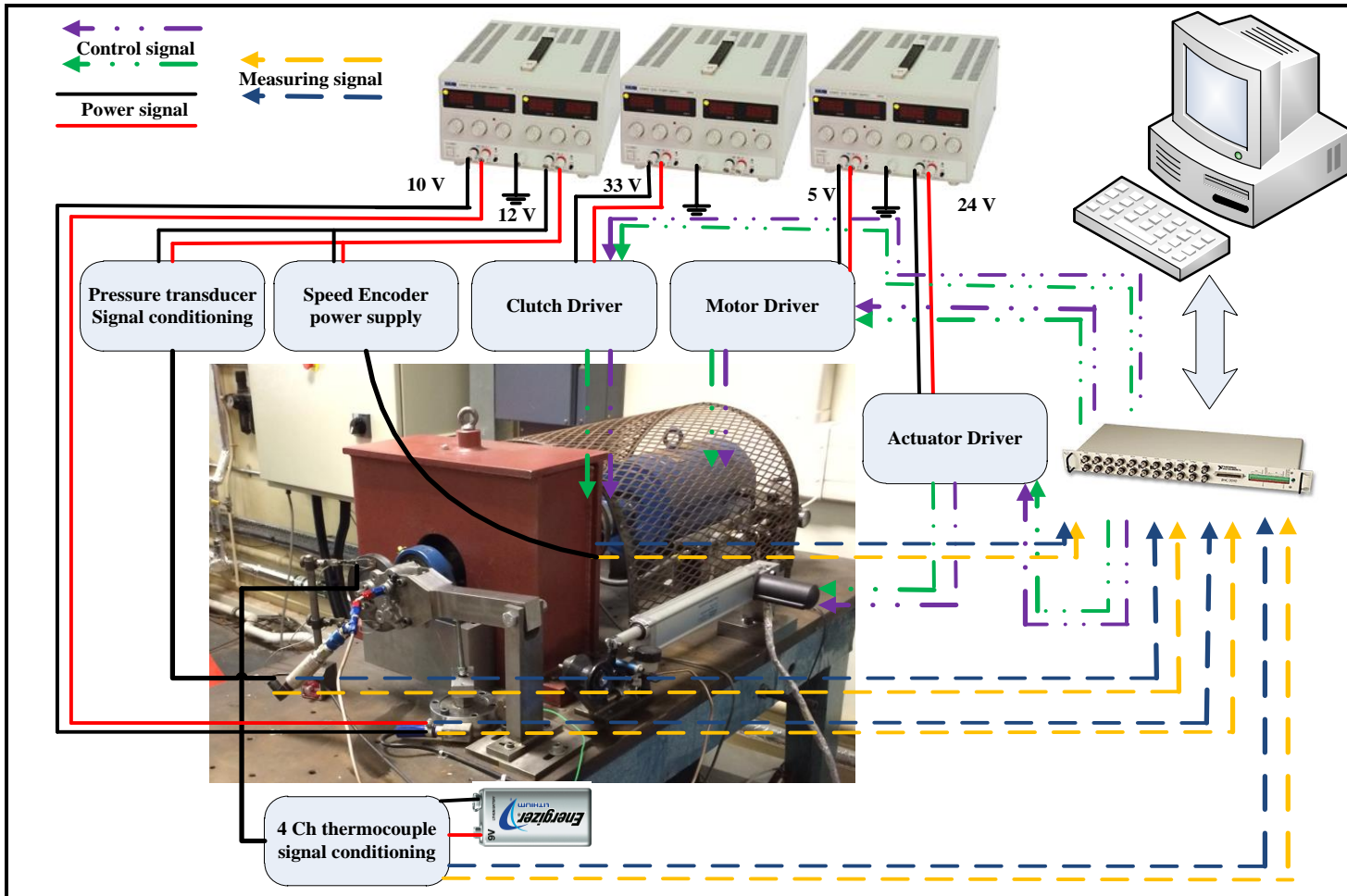


Figure 5.32: Experimental setup for small scale test rig.

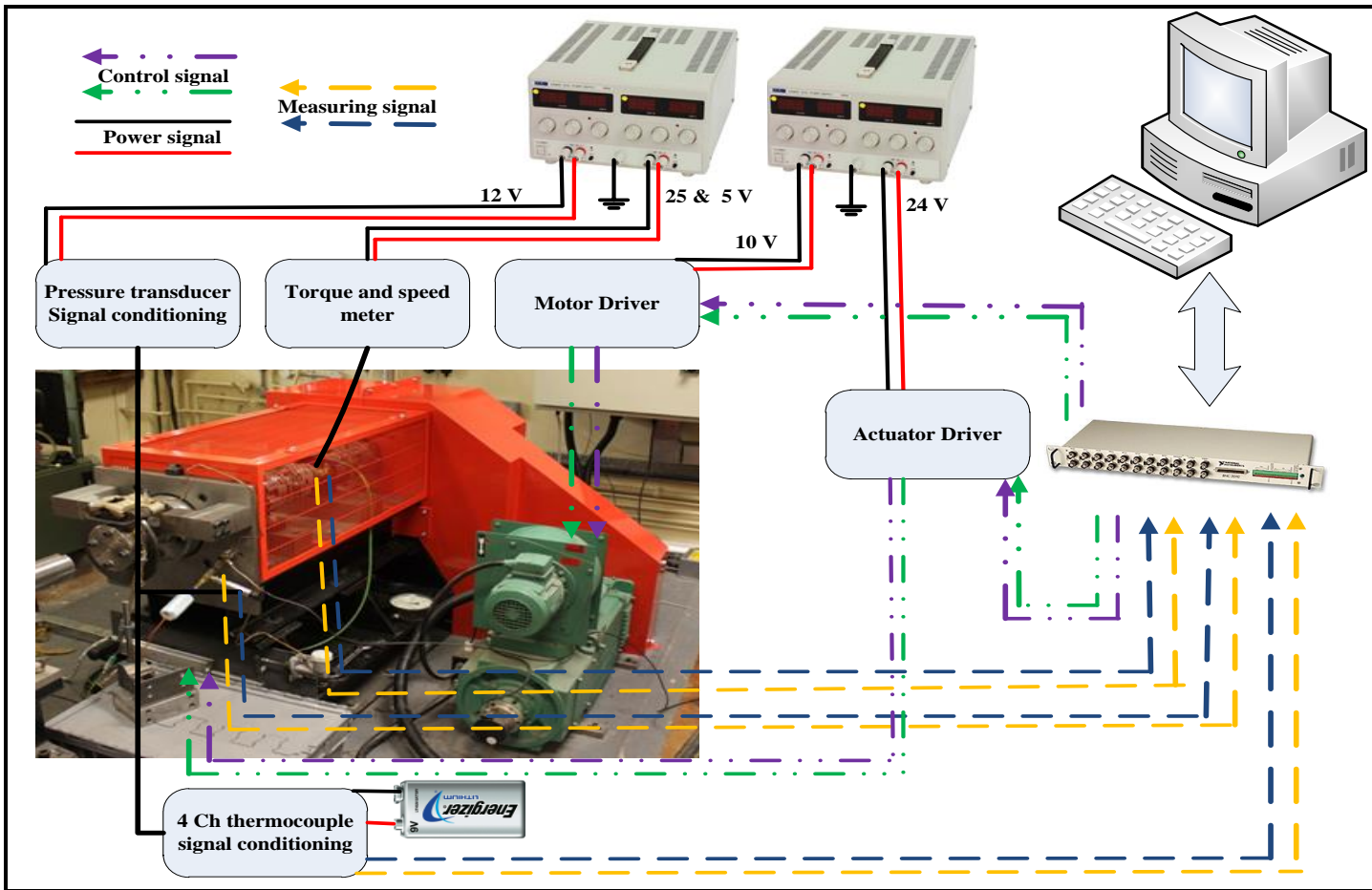


Figure 5.33: Experimental setup for full scale test rig.

In-house software similar to that developed for the small scale dynamometer was used in the full scale dynamometer with some modifications. The software developed for the small scale equipment was capable of performing two different tests, which were drag braking and constant g stop braking. In the modified software for the full size rig, drag braking events were the only braking events which could be performed. Also, in the full size rig there is no clutch unit to engage and disengage the main drive shaft. In the modified software the user needed to specify the rotational speed of the motor and the drag brake pressure. The rig was designed to accommodate different braking conditions in a safe environment. Safety procedures used in the small scale rig were adopted for the full scale rig to make sure that all the tests were conducted in a safe environment.

5.4.2 Sensor calibration

Sensors and actuators played a crucial role in operating the test rig. There were four types of sensor used in the test rigs; namely a load cell, pressure transducer, thermal camera, thermocouples and shaft encoder. In addition, there were two actuators used in the small scale rig: the linear actuator and pneumatic clutch. The same linear actuator was used for the full size rig to control the braking pressure.

a. Brake torque

The brake torque of the small scale brake dynamometer was recorded using a load cell system, as explained earlier. The load cell (REP transducer, type TC4) was used to estimate the brake torque by measuring the transmitted force through the caliper lever arm shown in Figure 5.21. The load cell was calibrated by applying known dead weight loads to the load cell over the low load region in compression only. For calibration over the higher load region the weight loads were applied using a manual mechanical press, manufactured in 1963 (Desnison Universal Testing machine), shown in Figure 5.34. In both cases, the load was applied and removed several times in order to check the consistency of the data.

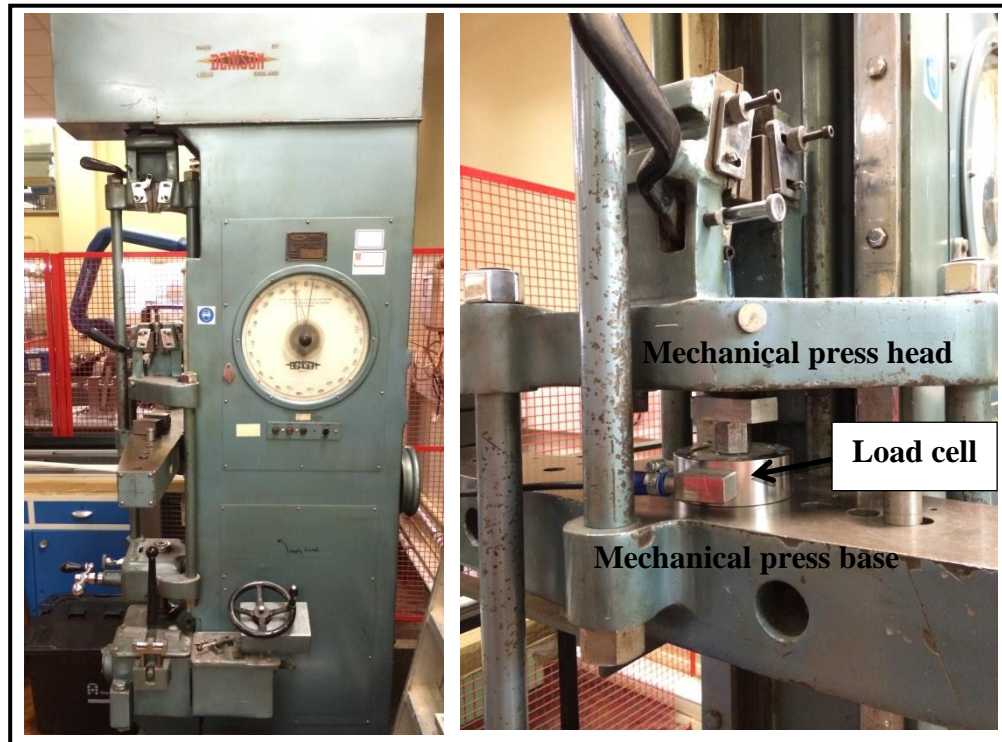


Figure 5.34: Manual mechanical press arrangement for compression loads.

The mechanical set-up for the load cell calibration is shown in Figure 5.34. The values of the output voltage were recorded using LabView code. Linear regression was used to find the linear relation between the applied load and the voltage output in compression, as shown in Figure 5.35. The linear regression equation was used in the LabView code to evaluate the braking force and then use this value to find the brake torque by multiplying the force by the distance to the centre of the disc brake.

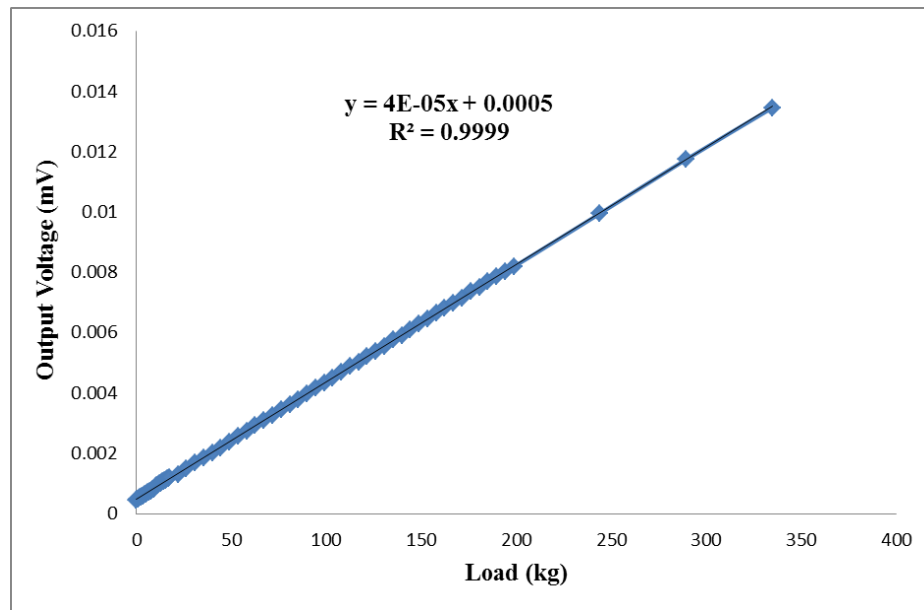


Figure 5.35: Linear regression between output voltage and applied load for load cell calibration.

In the case of the full scale brake dynamometer, the brake torque was recorded using an inline torque meter. The current torque meter is capable of measuring both the inline torque and speed of the motor. The torque and speed sensor was calibrated by the manufacturer. A detailed specification for the torque meter is given in Table 5.6.

Table 5.6: Torque meter (TORQUEMASTER TM 213)

Nominal torque	Maximum ~ 500 Nm
Rotational speed	Minimum: 10 rpm
	Maximum: 10000 rpm
Bearing lifetime	5000 hours
Torsional stiffness	95800 Nm/rad
Resistance	500 Ω
Voltage	20 to 30 VDC

b. Brake pressure

The inline brake pressure for both full and small scale brake dynamometers was recorded using a pressure transducer (RS TYPE 461) [122]. It was important to calibrate the pressure transducer for use in the full and small scale rigs in order to ensure reliable test results for the calculation of friction coefficient in particular. The calibration of any pressure transducer or pressure gauge is achieved by connecting it to a well know pressure source and recording the output voltage. A hydraulic dead weight tester (shown in Figure 5.36) was used to calibrate the pressure transducer by varying the dead weight applied to the hydraulic system.

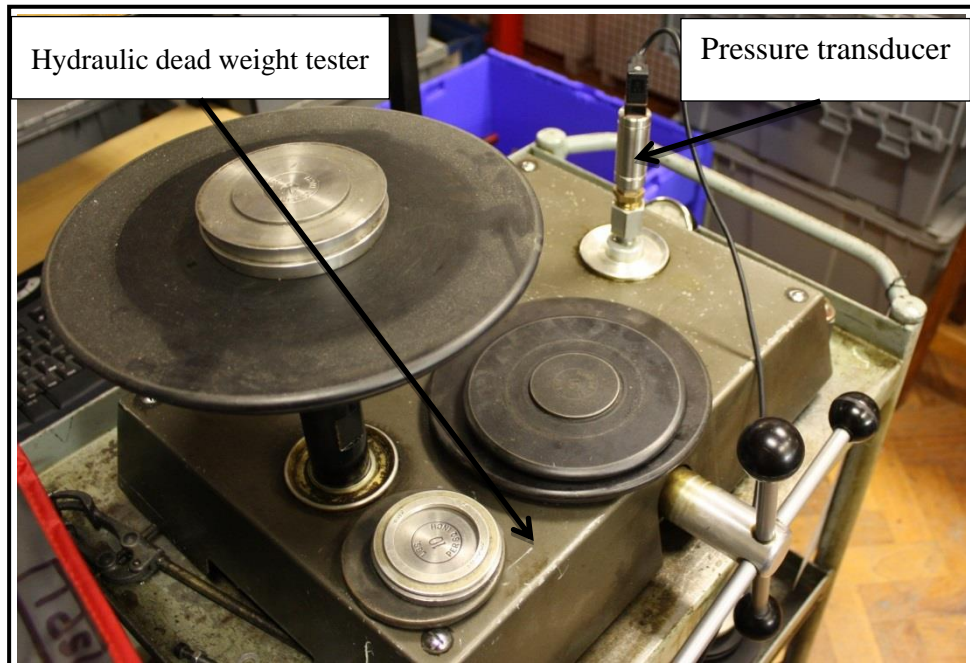


Figure 5.36: Hydraulic dead weight tester for calibrating the pressure transducer.

The set-up of the pressure transducer calibration is shown in Figure 5.36; the output voltage was recorded using LabView code. According to the pressure transducer data sheet, the output voltage was 0 to 5 Volts. The pressure transducer range was between 0 and 25 bar, this implies that for every 1 bar pressure the output voltage was 0.25 Volts. The calibration process was carried out using the hydraulic dead weight tester in order to ensure the measured data was reliable. The pressure was applied several times in upward and backward directions in order to check the consistency of the data. Linear

regression was used to find the linear relation between the hydraulic pressure and the output voltage, as shown in Figure 5.37. The linear regression equation was used in the LabView code to evaluate the brake line pressure during the tests. Based on the pressure transducer data sheet the accuracy of the output voltage is $\pm 0.25\%$.

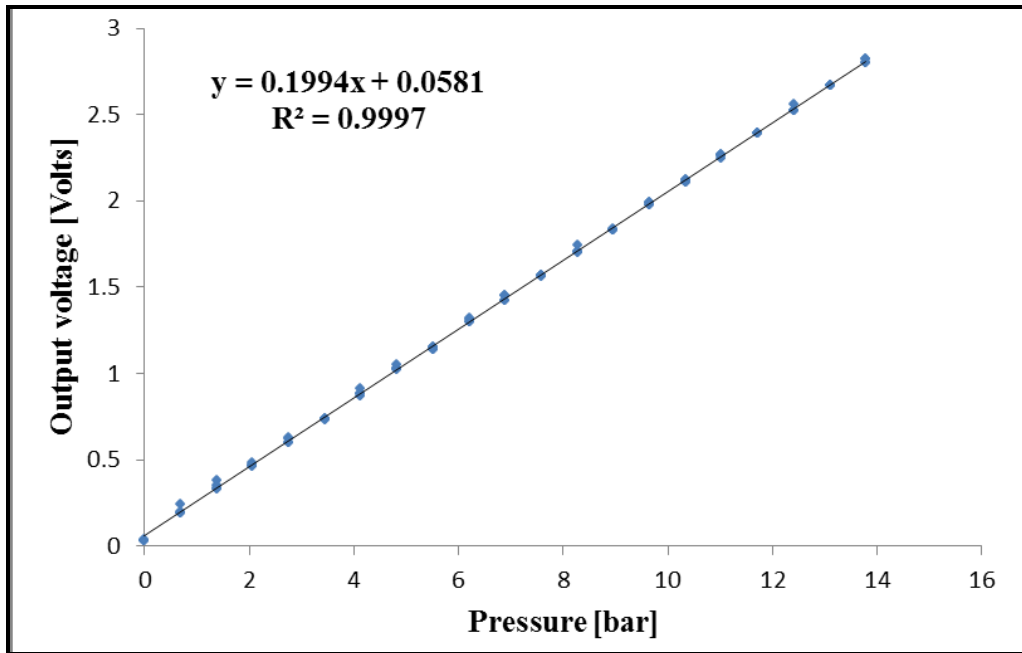


Figure 5.37: Linear regression between output voltage and hydraulic pressure for pressure transducer calibration.

c. Calibration of thermocouples and thermal camera

In the current research, K-type thermocouples were used to record the surface temperature of the disc brake rotor and the temperature inside the brake pad for both full and small scale brake dynamometers. The thermocouples were composed of two different metals which generate a small voltage when joined together, and in the current research they were calibrated using two different methods: using a series of fixed points; and comparison with reference thermocouples in stabilised baths. A water bath was used to generate the different fixed temperature points and a standard thermocouple was utilized as a reference. Linear regression was used to define the relation between the temperature and the output voltage, as shown in Figure 5.38. The linear regression equation was used in the LabView code to evaluate the temperature of the various

thermocouples in the small scale test rig. The accuracy of thermocouple output is $\pm 1.5^{\circ}\text{C}$ based on the thermocouples data sheet. The high speed thermal camera was calibrated by the manufacturer using a calibration process called CNUCTM. This process provides stable measurement and beautiful imagery.

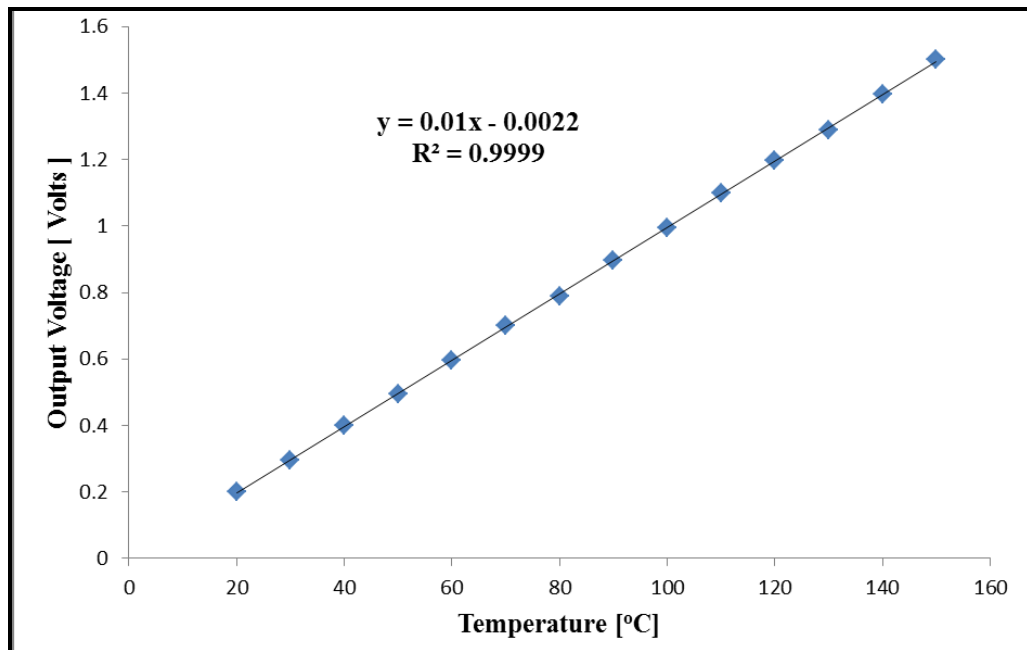


Figure 5.38: Linear regression between output voltage and temperature for thermocouple calibration.

d. Shaft encoder calibration for small scale rig

The shaft encoder system was used in the current research to evaluate the speed of the small scale rig shaft. The rotational speed of the test rig was calculated based on the knowledge of the number of holes in the disc and the output signal of the sensor; a detail description of the system was given in section 5.3.1.6. The shaft encoder was calibrated based on knowledge of the motor speed as the motor speed is a function of the input voltage, and by varying the input voltage the motor speed can be changed accordingly. The accuracy of the shaft encoder system depends on the number of holes around the encoder disc. In the current setup, an average speed was calculated in order to determine a more precise value of the rotational speed. The DC motor was calibrated by the manufacturer, so the calibration of the encoder was carried out based on the motor calibration. In addition, a tachometer was used to validate the accuracy of the shaft

encoder. It was found that the error in measuring rotational speed of the test rig was ± 20 rpm; this error was due to the efficiency of the motor and the number of holes in the encoder disc.

e. Linear actuator calibration

The linear actuator used in the current study to control the hydraulic pressure of the brake was calibrated by the manufacturer. Different approaches were investigated to control the hydraulic pressure. It was found that using a look-up table approach with closed loop feedback was the best method. The look-up table approach reduces both the overshoot in the system and the time needed to reach the desired pressure. The main problems with the other types of control were the overshoot and the pressure oscillation around the desired value. In order to apply the look-up table approach, the input voltage of the linear actuator needed to be evaluated against the hydraulic pressure to find the relation between the voltage and the pressure. The calibrated pressure transducer was used to find the pressure at different actuator input voltage. Polynomial (4th order) regression was used to evaluate the relation between the brake hydraulic pressure and the input voltage, Figure 5.39, for use in the control algorithm.

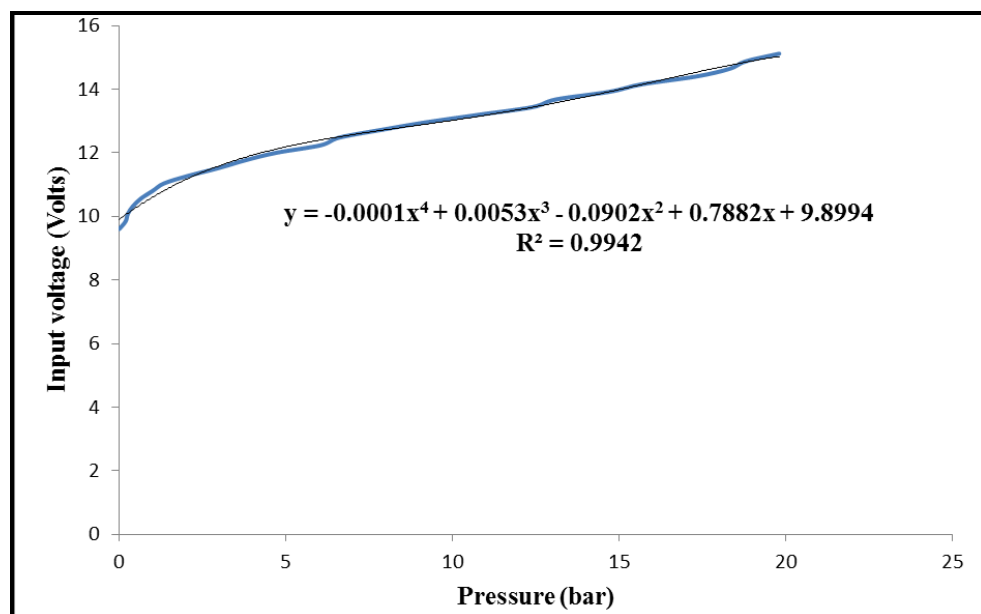


Figure 5.39: Polynomial regression between actuator input voltage and brake line pressure for linear actuator.

5.4.3 Test rig commissioning

The small scale brake dynamometer was commissioned and validated with a series of tests in order to make sure that the rig was working as desired without any issues. Many parameters were monitored during the commissioning, such as: the vibration noise, the alignment, data recording and rig general performance. It was noticed that the surface temperature of the two bearings increased, especially that of the bearing close to the flywheel. Bearing temperatures were monitored using thermocouples, Figure 5.40, and it was found that they reached a steady state after some time, at an acceptable value. Figure 5.41 shows the surface temperature of the bearings without applying any braking conditions.

Another issue observed during the commissioning process was a delay in the recording of braking force by the load cell. This has an impact on the evaluation of the coefficient of friction. Further investigation was carried out to address the load cell reading problem and to provide a possible solution. It was found that the load cell amplifier has a built in filter which delayed recording of the signal by the LabView code. In order to overcome this, two possible solutions were suggested as follows: design another amplifier without the filter, or connect the load cell directly to the Ni-DAQ card. The second approach was chosen, and although the output signal was small and noisy, it was possible to resolve this issue during the data analysis. A simple test was carried out in order to evaluate the load cell response with and without the filter using the suggested approach. It showed that this method improved the response speed of the load cell signal by about 0.5 s.

All the major and minor issues in the small scale test rig were resolved and the parameters tuned to make sure that the recorded data were reliable and comparable. The test rig was then used to replicate different braking conditions to make sure it functioned as desired.

A summary of the commissioning test output parameter which includes the surface temperature of the disc, the temperature inside the pad, the speed of the motor, the coefficient of friction, the brake pressure, and the brake torque are shown in Appendix

B. The results show that the test rig could evaluate different braking conditions and the data were recorded at a sufficient rate to make sure that the output results were reliable. All the issues specified earlier were resolved as shown in the commissioning results.

The full scale brake dynamometer was commissioned using the same procedures followed for the small scale dynamometer. The output data from the full scale version shows stable results as shown in Appendix B.

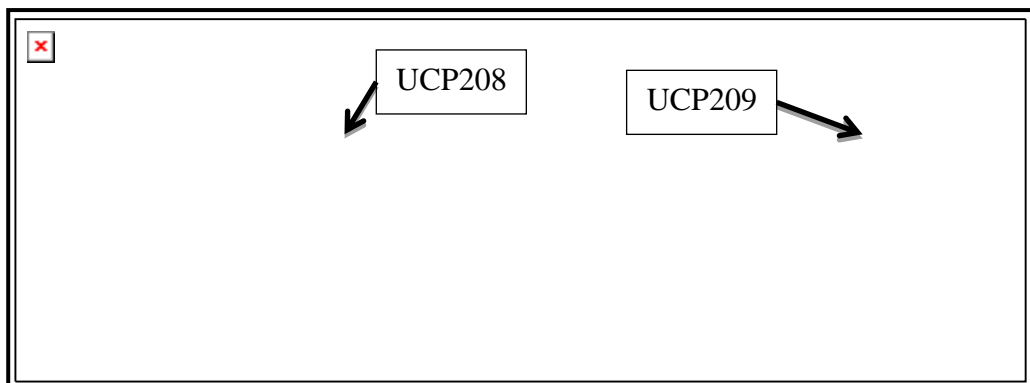


Figure 5.40: Position of the thermocouples on the bearings.

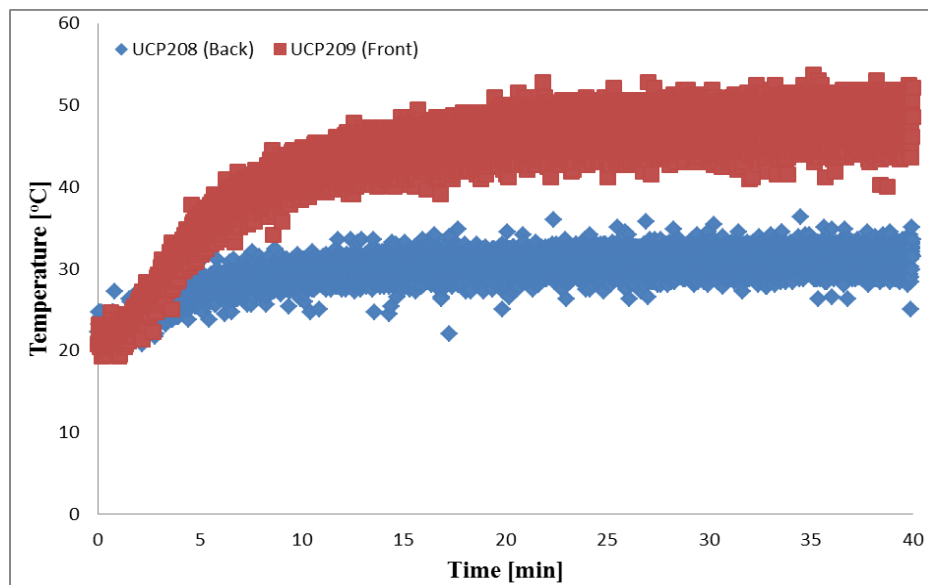


Figure 5.41: Bearing surface temperature without braking condition at 1500 rpm.

5.5 Requisition of test samples

In this research the main aim is to investigate the use of a lightweight disc brake instead of the conventional cast iron disc brake. It was found from the literature that the best candidates to use in this brake application would be aluminium metal matrix composite (Al-MMC) and aluminium alloy because of their properties which were previously mentioned in the literature review Chapter. In this research, aluminium metal matrix composite (AMC640XA) and aluminium alloy (6082) were used for the small scale disc brake in order to investigate the possibility of using such materials in the automotive industry. In addition, PEO coating was applied to both Al-MMC and Al-Alloy discs to improve the wear and corrosion resistance. The coating also provides a low thermal conductivity which acts as a thermal barrier for the substrate material.

Five small scale solid brake rotors were investigated: grey cast iron, forged aluminium alloy (6082), the same 6082 alloy but with an alumina surface layer applied by plasma electrolytic oxidation (PEO), cast aluminium MMC (AMC640XA), and the same MMC again with a PEO alumina surface layer. Figure 5.42 shows the CAD representation of the small scale discs.

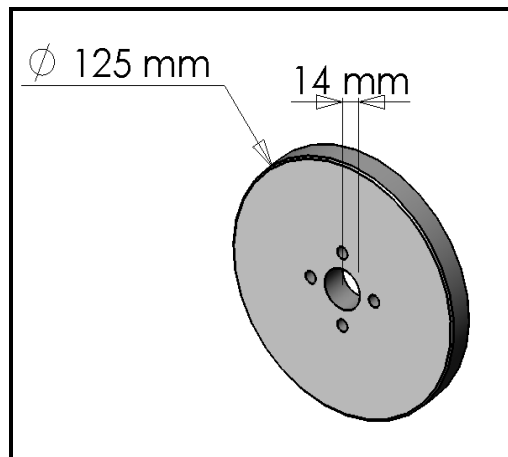


Figure 5.42: CAD representation of the reduced scale disc brake.

The brake pads were provided by TMDfriction Company and the material was designed specifically for use against aluminium discs with ceramic surfaces. It was an organic based friction material containing a low amount of metallic compounds (LowMet).

5.6 Summary

In this Chapter the scaling methodologies, based on constant energy density, are explained in detail. The selection of a vehicle for experimental investigation of the scaling methodology and thermal performance of lightweight disc brake rotors is described. The way in which the scaling methodology was used to design and develop the small scale brake dynamometer is explained. The general layout and design process of the small scale brake dynamometer is presented in detail. The development of the data acquisition facilities of the small scale test rig, based on LabView software, is described. The way in which an existing full scale brake dynamometer was modified in order to utilize the high torque motor and drive the disc brake rotor temperature to the extreme is set out. The layout of the full scale brake dynamometer is presented in detail. A general comparison between the developed small scale brake dynamometer and the full scale brake dynamometer is made. The small scale and full scale brake dynamometers were calibrated and commissioned in order to make sure that the output data was reliable. During commissioning, many limitations and difficulties were identified and addressed in order to achieve the desired aim. Finally, the identification and sourcing of test samples for use in the experimental and numerical analyses is presented.

CHAPTER 6:

THERMAL ANALYSIS USING FINITE ELEMENT MODELS

6.1 Introduction

The thermal analysis of solid disc brakes was investigated using the method of Finite Element analysis. Two different models were developed and investigated in this Chapter; the first is a two dimensional (2D) axisymmetric transient heat transfer model and the second is a three dimensional (3D) coupled temperature model. The 2D model was used to provide confidence that the correct conditions can be established in the 3D FE simulation. It also provides an opportunity to use Abaqus implicit FEA software. Furthermore, a 3D coupled temperature FE model that replicates the small scale test rig was created. The 3D model takes into account the thermal boundary conditions as well as the contact interface definition used in the small scale rig. Comparisons between the three different models (1D (developed in Chapter 4), 2D and 3D) are presented in detail in order to choose the model that best reproduces the thermal performance of a solid disc brake rotor. The nominated model will be validated against the experimental results and to carry forward the investigation of the thermal performance of lightweight disc brake rotors. Figure 6.1 shows the overall methodology used in this Chapter to choose the preferred model.

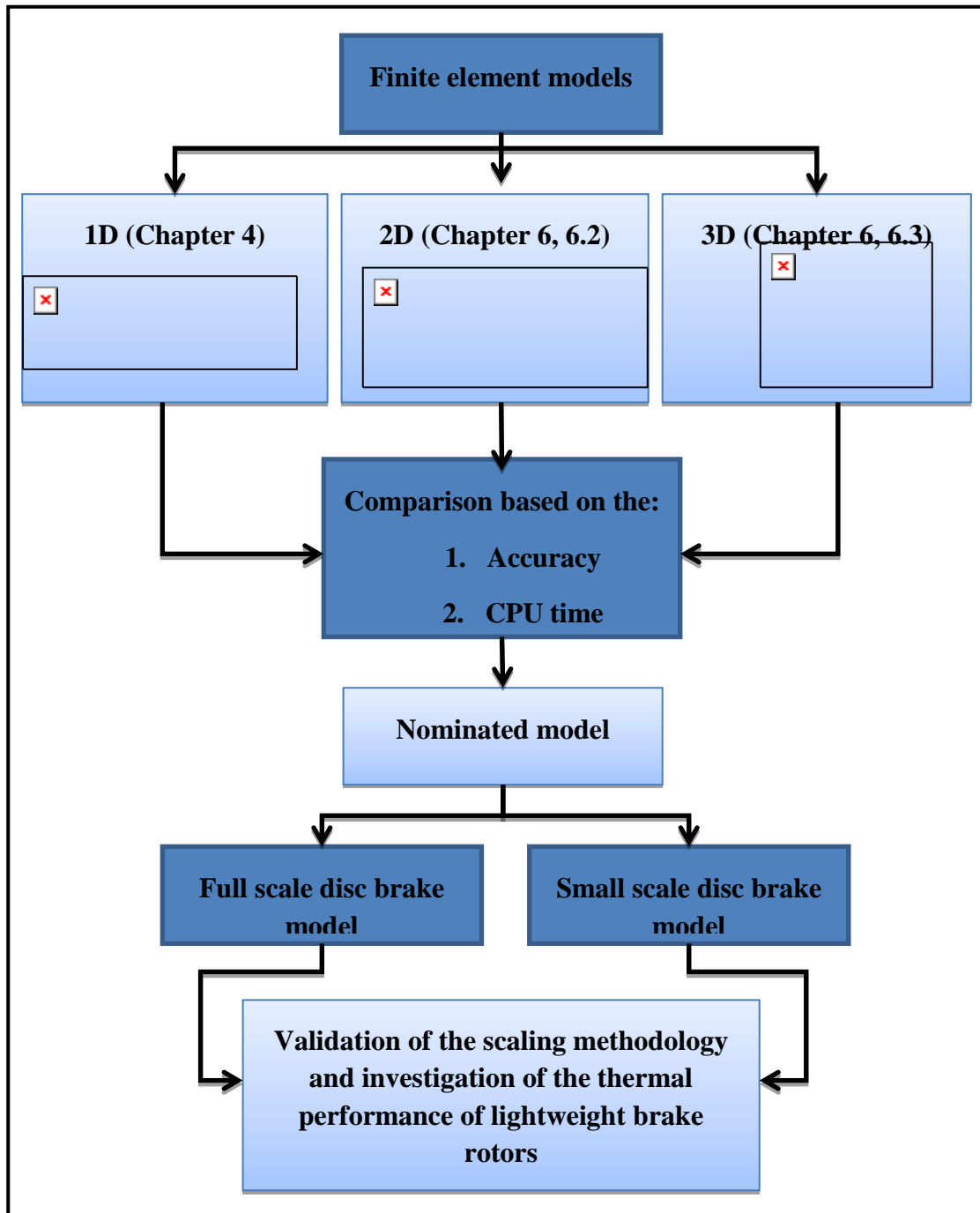


Figure 6.1: Finite element model selection.

6.2 Two dimensional axisymmetric transient thermal model for small scale discs

In this section a 2D axisymmetric transient model is described in detail using the small scale disc brake rotor as an example. The model setup, boundary conditions, mesh sensitivity and simulation steps are all presented. The small scale disc brake geometry and boundary conditions used in this model are given in Chapter 5. The disc brake material used in this analysis is grey cast iron, the properties of which are presented in Chapter 4.

6.2.1 Model setup and boundary conditions

In the 2D axisymmetric model the heat flux was applied directly to the surface of the pad as shown in Figure 6.2, where the top (smaller) block represents the pad and has dimensions 5×16 mm, and the disc is represented by the bottom (larger) block with dimensions 7×52.5 mm. Symmetry conditions were specified so that only one pad and half the disc needed to be included in the model.

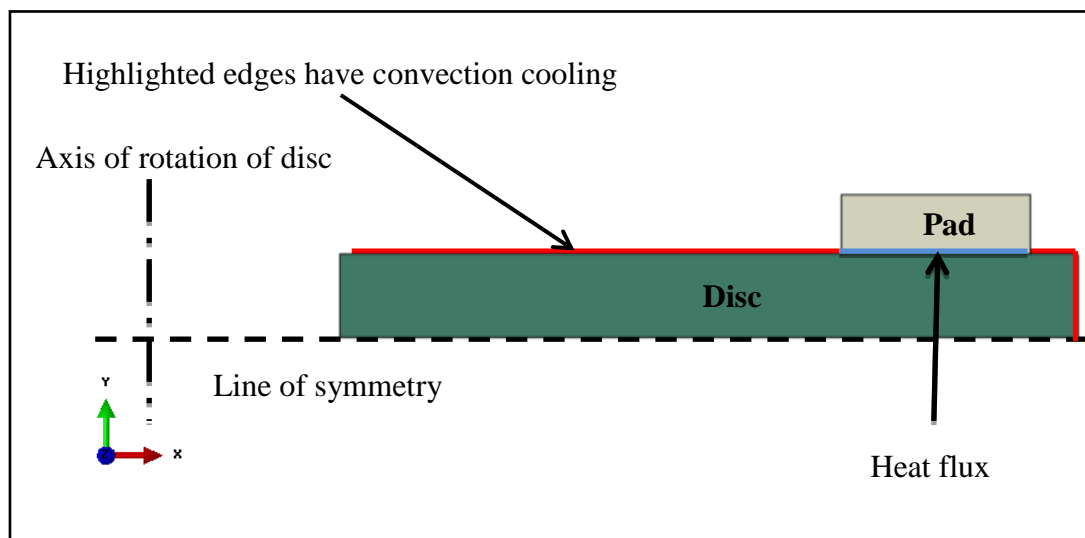


Figure 6.2: 2D axisymmetric thermal model setup and conditions.

Uniform heat flux at the rubbing surface was applied in the 2D model. Convective heat transfer was considered in the 2D model as shown in Figure 6.2. DC2D four node linear heat transfer quadrilateral element were selected from the Abaqus library [112]. The contact interface interaction between the disc and pad was defined as a surface to

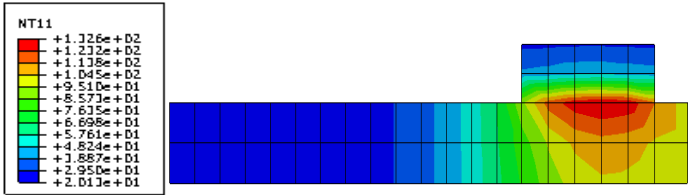
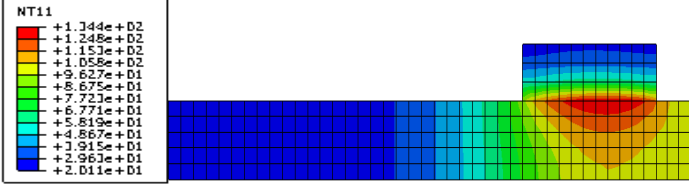
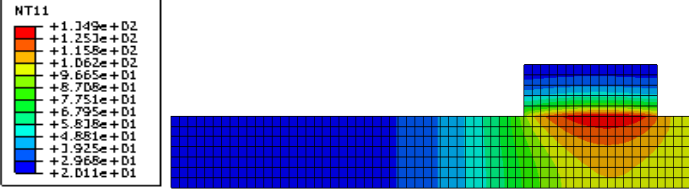
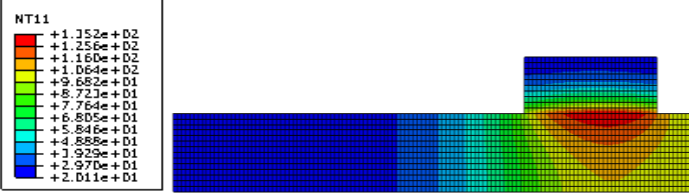

surface contact. Abaqus software defines the thermal conductance between the surfaces as a function of the gap and the clearance value for zero thermal conductance must be specified [112]. In this model it was assumed that there is no gap between the surfaces and both the pad and disc are always in full contact which means that the very high thermal conductance used in this analysis was applicable for zero clearance (no gap) between the surfaces ($1 \times 10^{15} \text{ W/m}^2\text{K}$).

6.2.2 Mesh sensitivity analysis

A mesh sensitivity analysis was carried out using a constant heat flux in order to find the minimum number of elements in the 2D model. A heat flux of $5 \times 10^5 \text{ W/m}^2$ over the pad/disc interface was used to investigate mesh sensitivity. An average convective heat transfer coefficient of $30 \text{ W/m}^2\text{K}$ was applied to all free surfaces of the model and the component initial temperature was set to 20°C . The simulation time for the analysis was 10 s and the incremental time step for all 2D models was set to 0.01 s. The maximum temperature at mean rubbing radius was monitored for different element sizes and the results are shown in Table 6.1.

The results show that the global element size has a small effect on the temperature distribution, especially below 0.5 mm. On the other hand, there is a trade-off between the number of elements (element size) and the simulation time, an element size of 0.5 mm was chosen for all the subsequent 2D axisymmetric simulations. Although a smaller element size would slightly more accurate results, it would take much longer to complete the analysis.

Table 6.1: 2D axisymmetric model mesh sensitivity analysis.

Global Element size [mm]	Maximum Temperature at mean rubbing radius [°C]	Temperature distribution at the end of the simulation [°C]	No. of Elements (CPU time)
3	132.6		56 (27.4 s)
1.5	134.4		255 (42.8 s)
1	134.9		531 (63 s)
0.5	135.2		2103 (178.3 s)
0.1	135.3		51911 (3725.4 s)

6.3 Three dimensional coupled temperature model for small scale discs

In this section, a 3D coupled temperature model that replicates the small scale test rig is investigated in detail. The model setup, boundary conditions and simulation steps are all presented. The small scale disc brake geometry and boundary conditions used in this model are obtained from Chapter 5. The disc brake material used in this analysis is grey cast iron, the properties of which are presented in Chapter 4.

6.3.1 Model setup

The 3D FE model was setup to replicate a drag brake application. This model is a coupled temperature model which considers only the heat transfer between the pad and disc. In this model the pad was kept stationary in space whilst the disc was allowed to rotate. The FE model was composed of a disc and pad, as shown in Figure 6.3. Due to symmetry, only one pad and half the disc thickness were included in the model. To avoid complexity, the caliper and back plate were not considered in this model.

In order to replicate the experimental conditions, forced cooling was applied to the free surfaces as shown in Figure 6.4. The disc was treated adiabatic so no heat transfer was allowed. The surrounding air temperature was assumed constant at 20°C based on the lab ambient temperature. The convective cooling coefficient on the disc rubbing surface was calculated in accordance with empirical equations 4.3, which were based on the rotor dimension, air properties and rotating speed of rotor [103].

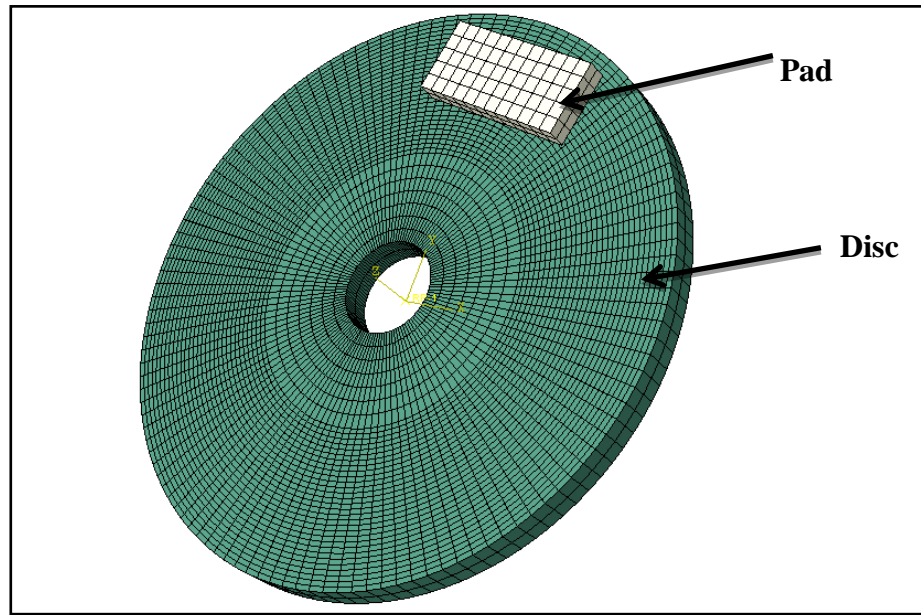


Figure 6.3: 3D FE model assembly.

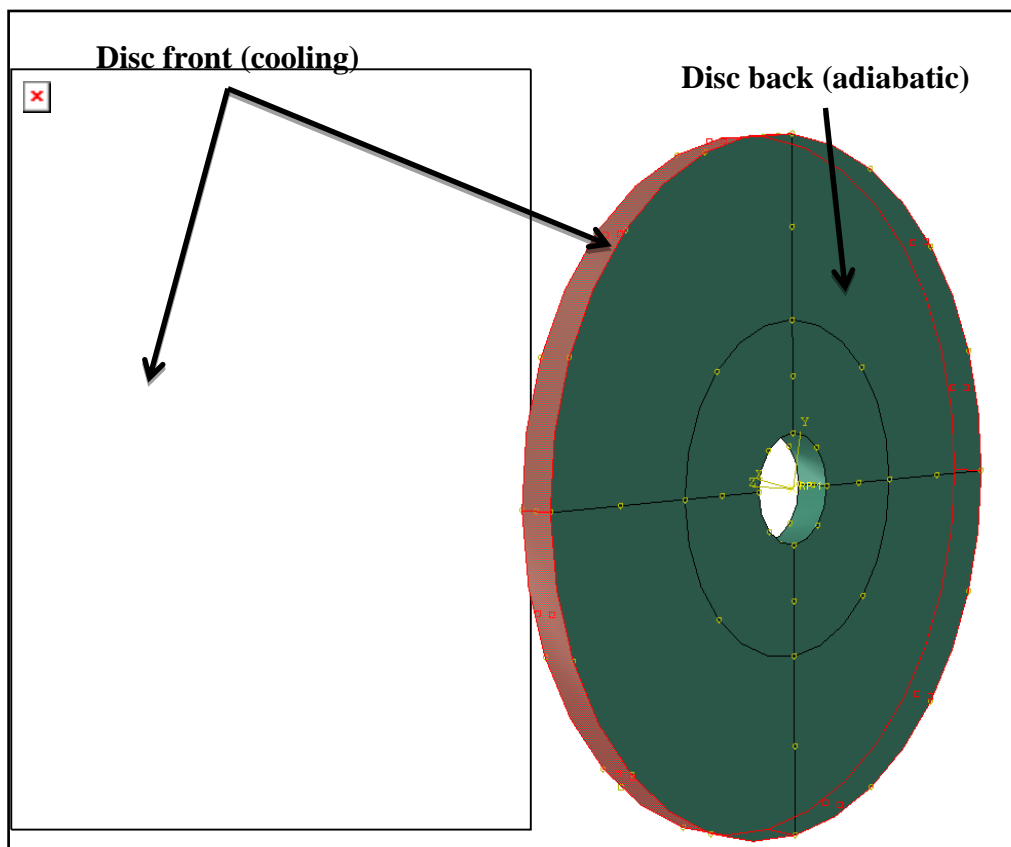


Figure 6.4: Thermal boundary conditions.

In the 3D FE model there are two steps, the initial step and the braking step. The initial step is when the pad is pressed against the disc and the braking step is when the disc rotates. The disc inner radius was coupled with a reference point in order to apply the boundary conditions to the solid disc. The rotational and translational boundary conditions involved in replicating a drag brake application were as follows;

i. Initial step

In this step the pad is pressed against the disc, ensuring that there is full contact between the two. This step activates the heat transfer between the pad and disc. In order to simulate this step all the displacement boundary conditions were constrained for both the disc and pad, except the Z direction displacement for the pad which was unconstrained as indicated in Figure 6.5.

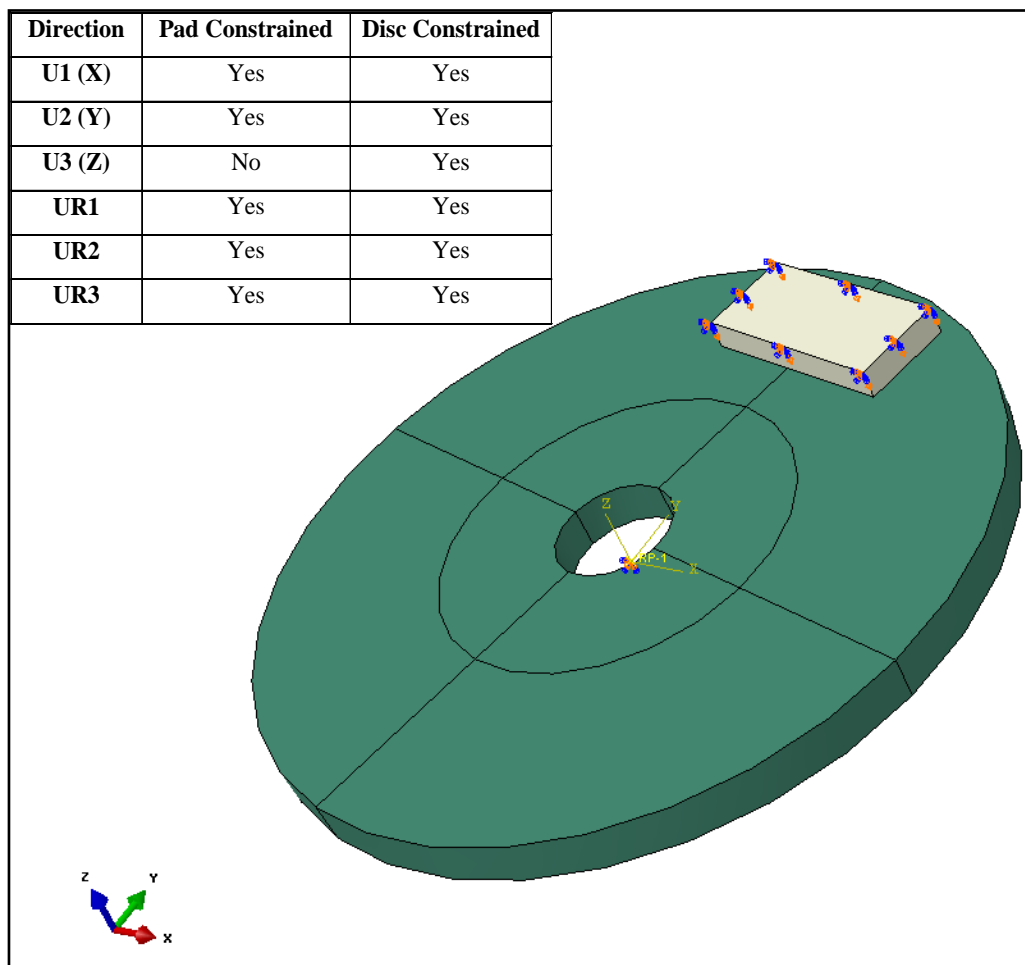


Figure 6.5: Disc and pad boundary condition before braking.

ii. Braking step

As explained above, in this step the disc rotates against the pad in order to simulate drag braking. The translational and rotational boundary conditions for the disc and pad were constrained in all directions except UR3 (rotation around z) for the disc, as indicated in Figure 6.6. In this step the disc will rotate against the pad and the heat will transfer between the disc and pad depending on the thermal resistance between the elements. The overall view of the 3D model steps is shown in Figure 6.7

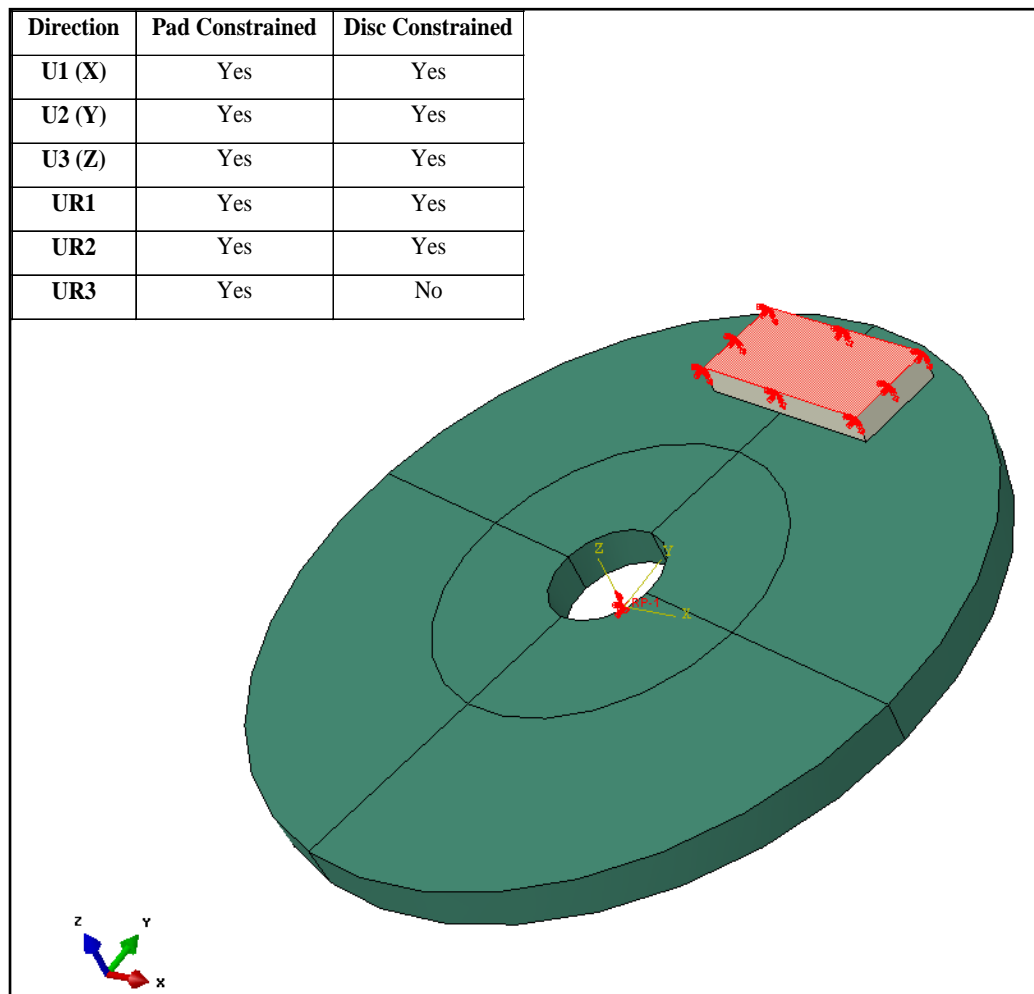


Figure 6.6: Disc and pad boundary conditions during braking.

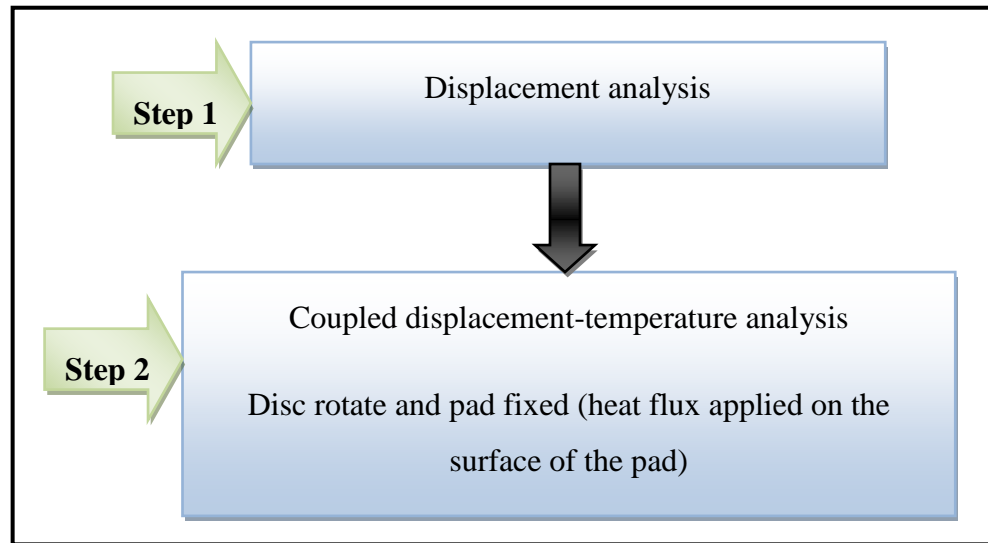
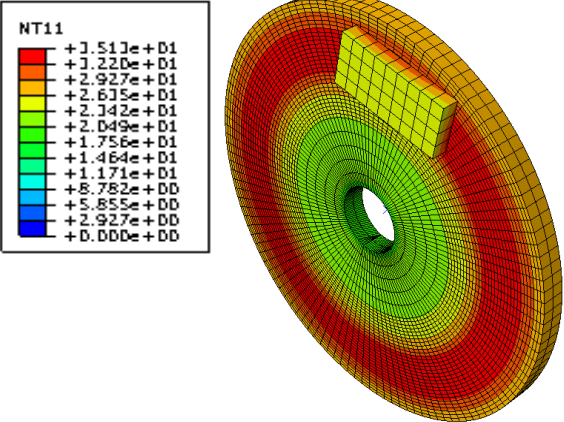
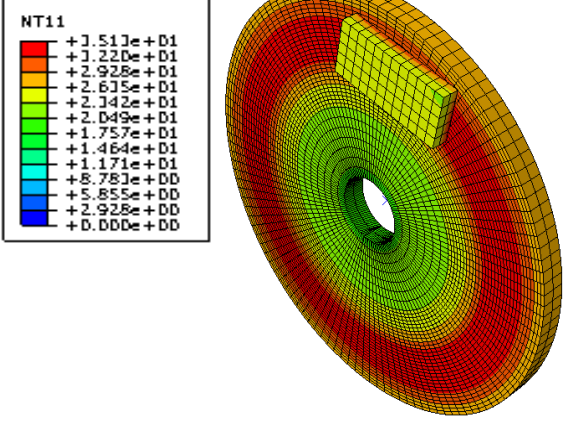
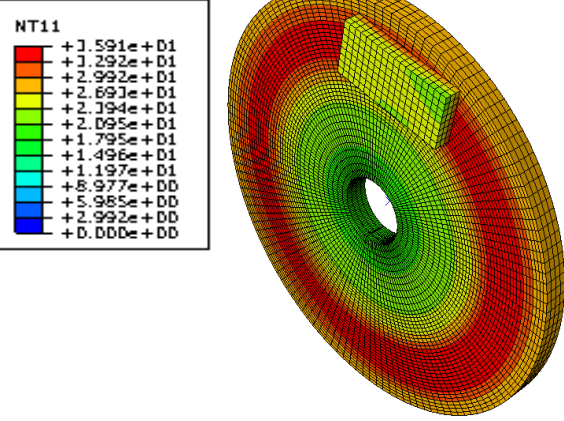


Figure 6.7: 3D model steps overview.

6.3.2 Mesh sensitivity analysis

A constant heat flux was used to find the minimum number of elements in the coupled 3D model which would provide a stable temperature. A heat flux of $5 \times 10^5 \text{ W/m}^2$ was applied to the surface of the pad. An average convective heat transfer coefficient of $30 \text{ W/m}^2\text{K}$ was considered and applied at the surface and circumference of the disc as for the 2D model, and the model initial temperature was set to 20°C . In this analysis the disc was rotated at a constant speed of 6 revolutions per second (drag brake, vehicle speed 20 km/h). The simulation time for the mesh sensitivity analysis was 10 s. The maximum temperature at the mean rubbing radius was monitored for different element sizes and the results are shown in Table 6.2.

Table 6.2: Coupled 3D model mesh sensitivity analysis.

Global Element size [mm]	Maximum Temperature at mean rubbing radius [°C]	Temperature distribution at the end of the simulation [°C]	No. of Element (CPU time s)
4	35.13		8651 (129654 s)
3	35.13		9315 (132506 s)
2	35.91		22449 (297682 s)

The results show that the element size has only a small effect on the temperature distribution. On the other hand, there is a trade-off between the number of elements (element size) and the simulation time. Although a smaller element size will give better results, it will take longer to simulate. In order to compare the 2D axisymmetric model and the 3D model, a 2 mm element size was chosen for the 3D model to provide accurate estimation of surface temperatures.

6.4 Comparison between the finite element models

In the current research, three different models were developed, namely the 1D thermal model (Chapter 4), the 2D axisymmetric thermal model, and the 3D coupled temperature model. These were investigated in detail and the temperature distributions through the disc for each model were examined. It was noticed that there was a trade-off between the CPU running time and the element size for each model, and also between the CPU time and the model complexity. One of the objectives of the current research is to validate the numerical results by comparison with the experimental results with a view to using thermal modelling to investigate different braking scenario which are hard to implement in the lab. In this section the thermal performance of the different models (1D, 2D and 3D) is investigated in order to identify the one which achieves the closest fit to experiment. This will then be used to further investigate the alternative lightweight brake disc rotors.

A constant heat flux (drag brake) was used to investigate the thermal performance of different disc brake models. In the current analysis the disc brake material is grey cast iron, the properties of which are presented in Chapter 4, the vehicle speed is 40 km/h and the brake torque is 80 Nm. An average heat transfer convection coefficient of $30 \text{ W/m}^2\text{K}$ was considered and applied to the surface and circumference of the disc, as shown earlier, and the component initial temperature was set to 20°C . The simulation time for the current analysis was 4 s and the time step 0.001 s. The disc maximum surface temperature at the mean rubbing radius predicted for the three different models are shown in Figure 6.8.

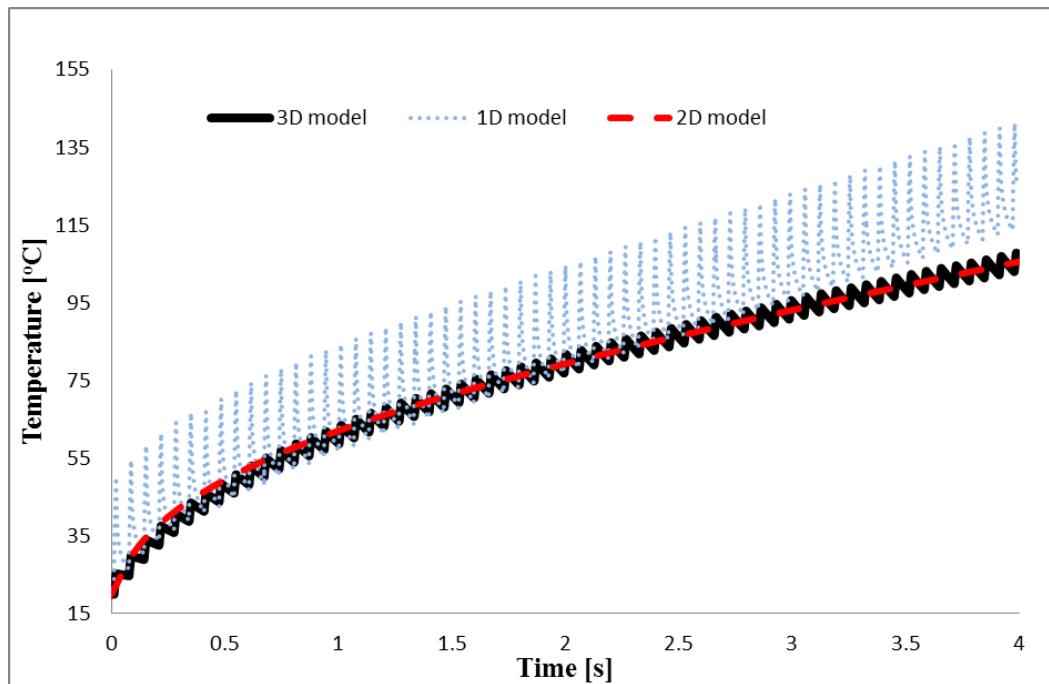


Figure 6.8: Surface temperature at mean rubbing radius for different disc brake models.

It can be seen that the three responses have the same trends but different magnitudes; the mean temperatures for the 2D and 3D models are very close. On the other hand, the mean temperature rise for the 1D model is higher than for the 2D and 3D models. The temperature trend was expected because in the 1D model the thermal mass is lower than that in the 2D and 3D models. In addition, the CPU time was monitored for the three models, as shown in Table 6.3 . It was found that there is a huge difference between the 1D, 2D and 3D models with respect to the CPU time. Although there is only a small difference in the temperature magnitude between the 2D and 3D models, there is a big difference in the computational time. The 2D axisymmetric model was therefore chosen for further use with the experimental validation and the lightweight disc brake analysis.

Table 6.3: CPU time for different thermal models.

Model	1D	2D	3D
CPU Time (hh:mm:ss)	00:30:20	02:52:33	65:21:05

6.5 Two dimensional axisymmetric model for full scale disc

Based on the above competitive study, a two dimensional axisymmetric transient heat transfer model for the full scale disc brake was developed in Abaqus in order to validate the scaling methodology experimentally and numerically. The disc brake geometry and dimensions are presented in Chapter 5. The same boundary conditions and techniques used in section 6.2 were applied in this model except that the heat flux was directly applied to both rubbing surfaces of the disc since symmetry conditions no longer can be applied due to the “top-hat” structure of the full size disc. Figure 6.9 shows the model setup and conditions.

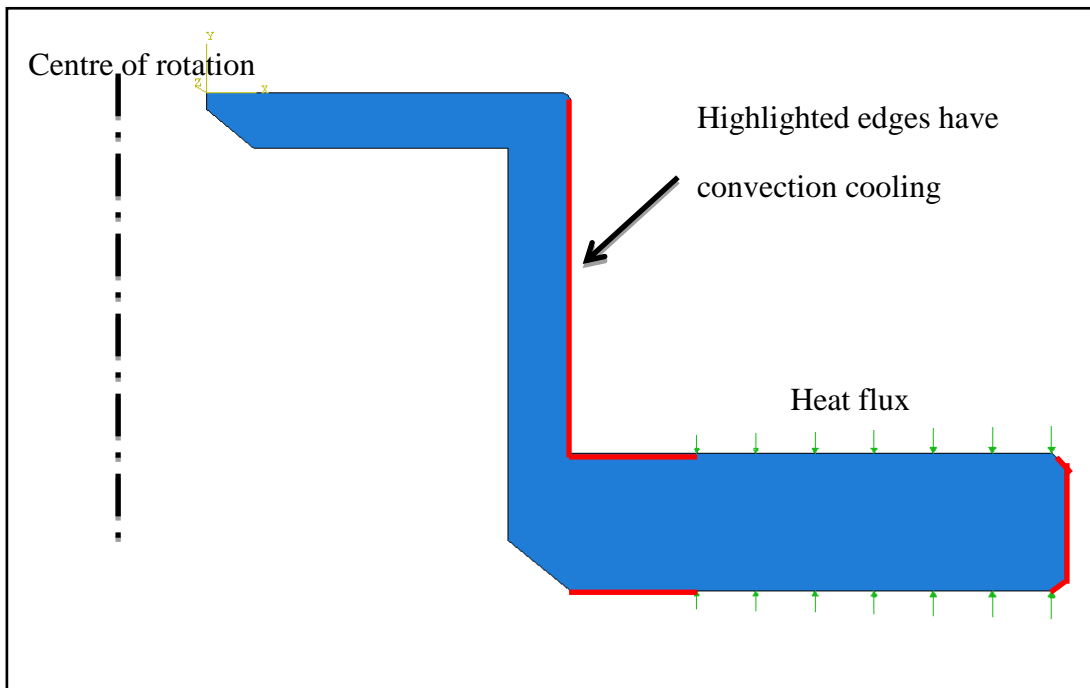


Figure 6.9: 2D axisymmetric thermal model setup and conditions for full scale disc.

In addition, the mesh sensitivity analysis was carried out for the current model and it was found that an element size of 1 mm gave very good results. Also the computational time was within the desired limits. This model will be used in the next Chapter to validate the experimental results and also to carry out a numerical comparison between the full and small scale disc brakes.

6.6 Two dimensional axisymmetric model for a small scale disc with coating

The two dimensional model developed in section 6.2 is valid for a small scale disc without coating. In the current research, a coated lightweight disc brake is investigated, and a finite element thermal model was developed for the coated small scale disc based on the 2D axisymmetric model described in section 6.2. The heat flux was applied directly to the rubbing surface of the coated disc based on the estimated heat partition ratio. The 2D model setup and boundary conditions are shown in Figure 6.10. The coating thickness and material properties were as given in Chapters 4 and 5.

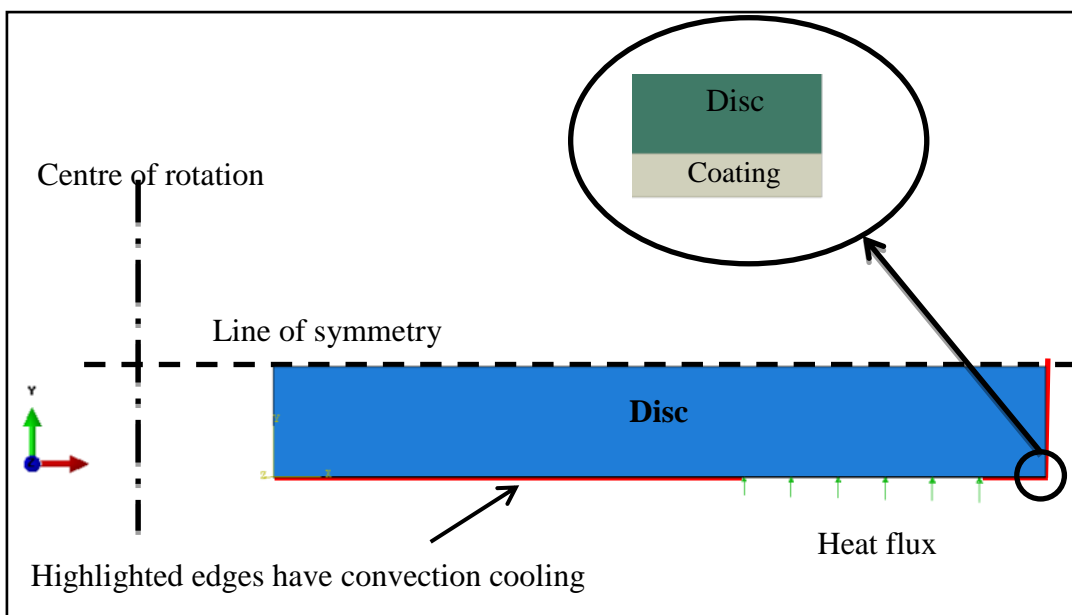


Figure 6.10: 2D axisymmetric thermal model setup and conditions for a coated small scale disc.

A mesh sensitivity analysis was carried out and it was found that in order to achieve good temperature distribution a very fine mesh is required. The element size in the current model is 50 μm which is equal to the coating thickness.

6.7 Summary

The 2D and 3D finite element models developed for the small and full scale discs have been presented in this Chapter. The model boundary conditions and setup were explained in detail; also a mesh sensitivity analysis for each model was carried out in order to simulate the thermal performance of the disc brake. The surface temperatures

predicted by three different disc brake models (1D, 2D and 3D) were investigated. It was found that the computational time for the 3D model is much higher than that of the 1D and 2D models. Furthermore, the average surface temperature of the 2D model is very close to the surface temperature of the 3D model which makes the 2D axisymmetric model the best candidate for further numerical analysis of the small and full scale disc brakes. A 2D axisymmetric model for the full scale disc was then developed to validate the scaling methodology numerically. Finally, a 2D axisymmetric model for the coated lightweight disc brake was developed based on the coating layer study reported in Chapter 4.

CHAPTER 7:

EXPERIMENTAL AND NUMERICAL RESULTS

7.1 Introduction

In this Chapter, the experimental and numerical analysis used to validate the scaling methodology and to evaluate the thermal performance of the different solid disc brake rotors, is explained. The experimental test matrix which was utilized in this Chapter was developed based on the SAE J2521 and SAE J212 standards. Two test rigs were used in the current research. The first was a small scale dynamometer and the second a full scale dynamometer. The two rigs were used for the thermal performance evaluation and the scaling methodology validation. The main purposes of the testing are to investigate the coated and uncoated solid disc brake rotors in terms of surface temperature distribution and also to validate the numerical models with the experimental results in order to investigate the temperature distribution of the solid disc brake rotor using the FEM.

A general overview of the present Chapter is given in Figure 7.1. The first section includes the main objective of the current Chapter, which was to use the brake dynamometers and the developed test matrix to investigate the thermal performance of lightweight disc brake rotors. The second objective was to validate the scaling methodology proposed in Chapter 5. The main objectives are satisfied by using the University of Leeds test rigs, including set-up, calibration and commissioning. The experimental results for the various applications were obtained and used to validate the numerical model developed in Chapter 6. Numerical analysis of the scaling methodology issues is explained in detail in the numerical analysis sections.

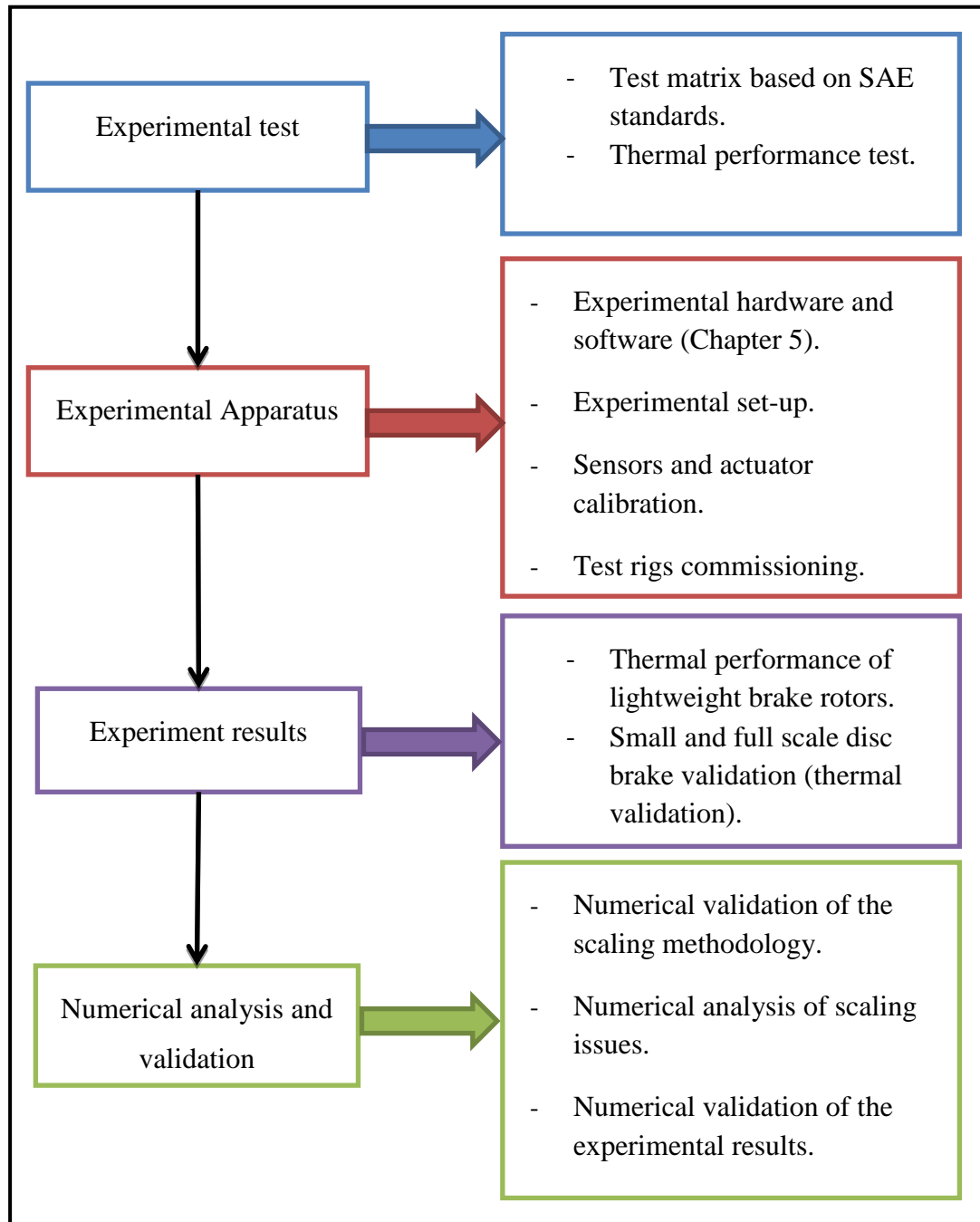


Figure 7.1: Overview of experimental work using brake dynamometer.

7.2 Test matrix development

In order to evaluate the thermal performance of lightweight disc brake rotors, an appropriate test matrix should be developed. In the current research, the test matrix shown in Table 7.1 was derived from the Society of Automotive Engineering (SAE) standards. It is based on SAE J2521 and SAE J212 [124, 125], although there is a big difference between the number of stops in the current test matrix and the SAE standards for the following reasons:

- The main aim of this research is to assess the brake rotor material not the friction pair.
- The initial temperature for most of the tests was 100°C, and this was achieved by applying hundreds of braking pulses in order to reach the desired start temperature.
- The coefficient of friction was monitored for all the tests and showed good consistency which gave the researchers confidence that this test matrix was appropriate even though the number of stops was far lower than in SAE J212.

Table 7.1: Test matrix for all brake rotors.

No.	Test Name	No. Stops	Simulation time for each stop	Rotational speed (rpm)	Brake pressure (bar)	Initial Temp. °C	Rig used
1	No - pressure	--	--	900	--	20	Small Scale rig
2	Pre-burnish check	10	Braking time	900	2.5	20	Small Scale rig
3	First (pre-burnish) effectiveness check	5	Braking time	900 & 1500	1.2	100	Small Scale rig
		5	Braking time	900 & 1500	2.5	100	Small Scale rig
		5	Braking time	900 & 1500	3.8	100	Small Scale rig
		5	Braking time	900 & 1500	5	100	Small Scale rig
		5	Braking time	900 & 1500	6.1	100	Small Scale rig
		5	Braking time	900 & 1500	7.3	100	Small Scale rig
4	Burnish	25	Braking time	1300	3	100	Small Scale rig
5	High speed stop test	10	Braking time	1850	6.4	100	Small Scale rig
6	Drag brake (low)	--	1 hour	900	Variable	Room temp	Small Scale rig
7	Drag brake (moderate)	--	1 hour	1500	Variable	Room temp	Small Scale rig
8	Drag brake (high)	--	1 hour	1850	Variable	Room temp	Small Scale rig
9	Drag brake (high)	--	Variable	620	Constant up to 3	Room temp	Full scale rig

7.3 Experimental and numerical results

In this section the experimental and numerical results for different small scale disc brake materials are presented and analysed in detail in order to characterise the thermal performance of the trial lightweight discs. In addition, the full scale Fiat Punto disc was investigated numerically and experimentally in order to validate the developed scaling methodology. The coefficient of friction for the different discs was monitored and evaluated during the braking tests for the full and small scale disc brake rotors. The experimental results for full and small scale disc brake rotors were validated using the 2D axisymmetric model from Chapter 6.

7.3.1 Characteristics of thermal results for small scale discs

The small and full scale brake dynamometers were used to complete the test matrix shown in Table 7.1 for the five small scale brake rotors. The results showed that the aluminium alloy (6082 –T6) disc could not withstand the braking conditions specified in Table 7.1 and scratches started to appear on the rubbing surface at relatively low temperatures (around 200°C), as shown in Figure 7.2. This is because, during a friction process, there are many small asperities that create localised areas of high pressure, and at these microscopically small locations the temperature becomes very high. This temperature can exceed the melting point of the Al-alloy, which means that the disc will melt at these spots thereby creating a rough disc surface. These peaks on the rough disc surface can then lead to further localised melting of the disc material which eventually results in complete disruption of the disc surface.

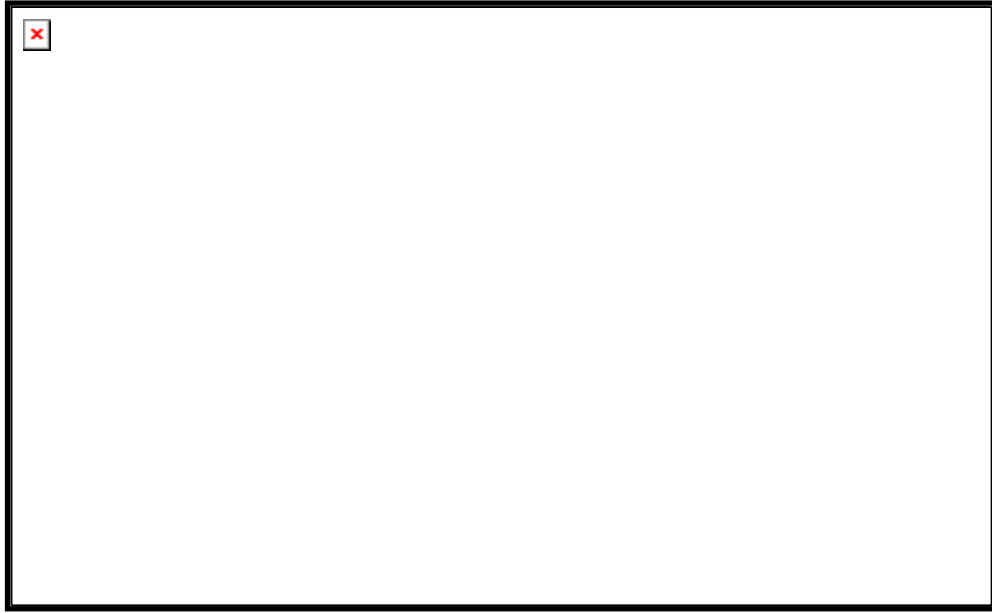


Figure 7.2: Uncoated aluminium alloy rotor after test showing degraded rubbing surface.

The uncoated aluminium MMC disc showed more resilience than the uncoated aluminium wrought alloy. However, scratches did start to appear on the rubbing surface albeit at a higher temperature (around 300-350⁰C) than for the aluminium alloy. The detailed temperature responses for the plain Al-MMC disc are shown in Figure 7.3. The friction performance of the Al-MMC disc is discussed in the next section.

The coated Al-alloy and the coated Al-MMC showed better thermal performance than the uncoated discs and lasted throughout the test matrix without any signs of surface disruption. The detailed temperature responses for the coated Al-MMC disc and coated Al-alloy disc are shown in Figure 7.4 and Figure 7.5 respectively, together with images of the rotor before and after testing where no damage can be seen. In addition, as a benchmark, the temperature responses of the grey cast iron are shown in Figure 7.6.

The coated wrought aluminium alloy disc brake rotor was further investigated using the high speed thermal imaging system in order to assess the thermal performance across the rotor surface as shown in Figure 7.7 for test 7. The thermal images show a similar surface temperature to the sliding thermocouples with emissivity equal to 0.95 which builds confidence in the thermocouple readings. The rubbing surface shows a uniform temperature distribution across the radial direction which demonstrates that the brake

pad was fully bedded in against the rubbing surface of the disc brake rotor. This gives confidence in the use of the proposed test matrix in the current study.

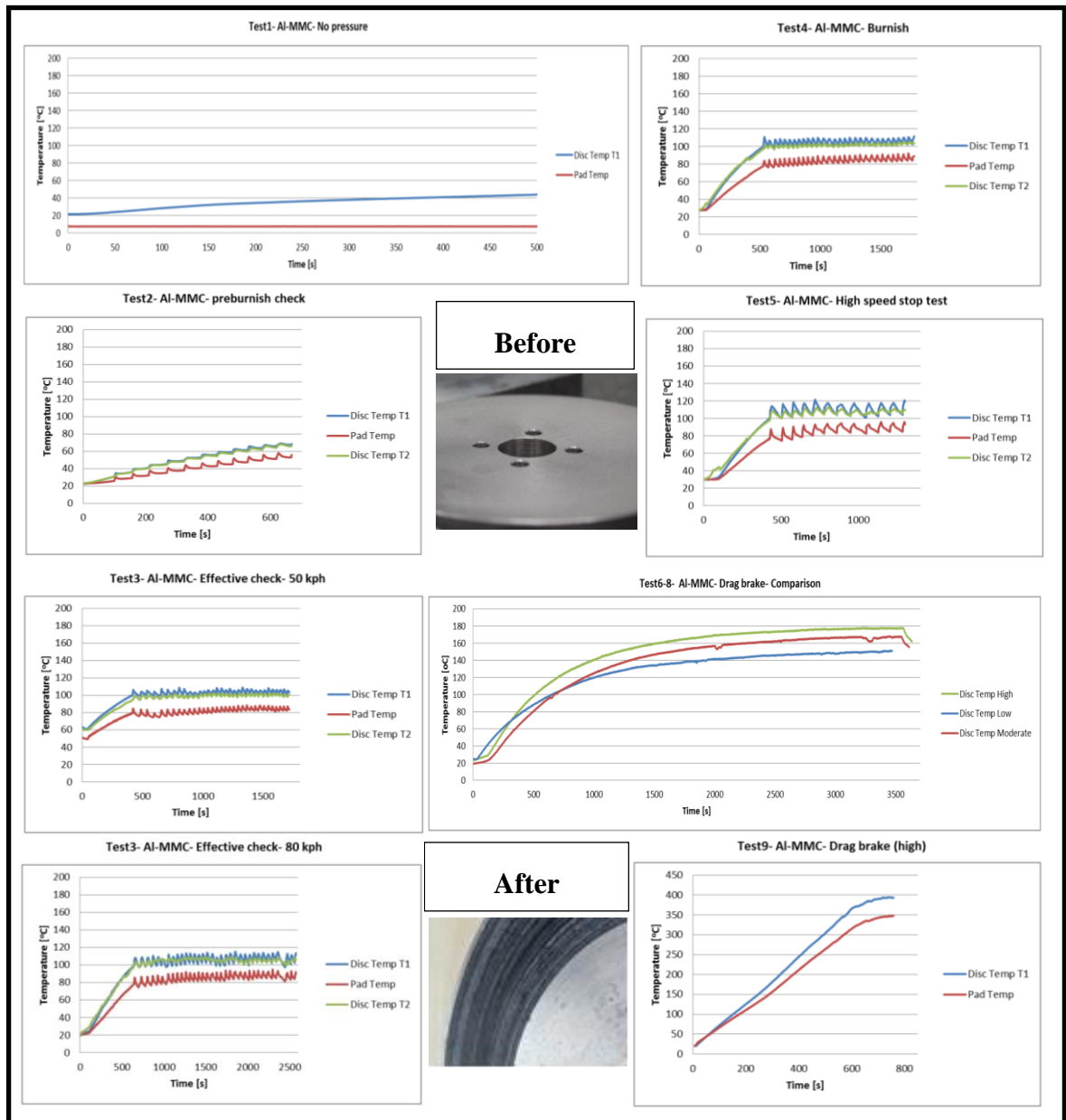


Figure 7.3: Temperature responses of the aluminium MMC disc.

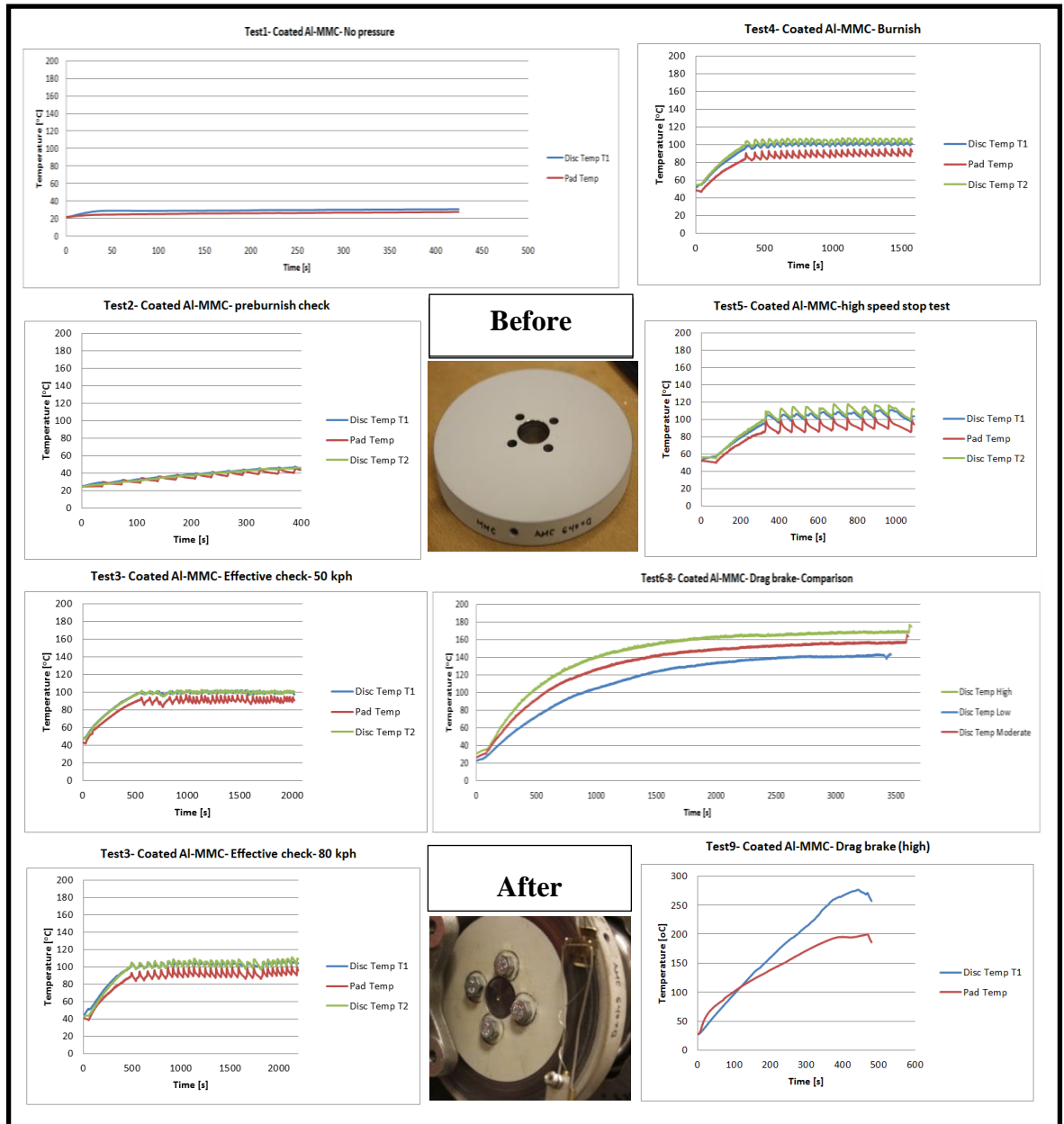


Figure 7.4: Temperature responses of the coated aluminium MMC disc.

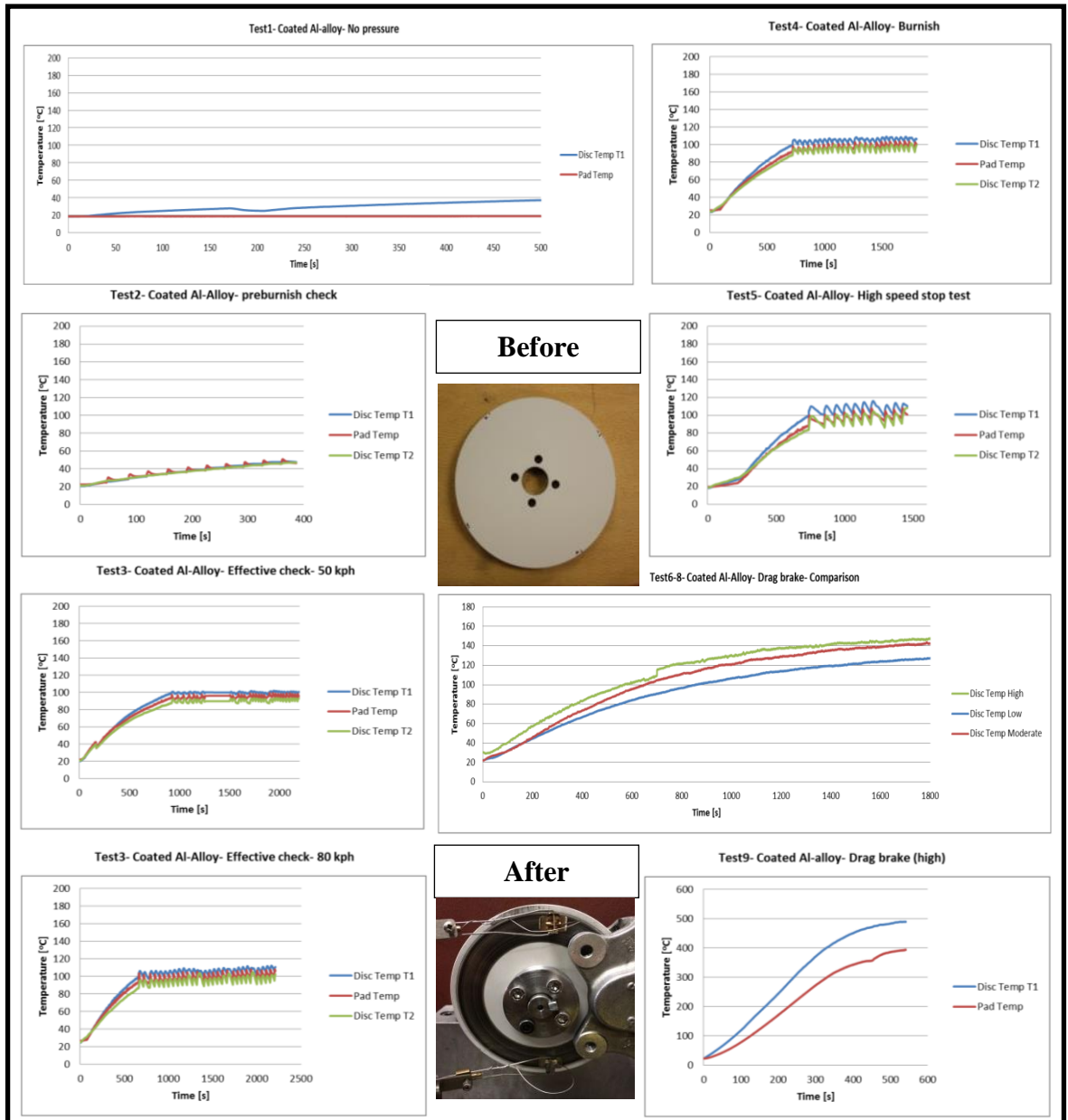


Figure 7.5: Temperature responses of the coated aluminium alloy disc.

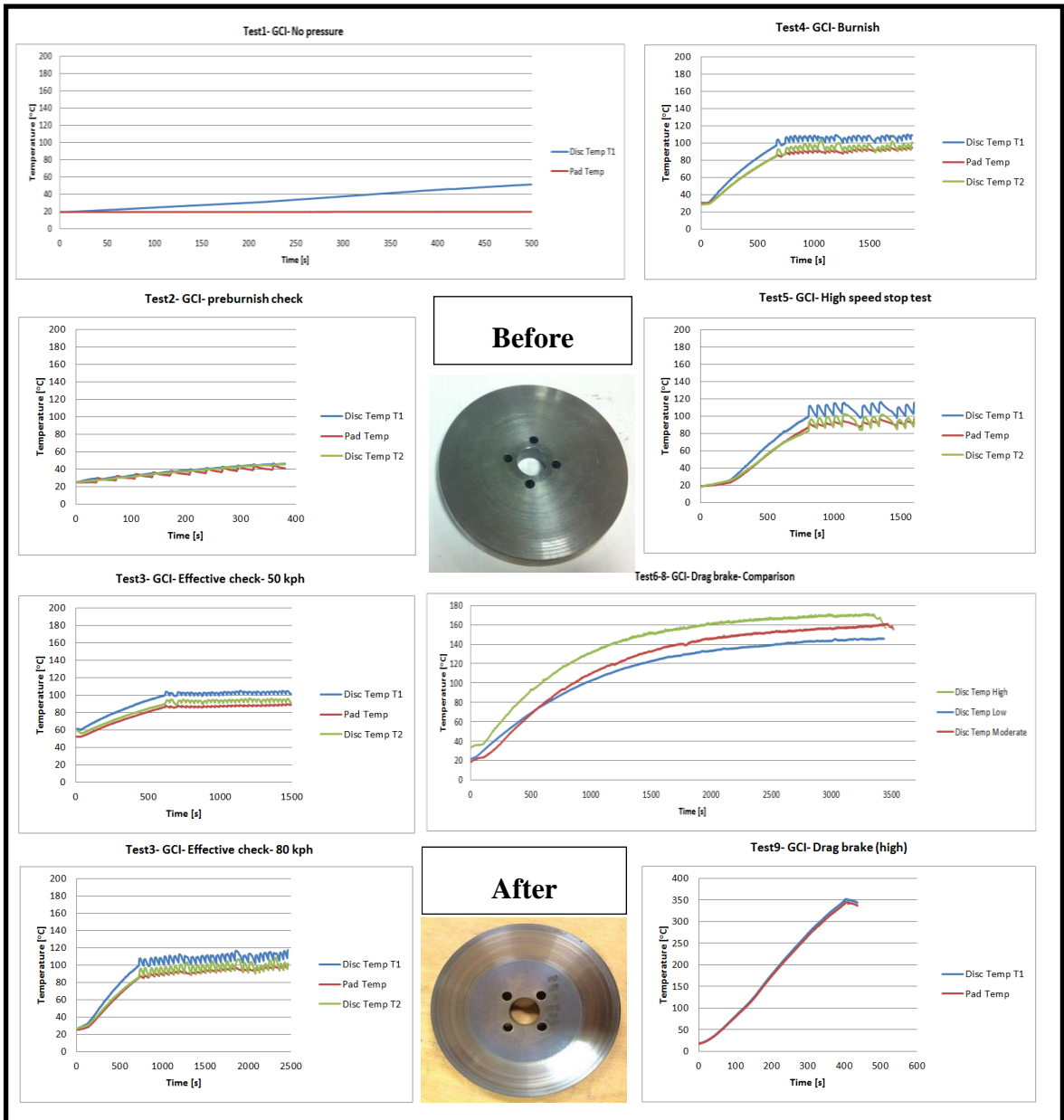


Figure 7.6: Temperature responses of the GCI disc.

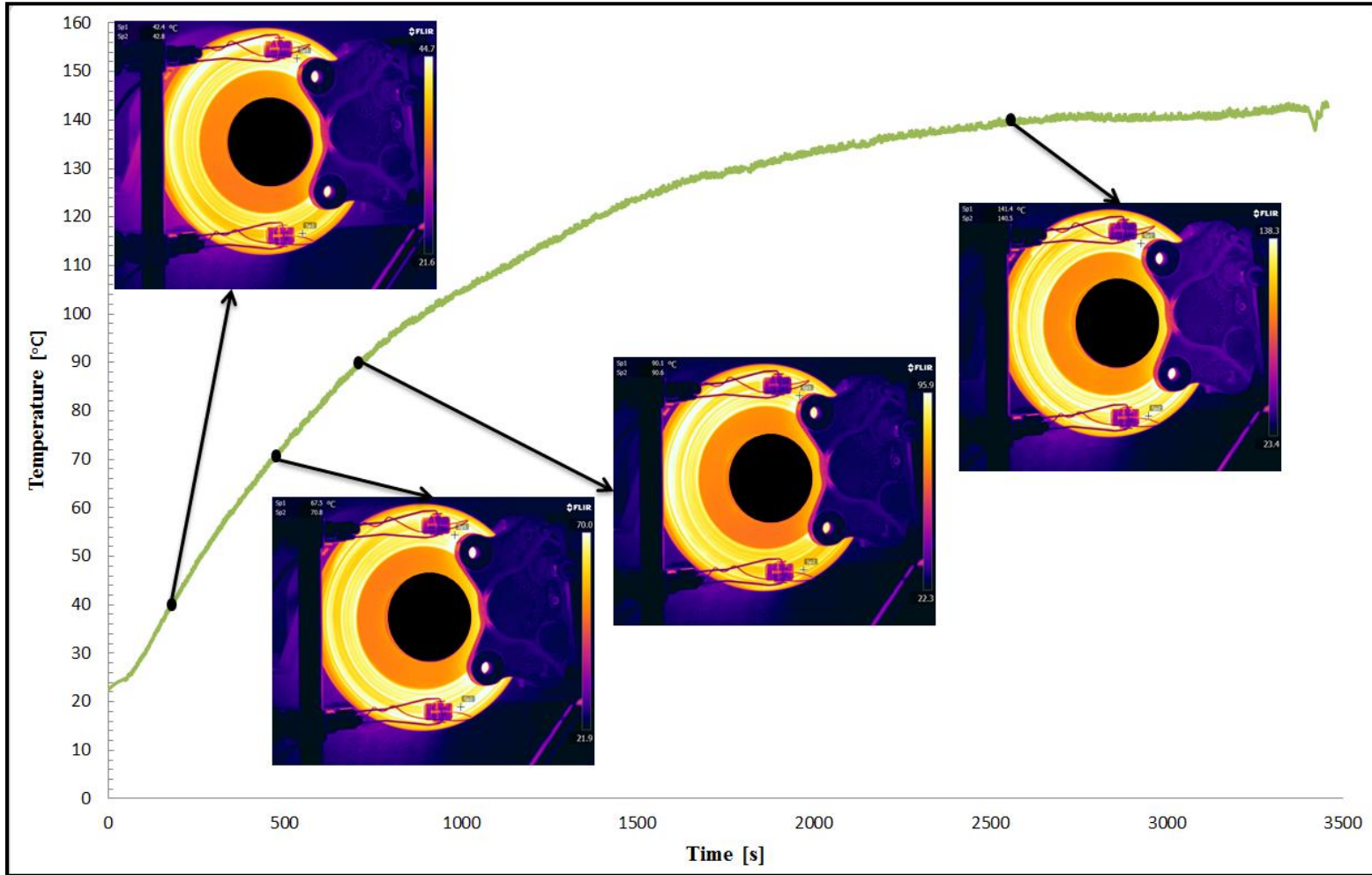


Figure 7.7: Temperature response of the coated aluminium alloy disc, Test 7.

The high speed thermal imaging system was used to compare the surface temperature obtained from the sliding thermocouples for a constant g stop. Figure 7.8 shows the surface temperature of the coated wrought aluminium alloy rotor using both sliding thermocouple and high speed imaging system (with emissivity = 0.95) for test 5 (constant g stop) . The results showed that there is a difference in the maximum surface temperature between the sliding thermocouples and the high speed thermal imaging system; the latter is in the order of 20°C than the thermocouple readings. This shows that the response of the sliding thermocouples is slower than that of the imaging system. Furthermore, the same comparison was carried out for a drag braking event as shown in Figure 7.9, which represents the surface temperature of the grey cast iron rotor test 9. The results show that the temperature obtained from the sliding thermocouple in the drag braking event is very similar to that measured by the high speed imaging system. This is because the drag braking event does not need a fast response measuring system as the temperature change is much slower than for the constant g stop event.

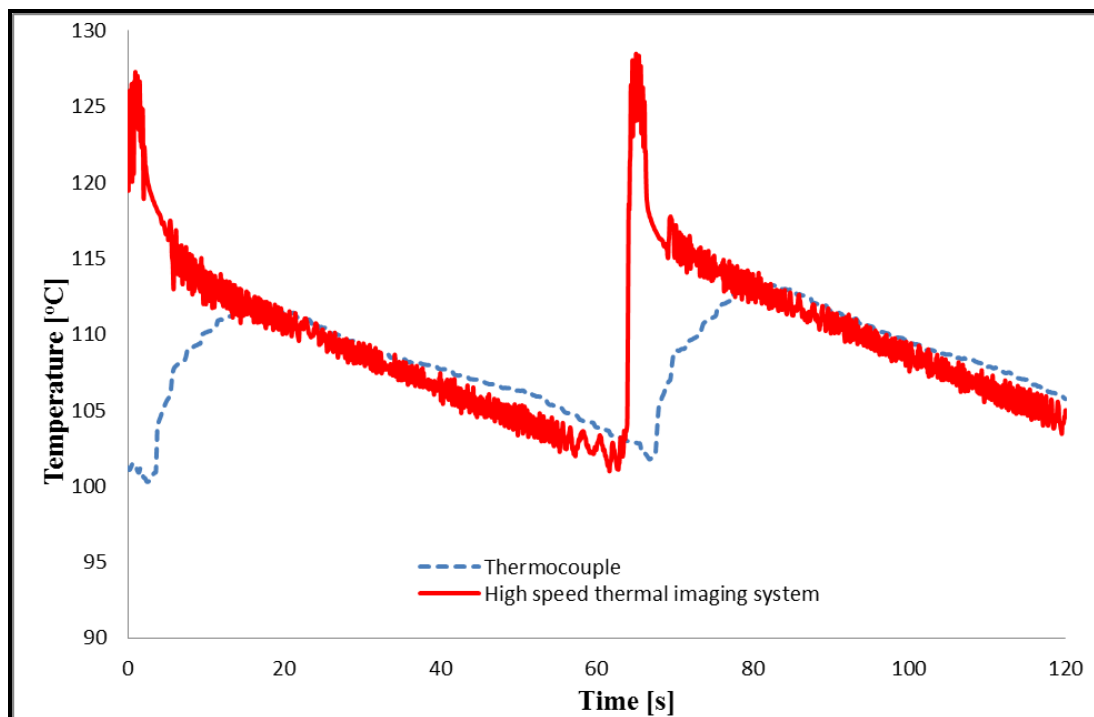


Figure 7.8: Comparison between the sliding thermocouples and high speed thermal imaging system for coated wrought aluminium rotor (test 5).

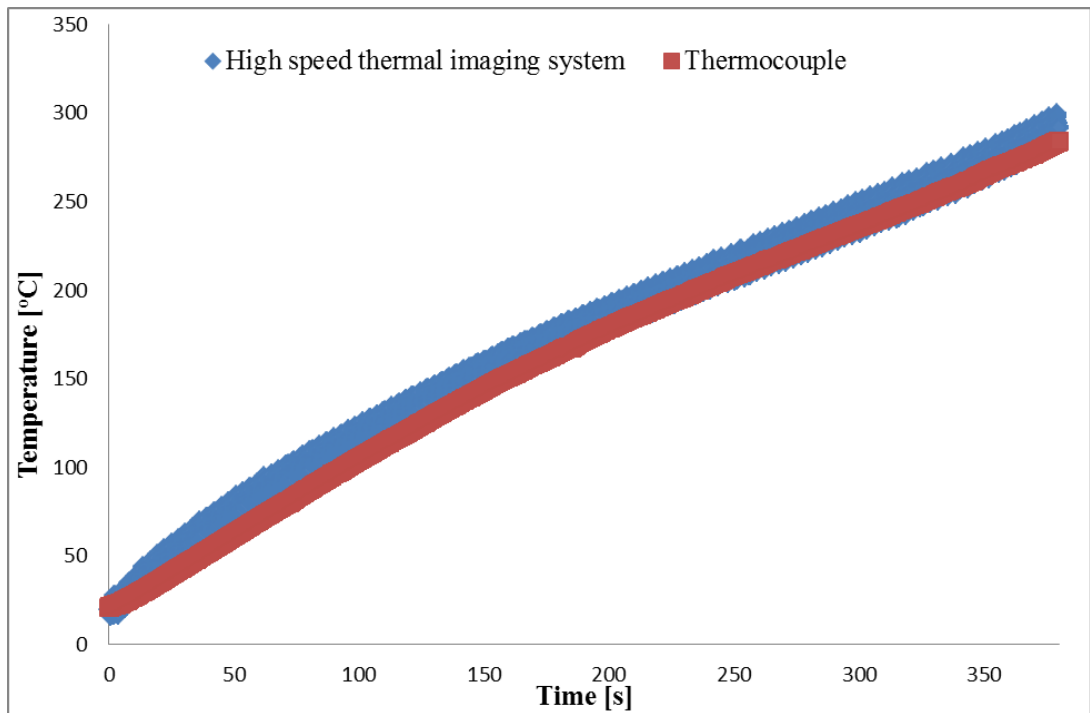


Figure 7.9: Comparison between the sliding thermocouples and high speed thermal imaging system for grey cast iron rotor (test 9).

The disc and pad temperatures measured by the thermocouples for the different lightweight small scale brake rotors are compared against the conventional grey cast iron disc in Figure 7.10 for test 9 as defined in Table 7.1. The results show that the grey cast iron disc has the lowest surface temperature, whilst the coated Al-alloy has the highest surface temperature for the same braking conditions. In fact it was found that the coated discs always had a higher surface temperature than the corresponding uncoated discs which was as expected due to the thermal barrier effect of the coating. Although the coated Al-alloy always had a higher surface temperature than the coated Al-MMC, the friction performance of the coated Al-alloy was much better as discussed in the next section and in Chapter 8. The temperature responses of the brake pads were in the same relative order as the disc surface temperatures with the coated Al rotor achieving the highest temperature at the end of the test.

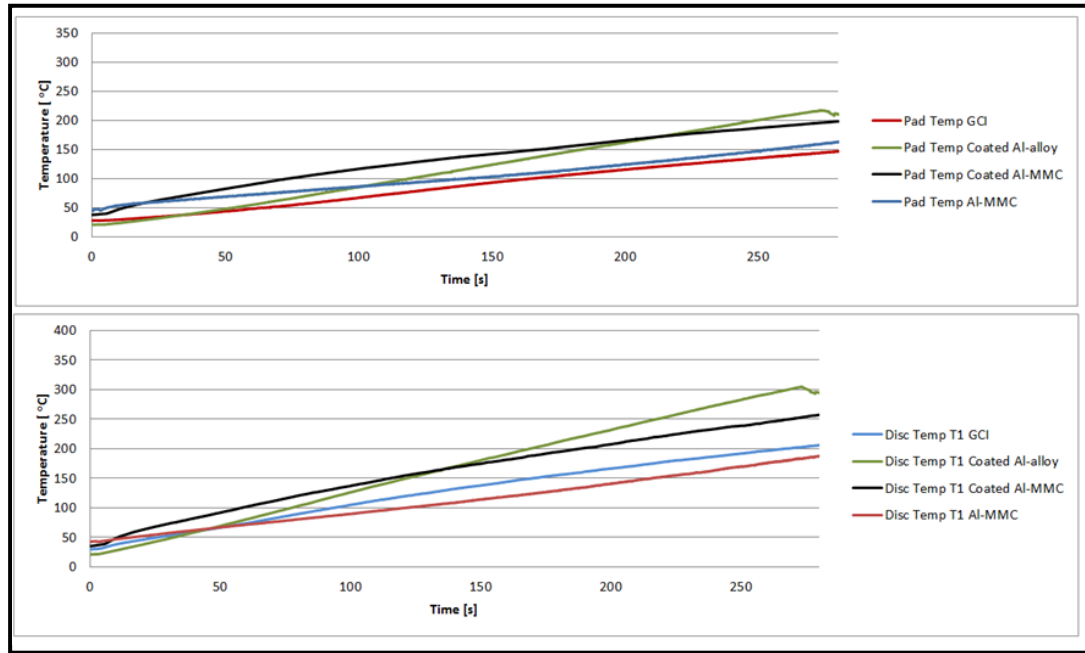


Figure 7.10: Temperature response of different disc brake materials.

The thermal performance of the small scale disc brake rotors manufactured from different materials and both with and without a thin alumina coating was investigated using an axisymmetric transient heat transfer model developed in Abaqus\standard (explained in Chapter 6). The boundary condition and model setup are shown in Figure 6.9. The rotors were meshed using 4-node linear axisymmetric heat transfer quadrilateral elements (DC2D4). A mesh sensitivity analysis was carried out in order to choose the optimum element size, as explained in Chapter 6. The heat flux was applied to the rubbing surface using a Matlab Mscript.

The experimentally obtained data was used to validate the 2D axisymmetric FE model. The heat flux was calculated based on the most extreme braking conditions (drag braking at a vehicle speed of 35 km/h for a vehicle with an average brake torque of 35 Nm, test 9) and applied in the Abaqus model. Two FE models were used; the first without coating and the second with a 30 μm alumina coating. The heat flux was calculated based on the experimental data using equation (7.1):

$$Q = \tau \cdot \omega \quad (7.1)$$

where τ is the measured braking torque and ω is the rig rotational speed (assumed constant). However, only a certain proportion of this heat flux is transferred into the disc, the remainder being transferred to the pad friction material. The proportion of heat transferred to the disc (the partition ratio) can theoretically be calculated from the respective thermal properties of the disc and pad materials using equation (7.2):

$$\gamma = 1 - \frac{1}{1 + \sqrt{\frac{\rho_p c_p k_p}{\rho_d c_d k_d}}} \quad (7.2)$$

From the published properties of the grey cast iron discs and estimated property of the pad materials, Equation (7.2) predicts $\gamma = 0.87$. However this equation takes no account of the transfer layer that can form on both rubbing surfaces and in practice a higher proportion of heat is often found to flow to the disc than suggested by equation (7.2). In the present case good agreement was found between the measured and predicted surface temperatures for a partition ratio of 95% which is similar to the value typically used by other researchers [13, 126]. Similar analysis was carried out for the coated Al-MMC disc to evaluate the partition ratio. It was found that partition ration of 90% give a very good agreement with the experimental results.

Figure 7.11 shows that the numerical and experimental disc surface temperatures for grey cast iron are in very good agreement. The numerical and experimental surface temperatures for the coated Al-MMC small scale disc are shown in Figure 7.12, and again the numerical results show good agreement with the experimental data.

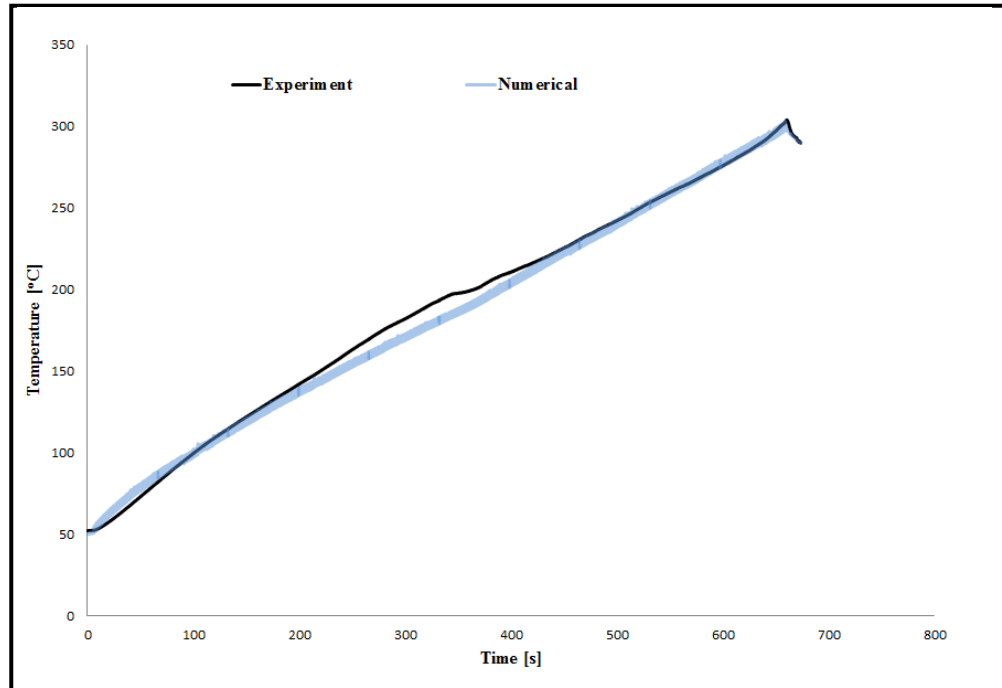


Figure 7.11: Numerical and experimental temperature response for the GCI disc.

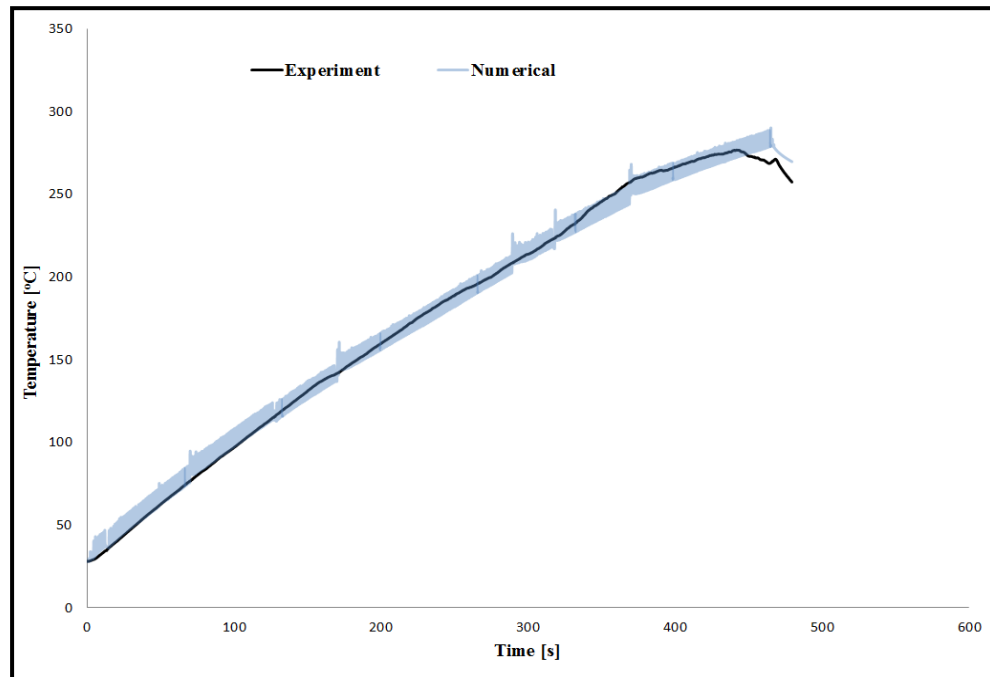


Figure 7.12: Numerical and experimental temperature response for the coated Al-MMC disc.

7.3.2 Full scale disc

The full scale Fiat Punto disc was used to validate the scaling methodology proposed in chapter 5, and the full scale brake dynamometer was used to evaluate the surface temperature of the disc while monitoring the brake torque. A detailed description of the disc brake geometry and the location of the sliding thermocouple is given in Chapter 5. As explained above, the full scale brake dynamometer is capable of performing drag braking only. Braking conditions and parameters from the scaling methodology shown in Chapter 5 (Table 5.4) were utilised. Figure 7.13 shows the temperature response for one of the tests (test 9) which were used to validate the scaling methodology.

The coefficient of friction for the full scale Fiat Punto disc was monitored during the test, Figure 7.14, and the average coefficient of friction was 0.37. As shown in Figure 7.14, the coefficient of friction for the full scale disc was stable during the test but as the surface temperature of the disc increased the coefficient of friction started to decrease, as expected.

In order to evaluate the friction performance of the Fiat Punto disc, the coefficient of friction was monitored at a higher temperature to investigate the fade behaviour of the disc, as shown in Figure 7.15, with the same braking conditions. According to Figure 7.15, the coefficient of friction starts to drop after the surface temperature reaches 300°C; this behaviour is called brake fade. The brake system used in the full scale brake test is a commercial system, so defining the fade behaviour will be very important in order to evaluate the thermal performance of the coated disc and compare the results with the current findings.

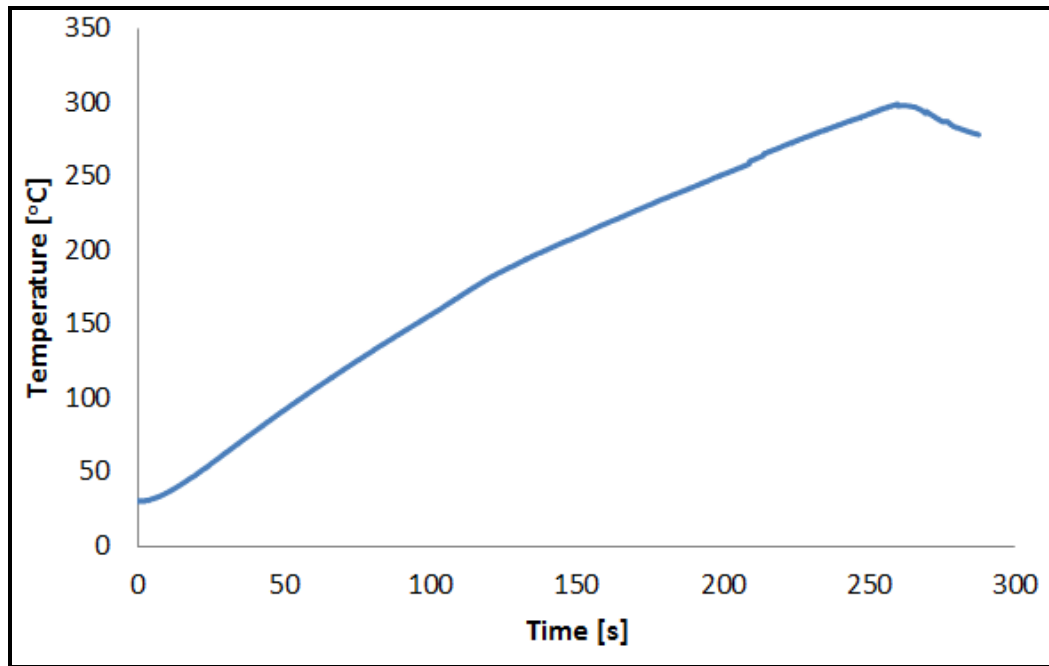


Figure 7.13: Measured disc surface temperature for the full scale disc brake rotor.

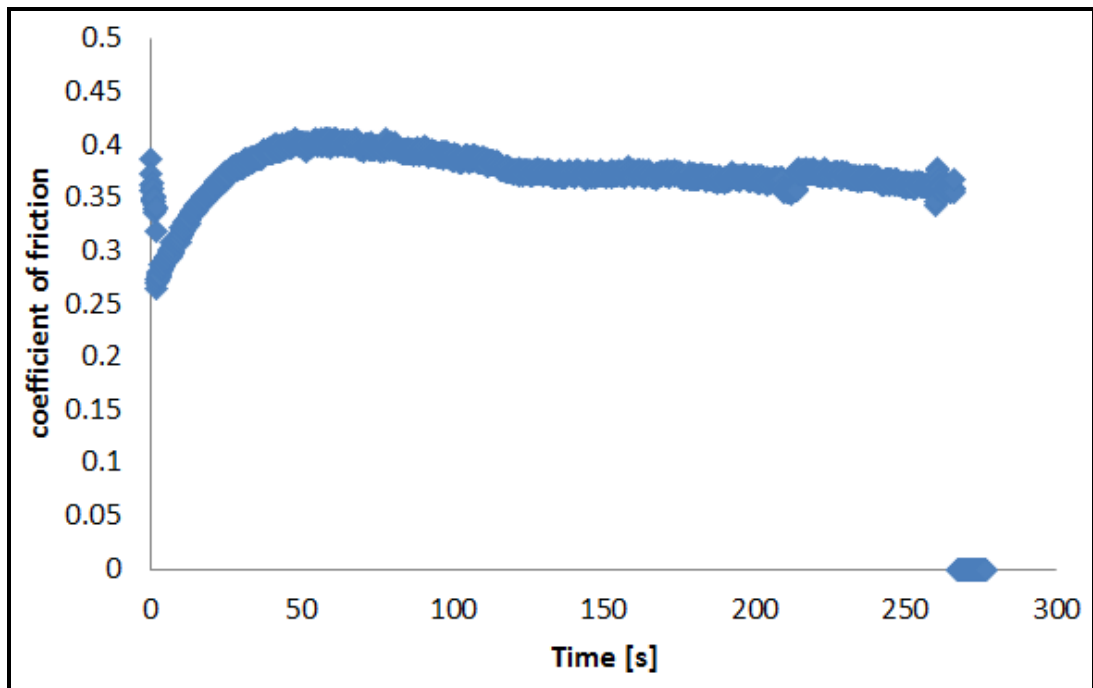


Figure 7.14: Coefficient of friction for the full scale Fiat Punto disc.

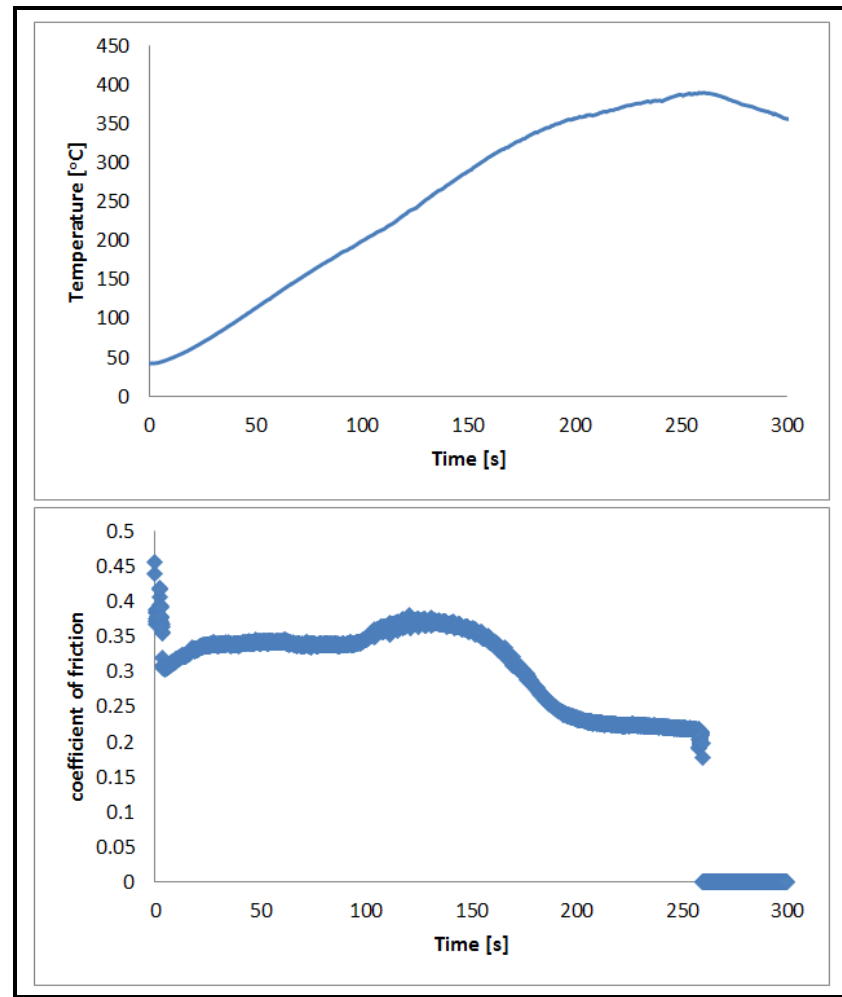


Figure 7.15: Temperature and COF response of the full scale disc brake.

7.3.3 Coefficient of friction

The coefficient of friction was calculated during a brake test according to the following equation [127]:

$$\mu = \frac{\tau}{2P \times A_{piston} \times r_d} \quad (7.3)$$

where A_{piston} is the area of the piston, P is brake line pressure, r_d is the mean rubbing radius, and τ is the braking torque. As explained above, the braking torque τ is obtained experimentally from the torque transducer for the full scale dynamometer and from the load cell for the small scale brake dynamometer.

The coefficient of friction for the various small scale disc brake rotors was monitored and calculated during the tests in order to evaluate their friction performance. The average coefficients of friction at temperature below 200°C are shown in Figure 7.16. According to the figures, the grey cast iron disc had the highest coefficient of friction compared to the others, and the coated disc brake rotors had a similar coefficient of friction while the plain Al-MMC disc had the lowest of all and at a level of about 0.2 which is not acceptable for a modern disc brake, However the friction material had not been optimised for the exposed MMC surface. The error bars in Figure 7.16 represent the standard deviation of the COF for various disc brake materials during the tests, which measures the amount of variation of the COF value during the test based on the average value. The standard deviation was calculated for one test with the surface temperature below 200°C.

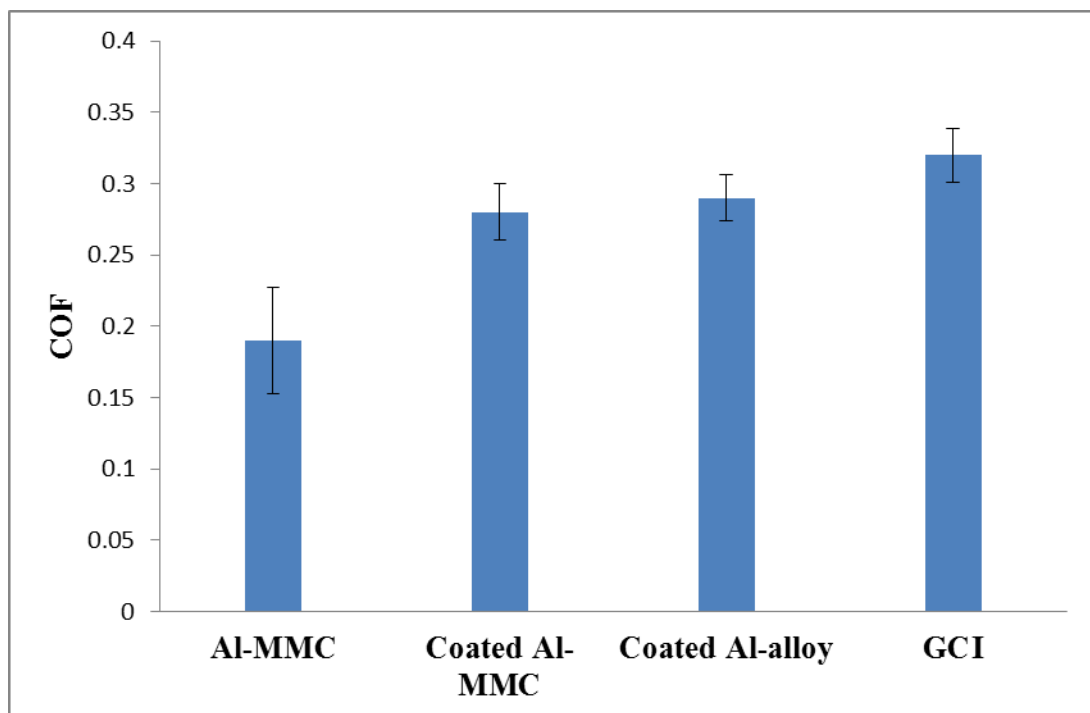


Figure 7.16: Average coefficient of friction for the small scale disc brake rotor.

Both coated discs had a similar low temperature coefficient of friction which was not much less than that of the cast iron rotor. However the friction performance of the coated wrought aluminium alloy was much better than that of the coated aluminium metal matrix composite at a higher surface temperature as shown in Figure 7.17 and

Figure 7.18. These results show that the friction performance of coated aluminium alloy is much better and more stable than that of the coated Al-MMC at temperature above 250°C.

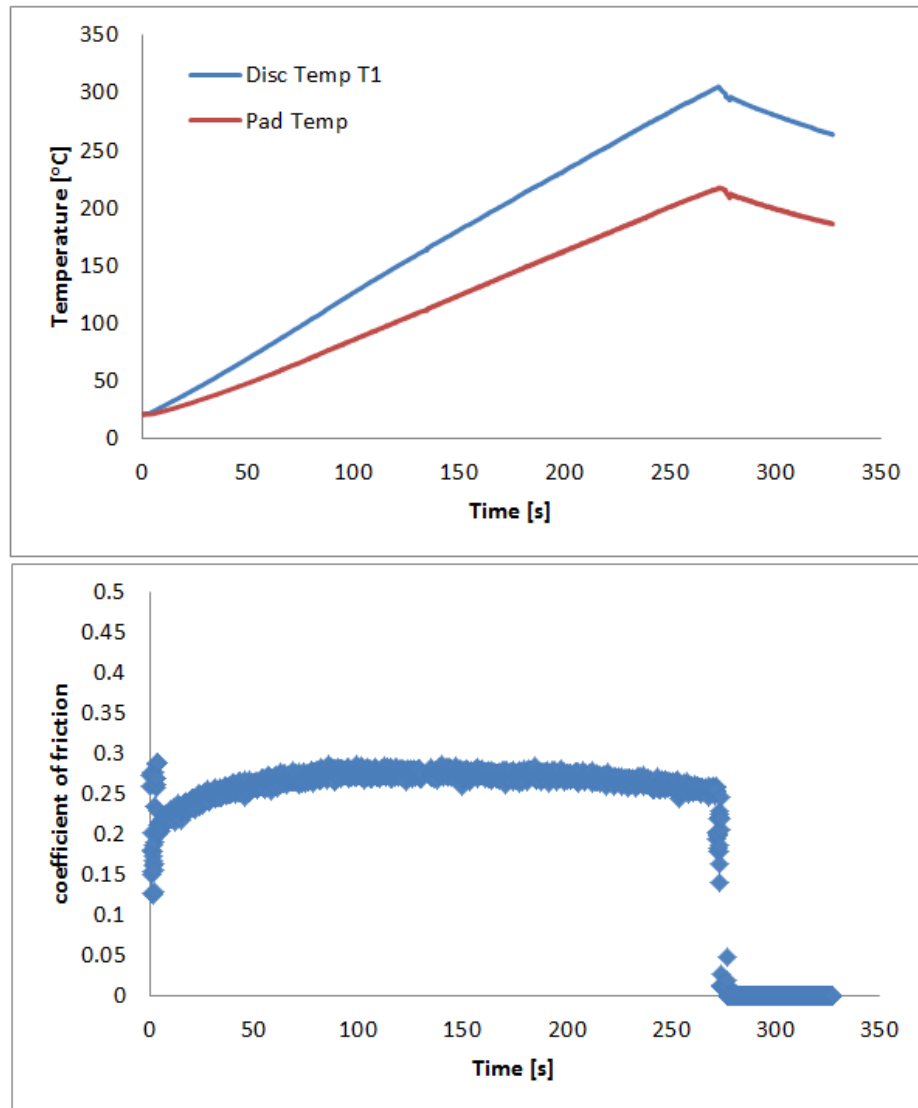


Figure 7.17: Temperature and COF response of the coated Al-alloy disc brake (test 9).

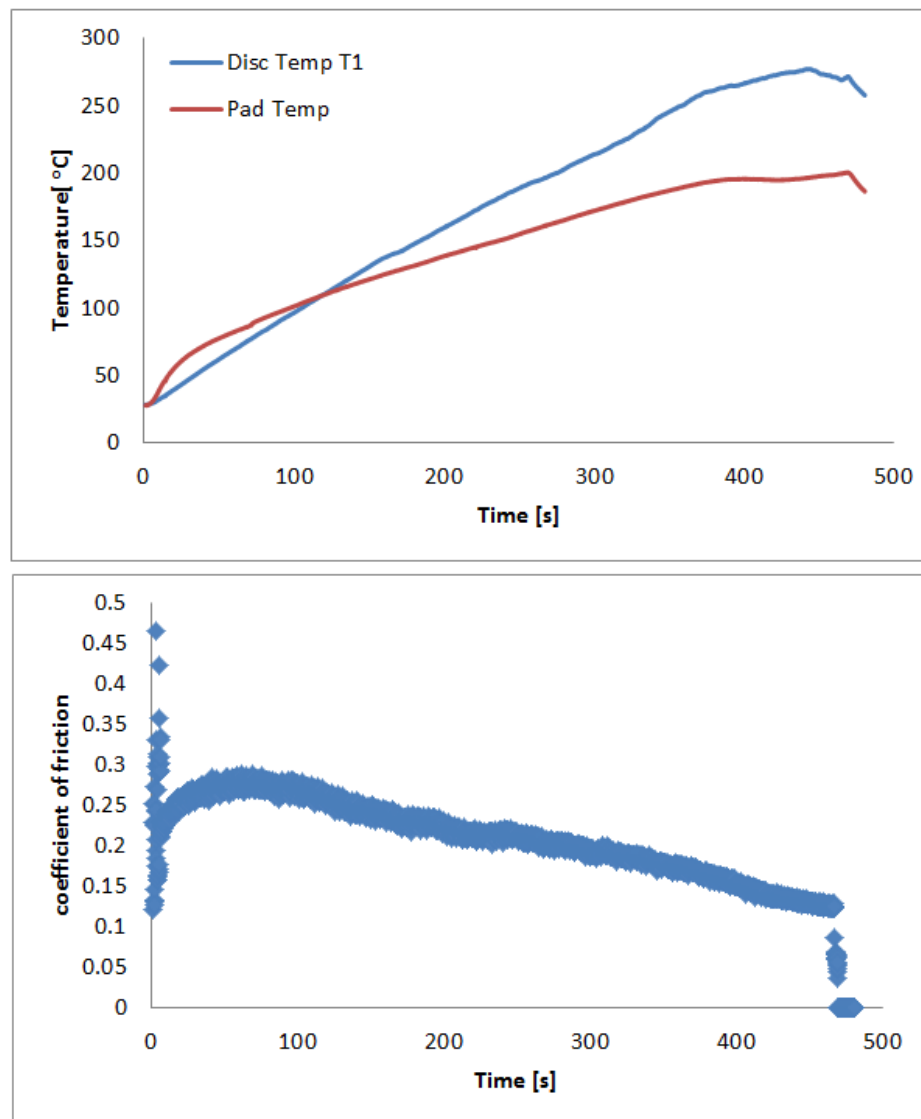


Figure 7.18: Temperature and COF response of the coated Al-MMC disc brake (test 9).

7.3.4 Observation of the coating layer during the test

The coated aluminium discs were observed and monitored during the test to identify any changes on the rubbing surface which included identifying the transfer layer. The surface appearance of the coated disc was light grey before the test, as shown in Figure 7.19. After several tests, a transfer layer had formed on the rubbing surface of the coated disc, as shown in Figure 7.20. The chemical composition and thickness of this layer are described in Chapter 8.

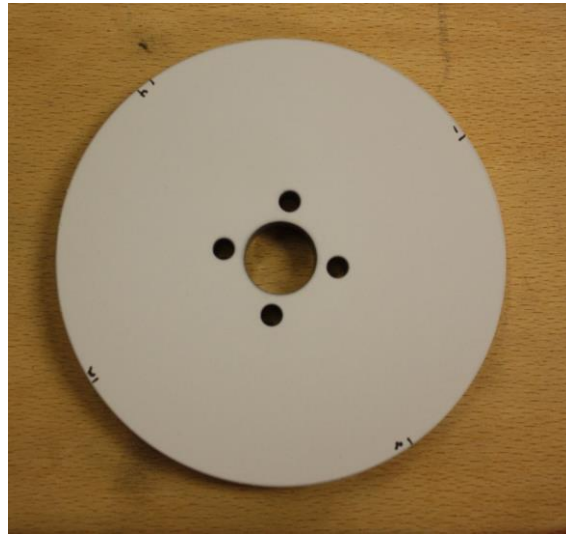


Figure 7.19: Surface appearance of the coated Al-alloy before the tests.

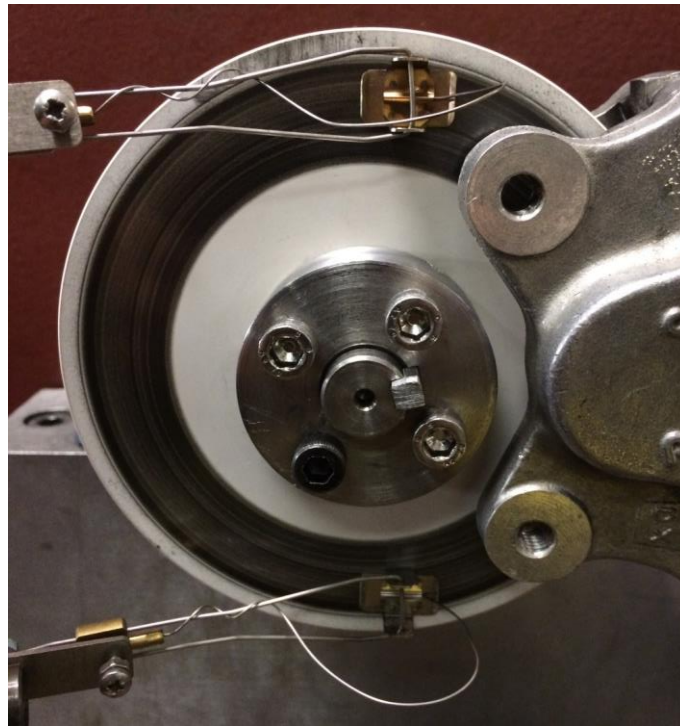


Figure 7.20: Surface appearance of the coated aluminium alloy after testing showing a dark transfer layer.

7.4 Scaling methodology validation

Two different braking conditions were used to validate the scaling methodology; both conditions simulate drag braking at a vehicle speed of 40 km/h. Condition 1 simulates drag braking for a vehicle with an average brake torque of 35 Nm for the full scale disc and an equivalent average of 7 Nm for the small scale disc which was calculated using equation (5.17). The surface temperature for both full scale and small scale discs was monitored at the mean rubbing radius and the results are shown in Figure 7.21. The surface temperature of the small scale disc showed good agreement with the surface temperature of the full scale disc with only a small difference of the order of 10°C. There are factors not accounted for in the scaling methodology that might have an effect on the temperature of both small and full sized discs. For example, the convective cooling rate may be different in each case because of the different disc dimension and rotational speed; also there may be an effect due to the different pad aspect ratios.

The second condition simulates drag braking for a vehicle at an average brake torque of 125 Nm for the full scale disc and an average of 24 Nm for the small scale disc with similar vehicle speed as condition 1. The surface temperature for both full scale and small scale discs was monitored at the mean rubbing radius and the results are shown in Figure 7.22. It was found that the surface temperature of the small scale disc was in good agreement with the surface temperature of the full scale disc with only a small difference, throughout the duration of the braking event.

The axisymmetric finite element models were used to investigate the scaling methodology and the thermal performance of the small and full scale solid discs. A two dimensional axisymmetric transient heat transfer model for both small scale and full scale discs was produced in Abaqus\standard, as explained in chapter 6. The model setup and boundary conditions for small scale solid discs and full scale discs are shown in Figure 7.23 and Figure 6.8 respectively. The models were meshed using 4-node linear axisymmetric heat transfer quadrilateral elements (DC2D4).

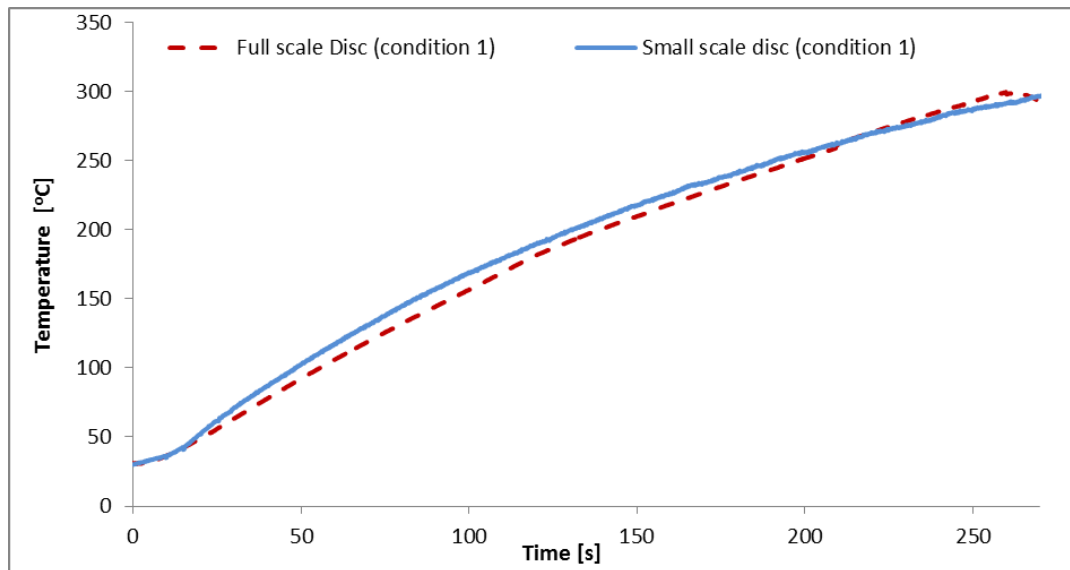


Figure 7.21: Disc surface temperature for small scale and full scale discs for condition 1.

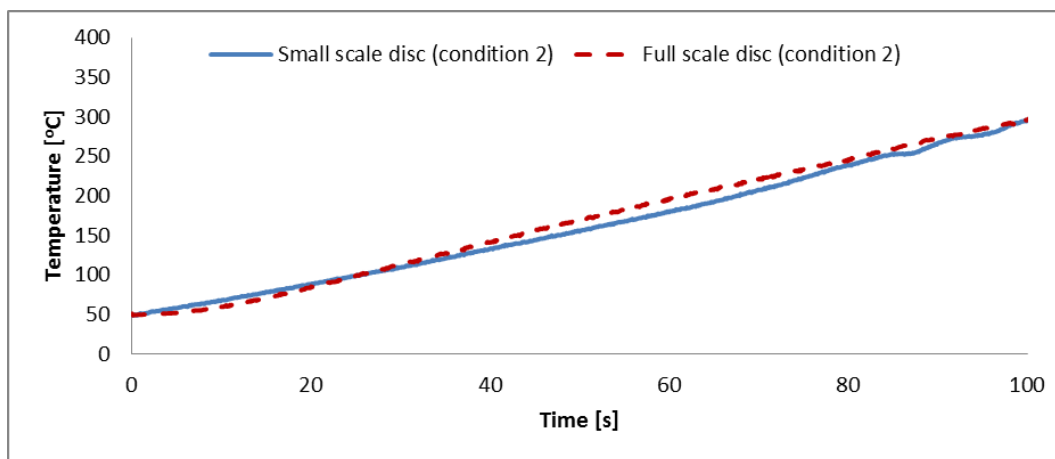


Figure 7.22: Disc surface temperature for small scale and full scale discs under condition 2.

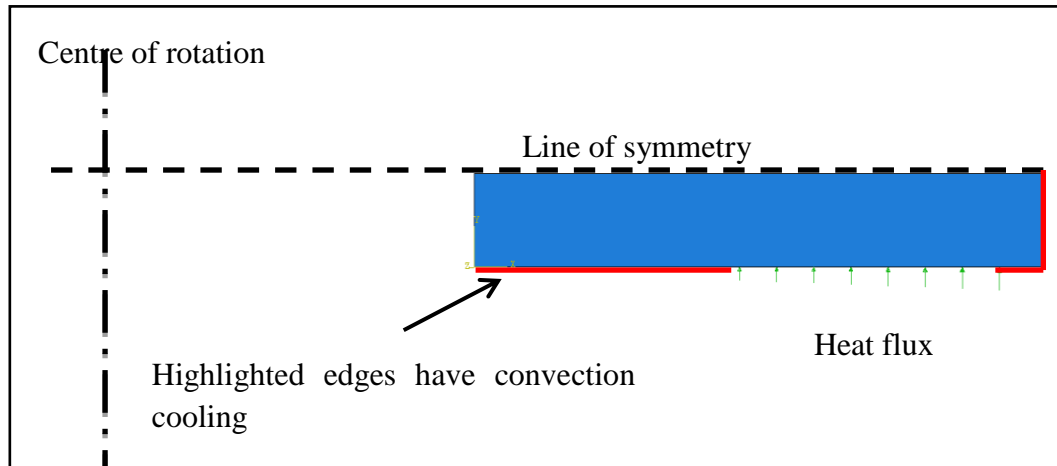


Figure 7.23: Two dimensional axisymmetric finite element model for small scale discs.

The full scale Abaqus model was validated against the experimental results; the heat flux was calculated using the experimental data (equation (7.1)). The numerical surface temperature at the mean rubbing radius was compared against the experimental results as shown in Figure 7.24. The very good agreements throughout the braking event demonstrate the validity of the numerical model.

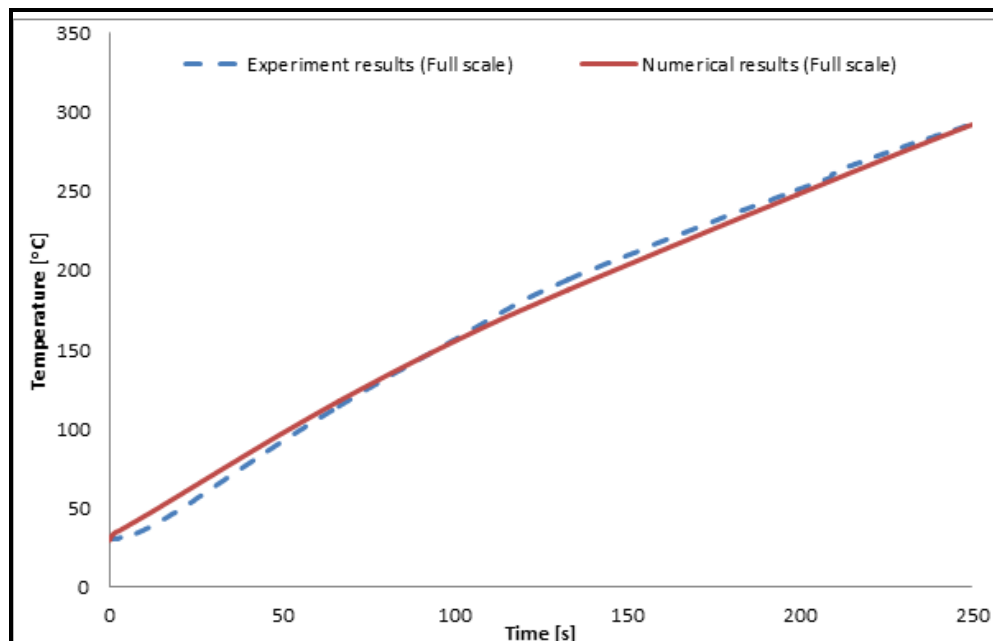


Figure 7.24: Validation of the full disc surface temperature.

Having validated the FE model against the experimental results, the 2D axisymmetric models were used to simulate very high speed drag braking in order to further investigate the thermal performance of both small and full scale discs. Figure 7.25 shows the surface temperature at mean rubbing radius for both small and full scale discs; the speed of the vehicle was 140 km/h and the full scale brake torque was 40 Nm. The results show a very good agreement with a very small difference which was expected as there are likely to be differences in the disc brake geometry explained earlier.

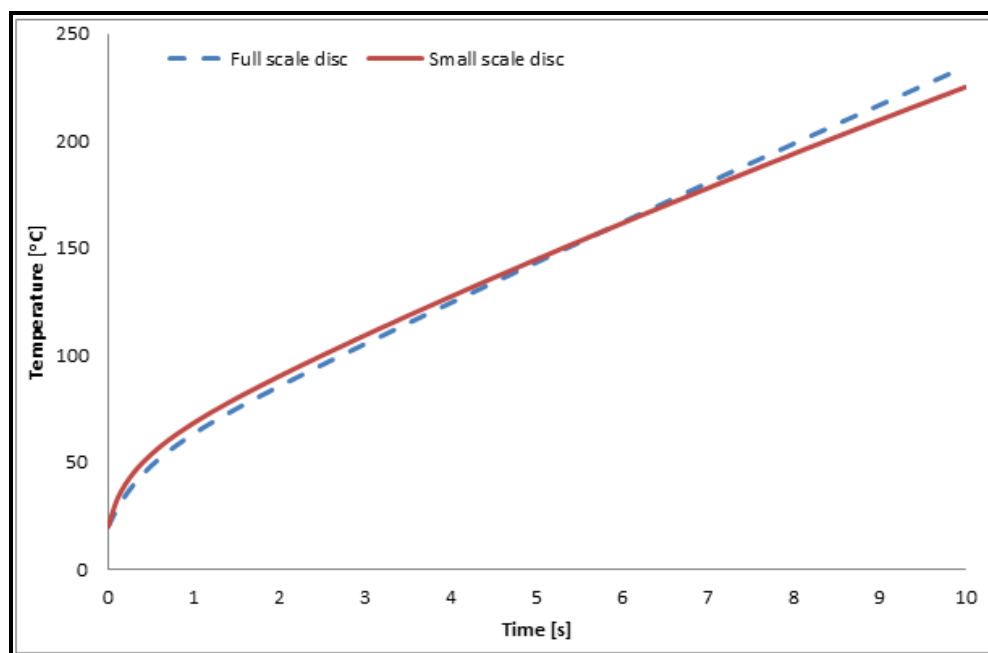


Figure 7.25: Numerical disc surface temperature for small and full scale discs during high drag braking.

The temperature distribution for both small and full scale discs at different time steps was investigated as shown in Figure 7.26 and Figure 7.27 respectively. It was noticed that the temperature distribution for both models was similar which proves that the scaling methodology can be used to investigate the thermal performance of disc brakes. In general there are small differences in the magnitude and this was due to different disc geometry between the small and full scale disc brake. Although the geometry of the full scale disc is slightly different (as shown in Chapter 5) to that of the small scale disc, their thermal distribution is almost the same, because in the scaling methodology the

thermal mass of the full scale disc was considered, in preference to the geometry. In addition, the convection cooling effect has an influence on the temperature distribution of full and small scale, because the full scale disc has a larger surface area than the small scale disc brake which improves the cooling behaviour and also affects the temperature distribution.

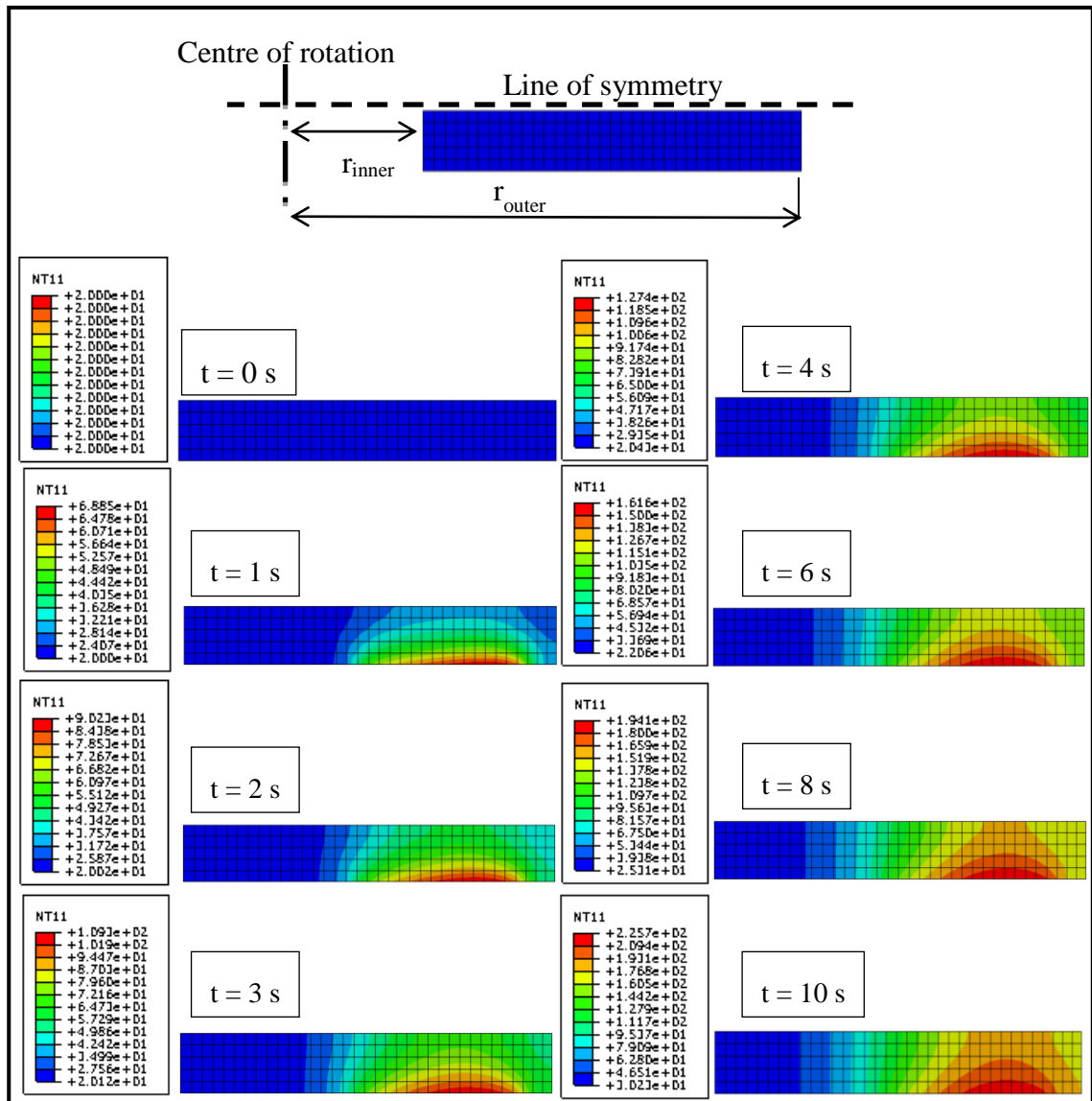


Figure 7.26: Temperature distribution of the small scale disc at different time steps.

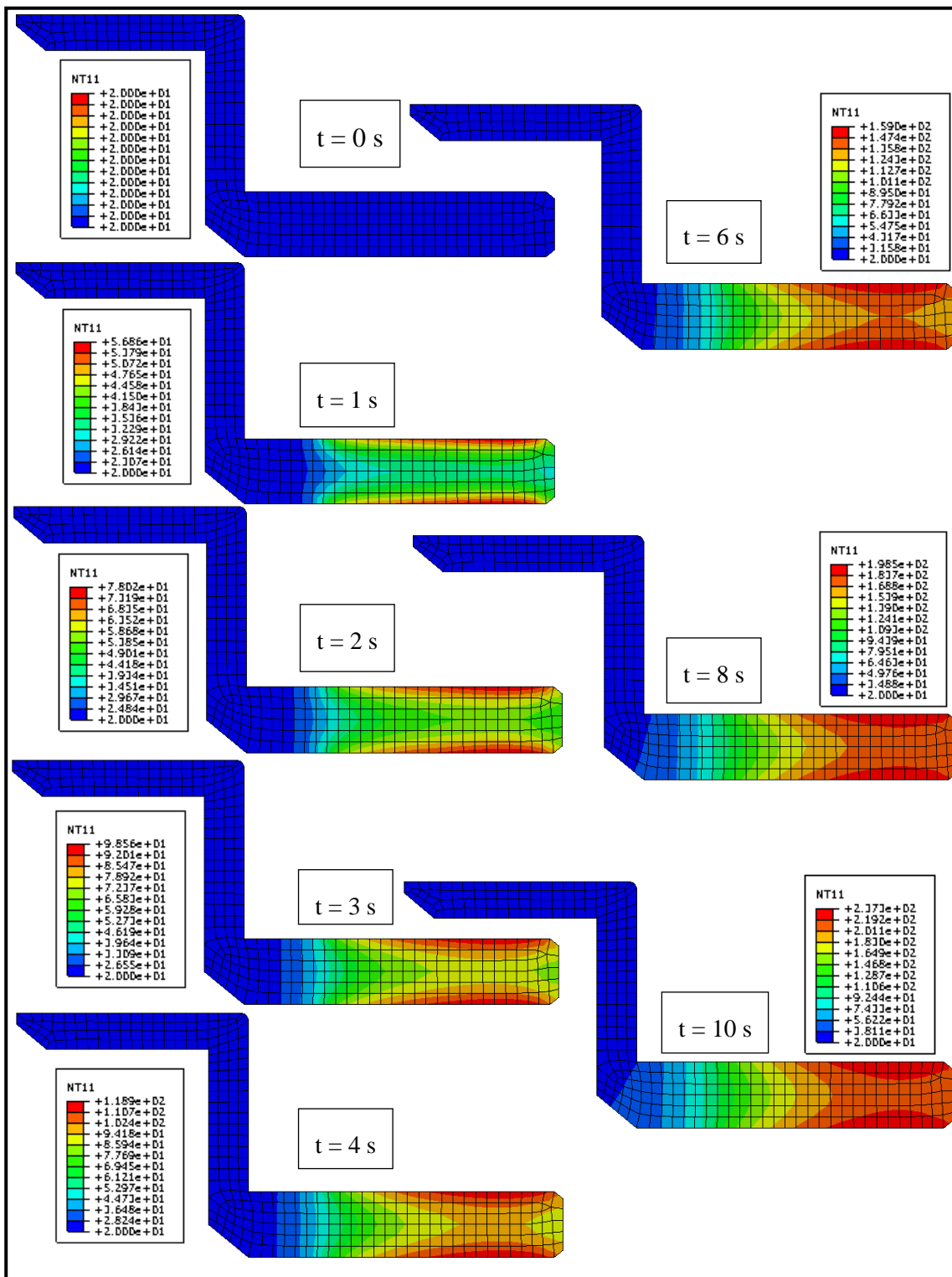


Figure 7.27: Temperature distribution of the full scale disc at different time steps.

7.5 Thermal performance of the failed coated wrought aluminium alloy disc brake rotor

The coated wrought aluminium disc was tested under very extreme braking conditions in order to evaluate its maximum operating temperature. It was found that the disc failed catastrophically when the surface temperature reached 550°C as shown in Figure 7.28. Since the substrate reached the melting temperature of the aluminium alloy (550°C). From the thermal image of the failed disc, the coating which covered the whole disc brake limited the dissipation of energy by natural convection and trapped all the heat inside the disc. This could be improved by coating the rubbing surface only thereby allowing the heat to dissipate more readily from uncoated surfaces.

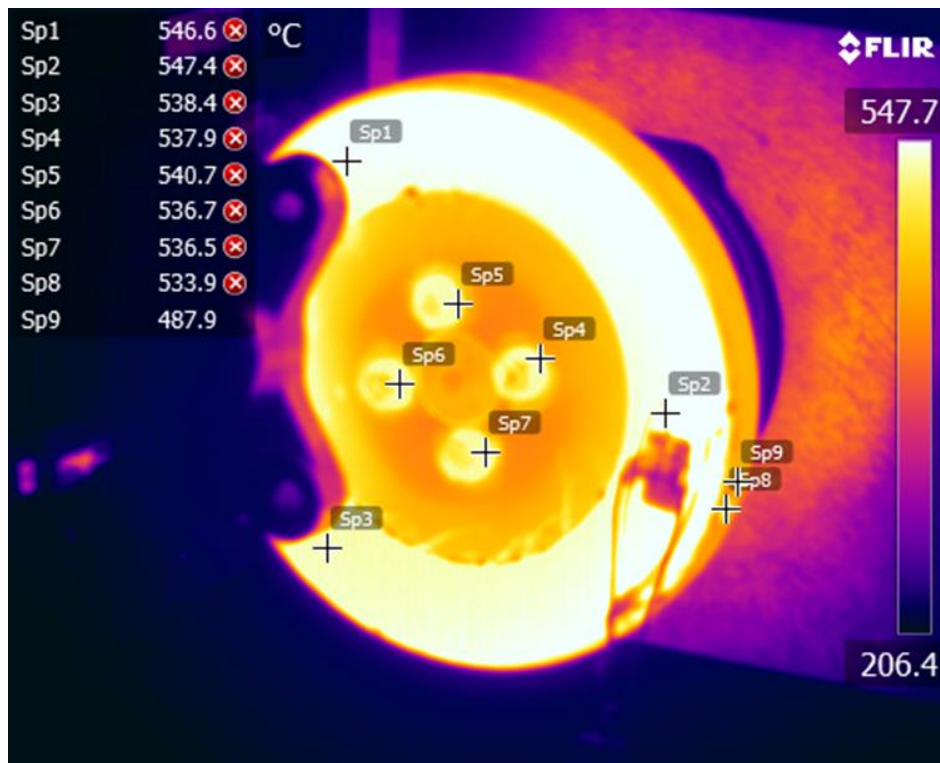


Figure 7.28: Temperature distribution of the coated wrought aluminium disc brake rotor before the catastrophic failure.

Based on the validated FE model, the effect of the vehicle mass on the maximum surface temperature of the coated brake rotor during a mountain descent was evaluated. The braking event selected for the current analysis was an extreme mountain descent lasting 23 minutes with an average slope of 12% and average vehicle speed of 80 km/h. The simulation results are shown in Figure 7.29 for both the coated aluminium alloy and standard grey cast iron discs. According to the experimental results the coated aluminium alloy disc brake rotor fails at 550°C surface temperature which implies a maximum vehicle mass of around 1700 kg for the front disc brake rotor for which x_f has been set to 0.7. However, to give an adequate safety margin, the maximum operation temperature of the coated aluminium alloy disc brake rotor was assumed to be 450°C which gives a maximum vehicle mass of 1400 kg for the front disc brake rotor. However the thermal performance of the coated front rotor could be further improved by optimising the disc design and the thermal properties of the disc materials which is considered in the following sections. The temperature response for a rear disc brake rotor was simulated for the same mountain descent as shown in Figure 7.29. To simulate the rear axle brake, the proportion of braking, x_r , was set to a realistic maximum of 0.4. The results indicate that the coated aluminium alloy rotor could find application in a rear disc brake assembly on vehicles up to 2000 kg mass.

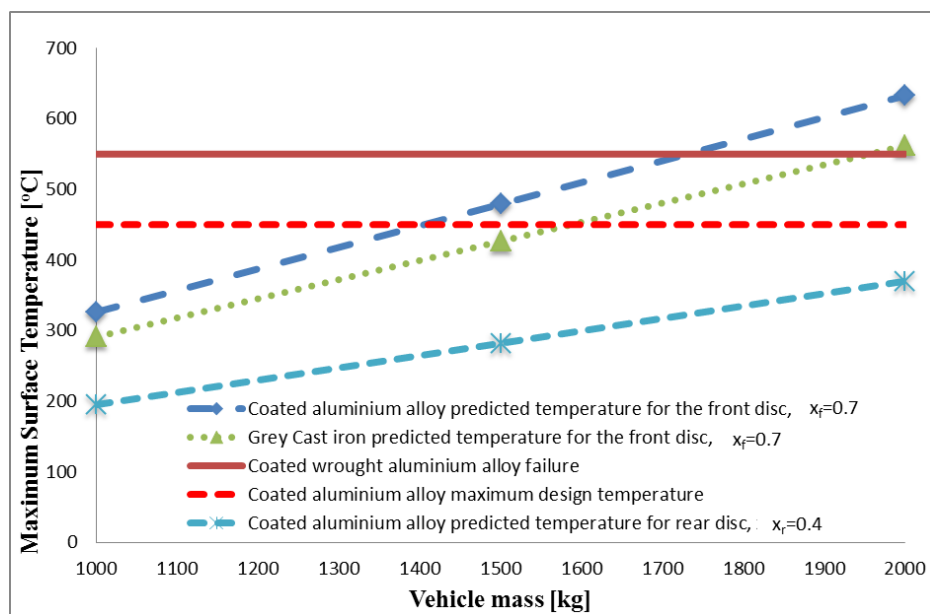


Figure 7.29: Effect of vehicle mass on the maximum temperature of the disc brake.

7.6 Summary

In this chapter the thermal performance of various disc brake rotors was investigated numerically and experimentally. A test matrix based on the well-known SAE standards was developed to assess the thermal and friction performance of the small scale disc brake rotors. The five selected small scale disc brake rotors were tested using the developed brake test matrix. The results show that, after CGI, the coated aluminium alloy had the best thermal performance of the lightweight rotors tested in terms of structural integrity at elevated temperature. The friction coefficient for the coated aluminium alloy was also more stable than for the plain Al-alloy, Al-MMC or coated Al-MMC rotors. The uncoated aluminium alloy and aluminium metal matrix composite rotors did not withstand the higher temperature on the rubbing surface and scratches began to appear at a relatively low temperature due to softening of the aluminium. The discs were tested to their limits to assess the thermal performance of each material both with and without a coating. The experimental results were validated with the numerical results obtained from the FE model and the results show a good agreement. The validated FE model will be used in future studies to explore different braking conditions and to investigate the optimum lightweight disc brake rotor design prior to full scale dynamometer and on-vehicle testing.

High speed thermal imaging system was used to monitor the surface temperature and confirm that the sliding thermocouples are fit for purpose. It was shown that the temperature obtained from sliding thermocouples was close to the thermal image system during the drag braking event. However, the sliding thermocouples show a slow response to rapid increase in surface temperature during the constant g stop braking event which is explained in section 7.4.1.

The reduced scale disc data was compared with the full scale disc data obtained from the brake dynamometer. The results obtained showed an excellent agreement between numerical and experimental results for both the full and small scale discs. The small scale brake dynamometer is an important tool that can be used to investigate the thermal performance of disc brakes at lower cost and in a shorter timescale. Also it can be used to investigate the friction behaviour of brake pads in the early design stage. The thermal

distribution of the full and small scale disc brakes was investigated using a two dimensional axisymmetric finite element model in Abaqus and the results showed that both models displayed almost the same behaviour. There are small differences in the thermal distribution because of the effect of cooling and aspect ratio. Furthermore, it was assumed that both full and small scale discs had the same convective cooling rate. In reality, full and small scale discs will have different convection cooling rates because of the different disc areas and rotational speed.

CHAPTER 8:

MATERIAL CHARACTERISATION

RESULTS

8.1 Introduction

Material characterisation analysis of various disc brake rotors and pads before and after the braking tests is presented in this chapter. Different techniques, such as optical and scanning electron microscopy, were used to investigate the microstructure of different disc brake rotor and pad materials in plan and cross-sectional view. In addition, the elemental compositions were analysed using the EDX technique for the lightweight disc brake rotors before and after the braking tests. The mechanical properties and the roughness of the various lightweight discs brake rotors with and without coating were studied and reported upon. Finally, coating durability and transfer layer analyses were carried out in order to evaluate the coating surface after the brake testing.

8.2 Microstructure and morphology analysis

This section describes how the microstructure of the coated and uncoated small scale disc brake rotors was investigated in order to evaluate the effect of braking on the surface of the disc brake rotor. The analysis was carried out before and after the braking tests, in order to identify any change in the surface texture. Various techniques were used to study the microstructure and morphology of the disc brake rotor substrates and coatings as explained in the following subsections.

8.2.1 Before braking tests

8.2.1.1 Wrought aluminium alloy substrate

The aluminium substrate used in the current research was wrought 6082-T6 alloy, as explained in previous chapters. An SEM image taken for the 6082-T6 wrought

aluminium is shown in Figure 8.1. This image showed some scratches on the surface which were generated during sample preparation and small white spots which were detected from the EDX analysis as silicon phases. The presence of silicon particles was expected for this type of aluminium alloy as explained in Chapter 3 and shown in Figure 8.2 region (b).

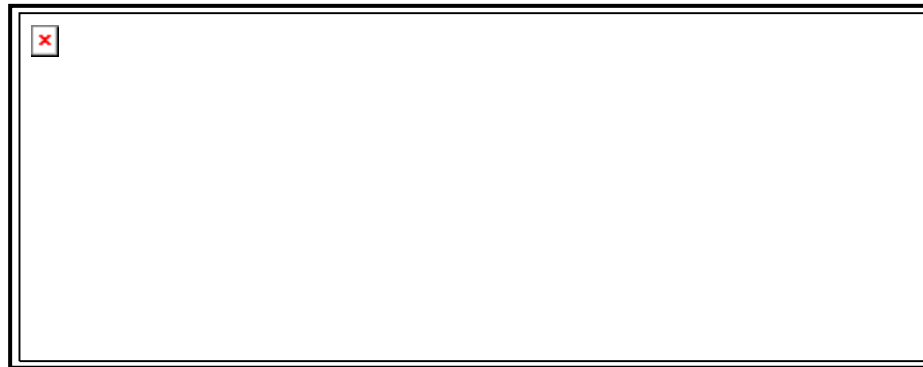


Figure 8.1: Surface morphology of wrought aluminium alloy before braking tests.

EDX analysis was carried out in different regions of the 6082-T6 aluminium alloy as shown in Figure 8.2, and various elements were detected apart from aluminium, namely silicon (Si), magnesium (Mg), copper (Cu), chromium (Cr), manganese (Mn), Titanium (Ti), and iron (Fe). It was found from the EDX analysis that the white coloured areas in the aluminium surface relate to high concentrations of silicon which is expected for this type of aluminium. The results for elemental composition obtained from the EDX analysis, shown in Table 8.1, are in a good general agreement with the values obtained from the literature presented in Chapter 3. Although EDX analysis is not an accurate technique for evaluating the elemental composition of a material, it is sufficiently accurate for the purposes of the current study. It was found that a higher percentage of silicon was present on the surface which might be because of the metallographic processing and the use of SiC paper for grinding/polishing the surface in particular.

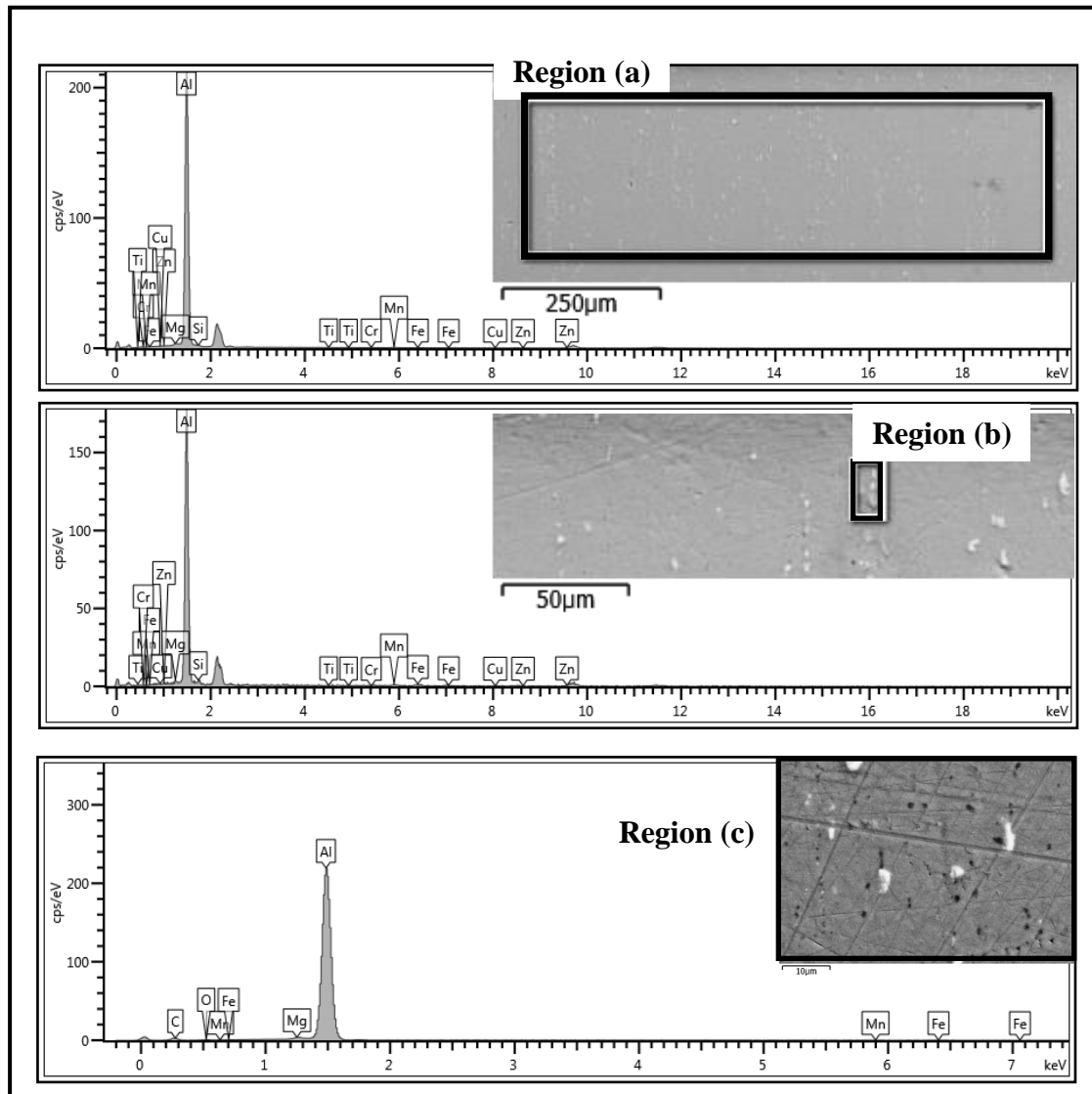


Figure 8.2: EDX analysis for wrought aluminium alloy before braking tests in three different regions (a), (b) and (c).

Table 8.1: Elemental composition (weight %) of wrought aluminium alloy 6082.

Element	Si	Mg	Mn	Fe	Cr	Cu	Zn	Ti	Al	Total
Region (a)	1.10	0.50	0.87	0.38	0.24	0.04	0.16	0.15	96.56	100
Region (b)	2.98	0.69	1.72	2.79	0	0.32	0	0	91.51	100
Region (c)	0.89	0.59	0.7	0.58	0.16	0.15	0	0.07	96.86	100

8.2.1.2 Aluminium metal matrix composite substrate

The aluminium metal matrix composite used in the current research was AMC640XA which consists of a high quality aluminium alloy (AA6061) reinforced by 40% silicon carbide particles. Its surface morphology is shown in Figure 8.3. In the SEM image the dark phase represents the metal and the white phase represents the SiC particles. In addition, Figure 8.4 shows the surface microstructure of the composite which consists of an aluminium matrix with SiC particles distributed throughout the surface.

EDX analysis was carried out for various regions of the aluminium metal matrix composite with results as shown in Figure 8.5. Elements detected, in addition to aluminium, were silicon (Si), carbon (C), magnesium (Mg), copper (Cu), chromium (Cr), manganese (Mn), Titanium (Ti), and iron (Fe). The composition (in weight %) in two different regions is presented in Table 8.2.

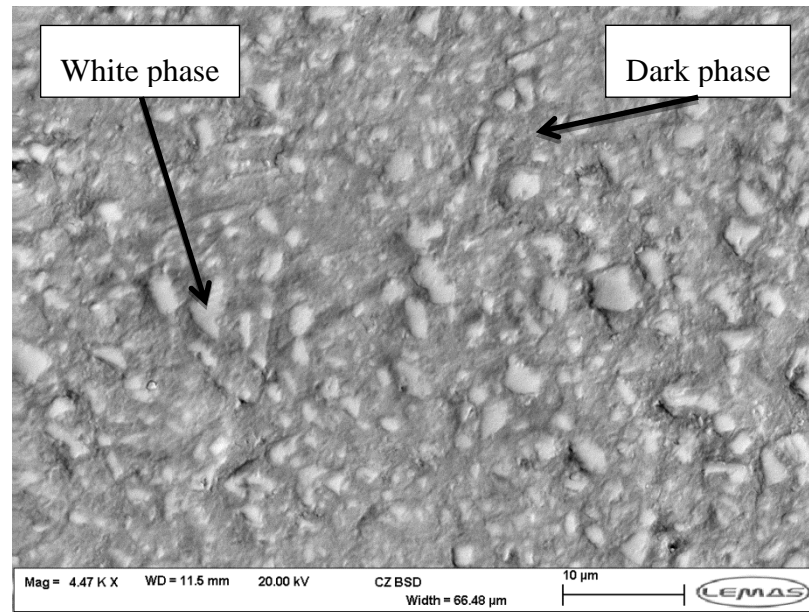


Figure 8.3: SEM micrograph showing surface morphology of the aluminium metal matrix composite before braking tests.

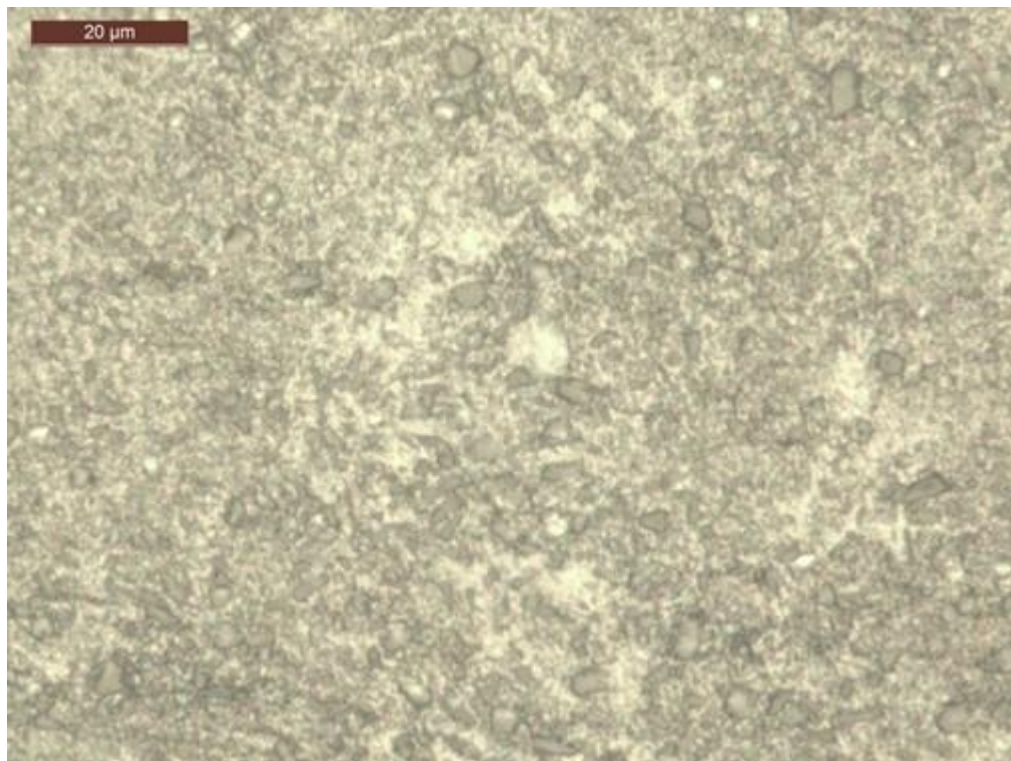
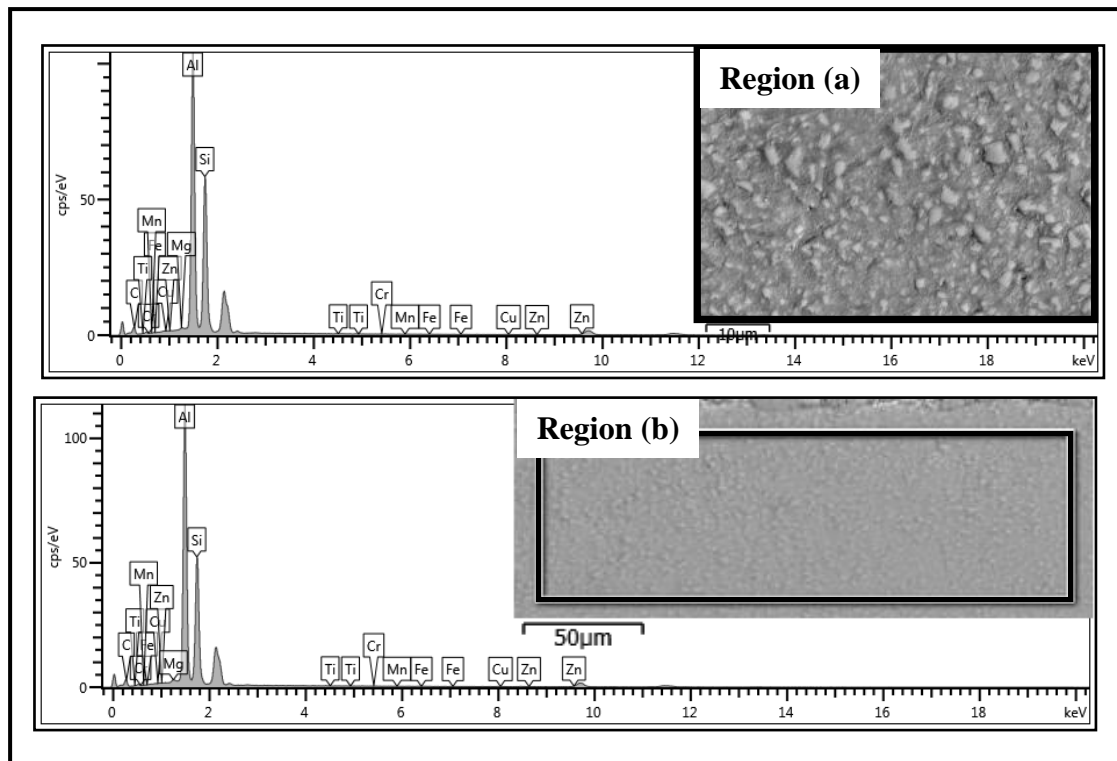


Figure 8.4: Optical micrograph of the microstructure of the aluminium metal matrix composite before braking tests.

Table 8.2: Elemental composition of the aluminium metal matrix composite (weight %).

Element	Si	Mg	Mn	C	Fe	Cr	Cu	Zn	Ti	Al	Total
Region (a)	30.51	0.2	0	34.8	0.13	0.02	0.15	0	0.05	34.12	100
Region (b)	27.36	0.3	0.04	35.5	0.16	0.06	0.24	0	0	36.22	100

**Figure 8.5: EDX analysis for the aluminium metal matrix composite before braking tests in two different regions (a) and (b).**

8.2.1.3 Plasma electrolytic oxidation coating

Typical SEM images for the PEO coated aluminium metal matrix composite and wrought aluminium alloy are shown in Figure 8.6 and Figure 8.7, respectively at two different magnifications. Figure 8.6 shows the surface of a 30 μm coating for the Al-MMC substrate, while Figure 8.7 shows the surface of a 50 μm coating for the wrought Al-alloy substrate.

The surface morphologies of the PEO coating of the Al-MMC and Al-alloy are very similar, as shown in Figure 8.6 and Figure 8.7 respectively. It can be seen that many particles with spherical, lamellar and irregular shapes formed on the surface (volcano-like eruptions) of the PEO coating. In addition, it can be seen from the SEM images that a number of small shrinkage holes had formed on the surface during the crystallisation phase. Their surface morphologies are characterised by macro-particles which resulted from spark discharge during the layer growth [89, 128, 129].

In this study it was found that there are two main layers in the PEO coating for both substrate materials as shown in the SEM's of Figure 8.8 and Figure 8.9 which present the cross sectional view for each coating. The first layer is the inner layer which is strongly adhered to the substrate and the second layer is the outer loose layer (porous top layer) as shown in Figure 8.8 and Figure 8.9 [128].

According to the SEM images of the cross section shown in Figure 8.8 and Figure 8.9, wrought Al 6082 has an extremely dense and uniform coating with alpha/gamma alumina [82, 128] as major constituents. This gives an extremely hard and durable tribo surface with stable CoF (reported in chapter 7) in addition to conferring a significant thermal barrier effect. On the other hand, only 60% of the Al-MMC, is 6061 alloy and the remaining 40 vol% consists of SiC particles. This high proportion of SiC presents considerable challenges to the PEO process and in fact to any surface modification process. The resulting coating is not very uniform with high levels of porosity. While the coating gives a considerable improvement in corrosion resistance compared to the MMC substrate [82], the tribological performance is poorer compared to the coated wrought alloy due to: a) lower density and softer coating; b) crumbling and subsequent detachment of the ceramic particles (alumina plus some SiC) which results in three-

body abrasion wear between the disc and the brake pad, similar to the effect of feeding sand into the rubbing interface.

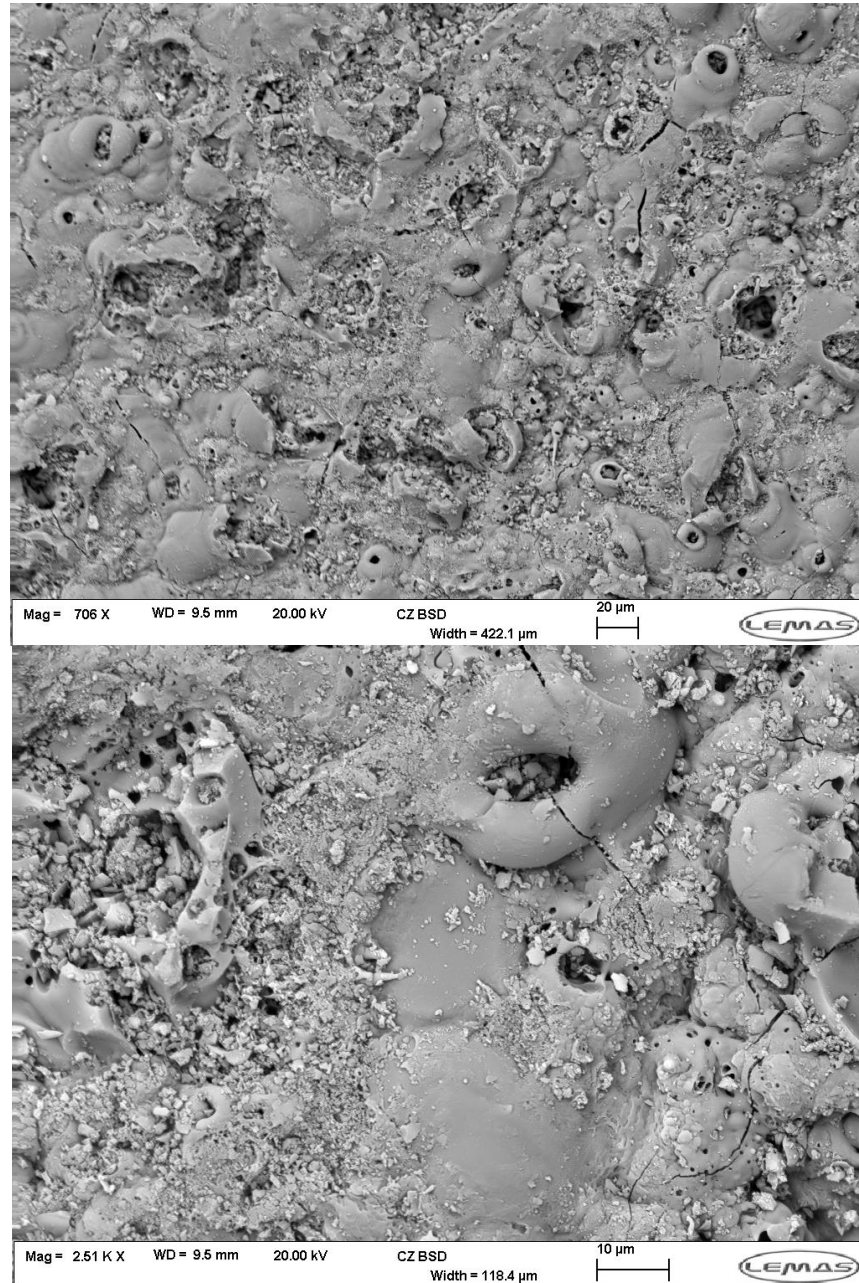


Figure 8.6: Surface morphology of PEO coating for the aluminium metal matrix composite substrate before braking tests.

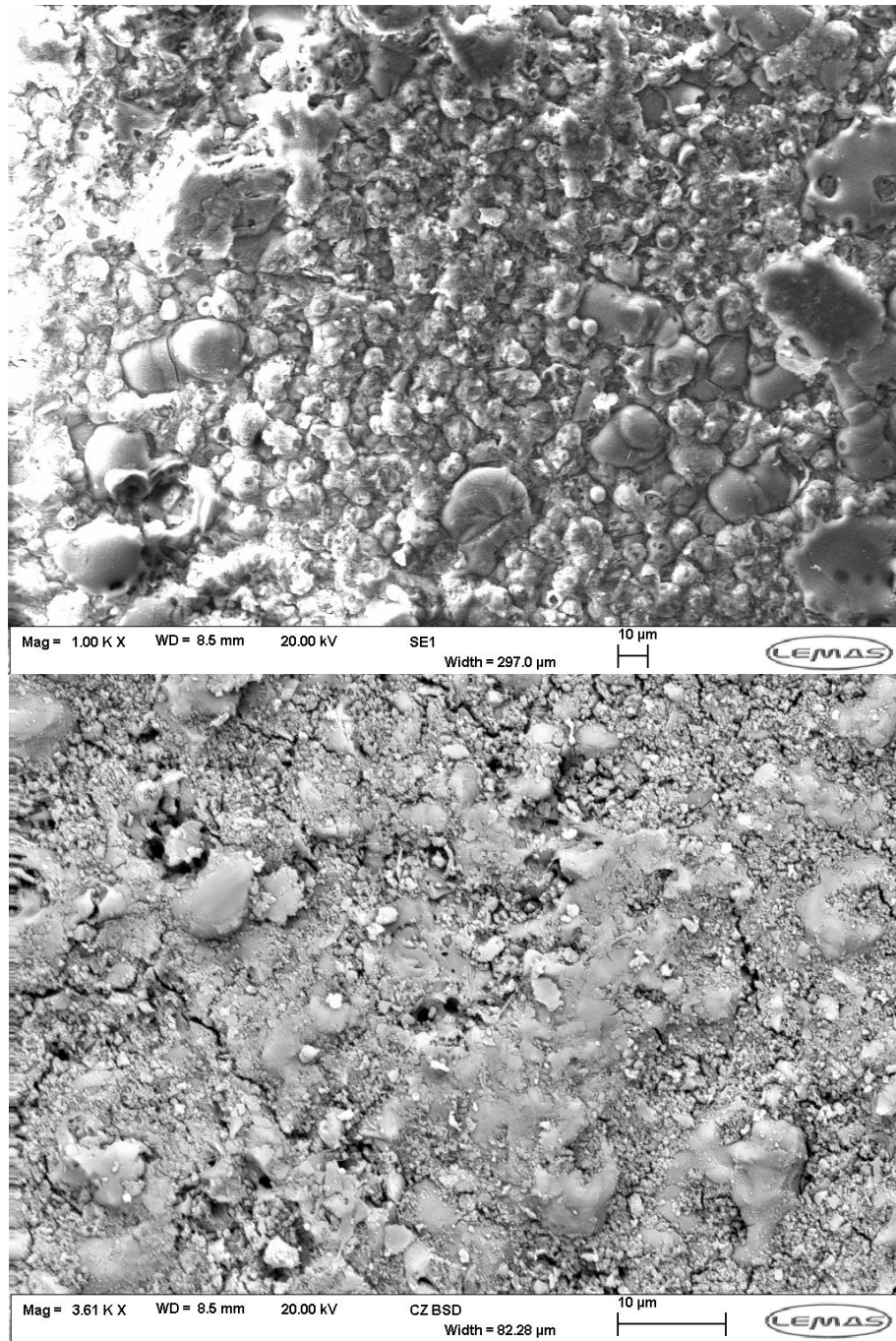


Figure 8.7: Surface morphology of PEO coating for the wrought aluminium alloy substrate before braking tests.

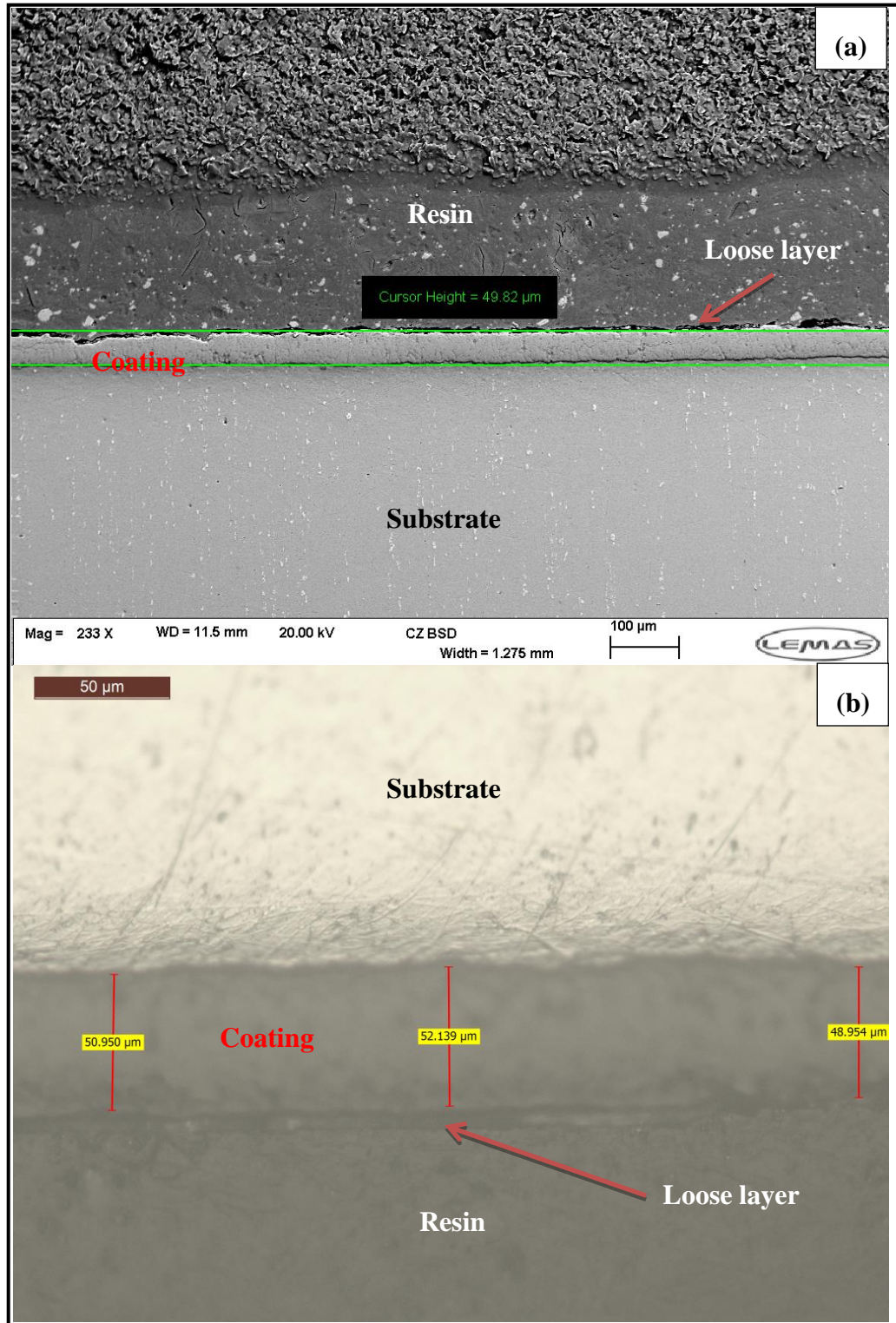


Figure 8.8: Cross sectional view for the coated wrought aluminium alloy substrate before braking tests: (a) SEM and (b) optical micrograph.

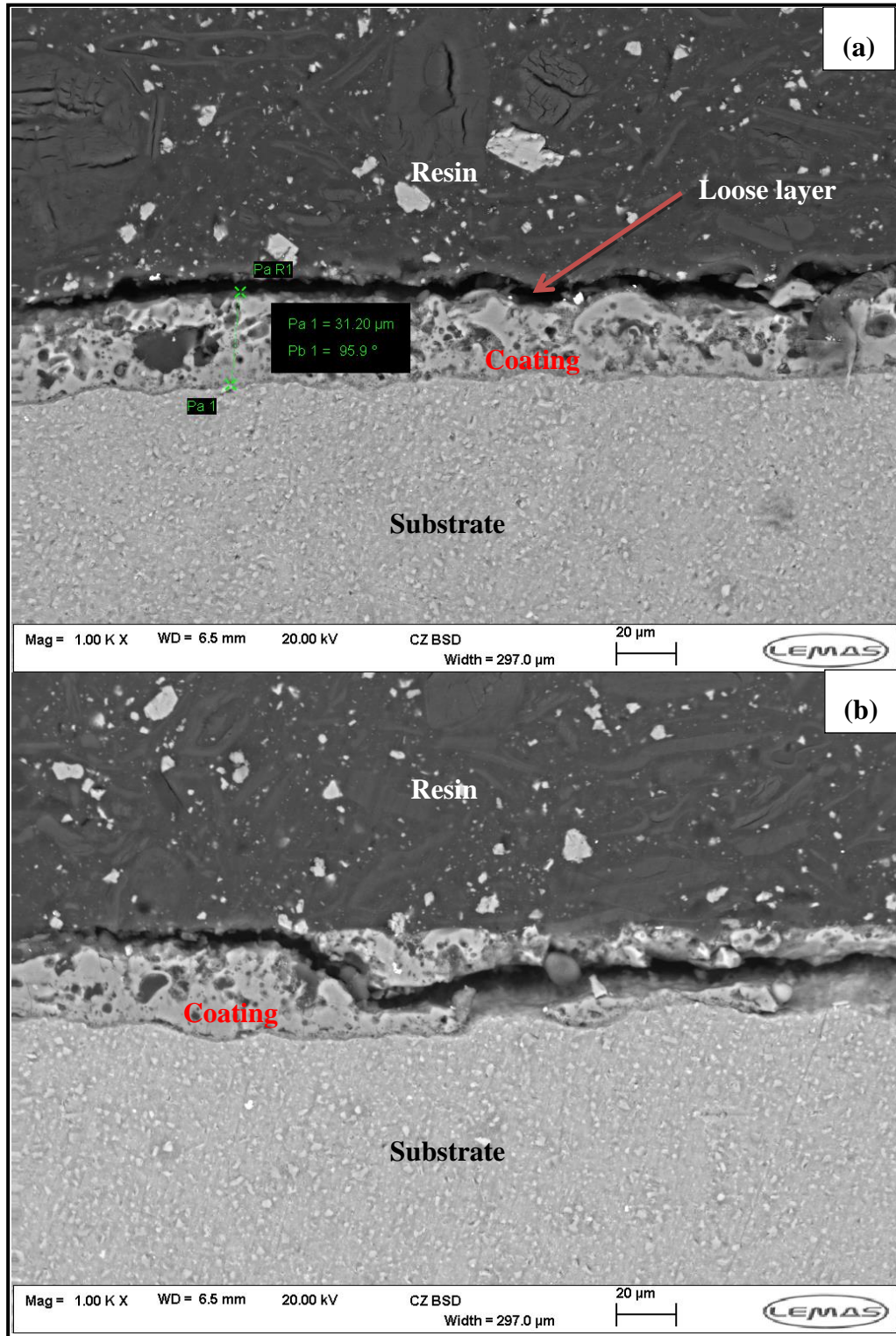


Figure 8.9: Cross sectional view for the coated aluminium metal matrix composite substrate before braking tests.

EDX analysis was carried out for the PEO coating on the wrought aluminium substrate which revealed that the main elements were oxygen (O) and aluminium (Al) as shown in Figure 8.10 and Table 8.3. These elements were expected to be found in the PEO coating. Also, the appearance of silicon in the cross sectional view might be due to the preparation process as SiC paper was used for grinding/polishing.

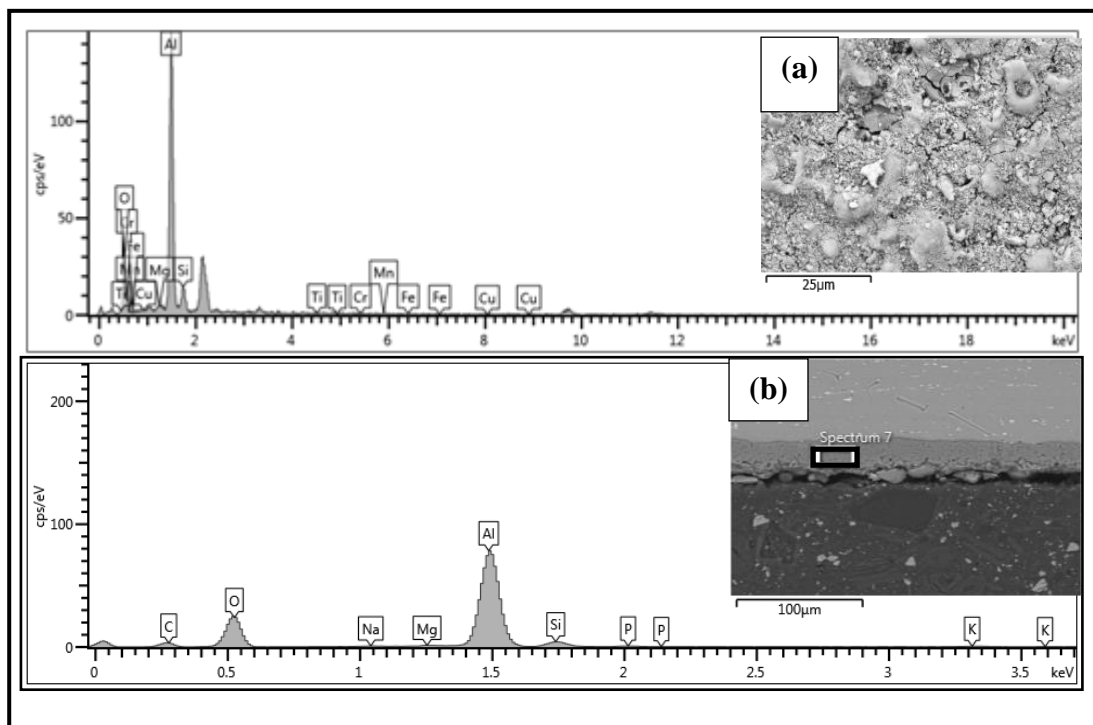


Figure 8.10: EDX analysis for coated wrought aluminium (6082) substrate before braking tests in two different regions (a) and (b).

Table 8.3: Elemental composition (weight %) of coated wrought aluminium alloy 6082.

Element	Si	Mg	Mn	Fe	Cr	Cu	O	Ti	Al	Total
Region (a)	7.87	0.55	0.62	0.25	0.29	0.03	40.51	0	49.88	100
Region (b)	4.52	0.32	0	0	0	0	44.40	0	49.23	100

The same EDX analysis used to evaluate the PEO coating for the aluminium MMC substrate revealed that the main elements were oxygen (O), silicon (Si), carbon (C) and aluminium (Al) as shown in Figure 8.11 and Table 8.4. It was found that a high percentage of silicon and carbon appeared on the coating surface. This was expected for the coating layer because the aluminium MMC consisted of 40% SiC particles. Also it was noticed that more aluminium (Al) was found on the layer close to the substrate as shown on Table 8.4 as would be expected.

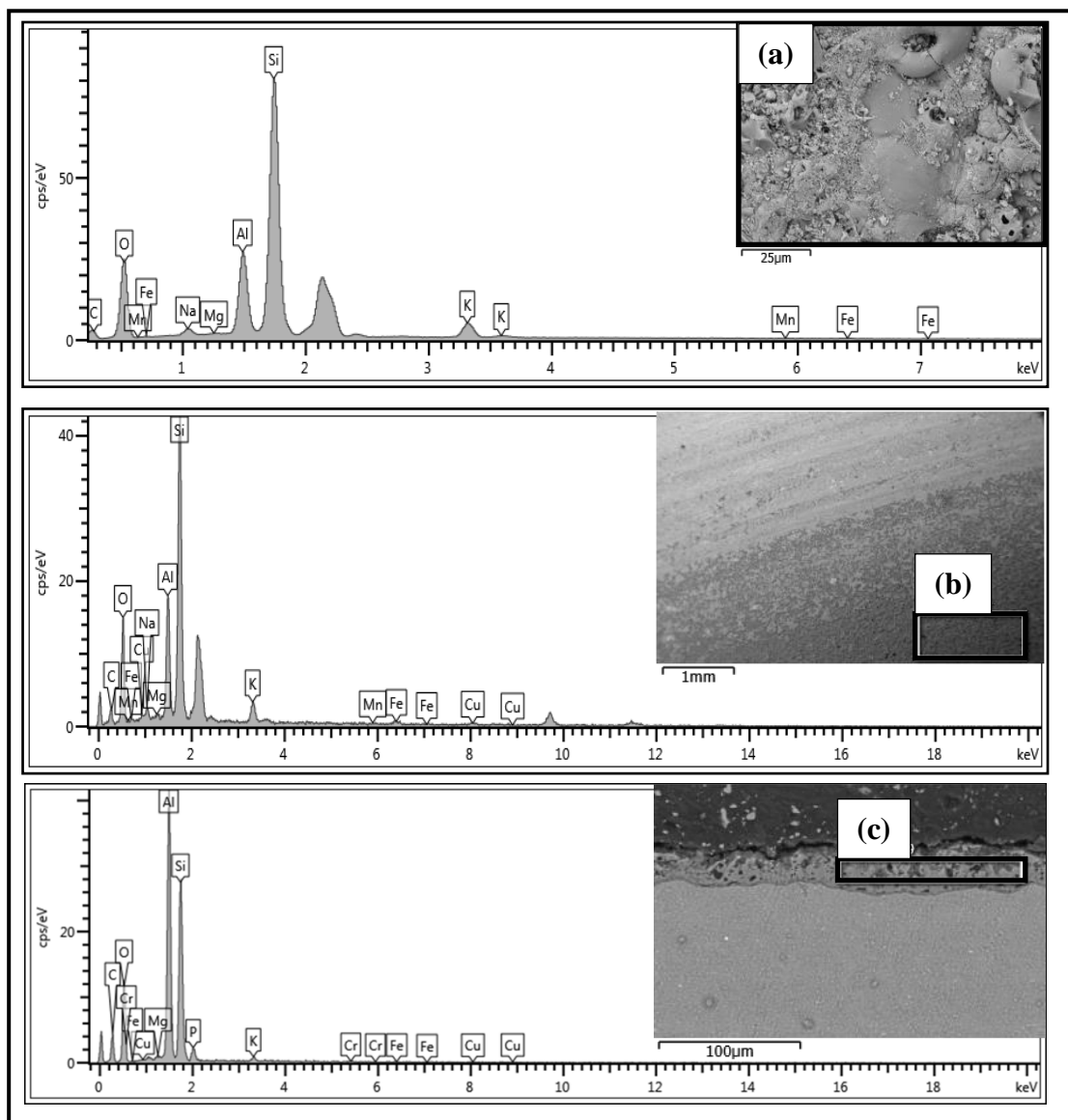


Figure 8.11: EDX analysis for the coated aluminium metal matrix composite substrate before braking tests in three different regions (a), (b) and (c).

Table 8.4: Elemental composition of the coated aluminium metal matrix composite (weight %).

Element	Region (a)	Region (b)	Region (c)
Si	34.38	29.89	16.64
Mg	0.1	0.34	0.22
Mn	0.08	0.22	0
Fe	0.24	1.49	0.07
K	3.4	3.32	0.58
Cu	0	1.44	0.26
C	13.16	15.6	32.11
O	37.73	35.29	29.18
Cr	0	0	0.18
P	0	0	1.55
Na	1.11	1.4	0
Al	9.8	11.02	19.2
Total	100	100	100

8.2.1.4 Brake pads

The brake pads used in the current research were manufactured by TMD Friction. They were designed specifically to rub against an alumina coating but were also found to produce acceptable levels of friction performance against standard cast iron and uncoated aluminium rotor brakes, as explained in Chapter 7. Most brake pad manufacturers do not specify the exact contents of their pad materials. In this section the elemental composition of the brake pads provided by TMD was investigated using EDX analysis in order to build up a basic knowledge about the contents which would later help to identify the transfer layer on the rubbing surface. TMD describe the current material as an organic based friction material which was designed to be as close as possible to the so called Low-Met (low metallic) material that is preferred by the European market. EDX analysis was carried out for various regions of the brake pads as shown in Figure 8.12.

According to the EDX analysis the main components in the brake pads are as follows: carbon (C), oxygen (O), iron (Fe), copper (Cu), zinc (Zn) and tin (Sn). Table 8.5 summarises the elemental composition of the brake pads in different regions by weight %. The elemental composition proves that the current brake pad is an organic pad with low metallic elements [130]. The results obtained were compared with published data and showed good agreement with typical weight percentages for the different elements [130].

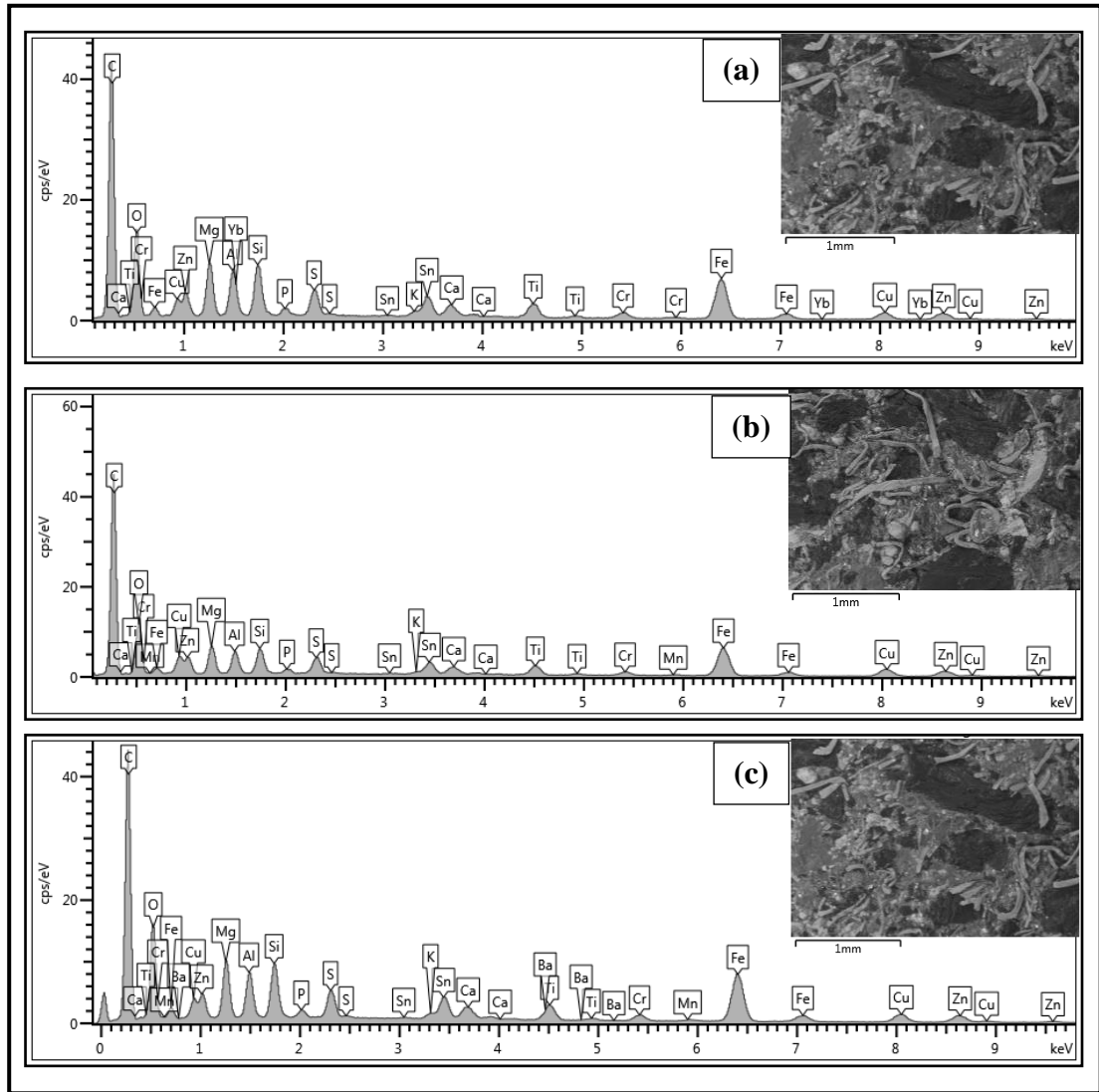


Figure 8.12: EDX analysis for the brake pad before braking tests in three different regions (a), (b) and (c).

Table 8.5: Elemental composition of the brake pad (weight %).

Element	(a)	(b)	(C)
C	55.35	59.17	55.23
O	17.57	14.94	16.95
Mg	2.61	1.95	2.59
Al	1.82	1.33	1.76
Si	1.98	1.38	1.96
P	0.32	0.28	0.30
S	1.14	0.98	1.11
K	0.27	0.18	0.28
Ca	0.17	0.20	0.15
Ti	1.39	1.31	1.33
Cr	0.74	0.63	0.73
Fe	7.73	7.57	8.40
Cu	2.46	3.65	2.61
Zn	3.02	3.40	2.85
Sn	3.38	2.87	3.46
Yb	0.06	0	0
Mn	0	0.16	0.10
Ba	0	0	0.18
Total	100.00	100.00	100.00

8.2.2 After braking tests

8.2.2.1 Disc brake rotor

In this section, those lightweight small scale disc brake rotors that survived the braking test matrix were evaluated using EDX analysis to determine the effect of braking on the elemental composition of the disc rubbing surface; in other words, to evaluate the transfer layer between the brake pad and discs. The two discs that withstood the test

matrix were the coated aluminium alloy and the coated aluminium MMC discs. Although the tribological performance of the coated aluminium alloy was much better, as shown in Chapter 7, EDX analysis for both discs was carried out.

The rubbing surface of the aluminium alloy was examined using EDX analysis and the results of the rubbing surface elemental composition are shown in Figure 8.13 and Table 8.6. EDX analysis of the rubbing surface showed that a 3rd layer had developed on the rubbing surface which consisted of a combination of the disc and pad materials as shown in Table 8.6. The main elements which transferred from the brake pads to the rubbing surface were: carbon (C), iron (Fe), copper (Cu), zinc (Zn) and tin (Sn). An EDX map for the rubbing surface was developed, as illustrated in Figure 8.14, which shows the distribution of the main elements on the rubbing surface. It can be seen that both iron and copper are distributed all over the rubbing surface and there are small areas where aluminium is present.

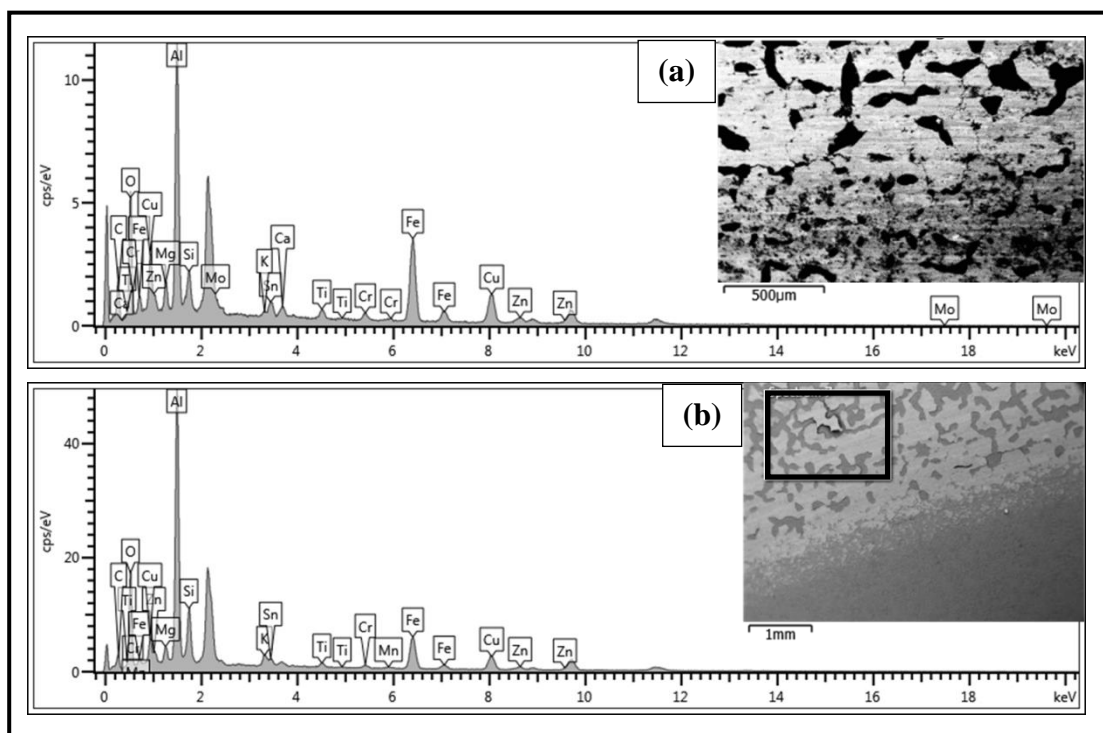


Figure 8.13: EDX analysis for the coated wrought aluminium substrate rubbing surface after braking tests in two different regions (a) and (b).

Table 8.6: Elemental composition of the coated wrought aluminium alloy rubbing surface after braking tests (weight %).

Element	(a)	(b)
C	19.22	9.63
O	19.49	24.46
Mg	2.22	1.78
Al	16.97	26.71
Si	2.18	5.97
K	0.35	1.56
Ca	0.29	0
Ti	1.09	0.85
Cr	1.07	0.70
Fe	18.80	12.62
Cu	12.62	10.44
Zn	2.23	1.97
Sn	3.46	2.97
Mn	0	0.35
Total	100.00	100.00

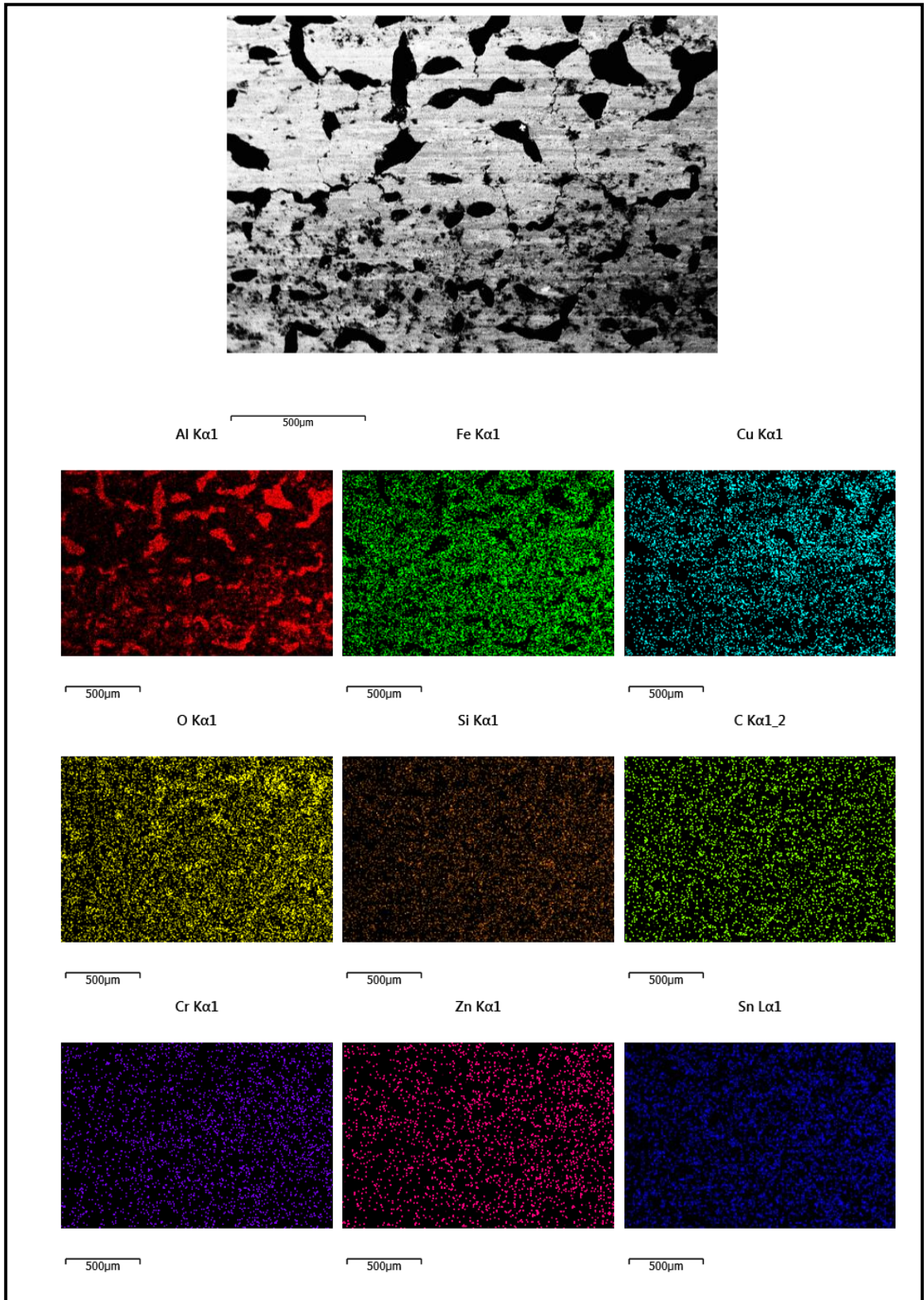


Figure 8.14: EDX map image of the coated aluminium alloy rubbing surface of disc brake rotor after testing.

Although the coated Al-MMC disc did not show good friction performance, the transfer layer material from the brake pads to the disc was investigated, as shown in Figure 8.15 and Table 8.7. Similar to the coated Al-alloy, the main elements transferred from the brake pads to the rubbing surface of the coated MMC rotor were iron (Fe), copper (Cu), zinc (Zn) and tin (Sn) as highlighted in Table 8.7. The presence of carbon in the coating prior to testing makes it difficult to determine whether the carbon elements had transferred from the brake pads to the rubbing surface. In addition, EDX analysis is not a good technique for evaluating the weight % of carbon. The EDX map analysis of the coated Al-MMC disc cross section is shown in Figure 8.16. The map results show that the main elements on the transfer layer are iron and copper which are present on the top of the coating layer. In addition, the SEM image of the cross section shows the variation in the coating thickness after braking, which was in the order of 10-15 μm . Detailed investigation of the coating thickness after the braking tests is presented in section 8.5.

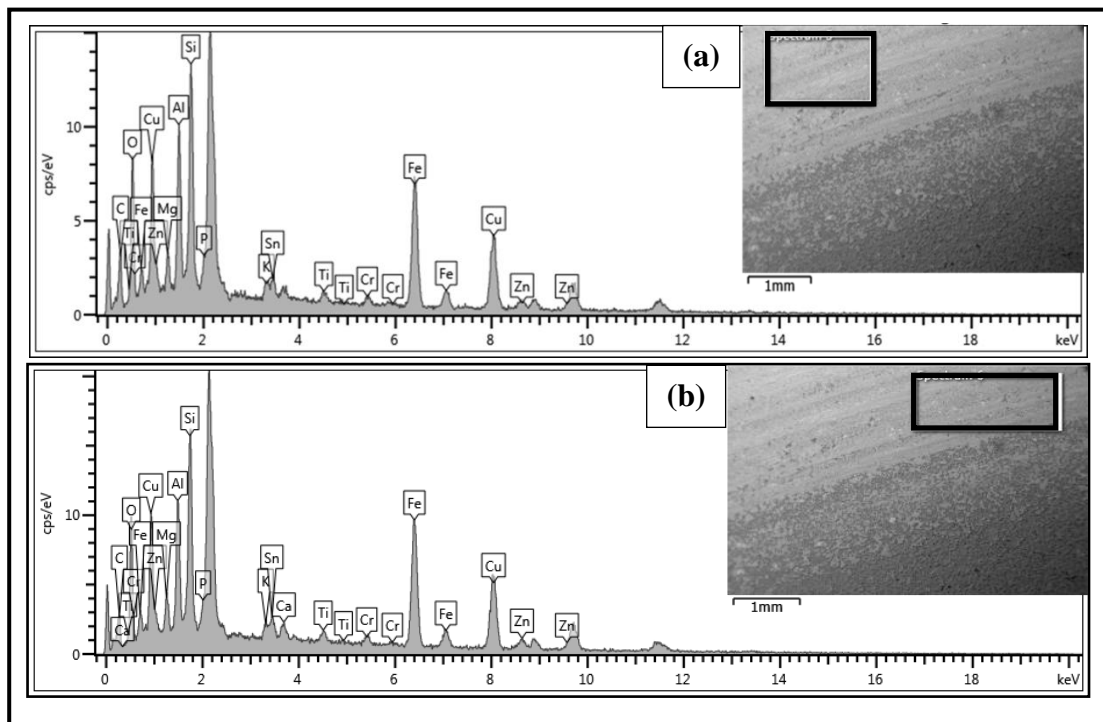


Figure 8.15: EDX analysis for the coated aluminium metal matrix composite substrate rubbing surface after braking tests in two different regions (a) and (b).

Table 8.7: Elemental composition of the coated aluminium metal matrix composite rubbing surface after braking test (weight %).

Element	(a)	(b)
C	15.26	12.33
O	15.53	13.65
Mg	2.15	2.53
Al	7.63	7.02
Si	9.45	9.50
K	1.09	0.93
Ti	0.90	0.91
Cr	0.93	1.05
Fe	19.56	21.03
Cu	21.61	23.83
Zn	2.52	3.12
Sn	3.37	3.72
Ca	0	0.37
Total	100.00	100.00

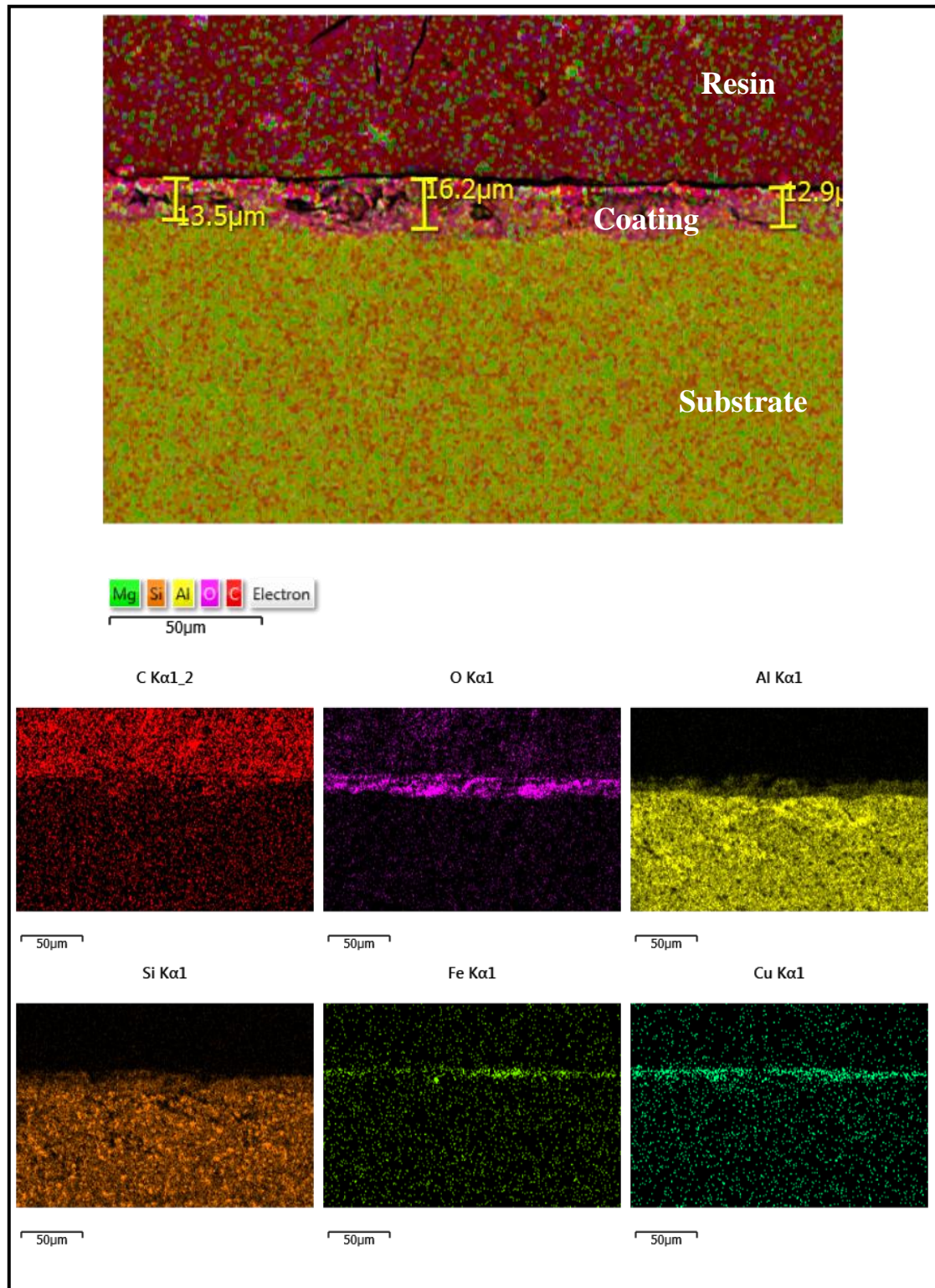


Figure 8.16: EDX map image of the coated aluminium metal matrix composite rotor cross section after testing.

8.2.2.2 Brake pads

The average thickness of the brake pads used in the current study was measured before and after the tests using Micrometre. The results shown in Table 8.8 indicate that the wear rates against both the grey cast iron and the coated aluminium alloy rotor are similar. On the other hand, the wear rate on the brake pads for the plain aluminium is the highest because of the groove formation on the rubbing surface, as explained in Chapter 7. In addition, the brake pads that were used against coated aluminium MMC showed a better wear rate than when compressed against the uncoated substrate. However both brake pads showed a higher wear rate than that the associated with the coated aluminium alloy which might be because of the presence of SiC particles in the coated MMC disc surface. This is a general overview of the variation in thickness for brake pads before and after the braking tests and further investigation should ideally be carried out.

Table 8.8: Brake pad thickness variation before and after braking tests

Disc material	Before testing (mm)	After testing (mm)	Difference (mm)
Coated wrought aluminium (6082)	4.55	4.5	0.05
Coated aluminium metal matrix	4.97	4.85	0.12
Plain aluminium metal matrix	4.95	4.75	0.2
Grey cast iron	4.9	4.84	0.06
Plain wrought aluminium (6082)	4.92	4.3	0.62

8.3 Surface hardness measurements

Micro-hardness tests were carried out for the plain alloy and MMC rotors to investigate their hardness with and without coating. It was found that the PEO coating improved the hardness of the substrate for the wrought aluminium alloy by a factor of 8 while it improved the hardness of the Al-MMC by a factor of 5, as shown in Figure 8.17. It was too difficult to investigate the hardness of the PEO coating without polishing the samples as it was not easy to see the indentation on the coating surface. All the coating samples were polished before the micro-hardness tests. The results obtained showed good agreement with reported results [35, 89, 128]. Overall the PEO coated Al-MMC had by far the highest hardness, perhaps due to SiC phases in the coating for the silicon rich MMC. On the other hand, the hardness of the coated surface of the Al-alloy was lower than expected possibly due to deformation of the alloy substrate in response to the relatively high surface loading (1 kg). The error bars in Figure 8.17 represent the standard deviation of the Hardness value for various disc brake materials as explained in Chapter 3.

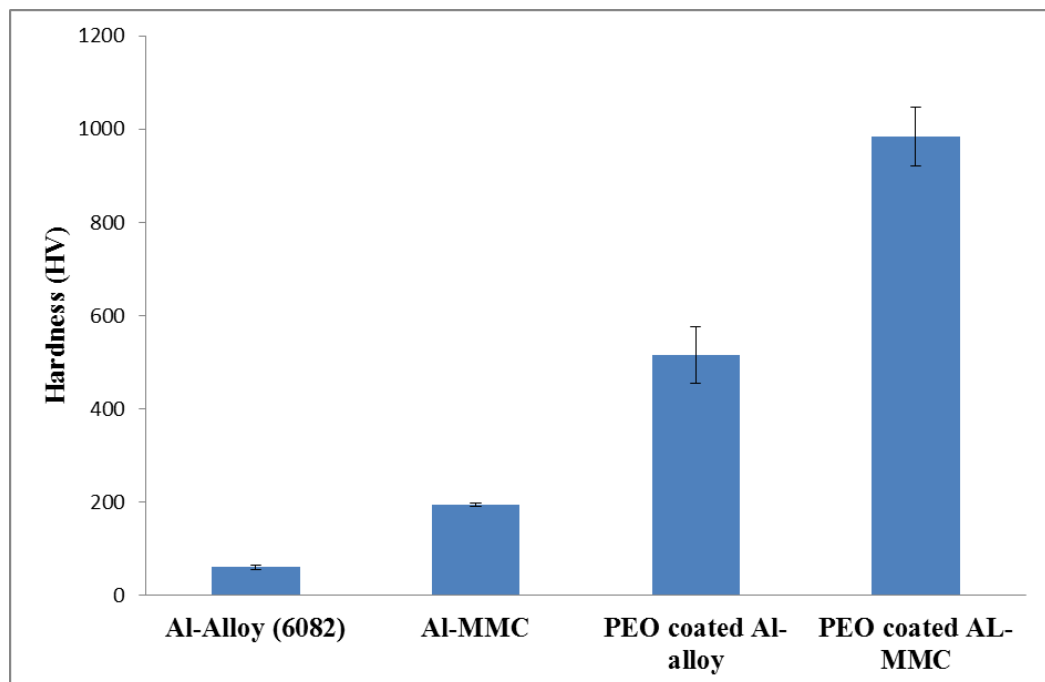


Figure 8.17: Micro-hardness tests of the materials surface

8.4 Roughness analysis

The surface roughness of all the discs was measured, with the results shown in Figure 8.18. The roughness value is important to consider in this project as affects the wear rate. It can be seen that the coated Al-MMC had the highest surface roughness before test due to its surface morphology. The surface roughness of the plain Al-MMC increased after braking tests due to the scratches formed on the rubbing surface, as explained in Chapter 7. The roughness values for both grey cast iron and coated aluminium alloy are seen to be more stable and there was no marked difference between the roughness values before and after the braking tests. The error bars in Figure 8.18 represent the standard deviation of the Ra value for various disc brake materials before and after braking at different location as explained in Chapter 3.

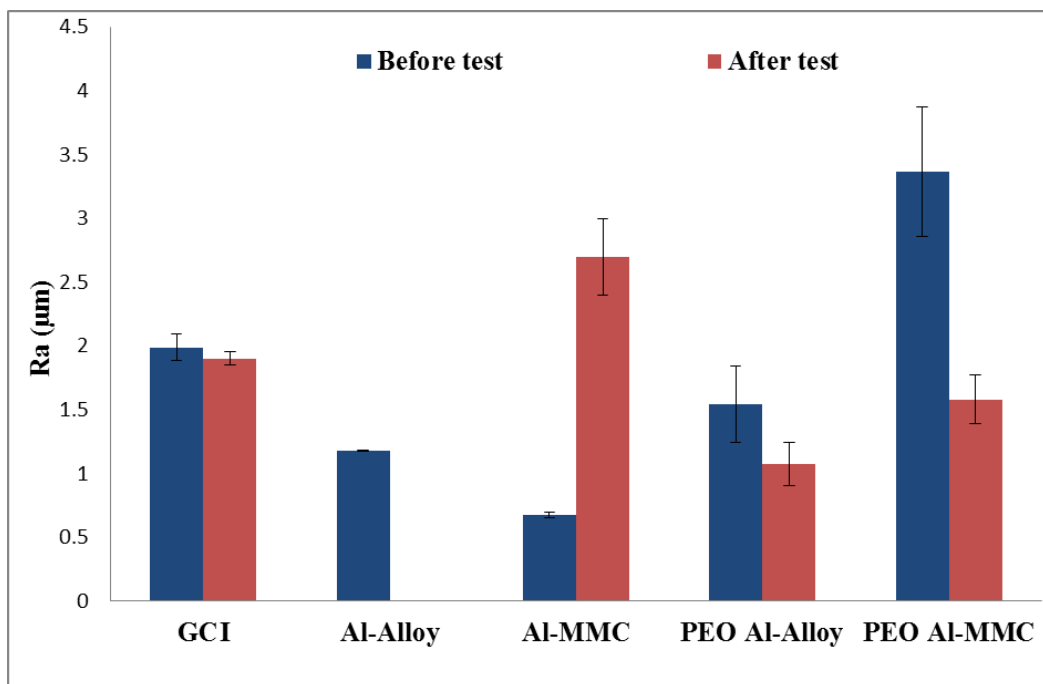


Figure 8.18: Roughness values for the discs before and after the braking tests.

8.5 Coating durability and transfer layer analysis

The coating thicknesses of the Al-alloy and Al-MMC substrate were measured before and after the braking test using the NP Flex optical interferometer (Brucker), as well as the optical and electron scanning microscopes. It was found that the coating thickness

for the Al-MMC substrate was an average 30 μm before the test and 15-20 μm after the test, while the coating thickness of the coated Al-alloy was 50 μm before the test and 49 μm after the test.

Figure 8.19 shows the SEM micrograph images of the coated aluminium alloy and aluminium MMC cross sections after the testing. Based on the EDX characterisation and these SEM images, it was concluded that the Al-alloy had a very dense and uniform coating with alpha/gamma alumina [26, 131] as main elements compared with the Al-MMC. This tends to give a tremendously hard and robust tribo surface with a stable coefficient of friction and, in addition, a good thermal barrier effect as explained in section 8.2.

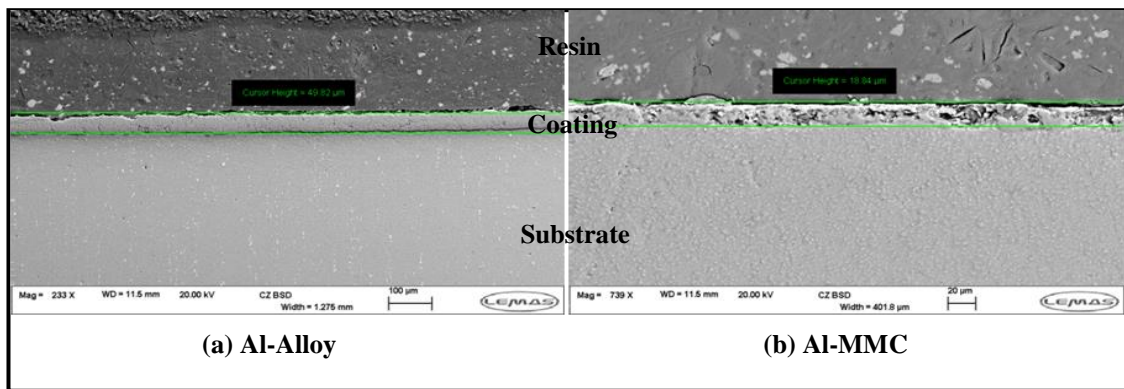


Figure 8.19: SEM images of the coated aluminium alloy and aluminium MMC cross sections after the testing [132].

The NP Flex optical interferometer (Bruker) was used to investigate the surface profile after the braking test, with the results as shown in Figure 8.20 which represents the 3D profile of the different disc brake rotors across a radial section of the rubbing surface. It was found that both coated and uncoated Al-MMC (Figure 8.20 (b) and (c)) were affected by the various braking tests while the coated Al-alloy had a more uniform and stable surface comparable to that of the standard grey cast iron shown in Figure 8.20 (d). In addition, the plain Al-MMC disc rubbing surface began to suffer from scratches when the surface temperature recorded by the sliding thermocouples exceeded (300-350) $^{\circ}\text{C}$. This was because the aluminium on the rubbing surface started to soften, thereby exposing the SiC particles and creating a rough disc surface.

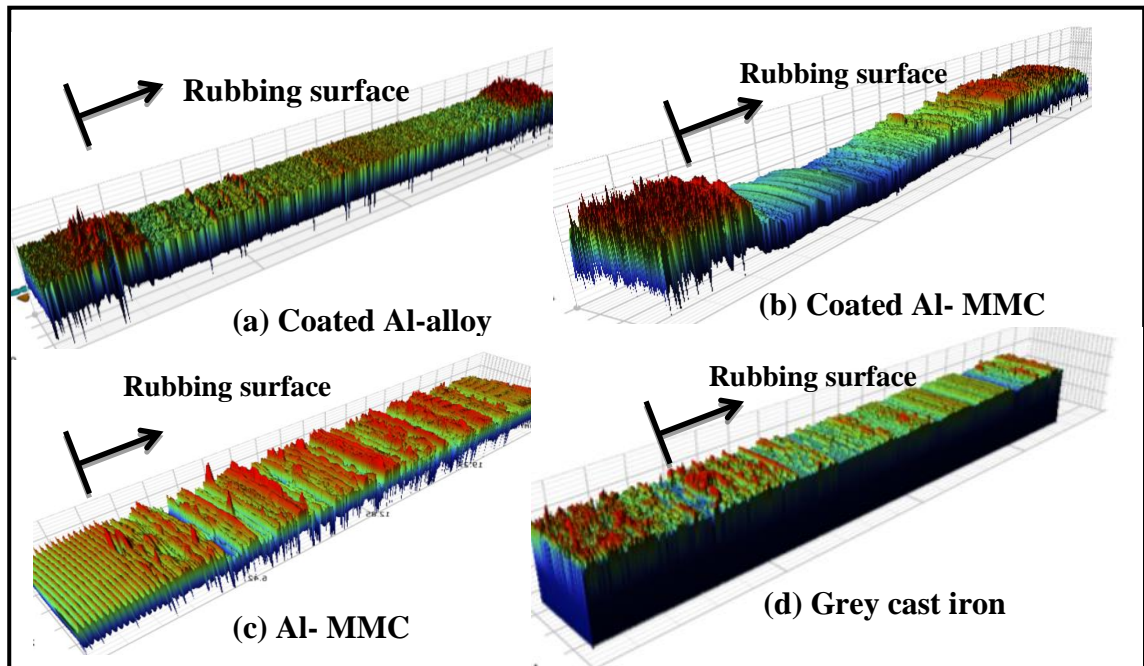


Figure 8.20: 3D profile of the disc brake rotor rubbing surface.

Furthermore, the transfer layer was investigated for the coated disc brake rotor using the NP Flex optical interferometer (Brucker), as well as the optical and scanning microscopes. It was found that an average of 2-4 μm of transfer layer was developed on the rubbing surface which was a combination of the disc and pad materials. It is critical that the transfer layer is considered as it changes the thermal interaction between the disc and pad. Figure 8.21 shows the EDX map image of the coated aluminium alloy disc after the testing. It shows the material transferred from the brake pads to the rubbing surface. As shown on the rubbing surface of the coated aluminium alloy rotor that the main element transferred from the brake pad are: iron and copper compared to the normal coated surface.

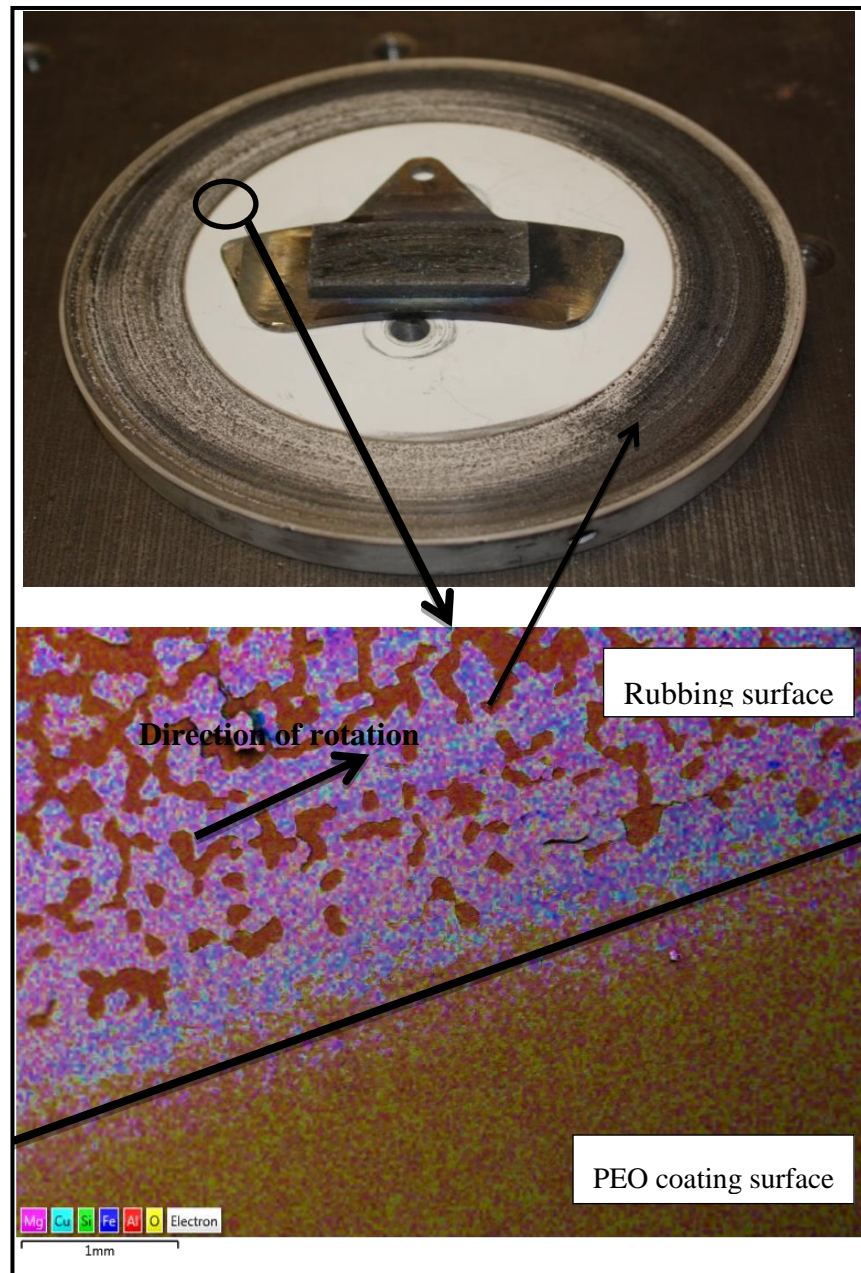


Figure 8.21: EDX map image of the coated aluminium alloy disc brake rotors after testing.

8.6 Characterisation of the failed coated wrought aluminium disc brake rotor

The coated aluminium alloy disc brake rotor was tested under extreme braking condition until disc was failed when reached 550°C as explained in Chapter 7. The coated wrought aluminium disc brake rotor after the catastrophic failure is shown in Figure 8.22. Visual inspection of the failed disc brake rotor showed that the failure

occurred around the inner radius of the rubbing surface circumferences as shown in Figure 8.22a which was expected as the disc beyond this region experiences the maximum temperature. Although the disc shattered in a number of separate pieces, Figure 8.22b, the coating on the rubbing surface remained attached to the pieces and to the remaining central rotor section. The fracture surface of the failed alloy material had a very fibrous appearance (Figure 8.22c) indicating the highly uniaxial nature of the crystalline nature of the wrought alloy. In order to confirm this behaviour SEM analysis for the failed disc was carried out as outlined below.

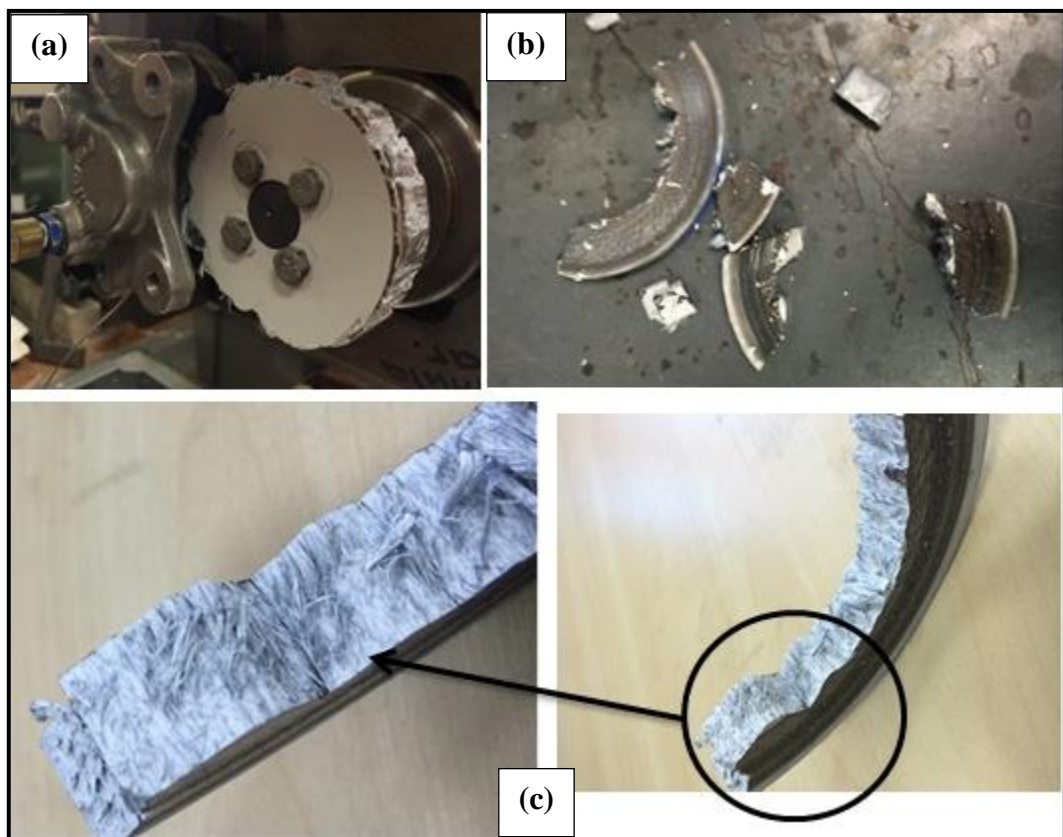


Figure 8.22: Coated wrought aluminium disc brake rotor after extreme braking condition.

The wrought aluminium disc brake rotor was machined from a forged billet that caused the grain boundaries to form predominantly in the axial direction. This led to failure at the grain boundaries around the circumferences of the disc and in order to confirm these small samples of the rubbing surface of the failed rotor were investigated using SEM. The coating layer of the prepared sample was removed by grinding in order to

investigate the grain boundaries structure and mode of failure. The sample was coated with gold in order to have good SEM images as shown in Figure 8.23. The white spots on the sample consist of silicon, iron, magnesium, manganese and copper. The SEM images indicate that the failures occurred along the grain boundaries [133].

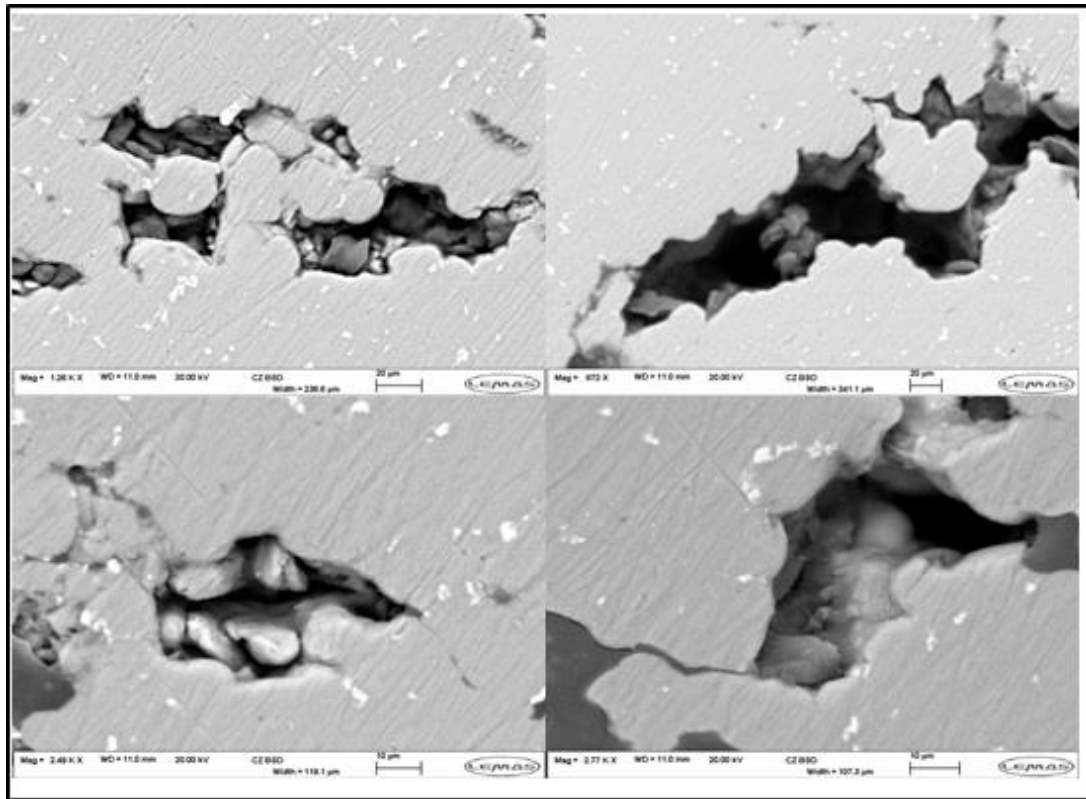


Figure 8.23: SEM images of the failed coated aluminium alloy rubbing surface.

8.7 Summary

The disc brake rotors were investigated before and after braking test using different technique. The microstructures of the rotors were analysed using optical and scanning electron microscopy in plan and cross sectional view. The elemental composition of the rotors were analysed before and after braking test using EDX analysis. Also the same technique was used to identify the transfer layer on the disc rubbing surface. The mechanical properties of the coating and substrates were obtained using the micro hardness machine, Furthermore; the coating durability was carried out to evaluate the

coating before and after the braking tests. The following points summarise the material characterisation results from the current study:

- In the SEM image of the PEO coating (Figure 8.8 and Figure 8.9), a loose layer was observed between the resin and the outer layer of coating.
- The PEO alumina layer adhered well to the aluminium alloy substrate and was more uniform when compared to that on the aluminium metal matrix composite (Figure 8.19).
- The PEO coatings significantly improve the hardness of the substrate (Figure 8.17) with the PEO coated Al-MMC having by far the highest hardness.

CHAPTER 9:

DESIGN OF EXPERIMENT AND OPTIMISATION ANALYSIS

9.1 Introduction

The results obtained in the previous Chapters showed that the PEO coated wrought aluminium disc brake rotor could potentially be used in the automotive industry. The 2D axisymmetric finite element models derived in chapter 6 were used in the current analysis in order to find the optimum coated disc brake rotor thickness. A Taguchi analysis was applied to the validated finite element model allowing for consideration of all the critical design and material factors. Based on the results of the Taguchi analysis, a parametric sensitivity analysis was carried out to define the parameters that affect the thermal performance of the lightweight disc brake rotor. Optimisation analysis was then carried out based on the Taguchi study to find the optimum disc brake rotor thickness. The optimum design was then validated using the numerical model to simulate a well-known 'worst case' braking event.

9.2 Nominated finite element models

The finite element model used in the current study is the same model derived and explained in Chapter 6; namely the axisymmetric transient heat transfer model. The main advantages of using this model are as follows: it has been validated with the experimental results and showed generally very good agreement as described in Chapter 7. The model geometry can be changed easily to accommodate amendments to the various parameters that were used in the current analysis. The computational time to run various braking events is acceptable as the optimisation study required more than 60 runs to be simulated.

9.3 The Taguchi study

In the development of the numerical model explained in Chapter 6, there were many factors and parameters in the disc brake design which could be modified. These factors could improve and optimise the design, especially for the coated lightweight disc brake rotor. The main problem was that the number of factors that needed to be considered in order for the study to be valid would require a large number of numerical experiments. In order to simplify the proposed exercise, a Taguchi analysis was performed to find the influence of different parameters and factors on the thermal performance of small scale solid disc brake rotors.

9.3.1 Fundamentals

The Design of Experiments approach was developed by Taguchi as a process for evaluating all possible methods of reaching a desired objective, both efficiently and reliably [134]. The Taguchi technique is widely used in design and manufacturing processes in order to find the optimum combination of parameters. Also, this technique allows the designer to assess the effect of various factors on the quality of the product. Taguchi defined the factors as either external or internal, where internal factors are those which can be modified by the designer and external factors are those which cannot be modified in a product [135].

In the current study, L_8 and L_{12} orthogonal arrays were used for the uncoated and coated disc brake rotor investigation respectively. The uncoated disc brake rotor model had six factors that needed to be investigated at two finite levels, whilst the coated disc brake rotor model had eight factors that needed to be studied at two finite levels, as explained below. The defined orthogonal array, which presents the number of runs for each model with the different factors at different combinations of levels, was used to investigate the effect of the different factors on the critical output, which is the maximum temperature of the disc.

In order to maximise the robustness of the exercise, the signal-to-noise (S/N) ratio was used to calculate the so-called “main effect” of each parameter. The main advantages of using the S/N ratio are that it measures relative quality and is independent of the mean

value. It also reflects the variability in the response of a system caused by noise factors and does not introduce unnecessary complications [136].

The S/N ratio is calculated from the following equation [135]:

$$\frac{S}{N} = -10 \log_{10}(V) \quad (9.1)$$

in which the variance V is given by:

$$V = \frac{1}{N} (Y_1^2 + Y_2^2 + \dots + Y_N^2) \quad (9.2)$$

where V is the variance, N is the number of data points and Y_i is the value of the i^{th} data point (i.e. in this case, the maximum disc temperature). The main effects are then calculated by finding the difference between the S/N ratio between level 1 and 2 of the particular factor; the higher the value, the greater is the influence that the factor has on the “main effect”, which is the maximum rotor surface temperature.

9.3.2 Uncoated disc brake rotor

The Taguchi analysis was carried out for the uncoated disc brake rotor model explained in Chapter 6. The selected factors used for the current analysis are shown in Table 9.1 at two different levels and the L8 Taguchi matrix is presented in Table 9.2, factor G was not used in the current analysis as the number of factor used in this study are six. The factors that have been selected are: disc thickness, partition ratio, disc density, disc thermal conductivity, disc specific heat and convection coefficient. The factor ranges were selected based on the literature for different materials from lightweight aluminium alloy up to steel and cast iron discs. The brake event parameters selected for carrying out the Taguchi study were as follows: drag braking for 10 s, with a constant vehicle speed of 60 km/h down an average slope of 12% with an equivalent vehicle mass of 1400 kg which is typical of the conditions experience by a vehicle during part of the Grossglockner descent. The reason for not considering the full 23 minute of the Grossglockner descent is the very large computational time required for such a run.

Table 9.1: Factors selected for the Taguchi study with their maximum and minimum levels for the uncoated disc brake rotor.

Factor		Level	
		1	2
A	Disc thickness (mm)	5	15
B	Disc/pad partition ratio	0.83	0.95
C	Density (kg/m³)	2700	7900
D	Thermal conductivity (W/m²K)	48	240
E	Specific heat (J/kgK)	450	900
F	Convection coefficient (W/m²K)	30	70

Table 9.2: L₈ Taguchi matrix.

Run	Factors						
	A	B	C	D	E	F	G
1	1	1	1	1	1	1	1
2	1	1	1	2	2	2	2
3	1	2	2	1	1	2	2
4	1	2	2	2	2	1	1
5	2	1	2	1	2	1	2
6	2	1	2	2	1	2	1
7	2	2	1	1	2	2	1
8	2	2	1	2	1	1	2

The axisymmetric uncoated disc brake rotor model was used to simulate the thermal performance of uncoated disc brake rotors for the different factor combinations presented in Table 9.1 and Table 9.2. The temperature distributions at the end of the drag braking event are shown in Figure 9.1.

A summary of the Taguchi study for the current analysis is presented in Table 9.3, where the maximum temperature of the disc is shown for the different factor combinations. It can be seen that the highest disc temperature was obtained in run 1 where the disc thickness was at its lowest value. The lowest disc temperature was in run 6 where the disc thickness was at its highest value. This is because the thermal inertia of the disc is directly related to its size.

The S/N analysis was carried out based on equations (9.1-9.3) and the calculated results are presented in Table 9.4 and Figure 9.2. The results show that disc thickness has the largest effect on the maximum disc brake temperature. On the other hand, convection coefficient has the lowest effect on the maximum disc temperature which may be because a solid disc brake rotor was used and therefore there is no convective heat loss from the vanes. The other selected factors have almost the same effects on the maximum disc brake temperature. Although the thermal properties of the disc have an effect on the disc brake temperature, in reality it is difficult to design a material with specific thermal properties. In addition, the partition ratio is dependent on the thermal properties of both the disc and pad material which is complicated to control. It was concluded that the disc brake thickness has the largest effect on the maximum disc brake temperature and this factor will be used in the optimisation analysis. The results obtained from the current analysis agree well with other published results [19].

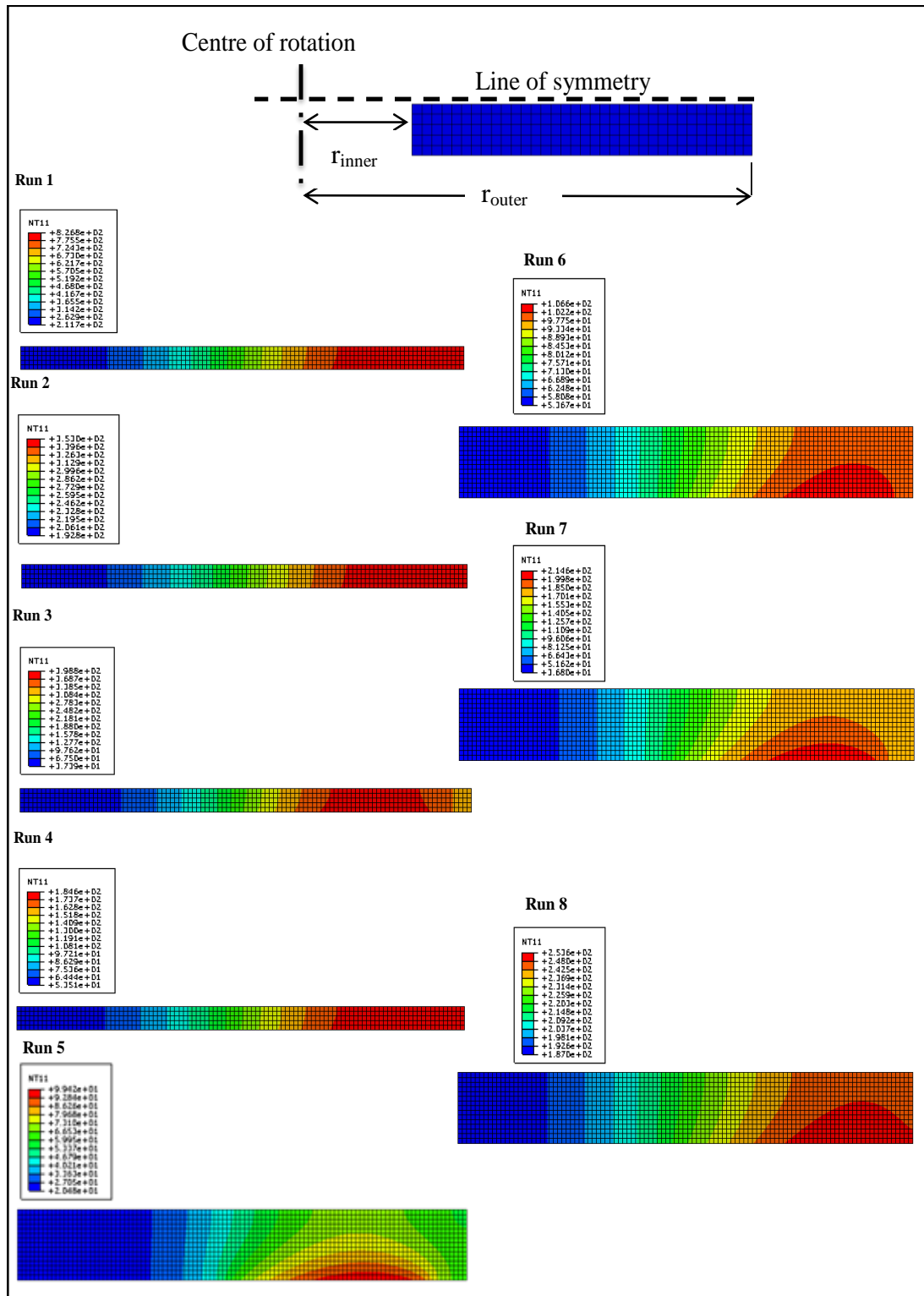


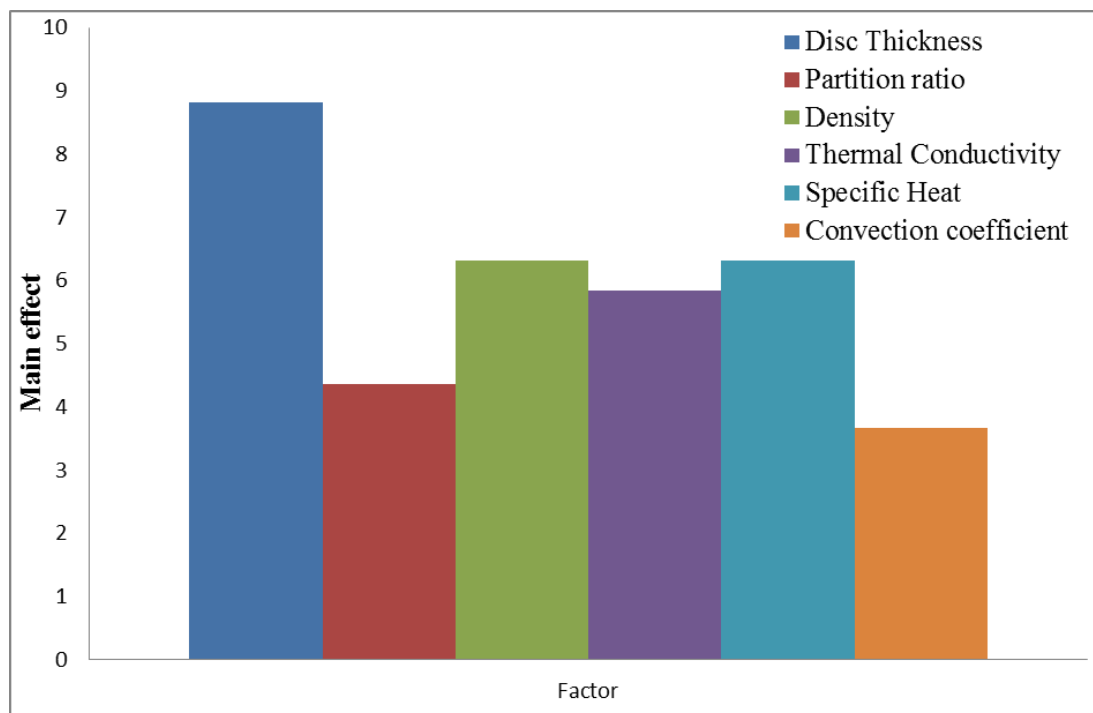
Figure 9.1: Temperature distribution at the end of the braking event for the Taguchi study for the uncoated disc brake rotor.

Table 9.3: Results of the L_8 Taguchi study of the uncoated disc brake rotor.

Run	Factor						Maximum surface temperature (°C)
	A	B	C	D	E	F	
	Disc thickness (mm)	Partition ratio	Density (kg/m ³)	Thermal conductivity (W/m ² K)	Specific heat (J/kgK)	Convection coefficient (W/m ² K)	
1	5	0.83	2700	48	450	30	826.8
2	5	0.83	2700	240	900	70	353.0
3	5	0.95	7900	48	450	70	398.8
4	5	0.95	7900	240	900	30	184.6
5	15	0.83	7900	48	900	30	99.4
6	15	0.83	7900	240	450	70	106.6
7	15	0.95	2700	48	900	70	214.6
8	15	0.95	2700	240	450	30	253.6

Table 9.4: S/N Ratio and main effects for the uncoated disc brake rotor.

Level	Factor					
	A	B	C	D	E	F
	Disc thickness (mm)	Partition ratio	Density (kg/m ³)	Thermal conductivity (W/m ² K)	Specific heat (J/kgK)	Convection coefficient (W/m ² K)
1	-53.98	-53.16	-53.6	-53.51	-53.60	-52.96
2	-45.17	-48.80	-47.29	-47.67	-47.29	-49.30
Main effects	8.81	4.36	6.31	5.83	6.31	3.65

**Figure 9.2: Main effects for the uncoated disc brake rotor.**

9.3.3 Coated disc brake rotor

The results obtained from the uncoated disc brake rotor show that the disc thickness has the largest effect on the maximum disc brake temperature. The same analysis used in the previous section was used in the current section where the effect of coating thickness and coating thermal properties was included with different factors and Taguchi matrix as shown in Table 9.5 and Table 9.6. The factors I, J and K was not used in this analysis as the number of factor selected are eight factors.

The maximum disc brake temperature and the S/N ratios were calculated for the different combinations (shown in Table 9.5), with the results as shown in Table 9.7 and Table 9.8 respectively. The summary of these results in Figure 9.3 indicates that the substrate thickness has the largest effect and the substrate thermal conductivity the second largest effect. Overall the coating thickness has the smallest effect on the maximum disc brake temperature.

From this analysis it was concluded that the substrate thickness is the main factor that has the largest effect on the maximum surface temperature. This is because the thermal inertia of the disc is directly related to its size. The coating thickness has the smallest effect on the maximum surface temperature but it is used in the following optimisation analysis as it has a major influence on the cost and processing time of the PEO process. It is also a parameter that can be relatively easily controlled compared to the material properties of the alumina coating which are largely pre-determined.

Examination of Table 9.7 shows that run 7 gave the lowest maximum surface temperature. The factors selected for this run satisfy the best values recommended by the main effects shown in Figure 9.3, i.e. maximization of substrate thickness, maximisation of substrate thermal conductivity and maximisation of the coating thermal conductivity; therefore a confirmation run was not deemed necessary.

Table 9.5: Factors selected for the Taguchi study with their maximum and minimum levels for the coated disc brake rotor.

Factor		Level	
		1	2
A	Disc thickness (mm)	5	15
B	Disc density (kg/m³)	2700	3100
C	Disc thermal conductivity (W/m²K)	90	240
D	Disc specific heat (J/kgK)	800	900
E	Coating thickness (µm)	30	100
F	Coating density (kg/m³)	2700	3200
G	Coating thermal conductivity (W/m²K)	0.5	4
H	Coating specific heat (J/kgK)	800	895

Table 9.6: L₁₂ Taguchi matrix

Run	Factors										
	A	B	C	D	E	F	G	H	I	J	K
1	1	1	1	1	1	1	1	1	1	1	1
2	1	1	1	1	1	2	2	2	2	2	2
3	1	1	2	2	2	1	1	1	2	2	2
4	1	2	1	2	2	1	2	2	1	1	2
5	1	2	2	1	2	2	1	2	1	2	1
6	1	2	2	2	1	2	2	1	2	1	1
7	2	1	2	2	1	1	2	2	1	2	1
8	2	1	2	1	2	2	2	1	1	1	2
9	2	1	1	2	2	2	1	2	2	1	1
10	2	2	2	1	1	1	1	2	2	1	2
11	2	2	1	2	1	2	1	1	1	2	2
12	2	2	1	1	2	1	2	1	2	2	1

Table 9.7: Results of the L_{12} Taguchi study of the coated disc brake rotor.

Run	Factor								Maximum surface temperature [°C]
	A	B	C	D	E	F	G	H	
	Disc thickness (mm)	Disc Density (kg/m ³)	Disc Thermal conductivity (W/m ² K)	Disc Specific heat (J/kgK)	Coating thickness (µm)	Coating density (kg/m ³)	Coating thermal conductivity (W/m ² K)	Coating specific heat (J/kgK)	
1	5	2700	90	800	30	2700	0.5	800	368
2	5	2700	90	800	30	3200	4	895	350
3	5	2700	240	900	100	2700	0.5	800	326
4	5	3100	90	900	100	2700	4	895	296
5	5	3100	240	800	100	3200	0.5	895	321
6	5	3100	240	900	30	3200	4	800	233
7	15	2700	240	900	30	2700	4	895	104
8	15	2700	240	800	100	3200	4	800	118
9	15	2700	90	900	100	3200	0.5	895	204
10	15	3100	240	800	30	2700	0.5	895	120
11	15	3100	90	900	30	3200	0.5	800	138
12	15	3100	90	800	100	2700	4	800	137

Table 9.8: S/N Ratio and main effects for the coated disc brake rotor.

Level	Factor							
	A	B	C	D	E	F	G	H
	Disc thickness (mm)	Disc Density (kg/m ³)	Disc Thermal conductivity (W/m ² K)	Disc Specific heat (J/kgK)	Coating thickness (μm)	Coating density (kg/m ³)	Coating thermal conductivity (W/m ² K)	Coating specific heat (J/kgK)
1	-50.06	-48.55	-48.49	-48.02	-47.73	-47.93	-48.45	-47.63
2	-42.95	-46.94	-46.68	-47.03	-47.91	-47.71	-47.10	-48.01
Main effects	7.10	1.61	1.81	0.98	0.18	0.21	1.35	0.38

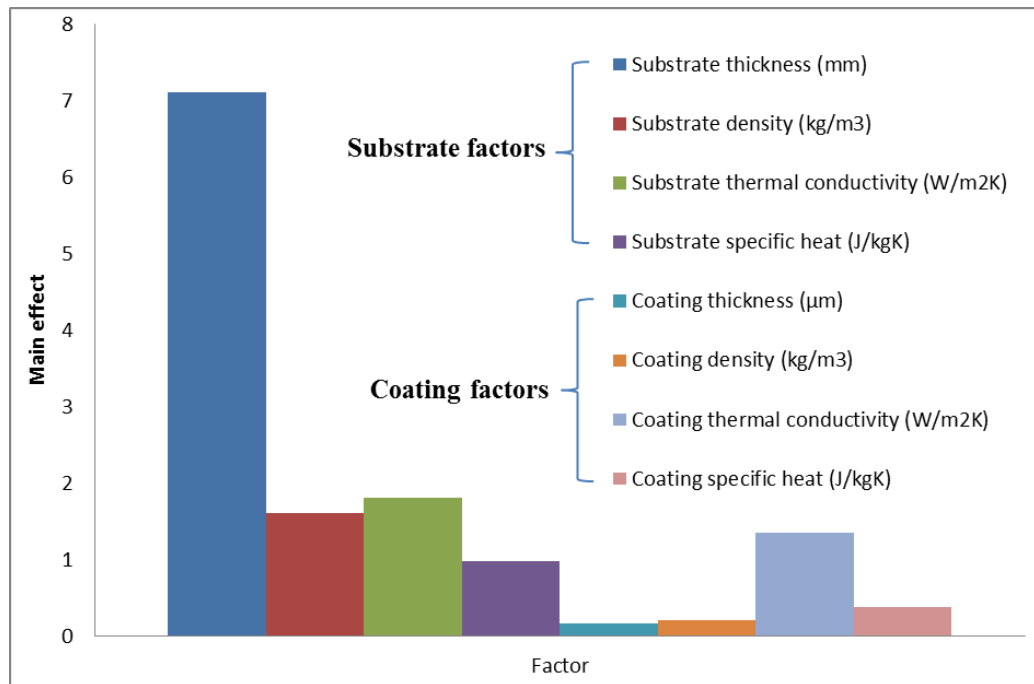


Figure 9.3: Main effects for the coated disc brake rotor.

9.4 Optimisation analysis

The coated aluminium alloy disc has already been shown to have very good thermal and tribological performance. In this section, a genetic algorithm was used to investigate the optimum thickness of the coating and the disc brake substrate in order to further improve the thermal performance. The material properties assumed were similar to the material properties used in the previous analysis for the PEO coated aluminium alloy (6082) rotor with the same overall geometry. The optimisation problem defined in the current section is to minimise the weight of the disc brake rotor by minimising the total thickness of the coating (t_c) and substrate (t_s) based on the following constraints: the maximum temperature at the surface of the coating must be less than 550°C ; the maximum temperature in the substrate must be less than 450°C ; the coating thickness must be in the range 30-100 μm ; and the disc thickness must be in the range 5-15 mm. These parameters were selected based on material limitation and overall size constraints.

Determining the best combination of design variables located within the design space is a typical optimisation problem. In this case, two design variables were investigated: namely, coating thickness (t_c) and substrate thickness (t_s). Simulating every possible combination of even just these two variables would be far from straightforward, so in order to find the best combination, meta-modelling was used which provides an accurate set of results using the minimum number of experiments or simulations [48].

The Optimal Latin Hypercube (OLH) approach was used to produce 30 different combinations of the selected design variables. This approach distributes the design variables in the design space uniformly within the lower and upper limits of each variable. The selected OLH approach is a combination of two parts, which use build and validation models. The main advantage of the two model approach is that it maximises the uniformity of the variables in the design space.

The OLH building and validation points were generated uniformly by using the permutation genetic algorithm (PermGA) [48]. The two design variables were distributed uniformly through the space within the lower and upper limits to form 30 different combinations of building and validation points as shown in Figure 9.4. The building points were used to construct the output response surface of the design variable. The validation points were used to ensure that the fitted response surface accurately reflect the system behaviour and can therefore be used with confidence to carry out the optimisation exercise

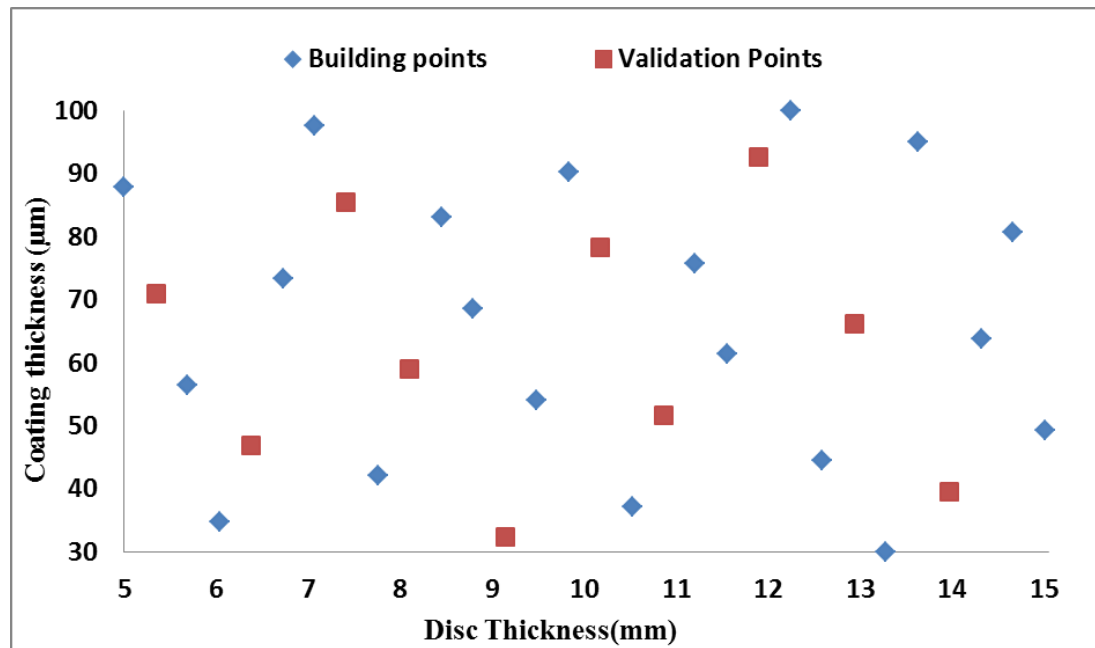


Figure 9.4: Building and validation points.

The axisymmetric transient finite element model for the coated aluminium alloy rotor was used to investigate the 30 combinations using Abaqus software. The braking event selected for the simulation was as follows: high rate constant g stop with an initial vehicle speed of 205 km/h (the maximum specified speed from a punto) and deceleration of 1 g for a vehicle mass of 1400 kg. The main reason for choosing this braking event was to generate the maximum achievable surface temperature on the rotor within a reasonable computational run time. The maximum surface temperature of the coating and the substrate was monitored throughout the simulation and used to obtain an approximate response within the design space using the moving least squares approximation method as shown for the coating and substrate maximum temperatures in Figure 9.5 and Figure 9.6 respectively. These results confirm that the substrate thickness has a much stronger influence on the surface temperatures of both the coating and substrate compared to the coating thickness.

The optimisation problem was then solved using the genetic algorithm (GA) option of Hyperstudy v12 [137]. The main objective was to minimise both the coating and substrate thickness, thus reducing the total weight of the brake rotor, in accordance with the constraints defined previously. The results show that the optimum point that met all

the constraints and the objective function was $t_s = 12.24$ mm and $t_c = 30$ μm given a total disc thickness of 12.25 mm. This design will be used in the following section to make sure that it meets the various braking application requirements.

A comparison between the predicted optimum results and the simulation results for this particular design variable is shown in Table 9.9. It can be seen that the maximum temperatures for the coating and for the substrate predicted by the optimisation algorithm are very similar to those of the actual simulation which gives confidence in the validity of the optimisation algorithm.

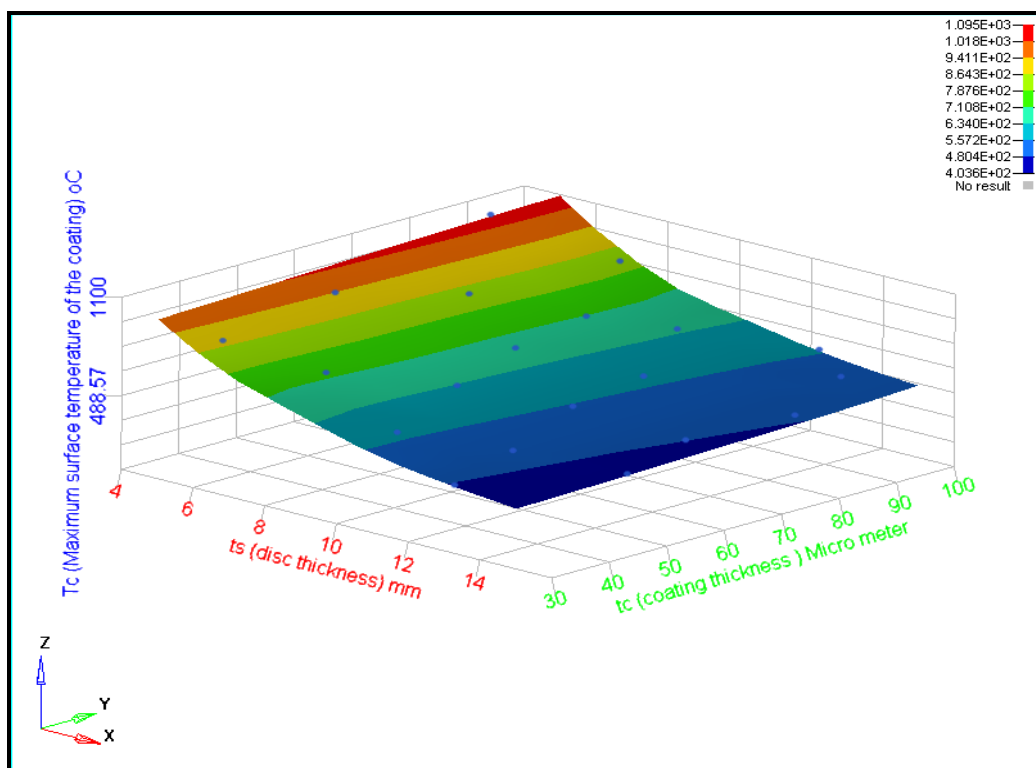


Figure 9.5: Response surface of maximum surface temperature of the coating for the two design variables.

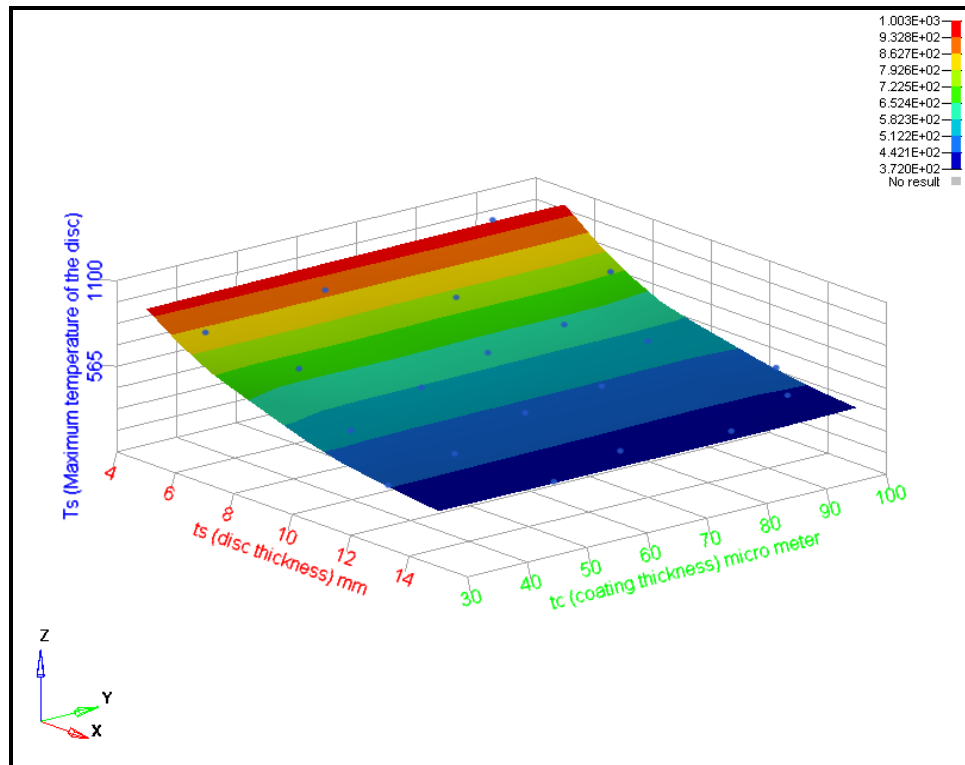


Figure 9.6: Response surface of maximum temperature of the substrate for the two design variables.

Table 9.9: Optimum and simulation results of the two design variables.

Design variables		Optimisation algorithm predictions		Actual simulation results		Error	
Disc thickness (mm)	Coating thickness (µm)	Tc (°C)	Ts (°C)	Tc (°C)	Ts (°C)	Tc (°C)	Ts (°C)
12.24	30	472	443	473	445	0.42	0.46

9.5 Validation of the optimum results

The optimum results obtained in the previous section were used to investigate the thermal performance of the coated disc brake rotor for a small sized vehicle (1400 kg fully loaded) during two extreme braking events as follows:

1. Long continuous drag braking (Grossglockner Alpine descent) lasting 23 min. Average slope of 12% and average vehicle speed of 80 km/h.
2. High rate constant g stop with a vehicle speed of 205 km/h and deceleration of 1 g.

The temperature distribution at the end of the Grossglockner descent is given in Figure 9.7. The results showed that the temperatures for the coating surface and the substrate were within the limits defined in the optimisation problem. This means that the optimisation exercise resulted in an acceptable thermal performance for the coated aluminium alloy disc brake rotor under extreme drag braking conditions.

The same model was used with the second braking event, which was the high g stop. The maximum surface temperature of the coating and substrate is shown in Figure 9.8 during and after the braking event. In addition, the temperature distribution during the test at different time steps is shown in Figure 9.9. The results indicate that for the high g stop, the optimum disc brake model again shows acceptable thermal performance and the temperature predicted is within the safe design limits for both the coating and substrate.

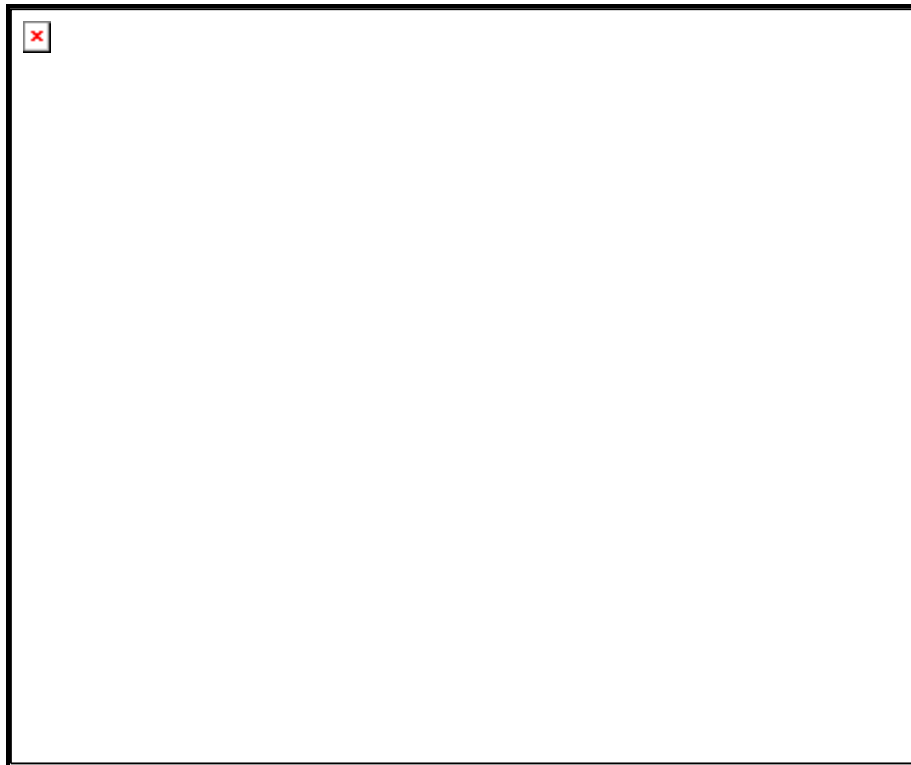


Figure 9.7: Temperature distribution of the coated small scale disc brake rotor at the end of simulation for the Alpine descent.

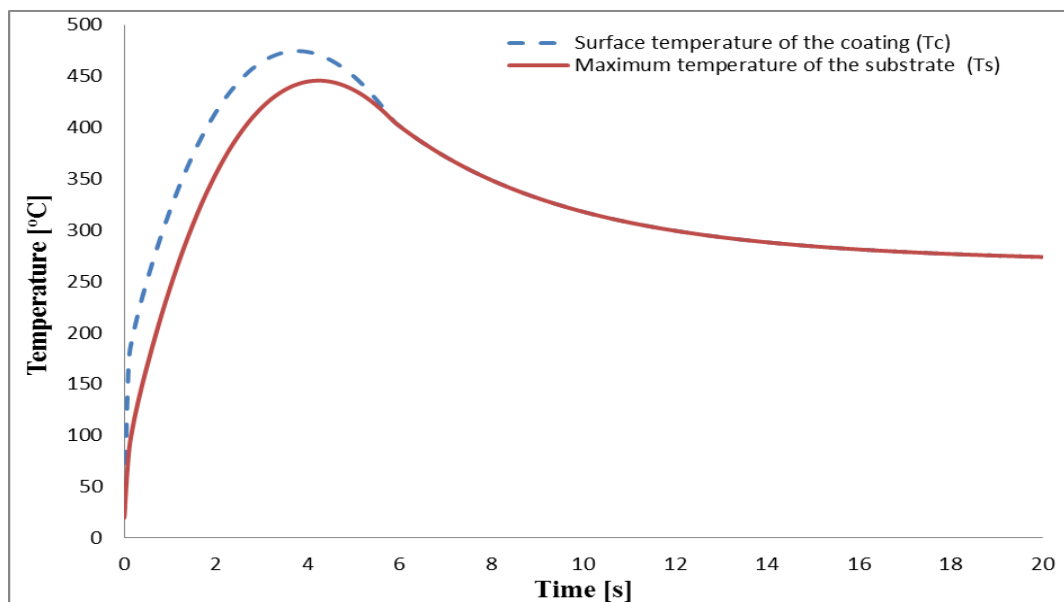


Figure 9.8: Maximum temperature on the coating and substrate outer surfaces during the high g braking test.

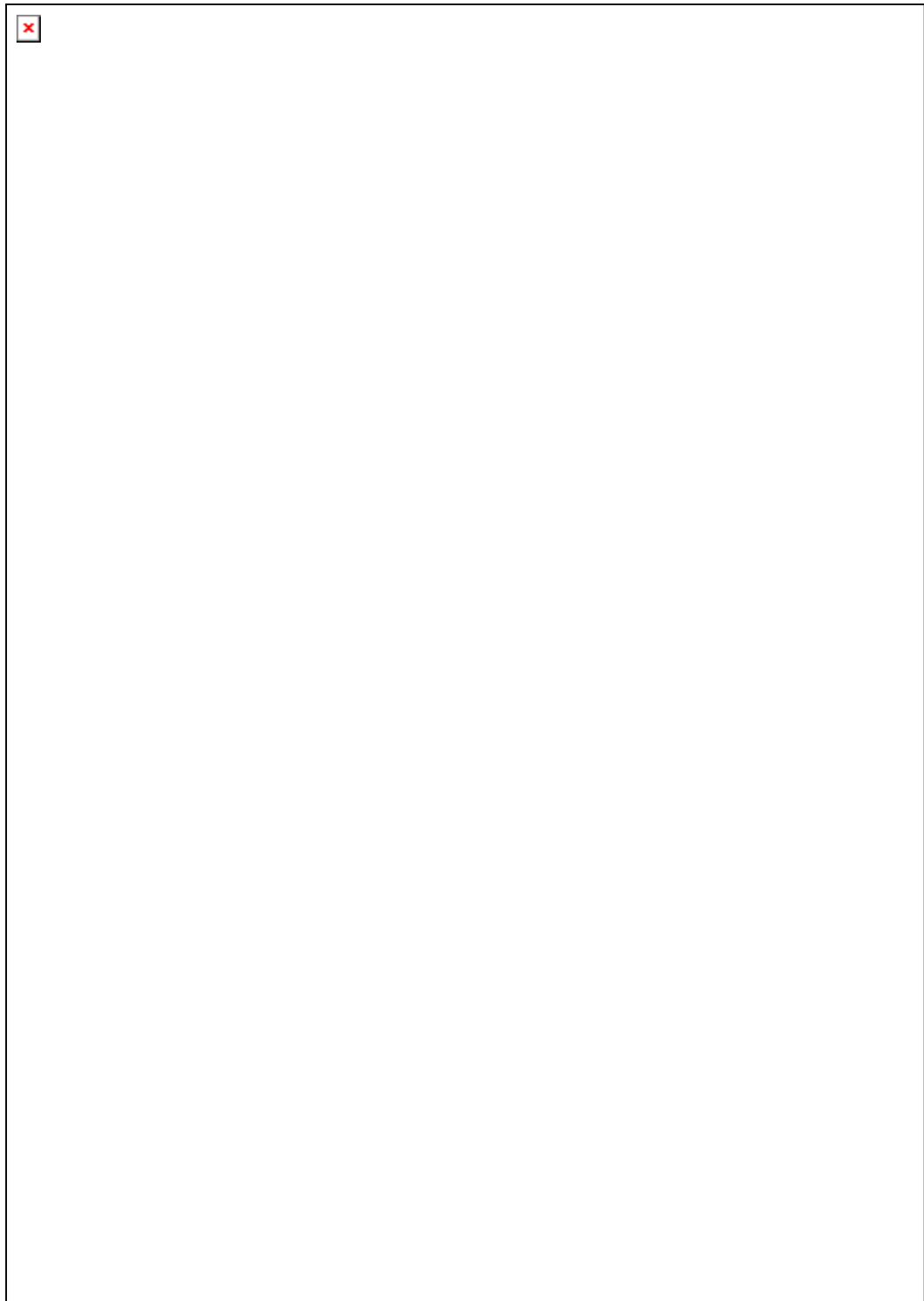


Figure 9.9: Temperature distribution of the coated small scale disc brake rotor for the high rate constant g stop.

9.6 Summary

A sensitivity analysis for the various brake rotor factors was undertaken using the Taguchi approach. The Taguchi analysis showed that substrate thickness has the largest effect on the predicted temperature distribution through the disc brake rotor. Material properties also have an influence on thermal performance but designing a material with specific thermal properties would be far from easy. The optimisation analysis was carried out based on the genetic algorithmic technique and the Optimal Latin Hypercube Design of Experiment. The design variables for the optimisation problem were the coating and substrate thicknesses. The optimum design variables were found to be a coating thickness (t_c)=30 μm and disc thickness (t_s)= 12.24 mm. The results show that this optimised design can withstand two different and very aggressive braking events for a vehicle of total mass 1400 kg. The current optimisation analysis could be used with a more complex disc brake geometry, such as a ventilated rotor, to allow greater heat loss by convection and therefore a greater vehicle mass and/or greater factor of safety.

CHAPTER 10:

DISCUSSION OF KEY FINDINGS

10.1 Introduction

The selection of a specific material is highly dependent on its functionality within its operational environment. There are many applications in the automotive industry which require low weight, manufacturability, machinability and a high strength to weight ratio. This thesis has consequently investigated the possibility of replacing a cast iron disc brake rotor with a lightweight alternative that is based upon an alumina coated aluminium alloy. The main contribution of this work has been to verify the use of a PEO coating on an aluminium alloy surface to enhance the performance of the evolving lightweight disc brake application. The main aim of this chapter is to draw together and discuss the findings and analysis presented throughout the thesis in order to evaluate their impact on the outcome. A detailed discussion of the results is presented in each chapter and the following sections discuss the findings and limitations of a coated aluminium alloy as a candidate disc brake rotor from an experimental and numerical perspective.

10.2 The importance of numerical and experimental analysis in the area of lightweight disc brake rotor

Replacing the conventional grey cast iron disc brake with an alternative lightweight material such as an aluminium alloy is a great challenge and one that is worth pursuing in order to reduce vehicle emissions to the environment. To address this challenge, the present research utilised the development of both numerical and experimental approaches to fully investigate the thermal and tribological performance of a lightweight disc brake rotor concept.

A thorough literature review was carried out on fundamental theories of the thermal analysis of disc brake rotors. It was identified that numerical modelling is an essential tool with which to investigate the thermal performance of a disc brake rotor. In addition, it was concluded that aluminium alloys and aluminium metal matrix composites are the best candidates for the lightweight brake rotor application because of their low cost and manufacturability as explained in detail in Chapter 2. Aluminium alloys have been widely used in the automotive industry but their limitations, such as low hardness, low melting temperature and corrosion resistance prevent them from being used in brake system applications without appropriate surface treatment. Experimental analysis was identified as necessary to assess the thermal and tribological performance of coated lightweight disc brake rotors and to validate the numerical models.

A one dimensional thermal model was first developed in Matlab to investigate the effect of various parameters on disc brake thermal performance and to understand the bulk thermal behaviour of solid disc brake rotors as discussed in Chapter 4. Overall it was found that the Matlab results showed good agreement with results generated by a similar 1D Abaqus FE model and with those in the literature as shown in Figure 4.10. In addition the Abaqus FE software was used to study coated rotors using different modelling approaches. The numerical study showed that there are approximate techniques which can be used to model the coating layer which reduced the simulation time and the memory usage within Abaqus. In particular, the thermal resistance modelling approach, which does not explicitly model the thin coating layer, reduced the analysis time by up to 25% and also significantly reduced the computer memory needed for such analysis. Specific code was developed to link the Abaqus finite element model to Matlab software and this further reduced the simulation time (up to 65%) and allowed more complicated analyses to be conducted in Abaqus, for example repetitive braking events. The outcomes from the 1D transient thermal model were used to develop the scaling methodology and to design the test rig in order to carry on the experimental analysis.

A scaling methodology was derived based on constant energy principles with the aid of the one dimensional model developed in Chapter 4 and used to design a small scale brake dynamometer to be employed alongside the existing full size dynamometer to

investigate the thermal performance of small scale disc brake rotors. All the equipment used in the brake testing was calibrated based on well-established standards and procedures. Both test rigs were commissioned and showed good operating performance. LabView software was developed for both full and small scale brake dynamometers to monitor and control the test rigs and to apply the different braking conditions. The proposed scaling methodology was validated numerically and experimentally (as explained in Chapter 7). The results showed good agreement between the full and small scale disc brake rotors with only small differences in surface temperatures due to a combination of the following:

- The effect of convective cooling was not considered in the scaling methodology which might have an impact on the temperature distribution and magnitude.
- There is a small difference in the disc brake geometry between the full and small scale disc brakes, principally the “top hat” structure of the full size disc brake rotor was not present in the small scale rotor.
- The aspect ratio of the brake pad was not considered in the scaling methodology; this has been shown to influence the thermal performance of a disc brake [138, 139].

Different finite element models of the disc brake rotor were developed using Abaqus software to permit detailed interpretation of the experimental results. It was shown that the axisymmetric FE model was the best candidate for the current research compared to the one and three dimensional models for various reasons, but mainly simulation time (CPU).

The thermal response of the full and small scale disc brakes was also investigated using an axisymmetric finite element model and the results confirmed that both discs experienced almost the same maximum surface temperatures under the equivalent simulated braking event. Although there are detailed differences in the temperature distributions because of the effect of different convective cooling regimes and the differing disc geometry, overall the results demonstrated that the scaling methodology

can be used with confidence in the design and development of automotive disc brake systems

The five small scale discs were tested on the dynamometer according to the representative test matrix; the surface temperature of the discs were monitored during all the tests using rubbing thermocouples and a high speed thermal imaging camera (FLIR X6540SC). The friction coefficient between the disc and pad surfaces was evaluated from the hydraulic line pressure (normal load) and brake torque measured using appropriate transducers. The discs were driven to their upper limits in order to observe the effect of elevated temperature on the friction and coating materials. The results show that, after grey cast iron (GCI), the coated aluminium alloy had the best thermal performance of the lightweight rotors tested in terms of structural integrity at elevated temperature. The coefficient of friction of the coated aluminium alloy was stable during the test and showed better performance than the coated and uncoated Al-MMC especially at higher temperature. The CoF for the various disc brake rotors was monitored during the tests; results show that the CoF was close to 0.32 for all the rotors except the plain aluminium alloy where it was around 0.2 which is not acceptable for a modern disc brake. However it should be noted the friction material had been optimised for the alumina coated discs and not for the uncoated MMC surface on which silicon carbide particles may be exposed.

The coated aluminium alloy disc brake rotor operated up to a 500°C surface temperature without any problems and only failed when the surface temperature reached around 550°C. The catastrophic failure of the coated disc resulted from brittle fracture at the grain boundaries within the microstructure of the wrought billet from which the disc brake rotor was machined. Visual inspection of the failed disc brake rotor showed that the failure occurred around the inner radius of the rubbing surface circumferences as shown in Figure 8.22a which was expected as the disc material at this radial distances experience the maximum temperature. Although the disc shattered in a number of separate pieces, Figure 8.22b, the coating on the rubbing surface remained fully attached to the pieces and to the remaining central rotor section. The fracture surface of the failed alloy material had a very fibrous appearance (Figure 8.22c) indicating that the highly uniaxial nature of the crystallised structure of the wrought alloy had induced an

intergranular brittle fracture mode. The aluminium alloy rotors were machined from a forged billet in which the grain boundaries were formed predominantly in the axial direction with respect to the rotor. It is postulated that this led to failure at the grain boundaries around the circumferences of the disc.

On the other hand, the plain aluminium alloy and aluminium metal matrix composite rotors failed to complete the developed test matrix. This was due to surface damage occurring at relatively low temperatures of 200°C and 350°C respectively. In contrast, the coated Al-MMC rotor demonstrated good thermal performance and operated up to 400°C without any damage to the coating or the substrate. The main concern with the coated Al-MMC was the poor coating adhesion which was apparent from the material characterisation analysis.

10.3 Application of surface engineering techniques to understand the capabilities of aluminium alloy brake rotors

The surface morphology of the aluminium-based rotor materials before and after dynamometer testing was investigated using SEM. The variation in thickness of the coating was of the order of 2 µm for the wrought aluminium rotor which is much lower than that of the coated Al-MMC rotor where it was of the order of 10-15 µm, as explained in Chapter 8. The PEO coating on the wrought aluminium alloy was also denser and more uniform when compared to the coating on the Al-MMC substrate as shown by the SEM images of the coating cross section. The coating adhesion was much better for the aluminium alloy compared to Al-MMC, based on the variation of coating thickness which was obtained from the microscopic images. Furthermore, it was found that the PEO coating improved the hardness of the substrate for the wrought aluminium alloy by a factor of 8 to a HV of 500 while it improved the hardness of the Al-MMC only by a factor of 5 to a HV of 980. Based on the EDX characterisation and these SEM images, it was concluded that the Al-alloy had a very dense and uniform coating with alpha/gamma alumina [26, 131] as main elements compared with the Al-MMC. This tends to give a tremendously hard and robust tribo surface with a stable coefficient of friction and, in addition, a good thermal barrier effect as explained in section 8.2.

A transfer layer from the brake pads formed on the rubbing surface of all the aluminium and MMC rotors and the thickness of this layer was in the range 2-4 μm . It is critical that the transfer layer is considered as it changes the thermal interaction between the disc and pad. The transfer layer thickness and properties can be used in the numerical model to give more precise results by physically modelling the transfer layer instead of estimating the effect by means of the heat partitioning ratio between the disc and pad. The disc/pad heat partition ratios for the grey cast iron and coated aluminium alloy disc brake rotors were determined from the experimental data and found to be approximately 0.95 and 0.93 respectively. These partition ratios showed good agreement with those found in the literature.

10.4 Importance of optimisation analysis for coated aluminium alloy rotors

A Taguchi analysis, carried out for the small scale disc brake rotor, showed that the disc thickness had the largest effect on the predicted maximum surface temperature. Based on the Taguchi results, an optimisation analysis was developed for the coated aluminium alloy with a view to minimising the thickness (and therefore weight and cost) of the disc based on different constraints and braking conditions. Material properties have a strong influence on thermal performance but designing a material with specific thermal properties would be far from easy. The optimum design variables found from the optimisation analysis were a coating thickness of 30 μm and a disc thickness of 12.24 mm. The results show that the optimised design can withstand two different aggressive braking events: a prolonged Alpine descent and a repeated high speed Autobahn stop. It was concluded that the coated wrought aluminium rotor could be used to replace the conventional cast iron disc brake rotor in a small to medium sized vehicle taking into consideration appropriate safety margins. The current optimisation methodology can be used for more complex disc brake geometry, such as a vented rotor, in order to further reduce the weight of the disc brake or allow for the safe braking of a heavier vehicle.

One of the main issues with the alumina coated aluminium rotor used in the current research was that all disc surfaces were transferred to alumina which reduced the dissipation of the heat from the disc substrate. The alumina layer on the surfaces of the

disc worked like a thermal barrier (low thermal conductivity) which trapped the heat inside the disc brake substrate and accordingly increased the temperature of the substrate. This behaviour was monitored and observed using the high speed thermal imaging camera as explained in Chapter 7. It would be very advantageous to only coat the rubbing surfaces thereby allowing greater heat loss by convection from the free surfaces.

10.5 Industrial and academic implications for the current work

The results obtained in this research give good evidence that lightweight disc brake rotors can be used in the brake system with proper surface treatment such as PEO coating. One of the main advantages of the PEO coating process is that it is environmental friendly compared with other types of coating process [83]. The main issue with the PEO coating is the slow growth rate of the oxide layer and the high costs. Many researchers investigated the possibility of optimising the parameters of the PEO process in order to enhance the properties and reduce the cost [83, 86]. In this research, the enhancement of the PEO coating to the aluminium alloys substrate showed the huge potential for PEO coated rotor to be used in the braking application but manufacturing parts were not considered.

This thesis can contribute to the academic field in the different ways. Since the relation between the academic and industry fields in surface engineering is limited, this research would help to improve and strengthen the current relationship established between the academic partner (University of Leeds) and the industry (Keronite International). In addition, the subject of surface engineering in the automotive industry has been found to be important in improving and protecting the surfaces of the lightweight alloy brake rotor.

10.6 Summary

The scaling methodology and small scale brake dynamometer were shown to present good approach with which to investigate the thermal performance of a lightweight disc brake rotor in the laboratory with short time and low cost compared with conventional full scale method. The technique permitted the implementation and exploration of

design changes to the rotor concept that were suggested through the numerical analysis. The numerical and experimental approaches demonstrated reliability and consistency in assessing the temperature distribution and the tribological performance of the lightweight rotor. The results showed that the PEO coated aluminium alloy has the best performance compared to the other candidate lightweight rotors. It has been shown that PEO coating can improve the surface of the substrate which promotes the use of lightweight rotor technology in the automotive industry. The optimisation analysis was demonstrated to be effective in designing future lightweight rotors. Finally, the implication of the current work was reviewed in terms of both its industrial and academic dimensions.

CHAPTER 11:

CONCLUSIONS AND FUTURE WORK

11.1 Conclusion

Overall it was concluded that the next generation of lightweight brake rotors could be made from wrought aluminium alloy with an alumina coating, applied using a plasma electrolytic oxidation coating process. Thermal and tribological performances of the coated wrought aluminium alloy were as good as those for standard grey cast iron as explained above. Other findings from the current research are summarised as follows:

- The coating study in Chapter 4 showed that there are different numerical techniques which can be used to model the coating layer in Abaqus which improved the simulation time and the memory usage.
- It was shown that the two dimensional axisymmetric FEM was the best candidate for the current research compared to the one and three dimensional models for different reasons, but mainly to do with the simulation time (CPU).
- The proposed scaling methodology showed good potential for investigating lightweight brake rotors in the laboratory with short operating time and low cost. The scaling method has been validated numerically and experimentally, it showed very good agreement with the full size rotor results with only small differences due to various parameters explained in Chapter 7 and 10.
- Finite element models were developed and validated by comparison with the measured experimental results and showed good agreement. It has been demonstrated in this thesis that thermal modelling is a very important and powerful tool in designing and investigating the thermal performance of a lightweight disc brake rotor concept. In particular, the 2D axisymmetric finite element numerical model showed good agreement with the measured experimental results which gave confidence in using the developed model for further detailed investigation of the thermal performance of a lightweight brake rotor.

-
- It has been shown that the PEO coated Al-alloy had the best overall thermal and tribological performance compared to the plain rotor and the coated Al-MMC. The thermal performance of the coated aluminium alloy is much better than that of other lightweight disc brake rotors because of the following finding of this research.
 - The coated aluminium alloy disc brake rotor was able to withstands up to 500 °C surface temperature without any only problems and fails when the surface temperature reaches about 550 °C. On the other hand, the plain aluminium alloy and aluminium metal matrix composite unable to withstand the most severe braking conditions.
 - The coefficient of friction of the coated aluminium alloy was stable during the test and showed better performance than the coated and uncoated Al-MMC.
 - The thickness variation of the coating was of the order of 2 µm for the wrought aluminium which is much lower compared to the coated Al-MMC where it was of the order of 10-15 µm
 - The PEO coating on aluminium alloy is much denser and more uniform compared to the PEO coating on the aluminium metal matrix composite.
 - The coating adhesion is much better for the aluminium alloy compared to Al-MMC, as noticed in the material characterisation analysis.
 - The alumina coating improves the surface hardness of both wrought aluminium alloy and aluminium metal matrix composite as shown in Chapter 8.
 - Plasma electrolytic oxidation coating was shown to be a good surface engineering option to enhance the surface performance of lightweight materials used in the automotive industry.
 - The transfer layer was evaluated using material characterisation analysis and it was found to be 2-4 µm thick. The transfer layer thickness can be used in the numerical model to give more precise results.
 - Taguchi analysis was carried out for the small scale disc brake rotor and it showed that the disc thickness had the largest effect on the maximum surface temperature.
 - Based on the Taguchi analysis, optimisation analysis was developed for the coated aluminium alloy, with a view to minimising the thickness of the disc based on different constraints and braking conditions. The results showed that the current small scale disc brake rotor was sufficiently robust for a small passenger vehicle.

-
- The results of this study showed that a coated wrought aluminium rotor could be used to replace the conventional cast iron disc brake rotor in a small to medium sized vehicle taking into consideration good safety margins.

The significance of this research is, therefore, that it proves an ability to numerically and experimentally demonstrate the thermal performance of lightweight disc brake rotors made of aluminium alloy with the addition of optimised alumina coating treatments. The present work provides a wide range of information for the automotive researcher in the area of lightweight disc brake rotors for use in the design of future generations of such rotors. The techniques used to assess their thermal and tribological performance and to identify optimum designs are useful tools for researchers in this and related fields and can be expected to improve the design of future lightweight disc brake rotors.

11.2 Suggestions for future work

The present research work could be taking forward by adopting the following recommendations:

- There are a number of areas which need to be improved and further investigated in the scaling methodology as follows:
 - The effect of convection cooling needs to be considered in the scaling methodology since this is likely to have a significant influence on the thermal performance between the full and small scale disc brake rotors.
 - The brake pad geometry (aspect ratio) needs to be investigated in the scaling methodology.
 - The disc brake geometry (particularly the effect of the “top-hat” structure) should be considered in the scaling exercise to make sure that the results obtained for the full and small scale discs are valid.
- In order to replicate real world conditions for any vehicle, the flywheel inertia of the small scale rig needs to be increased according to the scaled vehicle weight and inertia.

-
- The material characterisation analysis shows that the thickness variation of the alumina coating on the aluminium alloy is much lower than for the Al-MMC but further investigations need to be conducted using scratch tests in order to measure the bonding strength for each material with the current PEO coating process.
 - The PEO coating process could be improved in order to achieve better bonding between the alumina coating and substrate especially with the aluminium metal matrix composite.
 - Further investigation of the wear and corrosion resistance of the PEO treated wrought aluminium alloy is essential to make sure that the nominated lightweight coated disc will withstand real world braking events and environmental conditions.
 - The microstructure of the substrate material should be investigated in order to avoid grain boundary failure by improving or changing the manufacturing process of the wrought aluminium alloy.
 - Coated aluminium alloy disc brake rotors with a vented design would improve cooling which might mean that such rotors could be adopted for heavier vehicles. Applying the PEO coating on the rubbing surface only would improve the heat dissipation by convection and thereby minimise the temperature reached in the substrate.
 - The pad material was kept fixed in the current experimental analysis in order to assess the lightweight disc brakes without the effect of different pad materials. Investigation of the effect of different pad materials is required to improve the thermal and tribological performance of both disc and brake pad and so produce a friction pair that is in every way optimised.

REFERENCES

- [1] European Federation for Transport and Environment AISBL. 2012 [Accessed December 2012]; Available from: <http://www.transportenvironment.org/>.
- [2] Kim, M. R., Ahn, B. K., Lee, J. M., and Jung, Y. K., "Numerical Investigation of Thermal Behavior in Brake Assembly During the ALPINE braking Mode," *SAE Technical paper, 2007-01-1021*, 2007.
- [3] Sheridan, D. C., Kutchev, J. A., and Samie, F., "Approaches to the Thermal Modelling of Disc Brakes," *SAE Technical Paper, 880256*, 1988.
- [4] El-Sharkawy, A. E., "Transient One-dimensional Thermal Analysis of Automotive Components for Determination of Thermal Protection Requirements," *SAE Technical paper, 2008-01-0733*, 2008.
- [5] Tonchev, A., Hirschberg, W., and Jagsch, S., "Investigation of the Thermal Vehicle Brake Behavior During the Vehicle's Development Phase by Co-Simulation," *SAE Technical Paper 2007-01-3935*, vol., 2007.
- [6] Nutwell, B. and Ramsay, T., "Modelling the Cooling Characteristics of a Disk Brake on an Inertia Dynamometer, Using Combined Fluid Flow and Thermal Simulation," *SAE Technical paper, 2009-01-0861*, vol., 2009.
- [7] Alnaqi, A. A., Barton, D. C., and Brooks, P. C., *Thermal Performance of Monolithic and Coated Disc Brakes Using Abaqus and Matlab Software*, Vienna, Austria, SIMULIA Community Conference, 2013.
- [8] Zaid, M. A., Radzai, M. S., Ahmad, R., Ridzuan, M. M., Nurfaizey, A. H., and Afzanizam, M. M. R., "An investigation of disc brake rotor by finite element analysis," *Journal of Advanced Manufacturing and Technology*, vol. Vol. 3 No. 2, pp. 37-48, 2009.
- [9] Newcomb, T. P., "Transient temperatures attained in disk brakes," *British Journal of Applied Physics*, vol. 10, pp. 339-340, 1959.
- [10] Newcomb, T. P., "Temperatures reached in disc brakes " *J. Mech. Engng Sci*, vol. 2 (3), pp. 167-177, 1960.

-
- [11] Abbas, S. A., Cubitt, N. J., and Hooke, C. J., "Temperature distributions in disc brakes," *Proc. Instn Mech. Engrs*, vol. **184**(2A)(9), pp. 185-194, 1969-70.
- [12] Amin, A. M., Seri, S. M., and Raghavan, V. R., "Study of the temperature distribution in disc brakes by the method of order-of-magnitude analysis " *Regional Conference on Engineering Mathematics, Mechanics, Manufacturing & Architecture*, 2007.
- [13] Jun, K. J., Park, T. W., Jung, S. P., Lee, S. H., and Yoon, J. W., "Development of a numerical method to predict the alpine test result," *Proceedings of the Institution of Mechanical Engineers Part D-Journal of Automobile Engineering*, vol. 222, pp. 1841-1849, 2008.
- [14] Mcphee, A. D. and Johnson, D. A., "Experimental heat transfer and flow analysis of a vented brake rotor," *International Journal of Thermal Sciences*, vol. 47, pp. 458-467, 2008.
- [15] Talati, F. and Jalalifar, S., "Analysis of heat conduction in a disk brake system," *Heat and Mass Transfer*, vol. 45, pp. 1047-1059, 2009.
- [16] Adamowicz, A. and Grzes, P., "Analysis of disc brake temperature distribution during single braking under non-axisymmetric load," *Applied Thermal Engineering*, vol. 31, pp. 1003-1012, 2011.
- [17] Alsaif, M. A., Dahm, K. L., Shrestha, S., Dearnley, P. A., and Barton, D. C., *Plasma Electrolytic Oxidation (PEO) treated aluminium metal matrix composite rotors for lightweight automotive brakes*, France, 2010.
- [18] Bozic, G., Alnaqi, A. A., Brooks, P. C., and Barton, D. C., "Thermal Characterisation of Lightweight Brake Rotors for Passenger Car Application Using A small Scale Brake Dynamometer and One Dimensional Model," *Eurobrake 2012*, Germany, 2012.
- [19] Grieve, D. G., Barton, D. C., Crolla, D. A., and Buckingham, J. T., "Design of a lightweight automotive brake disc using finite element and Taguchi techniques," *Proceedings of the Institution of Mechanical Engineers. Part D: Journal of Automobile Engineering*, vol. 212(4), pp. 245-254, 1997.

-
- [20] Dahm, K. L., Black, A. J., Shrestha, S., and Dearnley, P. A., "Plasma Electrolytic Oxidation treatment of aluminium alloys for lightweight disc brake rotors," *IMEchE Conference on Braking*, York (UK), pp. 53-60, 2009.
- [21] Qu, J., Blau, P. J., and Jolly, B. C., "Oxygen-diffused titanium as a candidate brake rotor material," *Wear*, vol. 267, pp. 818-822, 2009.
- [22] Blau, P. J. and Meyer, H. M., "Characteristics of wear particles produced during friction tests of conventional and unconventional disc brake materials," *Wear*, vol. 255, pp. 1261-1269, 2003.
- [23] Bensalah, W., Elleuch, K., Feki, M., DePetris-Wery, M., and Ayedi, H. F., "Comparative study of mechanical and tribological properties of alumina coatings formed on aluminium in various conditions," *Materials & Design*, vol. 30, pp. 3731-3737, 2009.
- [24] Bolelli, G., Lusvarghi, L., and Barletta, M., "HVOF-sprayed WC-CoCr coatings on Al alloy: Effect of the coating thickness on the tribological properties," *Wear*, vol. 267, pp. 944-953, 2009.
- [25] Curran, J. A. and Clyne, T. W., "The thermal conductivity of plasma electrolytic oxide coatings on aluminium and magnesium," *Surface & Coatings Technology*, vol. 199, pp. 177-183, 2005.
- [26] Cui, S. H., Han, J. M., Du, Y. P., and Li, W. J., "Corrosion resistance and wear resistance of plasma electrolytic oxidation coatings on metal matrix composites," *Surface & Coatings Technology*, vol. 201, pp. 5306-5309, 2007.
- [27] Malayoglu, U., Tekin, K. C., Malayoglu, U., and Shrestha, S., "An investigation into the mechanical and tribological properties of plasma electrolytic oxidation and hard-anodized coatings on 6082 aluminum alloy," *Materials Science and Engineering a-Structural Materials Properties Microstructure and Processing*, vol. 528, pp. 7451-7460, 2011.
- [28] Sabatini, G., Ceschini, L., Martini, C., Williams, J. A., and Hutchings, I. M., "Improving sliding and abrasive wear behaviour of cast A356 and wrought

-
- AA7075 aluminium alloys by plasma electrolytic oxidation," *Materials & Design*, vol. 31, pp. 816-828, 2010.
- [29] Shrestha, S. and Dunn, B. D., "Advanced plasma electrolytic oxidation treatment for protection of light weight materials and structures in a space environment " *Advanced Surface Treatment*, vol., pp. 40-44, 2007.
- [30] Shrestha, S., Merstallinger, A., Sickert, D., and Dunn, B. D., *Some preliminary evaluations of black coating on aluminium AA2219 alloy produced by plasma electrolytic oxidation (PEO) process for space applications*, 2003.
- [31] Yerokhin, A. L., Nie, X., Leyland, A., Matthews, A., and Dowey, S. J., "Plasma electrolysis for surface engineering," *Surface & Coatings Technology*, vol. 122, pp. 73-93, 1999.
- [32] Gu, W.-C., Lv, G.-H., Chen, H., Chen, G.-L., Feng, W.-R., and Yang, S.-Z., "Characterisation of ceramic coatings produced by plasma electrolytic oxidation of aluminum alloy," *Materials Science and Engineering a-Structural Materials Properties Microstructure and Processing*, vol. 447, pp. 158-162, 2007.
- [33] Cui, S., Han, J., Li, W., Kang, S.-B., and Lee, J.-M., "Study on wear behavior of plasma electrolytic oxidation coatings on aluminum alloy," *Rare Metals*, vol. 25, pp. 141-145, 2006.
- [34] Kalkanci, H. and Kurnaz, S. C., "The effect of process parameters on mullite-based plasma electrolytic oxide coatings," *Surface & Coatings Technology*, vol. 203, pp. 15-22, 2008.
- [35] Curran, J. A., Kalkanci, H., Magurova, Y., and Clyne, T. W., "Mullite-rich plasma electrolytic oxide coatings for thermal barrier applications," *Surface & Coatings Technology*, vol. 201, pp. 8683-8687, 2007.
- [36] Tsang, P. H. S., Jacko, M. G., and Rhee, S. K., "Comparison of Chase and Inertial Brake Dynamometer Testing of Automotive Materials," *Wear*, vol. 103, pp. 217-232, 1985.

-
- [37] Sanders, P. G., Dalka, T. M., and Basch, R. H., "A reduced-scale brake dynamometer for friction characterization," *Tribology International*, vol. 34, pp. 609-615, 2001.
- [38] Anderson, A., Gratch, S., and Hayes, H., "A new laboratory friction and wear test for the characterization of brake linings."
- [39] Burkman, A. J. and Highley, F. H., "Laboratory Evaluation of Brake Lining Materials," *SAE Transactions*, vol. 76, pp. 125-&, 1968.
- [40] Kermc, M., Kalin, M., Vizintin, J., and Stadler, Z., "A reduced-scale testing machine for tribological evaluation of brake materials," *Life Cycle Tribology*, vol., pp. 799-806, 2005.
- [41] Desplanques, Y., Roussette, O., Degallaix, G., Copin, R., and Berthier, Y., "Analysis of tribological behaviour of pad-disc contact in railway braking - Part 1. Laboratory test development, compromises between actual and simulated tribological triplets," *Wear*, vol. 262, pp. 582-591, 2007.
- [42] Siroux, M., Cristol-Bulthe, A.-L., Desplanques, Y., Desmet, B., and Degallaix, G., "Thermal analysis of periodic sliding contact on a braking tribometer," *Applied Thermal Engineering*, vol. 28, pp. 2194-2202, 2008.
- [43] Wahlstrom, J., Soderberg, A., Olander, L., Jansson, A., and Olofsson, U., "A pin-on-disc simulation of airborne wear particles from disc brakes," *Wear*, vol. 268, pp. 763-769, 2010.
- [44] Akay, A., Giannini, O., Massi, F., and Sestieri, A., "Disc brake squeal characterization through simplified test rigs," *Mechanical Systems and Signal Processing*, vol. 23, pp. 2590-2607, 2009.
- [45] Voller, G. P., Tirovic, M., Morris, R., and Gibbens, P., "Analysis of automotive disc brake cooling characteristics," *Proceedings of the Institution of Mechanical Engineers Part D-Journal of Automobile Engineering*, vol. 217, pp. 657-666, 2003.

-
- [46] Kermc, M., Kalin, M., and Vizintin, J., "Development and use of an apparatus for tribological evaluation of ceramic-based brake materials," *Wear*, vol. 259, pp. 1079-1087, 2005.
- [47] Roussette, O., Desplanques, Y., and Degallaix, G., "Thermal representativity of tribological reduced-scale testing," *Comptes Rendus Mecanique*, vol. 331, pp. 343-349, 2003.
- [48] Narayanan, A., Toropov, V. V., Wood, A. S., and Campean, I. F., "Simultaneous model building and validation with uniform designs of experiments," *Engineering Optimization*, vol. 39, pp. 497-512, 2007.
- [49] Hughes, T. P. and Sperry, E., "*Inventor and Engineer*," MD: John Hopkins Press, Baltimore, 1971.
- [50] Maluf, O., Angeloni, M., Milan, M. T., Spinelli, D., and Filho, W. W. B., "Development of materials for automotive disc brakes," *Minerva*, vol. 4(2), pp. 149-158, 2004.
- [51] Duffy, J. E., "*Modern Automotive technology*," The Goodheart-Willcox Company, INC, United States of America, 2004.
- [52] Rowson, D. M., "The interfacial surface temperature of a disc brake," *Wear*, vol. 47, pp. 323 - 328, 1978.
- [53] Yano, M. and Murata, M., "Heat Flow on Disc Brakes," *SAE Technical Paper 931084*, vol., pp. 119 - 124, 1993.
- [54] Sakamoto, H., "Heat convection and design of brake discs," *Proceedings of the Institution of Mechanical Engineers Part F-Journal of Rail and Rapid Transit*, vol. 218, pp. 203-212, 2004.
- [55] Day, A. J., Tirovic, M., and Newcomb, T. P., "Thermal effects and pressure distributions in brakes," *Proc Instn Mech Engrs*, vol. Vol 205, pp. 199-205, 1991.
- [56] Brooks, P. C., Barton, D. C., Crolla, D. A., Lang, A. M., and Schafer, D. R., *A new approach to disc brake judder using a thermo-mechanical finite element model*, Birmingham, UK, 16-19 November 1993.

-
- [57] Eltoukhy, M., Asfour, S., Almakky, M., and Huang, C., "Thermoelastic Instability in Disk Brakes: Simulation of the Heat Generation Problem," *Proceeding of the COMSOL Users Conference*, Boston, 2006.
- [58] Cueva, G., Sinatora, A., Guesser, W. L., and Tschiptschin, A. P., "Wear resistance of cast irons used in brake disc rotors," *Wear*, vol. 255, pp. 1256-1260, 2003.
- [59] Zhu, Z.-c., Peng, Y.-x., Shi, Z.-y., and Chen, G.-a., "Three-dimensional transient temperature field of brake shoe during hoist's emergency braking," *Applied Thermal Engineering*, vol. 29, pp. 932-937, 2009.
- [60] Hwang, P. and Wu, X., "Investigation of temperature and thermal stress in ventilated disc brake based on 3D thermo-mechanical coupling model," *Journal of Mechanical Science and Technology*, vol. 24, pp. 81-84, 2010.
- [61] Neis, P. D., Kruze, G. A. S., and Ferreira, N. F., "Relation between the temperature of the disc measured with thermocouple and by thermography using a reduced scale dynamometer," *ABCM Symposium Series in Mechatronics*, vol. 4 pp. pp.907-913, 2010.
- [62] Barton, D. C., "Modelling of materials for automotive braking," *International Materials Reviews*, vol. 49, pp. 379-385, 2004.
- [63] Maleque, M. A., S.Dyuti, and Rahman, M. M., "Material Selection Method in Design of Automotive Brake Disc," *Proceedings of the World Congress on Engineering*, London, UK, 2010.
- [64] Polmear, I. J., "*Light alloys: metallurgy of the light metals*," E. Arnold, 1982.
- [65] Downs, A. J., "*Chemistry of aluminium, gallium, indium, and thallium*," Blackie Academic & Professional, London; New York, 1993.
- [66] King, F., "*Aluminium and its alloys*," Ellis Horwood, 1987.
- [67] European aluminium association. "The development of aluminium as a product", 2009 [Accessed 2012]; Available from: <http://www.alueurope.eu/development-aluminium-product/>.

-
- [68] Ron Cobden and Alcan Banbury, *Aluminium: Physical Properties, Characteristics and Alloys*, European Aluminium Association, 1994.
- [69] Gulf Aluminium Council. "Aluminium Application", 2013 [Accessed 2013]; Available from: <http://www.gac.ae/Aluminium-Applications.aspx>.
- [70] Davis, J. R., "*Surface Engineering for Corrosion and Wear Resistance*," ASM International, 2001.
- [71] Matthews, A., Artley, R., and P, H., "*2005 revisited - The UK surface engineering industry to 2010*," NASURF, 1998.
- [72] Morton, P. H., Institute of Metals, and Centre for the Exploitation of Science and Technology, "*Surface engineering and heat treatment: past, present and future*," Institute of Metals, 1991.
- [73] Adebisi, A. A., Maleque, M. A., and Rahman, M. M., "Metal Matrix Composite Brake Rotor: Historical Development and Product Life Cycle Analysis," *International Journal of Automotive and Mechanical Engineering*, vol. 4, pp. pp. 471-480, 2011.
- [74] European Cooperation for Space Standardisation, *Structural materials handbook - Part 5: New advanced materials, advanced metallic materials, general design aspects and load transfer and design of joints*, Netherlands, 2011.
- [75] Natarajan, N., Vijayarangan, S., and Rajendran, I., "Fabrication, testing and thermal analysis of metal matrix composite brake drum," *International Journal of Vehicle Design*, vol. 44, pp. 339-359, 2007.
- [76] Prasad, S. V. and Asthana, R., "Aluminum metal-matrix composites for automotive applications: tribological considerations," *Tribology Letters*, vol. 17, pp. 445-453, 2004.
- [77] Swift C. "Business Communications Company (BBC), Inch", 2009 2013 [Accessed 2013]; Available from: <http://www.bccresearch.com/market-research/advanced-materials/metal-matrix-composites-market-avm012d.html>.

-
- [78] Rajan, T. P. D., Pillai, R. M., and Pai, B. C., "Reinforcement coatings and interfaces in aluminium metal matrix composites," *Journal of Materials Science*, vol. 33, pp. 3491-3503, 1998.
- [79] Rosso, M., "Ceramic and metal matrix composites: Routes and properties," *Journal of Materials Processing Technology*, vol. 175, pp. 364-375, 2006.
- [80] Cui, S., Han, J., Du, Y., and Li, W., "Corrosion resistance and wear resistance of plasma electrolytic oxidation coatings on metal matrix composites," *Surface & Coatings Technology*, vol. 201 pp. 5306-5309, 2006.
- [81] Curran, J. A. and Clyne, T. W., "The thermal conductivity of plasma electrolytic oxide coatings on aluminium and magnesium," *Surface & Coatings Technology*, vol. 199, pp. 177-183, 2005.
- [82] Algahtani, A. M. A., "Optimising aluminium alloy surfaces for wear and corrosion controlled by Plasma Electrolytic Oxidation (PEO)," PhD, School of Mechanical Engineering, University of Leeds, Leeds, 2013.
- [83] Hussein, R. O., Nie, X., and Northwood, D. O., "Influence of process parameters on electrolytic plasma discharging behaviour and aluminum oxide coating microstructure," *Surface & Coatings Technology*, vol. 205, pp. 1659-1667, 2010.
- [84] Tekin, K. C., Malayoglu, U., and Shrestha, S., "Tribological properties of plasma electrolytic oxide coatings on magnesium alloys," *Tribology - Materials, Surfaces & Interfaces*, vol. 6, pp. 67-74, 2012.
- [85] Gu, W.-C., Lv, G.-H., Chen, H., Chen, G.-L., Feng, W.-R., and Yang, S.-Z., "PEO protective coatings on inner surface of tubes," *Surface & Coatings Technology*, vol. 201, pp. 6619-6622, 2007.
- [86] Yerokhin, A. L., Shatrov, A., Samsonov, V., Shashkov, P., Pilkington, A., Leyland, A., and Matthews, A., "Oxide ceramic coatings on aluminium alloys produced by a pulsed bipolar plasma electrolytic oxidation process," *Surface & Coatings Technology*, vol. 199, pp. 150-157, 2005.

-
- [87] Matykina, E., Arrabal, R., Skeldon, P., and Thompson, G. E., "Optimisation of the plasma electrolytic oxidation process efficiency on aluminium," *Surface and Interface Analysis*, vol. 42, pp. 221-226, 2010.
- [88] Demir, A., Samur, R., and Kilicaslan, I., "Investigation of the coatings applied onto brake discs on disc brake pad pair," *METALURGIJA*, vol. 48, pp. 161-166, 2009.
- [89] Shrestha, S., Shashkov, P., and Dunn, B. D., "Microstructural and Thermo-Optical Properties of Black Keronite PEO Coating on Aluminium Alloy AA7075 for Spacecraft Materials," *10th Symposium on Materials in a Space Environment*, Colliour, France, 2006.
- [90] Curran, J. A., *An Industrial Perspective of Coating Production on Titanium*, Keronite International Ltd, 2013.
- [91] Chi, Z., "Thermal Performance Analysis and Geometrical Optimization of Automotive Brake Rotors," Master of Applied Science, Mechanical Engineering, University of Ontario Institute of Technology, 2008.
- [92] Qian, C., *Aerodynamic Shape Optimization using CFD Parametric Model with Brake Cooling Application*, Detroit, Michigan, March 4-7, 2002.
- [93] Amouzgar, K., Rashid, A., and Stromberg, N., *Multi-Objective Optimization of a Disc Brake System by Using SPEA2 and RBFN*, ASME, Portland, Oregon, USA, 2013.
- [94] QU Jie and SU Hai-fu, "Optimization Design on Ventilated Disc Brake Based on Surrogate Model Technology," *Engineering Mechanics*, vol. 30, pp. 332-339, 2013.
- [95] Viana, F. A. C., Venter, G., and Balabanov, V., "An algorithm for fast optimal Latin hypercube design of experiments," *International Journal for Numerical Methods in Engineering*, vol. 82, pp. 135-156, 2010.
- [96] McKay, M. D., Beckman, R. J., and Conover, W. J., "A comparison of Three Methods for Selecting Values of Input Variables in the Analysis of Output from A computer Code," *Technometrics*, vol. 21, pp. 239-245, 1979.

-
- [97] Iman, R. L. and Conover, W. J., "Small Sample Sensitivity Analysis Techniques for Computer-Models, with an Application to Risk Assessment," *Communications in Statistics Part a-Theory and Methods*, vol. 9, pp. 1749-1842, 1980.
- [98] Lober, D. "Information about steel for metallographer ", [Accessed 13/07/2012]; Available from: <http://www.metallograf.de/start-eng.htm?werkstoffkartei-eng/0-6025/6025.htm>.
- [99] "KEY to METALS ", [Accessed 20/08/2012]; Available from: www.keytometals.com.
- [100] *Wrought aluminium and aluminium alloys for general engineering purposes: bars, extruded round tubes and sections*, BSI, London, 1998.
- [101] Warmuzek, M., "*Metallographic Techniques for Aluminum and Its Alloys*," Foundry Research Institute Krakow, Poland, 2004.
- [102] Incropera, F. P., Dewitt, D. P., Bergman, T. L., and Lavine, A. S., "*Fundamentals of Heat and Mass Transfer*," Sixth Edition ed., John Wiley and Sons Inc, 2007.
- [103] Limpert, R., "*Brake Design and Safety*," Society of Automotive Engineers, Inc, 1999.
- [104] Tirovic, M. and Voller, G. P., "Interface pressure distributions and thermal contact resistance of a bolted joint," *Proceedings of the Royal Society a-Mathematical Physical and Engineering Sciences*, vol. 461, pp. 2339-2354, 2005.
- [105] Day, A. J., "*Friction and Friction Materials*," University of Bradford, 2010.
- [106] "AMC640xa data sheet", [Accessed 04/10 2012]; Available from: http://www.amc-mmc.co.uk/640xa_data.htm.
- [107] "Aluminium Alloy // Commercial Alloy // 6082 - T6~T651 datasheet", [Accessed 04/10 2012]; Available from: http://www.aalco.co.uk/datasheets/Aluminium-Alloy_6082-T6~T651_148.ashx.

-
- [108] "Federal-Mogul eCatalog", [Accessed 04/10 2012]; Available from: <http://www.fmecat.eu/index-car.asp>.
- [109] Carslaw, H. S. and Jaeger, J. C., "*Conduction of Heat in Solids*," Second Edition ed., Oxford University Press, Oxford, 1959.
- [110] Lee, K. J., "Numerical prediction of brake fluid temperature rise during braking and heat soaking.," *SAE paper 1999-01-0483*, vol., 1999.
- [111] Jun, K.-J., Park, T.-W., Jung, S.-P., Lee, S.-H., and Yoon, J.-W., "Development of a numerical method to predict the alpine test result," *Proc. IMechE Part D: J. Automobile Engineering*, vol. Vol. 222, pp. 1841-1849, 2008.
- [112] *ABAQUS Documentation*, Dassault Systèmes, Providence, RI, USA, 2011.
- [113] Linck, V., Bayada, G., Baillet, L., Sassi, T., and Sabil, J., "Finite element analysis of a contact with friction between an elastic body and a thin soft layer," *Journal of Tribology-Transactions of the Asme*, vol. 127, pp. 461-468, 2005.
- [114] Gao, C. H. and Lin, X. Z., "Transient temperature field analysis of a brake in a non-axisymmetric three-dimensional model," *Journal of Materials Processing Technology*, vol. 129, pp. 513-517, 2002.
- [115] "<http://www.auto-data.net/en/>", [Accessed 10 Nov 2013].
- [116] Nexen Group Inc. "Metric L-600 950150 Shaft Mounted Clutch", <<http://www.nexengroup.com/default/products/details/id/950150>> [Accessed 26/08/ 2011].
- [117] Linear Mech, *ACME SCREW LINEAR ACTUATOR*, 2012.
- [118] Bozic, G., "Development and Modelling of a Small-Scale Brake Test Rig," MSc thesis, Mechanical Engineering, University of Leeds, Leeds, 2011.
- [119] Wilwood Engineering Inc. "Automotive", 2011 [Accessed 24/08/2011; Available from: <http://www.wilwood.com/>.
- [120] National Instruments Corporation. "BNC-2090", 2011 [Accessed 29/10/2011]; Available from: <http://uk.ni.com/>.

-
- [121] Honeywell. "HOA2001 Series Transmissive Optoschmitt Sensor", 2011 [Accessed 24/8/2011]; Available from: <http://sensing.honeywell.com/sensinghome>.
- [122] RS Components Ltd. "RS TYPE 461 PRESSURE TRANSDUCERS", 2011 [Accessed 13/09/2011]; Available from: <http://uk.rs-online.com/web/>.
- [123] TKsensors. "HTA1001 rubbing thermocouple ", 2011 [Accessed 21/07/2011]; Available from: <http://www.tksensors.co.uk/>.
- [124] "Brake system dynamometer test procedures—passenger Car-SAE J212 JAN98," 2000 SAE Handbook, Vol. 2, SAE Inc., Warrendale, PA, 2000, pp. 25.173–25.177
- [125] SAE International, *SAE J2521-Disc Brake Dynamometer Squeal Matrix*, Warrendale PA: SAE International, 2006.
- [126] Loizou, A., "Modelling and Simulation of Thermo-Mechanical Phenomena at the Friction Interface of a Disc Brake," PhD, School of Engineering, Design and Technology, University of Bradford, Bradford, 2012.
- [127] SAE International, *SAE J2521-Disc Brake Dynamometer Squeal Matrix*, Warrendale PA: SAE International, 2003.
- [128] Curran, J. A., "Thermal and Mechanical Properties of Plasma Electrolytic Oxide Coatings," PhD, University of Cambridge, 2005.
- [129] Lv, G.-H., Gu, W.-C., Chen, H., Li, L., Niu, E.-W., and Yang, S.-Z., "Microstructure and corrosion performance of oxide coatings on aluminium by plasma electrolytic oxidation in silicate and phosphate electrolytes," *Chinese Physics Letters*, vol. 23, pp. 3331-3333, 2006.
- [130] AMATO, F., FONT, O., MORENO, N., ALASTUEY, A., and QUEROL, X., "Mineralogy and elemental composition of brake pads of common use in Spain," *Spanish Mineralogical Society*, vol. Macla 16, pp. 154-155, 2012.

-
- [131] Xue, W., Wu, X., Li, X., and Tian, H., "Anti-corrosion film on 2024/SiC aluminum matrix composite fabricated by microarc oxidation in silicate electrolyte," *Journal of Alloys and Compounds*, vol. 425, pp. 302-306, 2006.
- [132] Alnaqi, A. A., Shrestha, S., Brooks, P. C., and Barton, D. C., "Thermal Performance of PEO Coated Lightweight Brake Rotors Compared with Grey Cast Iron," *Eurobrake 2014*, France, 2014.
- [133] Cochrane, R., *Aluminium grain boundaries failure*, Leeds, Personal Communication, 2014.
- [134] Taguchi, G., "*System of Experimental Design*," American Suppliers Institute, INC, Dearborn, Michigan, 1987.
- [135] Taguchi, G., "*Taguchi on robust technology development*," ASME Press, New York, 1993.
- [136] Fowlkes, W. Y. and Creveling, C. M., "*Engineering methods for robust product design: Using Taguchi methods in technology and product development*," Corporate & Professional Publishing Group, Reading, Massachusetts, 1995.
- [137] *Hyperstudy v12*, Altair Engineering, Inc., 2012.
- [138] Kuppanda, V. G., "Reduced scale testing and analysis of brake system," MSc, Mechanical engineering, University of leeds, Leeds, 2013.
- [139] Prabhu, V., "The importance of pad aspect ratio in thermal analysis of reduced scale brake," MSc, Mechanical engineering, University of leeds, Leeds, 2014.

APPENDIX A:

ASSEMBLY AND DISASSEMBLY

PROCEDURE

The general guidelines for assembling the small scale test rig are as follows:

1. Slide the two bearings and flywheel onto the main shaft.
2. Place the bearings onto their support blocks.
3. Fix the shaft to the bearings using the lock nut and washer.
4. Fix the shaft encoder on the shaft.
5. Slide the clutch unit onto the shaft.
6. Bolt the adapter to the clutch unit and the coupling to the adapter.
7. Slide and bolt the DC motor into place.
8. Fit the brake disc and bolt adapter onto the shaft and lock the bolts.
9. Assemble the caliper support.
10. Insert the pads into the caliper and fix it to the pivoted arm.
11. Adjust height over the load cell so that the support arm is horizontal and aligned with the shaft centre.
12. Mount the master cylinder and the linear actuator.
13. Connect and bleed the brake lines. Make sure to fit the pressure transducer close to the caliper.
14. Attach the sliding thermocouples.
15. Fit the flywheel and motor enclosure.

The small scale test rig disassembly is similar to the assembly process but in reverse order. The completed 3D model of the small scale test rig is shown in Figure A. 1 and the actual test rig is shown in Figure A. 2.

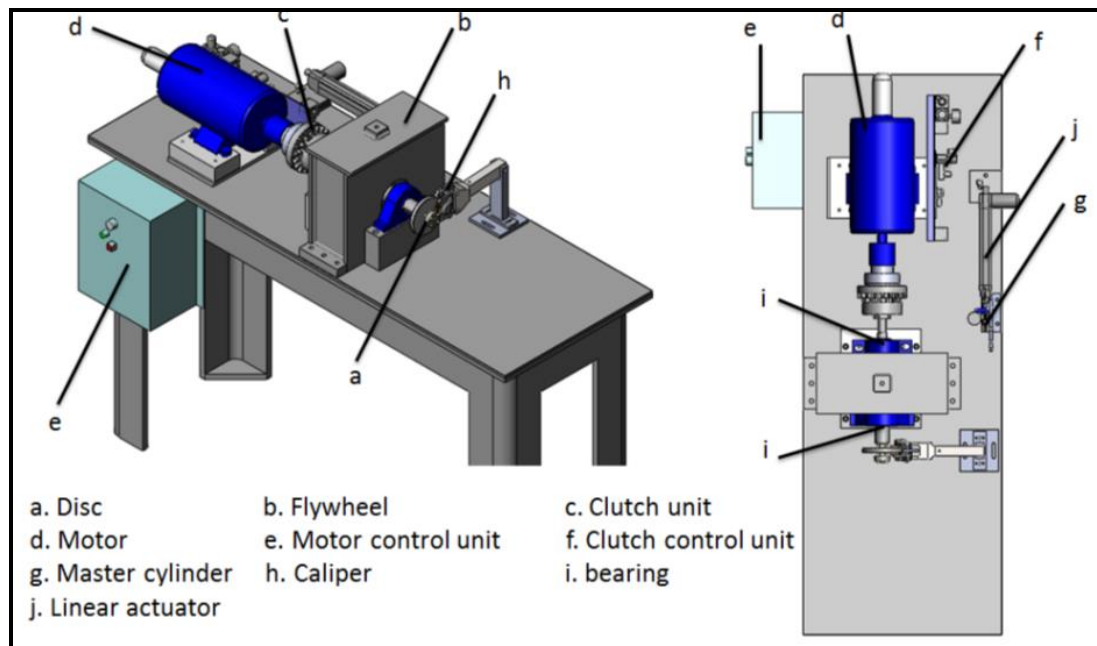


Figure A. 1: CAD representation of the main components of the reduced brake test rig.

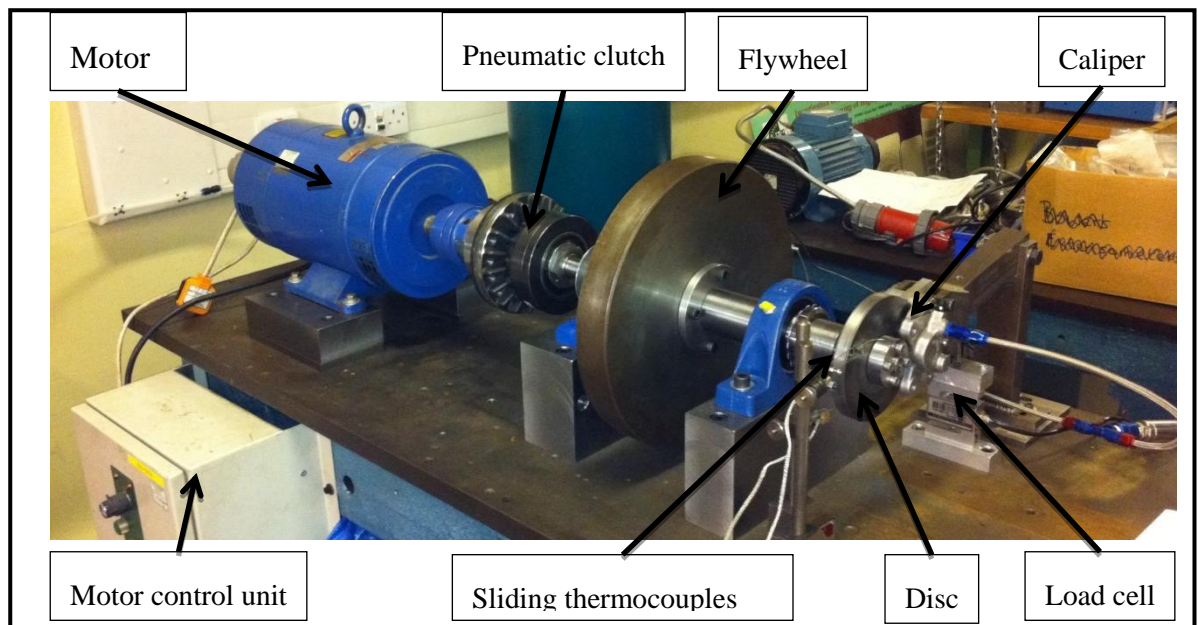


Figure A. 2: Small scale test rig.

Most of the design issues of the small scale test rig were handled by an MSc student who completed the load and stress analysis to make sure that the rig was safe to operate under different braking conditions [118].

APPENDIX B: TEST RIG COMMISSIONING OUTPUT

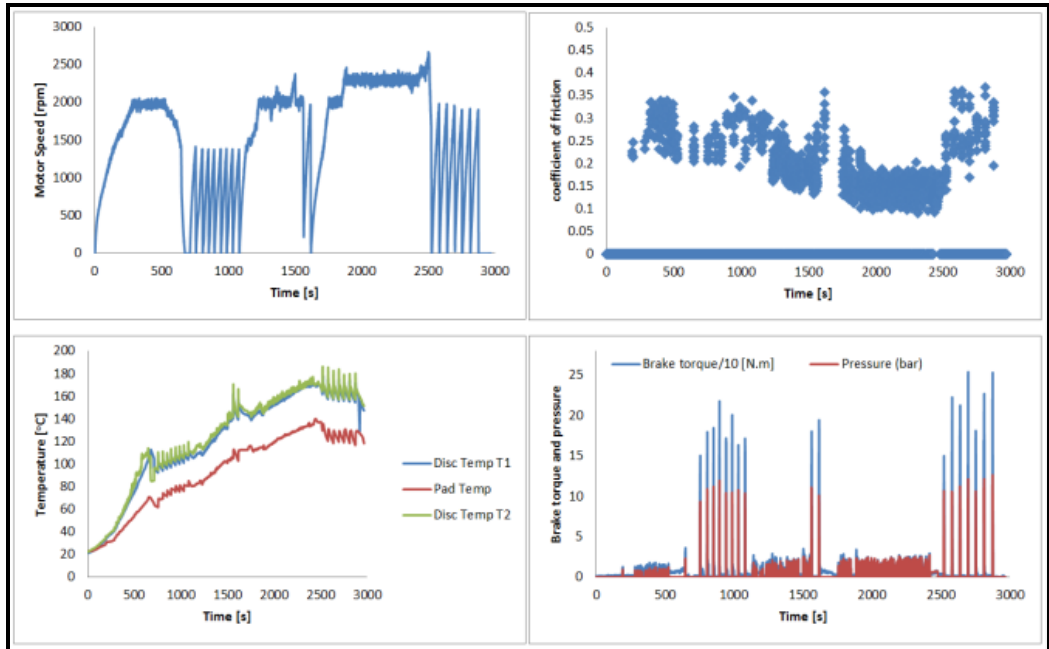


Figure B. 1: Commissioning results for small scale dynamometer.

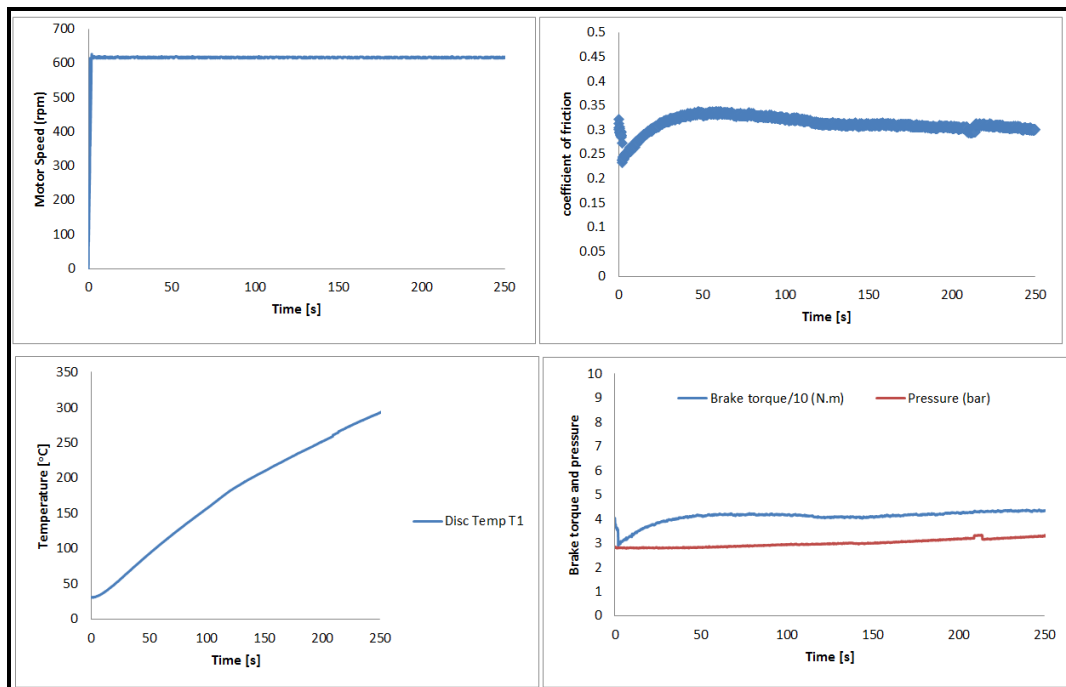


Figure B. 2: Commissioning results for the full scale brake dynamometer.

APPENDIX C: LIST OF PUBLICATIONS

Some parts of the current research work have been published or are in the process of being published as follows:

Paper	Status
G. Bozic, A. A. Alnaqi, P. C. Brooks, and D. C. Barton, "Thermal Characterisation of Lightweight Brake Rotors for Passenger Car Application Using A small Scale Brake Dynamometer and One Dimensional Model," <i>Eurobrake 2012</i> , Germany, 2012.	Published
A. A. Alnaqi, D. C. Barton, and P. C. Brooks, <i>Thermal Performance of Monolithic and Coated Disc Brakes Using Abaqus and Matlab Software</i> , Vienna, Austria, SIMULIA Community Conference, 2013.	Published
A. A. Alnaqi, S. Shrestha, P. C. Brooks, and D. C. Barton, "Thermal Performance of PEO Coated Lightweight Brake Rotors Compared with Grey Cast Iron," <i>Eurobrake 2014</i> , lille, France, 2014.	Published
A. A. Alnaqi, S. Shrestha, P. C. Brooks, and D. C. Barton, "Optimisation of alumina coated lightweight brake rotor," <i>SAE 2014-01-2501</i> , USA, 2014.	Published
A. A. Alnaqi, D. C. Barton, and P. C. Brooks, "Reduced scale thermal characterization of automotive disc brake," <i>Applied thermal engineering</i> , 2014.	Published
A. A. Alnaqi, S. Kosarieh, D. C. Barton, P. C. Brooks, and S. Shrestha, "Material characterisation of lightweight disc brake rotors," <i>Surface and Coating Technology</i> , 2014.	Processing